CHARACTERIZING TWO CARBONATE FORMATIONS FOR C0$_2$-EOR AND CARBON GEOSEQUESTRATION: APPLICABILITY OF EXISTING ROCK PHYSICS MODELS AND IMPLICATIONS FOR FEASIBILITY OF A TIME LAPSE MONITORING PROGRAM IN THE WELLINGTON OIL FIELD, SUMNER COUNTY, KANSAS.

by

ANTHONY LUECK

B.S., Iowa State University, 2012

A THESIS

submitted in partial fulfillment of the requirements for the degree

MASTER OF SCIENCE

Department of Geology
College of Arts and Sciences

KANSAS STATE UNIVERSITY
Manhattan, Kansas

2017

Approved by:

Major Professor
Dr. Abdelmoneam Raef

Copyright

ANTHONY LUECK

2017

Abstract

This study focuses on characterizing subsurface rock formations of the Wellington Field, in Sumner County, Kansas, for both geosequestration of carbon dioxide (CO_2) in the saline Arbuckle formation, and enhanced oil recovery of a depleting Mississippian oil reservoir. Multi-scale data including rock core plug samples, laboratory ultrasonic P-&S-waves, X-ray diffraction, and well log data including sonic and dipole sonic, is integrated in an effort to evaluate existing rock physics models, with the objective of establishing a model that best represents our reservoir and/or saline aquifer rock formations. We estimated compressional and shear wave velocities of rock core plugs for a Mississippian reservoir and Arbuckle saline aquifer, based on first arrival times using a laboratory setup consisting of an Ult 100 Ultrasonic System, a 12-ton hydraulic jack, and a force gauge; the laboratory setup is located in the geophysics lab in Thompson Hall at Kansas State University. The dynamic elastic constants Young's Modulus, Bulk Modulus, Shear (Rigidity) Modulus and Poisson's Ratio have been calculated based on the estimated P- and S-wave velocity data. Ultrasonic velocities have been compared to velocities estimated based on sonic and dipole sonic log data from the Wellington 1-32 well. We were unable to create a transformation of compressional wave sonic velocities to shear wave sonic for all wells where compressional wave sonic is available, due to a lack of understandable patterns observed from a relatively limited dataset. Furthermore, saturated elastic moduli and velocities based on sonic and dipole sonic well logs, in addition to dry rock moduli acquired from core plug samples allowed for the testing of various rock physics models. These models predict effects of changing effective (brine + CO_2 +hydrocarbon) fluid composition on seismic properties, and were compared to known values to ensure accuracy, thus revealing implications for feasibility of seismic monitoring in the KGS 1-32 well vicinity.

Table of Contents

List of Figures

List of Tables

Acknowledgements

I want to thank my advisor Dr. Abdelmoneam Raef, whom without, this process for a time would have been like swimming in the dark without knowing the direction to shore.

Also, I want to thank Dr. Matthew Totten and Dr. Sambhudas Chaudhuri for being members of my committee and for their feedback.

Furthermore, I want to thank Dr. Lynn Watney from the Kansas Geological Survey (KGS) for providing the core plug samples which were fundamental to this study.

Finally, I want to thank the Kansas State University Department of Geology for providing the stable environment in which to complete this thesis.

Chapter 1 - Introduction

Carbon dioxide (CO_2) is on the rise within Earth's atmosphere, and continues rising in large part from anthropogenic sources and activities. Between the years 1750 and 2011, nearly half of all anthropogenic CO_2 emissions have occurred in the last 40 years (IPCC, 2014). From 1958 to 1972, the Mauna Loa Observatory in Hawaii recorded an atmospheric CO_2 concentration increase from 315ppm to 326 ppm (Keeling, 1976), and in 2014 it recorded a value of 397ppm (IPCC, 2014). CO_2 is a greenhouse gas; the higher the concentration of greenhouse gasses in the atmosphere, the warmer the average global temperature becomes. Rising temperatures and the resulting climate change in turn disrupts and affects many Earth systems including the cryosphere, ocean, forests, snowpack, river discharge fluctuations, permafrost degradation, glacial shrinkage, ocean surface warming, ocean circulation changes, hypoxia zone increases, precipitation changes, increased soil moisture drought, and increased tree mortality and decreased tree density (IPCC, 2014). These drastic and widespread changes over such a short period of time also cause deleterious effects for human populations worldwide. Climate change warming and precipitation trends are the cause of over 150,000 lives lost worldwide annually (Patz, 2005), and many human diseases are attributed to these dramatic climate fluctuations.

This study focuses in part on characterizing subsurface rock formations of the Wellington Oil Field in Sumner County, Kansas, for geosequestration of CO_2 and CO_2 enhanced oil recovery, through a robust subsurface lithofacies characterization workflow. Application of this study will aid efforts and increase knowledge of enhanced oil recovery in a depleting Mississippian oil reservoir, and of carbon dioxide sequestration in the underlying less known and less penetrated saline aquifer Arbuckle formation. Both geosequestration and enhanced oil

recovery require taking CO_2 from point sources on the Earth's surface, specifically from industry-related activities, and injecting it into the subsurface. Once the CO_2 is in the subsurface, it will naturally rise due to its buoyant nature in that environment; for this reason, it's important to monitor where the CO_2 plume might propagate, and be able to provide sequestration verification or detect leakage, to allow for awareness if it migrates close to the surface including into fresh water aquifers, or escapes back into the atmosphere.

Much effort and many studies have been conducted in hopes of improving subsurface characterization for causes apart from and concerning carbon sequestration and enhanced oil recovery (Lackner, 2003; Herzog, 2001). Rock physics fluid replacement modeling, including the Gassmann equations, has been an effective way to study the subsurface when all assumptions of the models are honored (Smith, 2003). Although uncertainties exist, rock physics continues to increase our understanding of the subsurface, and has become an invaluable tool for many related applications (Wang, 2001).

As an extension of the fluid replacement modeling efforts, and to determine the feasibility of CO_2 injections, 4D (time lapse) seismic modeling will also be explored. Future seismic 4D modeling, monitoring and verification efforts for CO_2 injections at our study site may benefit subsequently.

Finally, this study explores the ultrasonic frequency domain using laboratory velocity techniques on core plug samples, and integrates the information collected for use in fluid replacement modeling, and to shed more light on a persistent problem in the oil and gas industry. It is well known that dipole sonic well logs and the valuable shear wave velocity information they produce are scarce, due to their high expense to acquire and their relatively recent introduction to industry. If an inexpensive means such as laboratory-acquired ultrasonic data is

available to accurately transform compressional-wave sonic velocities to determine accurate *in situ* shear wave velocities, many industry and academic advances would result. Although laboratory-acquired ultrasonic frequency data currently holds warranted concerns (Grochau and Gurevich, 2009), this study attempts to shed more light on the matter in the context of core to well log compressional and shear wave velocity comparisons. This study in part looks to better understand the effect of frequency dependency on velocity variations.

With dual problems of global climate disruption from increased carbon dioxide emissions into the atmosphere, and current conventional oil and gas reservoirs inevitably becoming increasingly more difficult to find, it is hoped that knowledge gained from this study will benefit society, academia and industry.

Research Significance

Significance of this work lies in 1) acquiring baseline dry frame rock data to be used as inputs into various rock physics models, then comparing modeled results to *in situ* values to determine the most representative model for our subsurface zones of interest in the context of carbon dioxide sequestration and enhanced oil recovery efforts; 2) applying this determined most accurate rock physics model to the subsurface areas of interest to both increase formation characterization knowledge, and by predicting 3D seismic observations through better determining how effective fluids act, and thus determining the possibility of a detailed 4D CO_2 plume prediction and monitoring/ validation program for both the geosequestration and enhanced oil recovery efforts; 3) shedding more light on the possibility of obtaining cost-effective, easy to obtain, and accurate shear wave velocities through establishing a calibration between P-wave sonic and S-wave ultrasonic frequency velocities for wells lacking dipole sonic data, eliminating the necessity of this scarce and expensive information in industrial and academic applications.

Previous Research

Many previous studies have been conducted at the KGS 1-32 well and the Wellington Oil Field. Ohl and Raef (2014) characterized rock formations for carbon dioxide geosequestration using 3D seismic anomalies and a statistical lithofacies classification model. Tilley (2014) performed geochemical analysis of the Mississippian limestone and interpreted sequence stratigraphy. Huff (2014) performed a microbial and geochemical characterization to determine the possibility of microbial enhanced oil recovery. King (2013) determined fluid flow, thermal history and diagenesis of the Arbuckle Group and overlying units. Isham (2012) attempted analysis and calibration of *in situ* and laboratory velocity measurements for rock formation characterization. She also provided baseline data applicable to this study, including Vp, density and bulk modulus estimates, and theoretical Gassmann modeling based solely on theory for both limestones and sandstones with both sub-critical and supercritical CO_2 at varying porosities. Barker (2012) performed geochemical and mineralogical characterization of the Arbuckle aquifer and determined implications for CO_2 sequestration. Scheffer (2012) performed geochemical and microbiological characterization of the Arbuckle aquifer, determining in part the integrity of the caprock in a CO_2 storage scenario. Sirazhiev (2012) conducted a seismic attribute analysis of the Mississippian chert. Dr. Lynn Watney from the Kansas Geological Survey has also contributed heavily through published work to the understanding of the area.

Chapter 2 - Background

Carbon Dioxide in the Subsurface

CO_2 is commonly found in geological systems, therefore artificially engineering CO_2 accumulations in the subsurface may simply be harmlessly mimicking mother nature. Carbon dioxide is necessary for life to exist on Earth, and it naturally exists in the Earth's atmosphere, groundwater, rivers, lakes, ice caps and seawater. It is also naturally produced by hot springs, volcanoes, aerobic organisms, and carbonate rocks through dissolution in water and acids. Carbon dioxide is a colorless and odorless gas (at low concentrations), with a Molar mass of $44.01\frac{g}{mol}$, and with varying densities and phases based on the temperature and pressure conditions present. At standard temperature and pressure CO_2 is a gas and its density is $1.98\frac{kg}{m^3}$, however, it is able to exist in four distinct phases including solid, liquid, gas, or supercritical fluid. Figure 2.1 shows under exactly which pressure and temperature regimes carbon dioxide exists at which states. Vargaftik (1996) also describes CO_2 properties in terms of pressure and temperature variations for further reference.

Figure 2.1 A representation of which phase CO_2 occupies based on the environmental factors of pressure and temperature. Image modified from http://catalog.flatworldknowledge.com/bookhub/reader/26669?e=averill_1.0-ch11_s07
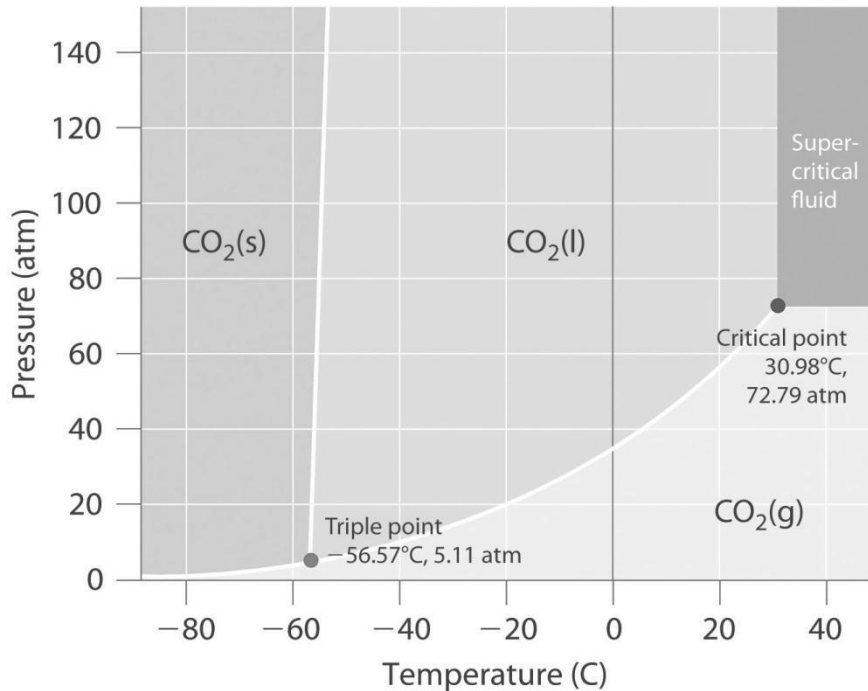
Relating this to subsurface conditions in the KGS 1-32 well where our core plug samples were extracted, we can expect to need relatively high pressures and temperatures within the target Mississippian and Arbuckle formations in order for CO_2 to be at a much desired supercritical state. The supercritical state is desired because under these conditions, the injected CO_2 takes up much less space and is compressed, allowing for much greater storage capacities within the formations. According to figure 2.2, a burial depth of approximately 800 meters is necessary to reach this goal; our formations of interest are each below 3 kilometers, thus easily attaining this benchmark.

Figure 2.2 A diagram depicting the changes in volume and density of a constant quantity of CO_2 due to changes in depth below the surface, i.e. due to changes in pressure. Image modified from CO2CRC (2008).

© CO2CRC
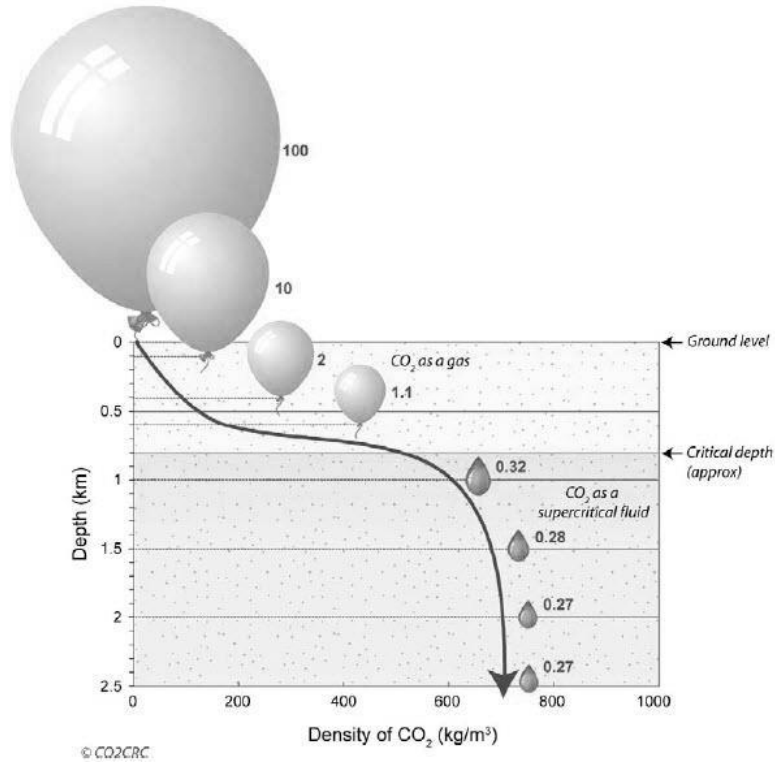
Geosequestration

Geosequestration of carbon dioxide into the subsurface is being refined as a remedy for handling the current atmospheric rise of CO_2 concentrations. Through either dissolution into brine, *in situ* precipitation by mineral carbonation, or traps in pore spaces of geological formations, CO_2 is able to be sequestered for millions of years, making the concept desirable (Gunter et al., 2000). Because of a need to reduce global atmospheric CO_2 concentrations, the United States Department of Energy has funded various carbon geosequestration projects, including the Arbuckle saline aquifer project in south central Kansas, among others (Gunter et al., 1996). Theoretically, deep, porous saline aquifers are considered good candidates for geosequestration and point-source sequestration efforts; the question of whether carbon geosequestration is feasible on a commercial scale in reality was tested during the Sleipner oil

and gas field sequestration project in the North Sea, which was the first commercial trial of such an idea (Herzog, 2001). CO_2 has been injected into the subsurface on several other occasions as well, including those from Emberley et al. (2005) and Romanak et al. (2012), as well as at Krechba, Algeria (Mathieson et al., 2009), Ketzin, Germany (Kazemeini et al., 2009), and also in various Chinese, Canadaian (Damen et al., 2005) and Texan (Holtz et al., 2001) locations. Despite promise, efforts to sequester CO_2 underground must be planned with much thoroughness; leaking just $2\frac{GtC}{year}$ could force generations beyond ours to consider recapture programs to deal with the leakage (Lackner, 2003).

Current sequestration methods considered most feasible include solubility trapping, capillary trapping, mineral trapping, hydrodynamic trapping, and stratigraphic trapping (Benson and Cole, 2008; Gunter et al., 1997). Solid phase sequestration, or mineral trapping, can only occur when reactive Ca and Mg aluminosilicates are present (conditions typically absent in clean limestones and sandstones, but present in 'dirty' sandstones and some mudstones), and only after the system has equilibrated, sometimes taking more than hundreds of thousands of years (Baines et al., 2004). Also, in all scenarios, the injected CO_2 may create chemical reactions which cause volume changes, thus potentially fracturing the affected areas through increasing stresses, which can cause enhanced transport of the CO_2 through the rocks (Rudge et al., 2010).

Saline aquifer storage capacity has been calculated at thousands of gigatonnes of emissions, or roughly 100 years' worth at current levels (Bickle, 2009). Our study site in Kansas is part of one of the largest saline aquifer systems in North America (Carr et al., 2005), known as the Ozark Plateau aquifer system, comprised of two components as shown in figure 2.3; the freshwater Ozark Plateaus aquifer system located primarily in Missouri and Arkansas, and the saline Western Interior Plains aquifer system located primarily in Oklahoma, Kansas, Nebraska

Colorado and Texas. The Western Interior Plains aquifer system, the area of CO_2 sequestration

interest, has been estimated capable of holding millions of tons of carbon dioxide, according to

the Department of Energy (DOE). Other DOE site characterization areas of interest for large

scale CO_2 geosequestration efforts also exist throughout the United States as seen in figure 2.3.

Figure 2.3 (Left) The Lower Paleozoic Ozark Plateau aquifer system and its two

components: the saline Western Interior Plains aquifer system which is of interest to CO_2

sequestration efforts, and the Ozark Plateaus aquifer system, which is freshwater. Image

modified from the Kansas Geological Survey (2015). (Right) DOE site characterization projects

for better large scale CO_2 sequestration understanding. Image modified from

http://energy.gov/fe/site-characterization-promising-geologic-formations-co2-storage.
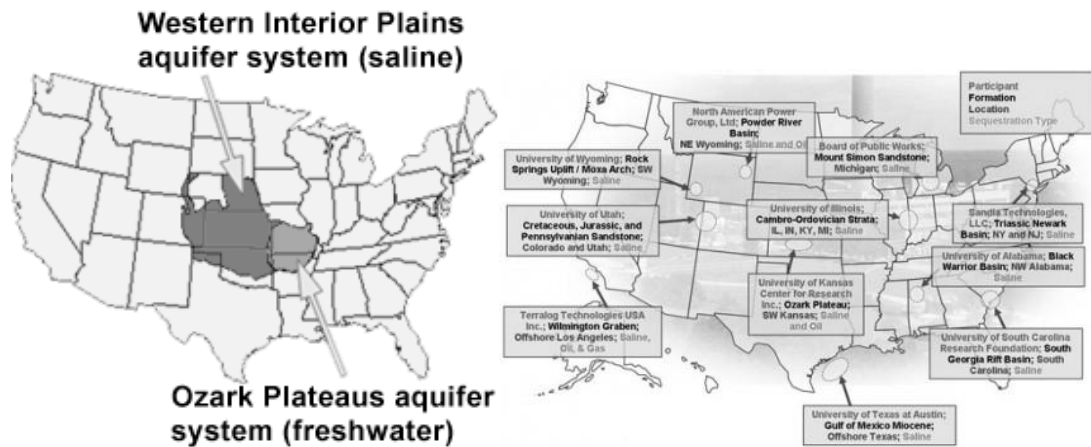
Certain requirements of the targeted subsurface formations for geosequestration of CO_2

must be met in order for the formation to be determined potential candidates. These requirements

include 1) good seal integrity of the units above the targeted formation, helping to trap the

buoyant CO_2 and keep it from rising, and ensuring a long-term isolation from overlying drinking

water sources and ultimately the atmosphere, 2) the availability of adequate space within the

formation from pore space to trap significant CO_2 amounts, 3) high permeabilities within the targeted formation to allow for the expansion of the injected CO_2 into the entire formation, 4) favorable brine chemistry to avoid salt precipitation in siliciclastics and other undesirable occurrences, and 5) favorable target formation mineralogy (Watney and Bhattacharya, 2009). To enable geosequestration efforts to proceed at large scales and beyond small-scale test efforts, evidence of large-scale storage capacities must exist, probable CO_2 plume behavior must be understood, and identification of excellent overlying seal integrity must be in place. Furthermore, injected CO_2 should ideally remain in a supercritical state, meaning *in situ* conditions must include temperatures above 87 degrees Fahrenheit and pressures greater than 1200 pounds per square inch (Daneshfar et al., 2009). The Arbuckle saline aquifer in south central Kansas meets these requirements, especially porosity as enhanced by fractures, karst features, hydrothermal alteration and dolomitization (Simo and Smith, 1997; Kupecz and Land, 1991; Merriam, 2005). The Mississippian formation at our study site meets these basic requirements as well.

In order for geosequestration to occur successfully, a unique characterization of the target subsurface formations is vital; techniques used today still include issues. A large challenge is the necessity of developing highly detailed subsurface lithofacies models capable of mapping subtle characteristics at smaller scales than is necessary for traditional hydrocarbon modeling. Extra attention is necessary since supercritical CO_2 has properties making it buoyant and mobile when buried at large depths through decreases in surface tension of interacting fluids (Brunner, 2010; Sundquist et al., 2008). Furthermore, the Arbuckle reservoir is composed of carbonates, making the challenge greater. Carbonates react with acidic groundwaters, and are heterogeneous in mineralogy and texture. To offset some of these difficulties, laboratory techniques have been used and validated from many field studies including Zemke et al. (2010) and Kaszuba (2005).

Following injection, the injected CO_2 plume migration must be monitored, ensuring no unexpected upward escape into unwanted formations. Plume migration is a factor of both the type of subsurface rocks present, and because the plume is buoyancy-driven. Low permeability and low porosity rocks do not allow for easy CO_2 plume migration through them, and thus are ideal seal rock types. It is important to integrate geophysical techniques including rock physics models to aid in the detailed characterization of these and other physical reservoir properties for time-lapse CO_2 plume monitoring post-injection, and for modeling pre-injection.

Enhanced Oil Recovery

Enhanced oil recovery (EOR) is a hydrocarbon production method conducted in an attempt to more effectively and totally extract hydrocarbons from the subsurface. During initial production stages, all that's required for hydrocarbons to be collected at the surface and sold is the reservoir's natural pressure pushing them up through the borehole. Secondary methods such as pressure-maintaining water and gas injections are implemented to maintain and increase this efficiency after the initial natural method begins to diminish. Enhanced oil recovery is any technique conducted after both natural and secondary efforts have been deemed insufficient for profitable economic production. Several enhanced oil recovery methods exist; the use of a particular method in preference to another depends on specific characteristics of the reservoirs in consideration: miscible gas injection, including the use of CO_2, water alternating gas injection, polymer flooding, surfactant use, and polymer gel flow diversion techniques are typically used for lighter oils, whereas heavy oils usually require steam and air injection methods (Muggeridge et al., 2014). Typical natural hydrocarbon recovery factors from oilfields worldwide is between 20-40%, but upwards of 50-70% through the use of EOR methods (Muggeridge et al., 2014).

This provides great incentive for the implementation and improving of the various techniques throughout the world.

During extraction, oil is primarily able to reach the surface because pressure at the bottom of the production well is greater than that of the hydrostatic head of the oil column in the well. As reservoir pressures decrease, so too does the rate of oil extracted through the well. If pressures continue falling to below the 'oil bubble point pressure,' initially dissolved gas from within the oil comes out of solution, flows preferentially to the production well due to its higher viscosity, and thus reducing the viscosity of the oil it came out of, further acting to reduce oil production rates (Muggeridge et al., 2014). Although water flooding, a secondary oil recovery method, is usually conducted before the bubble point is reached to prevent the increase in the reservoir oil viscosity, eventually the water flood effect wears out, and the initial problem occurs again. Carbon dioxide has an important effect in this context, as it is a miscible fluid able to both retain reservoir pressure and decrease the viscosity of the fluids it comes in contact with, including oil. This sudden change in viscosity of the reservoir oil now allows it to more freely flow to the well, and large production increases occur once again. Figure 2.4 is a visual representation of the geosequestration and EOR methods using CO_2, taking place in various subsurface situations.

Figure 2.4 This diagram shows how CO_2 might be sequestered into non-oil bearing formations for storage, and also into oil-bearing formations during EOR methods; in each hypothetical situation, extensive previous care should have been taken to ensure no escape conduits were identified. Image modified from http://hubpages.com/politics/Gary-Dolberry-on-Enhanced-Oil-Recovery#.
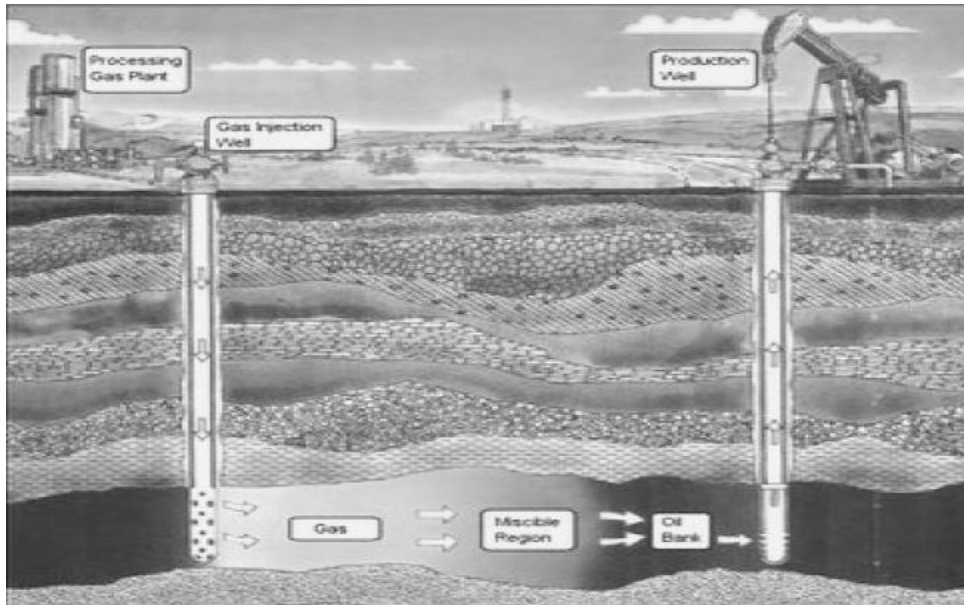
CO_2-EOR efforts may be conducted in the Mississippian Formation at our study. Specific EOR techniques are known to work best under varying conditions; our Mississippian reservoir target formation is carbonate, therefore certain EOR techniques can be initially confidently screened out as being less effective. 78% of EOR efforts worldwide from 2000 to 2010 have occurred in sandstone lithologies, with only 18% in carbonates, and gas injection held the majority of carbonate EOR attempts over thermal and chemical methods (Alvarado et al., 2010). Statistically-speaking, gas-injection is seen as the best scenario for effective extraction at our site. Furthermore, CO_2-EOR has historically been successfully executed in both waterflooded and mature carbonate reservoirs, both of which apply to our reservoir. If CO_2 continues to be available, and unless a new more effective EOR strategy is discovered, CO_2-EOR efforts will remain the most preferred recovery method for carbonate reservoirs (Alvarado et al., 2010).

Geomechanics

Geomechanics is the study of the behavior of soil and rock when interactions with stresses, temperatures and pressures occurs from a geologic perspective. Soil mechanics and rock mechanics are the two main sub-disciplines, and this study makes use of the rock mechanics discipline. Rock mechanics is the study of the physical characteristics and mechanical behavior of rock masses and their responses to forces in their environments. Rock mechanics has emphasis in rock mass characterization, including the analysis of joints and faults, rock fabrics, rock-forming minerals, stresses and strains, rock surface friction, failing rock deformation, linear elasticity including Hooke's law, inelastic behavior, wave propagation in rocks, poroelasticity and thermoelasticity (Jaeger et al., 1969). Geological applications can include rock breakage, faulting, earthquake mechanics, rock drilling, mining, tunnel building, road cuts, and within the petroleum industry.

In the petroleum industry, rock mechanics is used to reduce drilling risk and to optimize reservoir characterization. It can be applied to problems such as well-completion design, well placement, hydraulic fracturing optimization, borehole stability and optimal orientation with respect to the propagation direction of hydraulic fractures, and to determine modulus of elasticity and *in situ* rock stresses. Information gathered can be used to evaluate and better understand various reservoir parameters including density, velocity, permeability and porosity, in order to help construct various kinds of geomechanical models. Rock mechanics is tied to the disciplines of geology, petrophysics, geophysics, reservoir engineering and rock physics, and through this integration, can help to ensure comprehensive solutions to various related problems. This study makes use of rock mechanics in the form of elastic moduli and their associated velocity derivations as inputs into rock physics models applied to CO_2 plume modeling in southern Kansas.

Elastic Constants

Elastic moduli are a set of constants which define properties of materials which are subjected to stress and subsequently deform as a response to the applied stress. Elasticity is a property of matter which allows it to oppose deformation; it is thus a measurement of a specimen's stiffness. Hooke's law explains this behavior, stating that for insignificant deformations, the resulting strain is proportional to the stress applied. Ratios of stress to strain are used for their calculation, with stress defined as a force applied per unit area, and strain defined as the fractional distortion resulting due to the acting force. Figure 2.5 shows in graphical form an expected stress-strain relationship in brittle materials. Understanding elastic properties in carbonates is known to be especially challenging due to their complicated nature and make-up (Gegenhuber and Pupos, 2015). Acquiring elastic property information from carbonates using laboratory measurements is a focus of this paper.

Figure 2.5 A typical stress-strain relationship for brittle materials, including rocks. Stress is represented on the y-axis, and strain on the x-axis. Image modified from Beer et al. (2009).
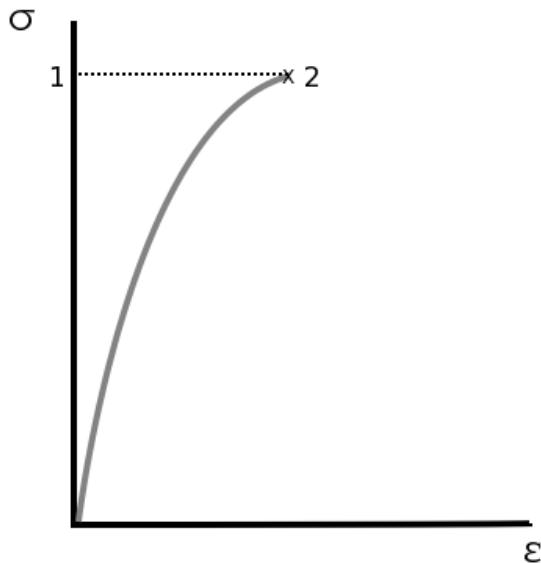
Many geologically-distinct disciplines require elastic constants: production engineering, hydraulic fracture design engineers to help optimize fracture treatments, geologists to better understand *in situ* stress regimes in reservoirs which have been naturally fractured, and geophysics to improve seismic models, interpret attributes and improve synthetic seismograms (Crain, 1978).

Both static and dynamic techniques are used, and able to extract elastic moduli; static techniques are derived in a laboratory setting from either non-destructive tri-axial stress strain tests, or from a destructive method called the chevon notch test which uses physical compression or other applied forces until the specimen is crushed. Dynamic elastic techniques are non-destructive and measure the ratio of stress to strain under vibratory conditions, including sending high frequency wave pulses through the rock sample under *in situ* overburden pressure and measuring how long the wave impulse takes to propagate through the core sample. Discrepancies can exist between methods however. Previous studies including Cheng and Johnston (1981), Rzhevsky and Novick (1971), and Fjaer (1999) all state that the dynamic elastic modulus in dry rocks is either similar to or higher than the static modulus of the same rocks, with increasing fluid saturation correlated to higher dynamic values. Saturating effects also tend to reduce rock strength through either stress corrosion (Atkinson and Meredith, 1987), a reduction of surface energy (Colback and Wild, 1965), and/ or capillary pressure reduction and chemical effects (Chang et al., 2006). This study will employ the use of the laboratory high frequency pulse dynamic elastic moduli technique, as have Jizba (1991), Carmichael (1982), Bradford et al. (1998), and Horsrud (2001). Calibration between dynamic to static elastic constants has been attempted by past studies, though this study will not.

Elastic moduli can also help predict formation strengths, with strength-physical property relationships for subsurface rocks of interest usually developed through a calibration of laboratory tests on relevant core plug samples. The gathered elastic moduli information can be applied to well stimulation, borehole and perforation stability, and rock velocity analysis since many of the same factors affecting the strength of rocks affect other properties including porosity and velocity. In velocity analysis, body wave velocity estimates depend on these elastic constant values and the density of the rocks they propagate through. Limestone and dolomite strength can vary quite significantly even within the same formation however; Chang et al. (2006) displayed that for low porosity, high velocity and high stiffness formation conditions, strength can vary by almost a factor of four regardless of the method used to estimate strength.

Many elastic constants exist including Lame constant, Biot's constant, the modulus of compressibility, the P-wave modulus (or longitudinal or constrained modulus), and the brittleness coefficient. This study will focus on five specifically: the bulk modulus, the shear (rigidity) modulus, Young's modulus, Poisson's Ratio, and the bulk compressibility modulus.

Bulk Modulus (K) is defined as a homogeneous, isotropic and linearly elastic material's ability to resist volumetric stress, which depends on normal and shear stiffness, and is the volumetric stress divided by volumetric strain. It is a strength parameter which measures compressive strength, with a large value indicating the existence of a high resistance to compressional forces, and a low value meaning the substance is more compressible. In this study, $K = \frac{p(3V_p^2 - 4V_s^2)}{3}$, where p is density, V_p is compressional wave velocity, and V_s is shear wave velocity.

Bulk Compressibility Modulus is simply the inverse of the bulk modulus. In this study, the bulk compressibility modulus is $\frac{1}{K}$, where K is the bulk modulus.

Shear (Rigidity) Modulus (u) describes the tendency of an object to undergo a deformation of shape at constant volume when opposing forces are acted upon it, or an object's resistance to angular distortions/ shear strain. It is also defined as the ratio of shearing, or torsional, stress to shearing strain. Large shear modulus values indicate the existence of a large resistance to the effects of shearing or torsional forces. Fluids are not able to undergo shearing or shear stress, thus all have a shear modulus of zero. In this study, $u = pV_s^2$, where p is density and V_s is shear wave velocity.

Young's Modulus (E) describes tensile strength and elasticity, which is an object's tendency to deform along an axis when opposing forces have been applied along that axis, and can be thought of as a material's ability to compress or stretch through the quantification of how resistant it is to extensional deformation (Watt et al., 1976). It is also defined as the ratio of uniaxial compressive (tensile) stress to the resultant strain, and is an applied uniaxial stress divided by normal strain. A high Young's modulus value indicates a high resistance to extensional forces exists. In this study, $E = \frac{pV_s^2(3V_p^2 - 4V_s^2)}{V_p^2 - V_s^2}$, where p is density, V_p is compressional wave velocity, and V_s is shear wave velocity. Young's modulus in the petroleum industry can be used to design mechanisms of hydraulic fracturing, as the more rigid a rock is (indicating higher Young's modulus values), the narrower the fractures will be.

Poisson's Ratio (v) measures the geometric change in shape of an object under uniaxial stress, and is the lateral or transverse strain divided by longitudinal strain (Hill, 1963). It can be thought of how much a material will contract in all other directions if a stretching action of the material in one direction is applied. A high Poisson's ratio indicates a high difference in measured Vp and Vs velocities. Materials can have negative Poisson's ratios if when stretched, they expand in transverse directions, due to their molecular structures which are hinge-like; these

materials are known as auxetic materials; none will be handled in this study. In this work, $v = \frac{V_p^2 - 2V_s^2}{2(V_p^2 - V_s^2)}$, where V_p is the compressional wave velocity, and V_s is the shear wave velocity.

Poisson's ratio will be discussed in greater detail in later sections.

The equations of these elastic constants can be interrelated, so that if any two of the constants are known, the others can easily be calculated. The following interrelated equations come from The Rock Physics Handbook (Mavko et al., 1998): Bulk Modulus $(K) = \frac{Eu}{3(3u) - E} = u\frac{2(1+v)}{3(1-2v)} = \frac{E}{3(1-2v)}$, where E is Young's modulus, u is shear modulus, and v is Poisson's ratio.

Shear modulus $(u) = 3K\frac{1-2v}{2+2v} = \frac{3KE}{9K-E} = \frac{E}{2+2v}$, where K is the bulk modulus, v is Poisson's ratio, and E is Young's modulus. Young's modulus $(E) = \frac{3Ku}{3K+u} = 2u(1-v) = 3K(1-2v)$, where K is the bulk modulus, u is the shear modulus, and v is Poisson's ratio. Poisson's ratio $(v) = \frac{3K-2u}{2(3K+u)} = \frac{E}{2u} - 1 = \frac{3K-E}{6K}$, where K is the bulk modulus, u is the shear modulus and E is Young's modulus.

Rock Physics

One of the rock physics methods strives to characterize rock properties through the analysis of the propagation of seismic waves through those rocks (the composition of the rock dictates its stress-strain relationship and subsequently its seismic response). It aims to describe a subsurface formation through elastic rock properties (which affect how seismic waves travel through them) putting 'meat on the bones' of these interpretations and helping the seismic interpreter to combine rock properties with the seismic horizons they're observing through the extraction of more rock property information from the seismic wavelet. Typical rock physics areas of inquiry include fluid substitution, fluids and saturation, pore fluid properties, pressure,

porosity, clay content, temperature, density, texture, lithology, Vp and Vs, Vp/Vs ratio, shale properties and anisotropy (a directional or angular velocity dependence of seismic waves propagating through the Earth) (Wang, 2001). The discipline combines both geophysics and petrophysics (often making use of sonic, dipole sonic, and density logs and relating these to their influencing factors including pressure, elastic moduli, porosity, temperature and pore fluid), and can serve many significantly important roles in the geosciences, including aiding in the construction of synthetic sonic logs, creating links between rock properties and the amplitude vs offset response, and providing connections between elastic properties (measured either *in situ* or in the laboratory) and the intrinsic properties of rocks including porosity, pore shape, pore pressure, pore fluids, permeability, stresses, fractures, viscosity and mineralogy (Mavko et al., 1998). Through elastic data, density and porosity, rock physics can provide both the theoretical tools and understanding for better characterization of subsurface formations. Rock velocities and rock elastic parameters link physical rock properties to the seismic expression. Therefore, it can be used to predict subsurface properties, including pore fluids and lithologies derived from seismic attributes, including in areas where drilling hasn't occurred, which helps reduce risks.

Traditional rock physics modeling generally has three steps according to Ba et al. (2013): first, the properties of grain minerals are obtained using effective medium theories or mixing laws; second, elastic properties of the dry rock matrix are estimated using either effective-medium theories, experimental measurements, or empirical relations; and third, fluid substitution is conducted, mostly using the Gassmann's equations and the Wood law. Furthermore, Simm and Bacon (2014) group rock physics models into groups which are most commonly applied, and include theoretical bounds, empirical models, Gassmann's equation, contact models, and inclusion models. Theoretical equations attempt to suggest universally-correct relationships

using underlying assumptions, and empirical relationships derive their success in describing specific situations through experiments from a specific case. This study will make use of Gassmann's equations, which are theoretical.

Rock physics models are designed to establish predictive theories and relations between physical rock properties (including porosity, compressibility and rigidity) and the observed seismic response with the ultimate hope that the physical properties may be detected seismically. Indeed, they were originally developed to legitimize well log information in order to evaluate subsurface formations (Besheli, 1998). Laboratory-based analytical calibration methods, as conducted in this study, have been a great help to seismic-to-rock-property transforms (Jaiswal, 2014).

The rock physics discipline still requires refinement and improvement, especially for carbonates because of complicated pore geometries, mineralogy heterogeneities, and textural heterogeneities, and is thus an area of much recent research. Several issues currently remain, including the challenge of relating the small to the large scale (the micro, to thin section, to core, to well log, to seismic scales). This is a problem because in the case of comparing well log to core data, well log data would seem to be more accurate because it measures and represents a much larger volume of the subsurface. Also, the challenge of calibration and the lack of measured true shear wave velocities persist (Dewar and Pickford, 2001). Also, due to large advances in seismic acquisition and processing techniques over the last decade, advances in seismic-to-rock-property transforms for better mapping of fluids, porosity and lithology must now follow, and has been the focus of much rock physics research (Avseth et al., 2005). Sayers (2008) has a more comprehensive review of rock physics modeling concerns. Despite these problems, the petroleum industry has still benefitted greatly from rock physics, and has put many

applications into practice including the cross-plotting of both well log and seismic data, fluid substitution, S-wave velocity prediction, and 1.5D and 2D pre-stack seismic modeling (Dewar and Pickford, 2001).

Fluid Substitution Models

Rock physics models greatly increase our comprehension and understanding of technically difficult concepts, including fluid substitution modeling, which is a very important rock physics problem. To establish relationships between physical rock properties and the seismic expression, rock physics needs both elastic properties (of the rock frame and pore fluid), and accurate models for rock-fluid interactions. Fluid replacement models require inputs from a rock with an initial fluid, and then predicts and models the resulting characteristics of the same rock with a new, hypothetical substituting fluid. Validation of fluid replacement modeling comes from comparing *in situ* data, such as that from well logs and saturated laboratory rocks. Regardless of lithology, different substituting fluids change the elastic properties of rocks, and these changes are determined by applying fluid substitution models; the accuracy of these results has recently become more important in the United States because of greater interests in both CO_2 storage and CO_2 enhanced oil recovery (Purnamasari et al., 2014). Fluid replacement modeling is obviously beneficial for 4D time lapse seismic reservoir modeling and monitoring as well.

A variety of fluid substitution models exist, although very few have been developed specifically for the application to carbonate rocks, including limestones and dolomites. A carbonate rock physics model in general is difficult because when compared to siliciclastic rocks, carbonate pore systems are much more complex. This fact can cause velocity-porosity relationships to become highly scattered and less predictable, for example (Xu and Payne, 2009). Currently established fluid substitution models includes in part, the effective medium and elastic

22

contact theories which can estimate bulk and shear modulus and thus P-wave and S-wave velocities, the Gassmann theory, the Biot equations which cover a broader frequency range than the Gassmann theory, the Stiff Sand model, Marion's bounding average method, Biot-squirt model, the Mavko-Jizba squirt relations, and others (Wang and Nur, 1992; Mavko et al., 1998).

An important note should be made about a potentially important process conventional fluid replacement models fail to acknowledge, specifically the changes in rock properties (including porosity, permeability and acoustic wave velocities) induced by chemical changes as a result of the substituting fluid. Because fluid replacement models are purely mechanical, no attention has been paid to the sometimes dramatic effects of dissolution and precipitation during a substitution and mixing of fluids, in both siliciclastic and carbonate subsurface rocks (Vanorio et al., 2011). This observation may provide a means for the questioning of the validity of current models in 4D CO_2 plume prediction and monitoring efforts. Observed permanent rock matrix changes may have an effect on 4D seismic data, especially when precipitation and dissolution effects are large, and thus an additional model layer may be needed to address and examine the chemical-physical effects of reactive pore fluids. The difference between a rock's component parts including the matrix, pore space, grains and cement, can be seen in figure 2.6. As part of their study, Vanorio et al. (2011) examined the response of various CO_2-brine-rock systems, and through detailed analysis using high resolution time-lapse CT-scan and SEM images found the fluid substitution problem to be far from purely mechanical; direct observations of changes at the grain and pore scale were made. CO_2 injection into brine-filled formations was found to create chemical reactions, interphase mass transfer, and mechanical deformation leading to formation damage which included the precipitation and deposition of mineral salts clogging pore throats in sandstones, and calcite and pore dissolution (Hovorka, 2009). Because these potential effects

fundamentally change the baseline properties of the rock frame and thus some of the important inputs for fluid substitution models, this issue should be addressed further in the future and not continue to be ignored. A possible silver lining is that, when dolomitization is present, dissolution of grains can overall increase the permeability and porosity, aiding in the validation of the continuous pore space Gassmann assumption (Adam et al., 2006), and thus potentially making rocks under these conditions more applicable to the Gassmann model.

Figure 2.6 The four main components of a sedimentary rock; pore space, the matrix, cement, and the grains. The difference between the matrix and the cement is that the matrix material is the finer grain sized particles between the coarse grains, and cement is a binding material often precipitated from solutions which move through the formation through time. Image from http://www.tankonyvtar.hu/en/tartalom/tamop425/0038_foldrajz_mineralogy_Da/ch01s12.html
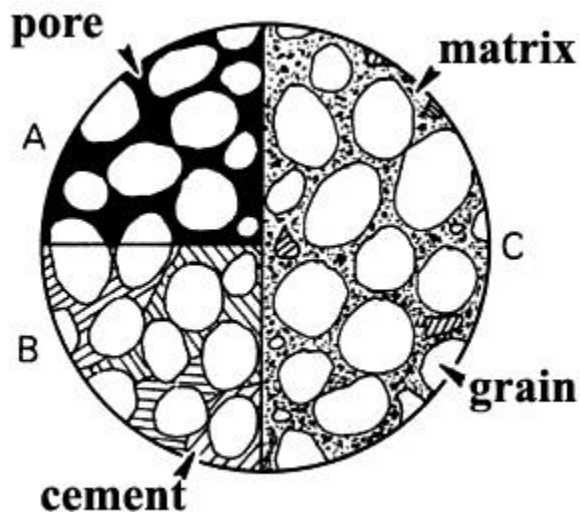
The main industrial applications of fluid replacement modeling are the interpretation of seismic signatures of EOR processes, modeling changes that occur in reflection seismic attributes from spatial changes in pore fluid distribution, and AVO analysis (Mavko et al., 1995).

Gassmann

The Gassmann fluid substitution model predicts changes in compressional wave and shear wave velocities after a fluid substitution has taken place, and is a very popular and common fluid replacement technique. The model describes rocks through the bulk moduli of a two phase media, the fluid and mineral matrix (Simm and Bacon, 2014), with the most common purpose of the equations being the calculation of the effect of fluid substitution on seismic properties through the use of the rock frame properties (Wang, 2001). Given an initial set of density and velocity values for a rock with an initial set of fluids, these equations allow for the computation of densities and velocities of that same rock with another set of fluids; it can predict the bulk modulus of a fluid-saturated porous rock with inputs of the bulk moduli of the pore fluid (gas, oil, water, or a mixture), frame (the rock sample with empty pores), and solid matrix (consisting of the rock-forming minerals). The equation can be written generally as, from Simm and Bacon (2014):

$$\frac{K_{sat}}{K_o - K_{sat}} = \frac{K_d}{K_o - K_d} + \frac{K_{fl}}{\Phi(K_o - K_{fl})}$$

$$u_{sat} = u_d$$

Where K_{sat} is the fluid saturated rock bulk modulus, K_o is the matrix material bulk modulus, K_d is the dry rock frame bulk modulus (the rock frame with all fluid removed), K_{fl} is the pore fluid bulk modulus, Φ is the porosity (fractional), u_{sat} is the fluid saturated rock shear modulus, and u_d is the dry rock frame shear modulus.

Although the equations can be algebraically manipulated to eliminate the necessity of the dry rock modulus as an input, it is nonetheless still often convenient to gather dry frame rock values from core samples, run tests on these core plugs, and then validate the results by comparing both velocities and elastic moduli of *in situ* well log values from the well the core plug was obtained. Five steps are necessary to complete this process, from Avseth et al. (2006): 1) Calculate and extract the bulk and shear moduli from the acquired compressional velocity, shear velocity, and density. 2) Transform the bulk modulus from dry to saturated through the rock forming minerals bulk modulus, the dry rock bulk modulus, the fluid bulk modulus, and the rock porosity. 3) Because the shear modulus, or rigidity, is not affected by fluid saturations or fluid type (pore fill), since shear waves do not travel through fluids, keep the shear modulus unchanged. 4) Correct the bulk density for the change in fluid. 5) Recalculate the newly fluid substituted velocities. The Gassmann equation in step two for saturated bulk modulus is as follows:

$$K_{sat} = K^* + \frac{(1 - \frac{K^*}{K_o})^2}{\frac{\Phi}{K_{fl}} + \frac{(1 - \Phi)}{K_o} - \frac{K^*}{(K_o)^2}}$$

Where Φ is porosity, K^* is the bulk modulus of the porous rock frame, K_{fl} is the bulk modulus of the pore fluid, K_o is the bulk modulus of the mineral matrix, and K_{sat} is the saturated bulk modulus (Mavko et al., 2009). This study will elaborate on these steps further in the methodology section.

The original Gassmann equations were derived for high porosity, unconsolidated sediments at low frequencies, and various assumptions are necessary for its perfect, ideal functioning, albeit some are impossible to realistically satisfy. Researchers applying the theory should make attempts to abide by these assumptions as best as possible, to ensure the most

accurate results possible. The assumptions are as follows, from Xu and Payne (2009), Wang (2001), Mavko et al. (2009), Smith et al. (2003), Adam et al. (2006), Wang and Nur (1992), and Simm and Bacon (2014): 1) The rock matrix and frame are macroscopically homogeneous (monomineralic) and isotropic, ensuring the measurement wavelength is long compared to the pore and grain sizes. Wavelengths from seismic to sonic frequencies (1Hz to 1MHz) generally meet these criteria for most rocks. 2) The pores are all interconnected, implying both high permeability and high porosity, and ensuring that within the time frame of half of the measurement wave's period, or cycle, a complete equilibrium of the flow of the pore fluid and pore pressure created by that passing wave has time to occur. Seismic and sonic wave-created pressure changes are generally able to equilibrate because enough time passes for fluid movement between pores; if equilibrium does not occur, an increase in pore stiffness and thus an increase in velocity is achieved. Therefore, the theory may not be applicable to ultrasonic methods due to the possible resulting velocity and elastic moduli dispersion. 3) Frictionless fluids, those with viscosities of zero, completely fill the pore spaces ensuring again a complete pore fluid flow equilibrium. 4) The studied rock-fluid system is elastic and closed, or sealed, and undrained, allowing no fluids to enter or exit through the surface of the rock (if the experiment is conducted in a laboratory setting). 5) The relative motion between the solid rock and enclosed fluid is negligibly small when compared to the movement of the entire saturated rock, essentially requiring the frequency to be zero, or the wavelength to be infinite, which is not possible, though the lower the frequency used the better. 6) The frame of the rock is not hardened or softened by interactions between the solid and the pore fluid (the two are not coupled); this assumption can never be guaranteed, as fluid-solid interactions always interact in some physical way, regardless of how dramatically. Nevertheless, a requirement of the equations is that porosity stays constant

and no chemical interactions occur. Although these assumptions may seem restrictive, with best results suited exclusively for clean sandstones with high to moderate porosity at low frequencies, a benefit of the method includes simplicity; pore geometry, inclusion geometry, rock symmetry and crack density are ignored, whereas other theories include these complicated factors as inputs (Adam et al., 2006).

This study is a multi-scale rock physics study, using core plug samples and well log data by comparing the Gassmann theory ultrasonic laboratory core plug results to *in situ* sonic well log data from within two carbonate rock formations. Although our study conditions do not fit every Gassmann theory assumption, many other authors have similarly proceeded with unideal combinations, either because reputable alternative models were too obscure or non-existent, developing a new robust model proves too difficult given today's understanding of carbonates, attempts to validate the Gassmann equations in carbonate rocks through introduced biases and calibrations were made, or the authors were simply curious as to whether the Gassmann model could work under their conditions, and if so, why, despite the breaches in assumptions. Kahraman (2007) found a good correlation between measured wet-rock compressional wave velocity and Gassmann wet-rock compressional wave velocity in various rock types, Adam et al. (2006) attempted to better understand the applicability of Gassmann's equations at unconventional seismic and ultrasonic frequencies, and limestones and dolomites have been laboratory tested with ultrasonic techniques by Wang et al. (1991), Marion and Jizba (1997), Wang (2000), Baechle et al. (2005), Rogen et al. (2005), and Grochau and Gurevich (2009) to attempt a better understanding of Gassmann, all reporting good statistical agreement between predicted and *in situ* values.

Ultimately, due to the complex, poorly understood carbonate multiscale pore systems, heterogeneities, other complexities, some authors are compelled to question and doubt the validity of the traditional Gassmann equations in carbonates, while others have found and claim it works perfectly well in their specific cases (Xu and Payne, 2009). Therefore, because at present, carbonate rock application of the Gassmann equations is unresolved, it is now of great importance to more fully understand why it works in some instances and not in others. This study's intent is similar in spirit to that of Jaiswal (2014) and the stiff sand model; though that model requires isotropic sandstones, their intent was not to show the Woodford Shale was either a clean sandstone or isotropic, but instead that their model can be applied to their formation rocks within acceptable error. Indeed, it is even possible, as Wang (2000) suggests, that the rock-fluid system is so complex that virtually every theory for such systems necessitates making major assumptions to reduce the mathematical complexities. Therefore, at least for the time being, one way forward is to continue accumulating laboratory predicted and *in situ* validated data to progress the knowledge of such systems.

Ultrasonic To Sonic Vs Transformation

Limitations of integrating geophysical methods to model carbonate reservoirs include transforming various datasets into accurate representations and legitimate versions of other datasets, allowing for better integration and more widespread use of various datasets to solve problems in a more cost-effective manner. Translating current geophysical information collected at ultrasonic frequencies to lower frequencies, and vice versa is one such unresolved issue (Grochau and Gurevich, 2009). Despite costly dipole sonic logs being relatively commonly acquired in wells today, a great need still exists for the derivation of shear waves from

compressional waves since many mature developed fields only have monopole (compressional wave) logs, and lack dipole shear wave data (Wang, 2001).

Many reasons exist why predicting shear wave velocities from compressional wave velocities is difficult, as there are many factors to consider. Acoustic velocities through rocks depend on factors of the rock through which the wave propagates, including but not limited to rock type, density, grain size, grain shape, texture, anisotropy, stresses, porosity, temperature, the presence of joints and bedding planes, and weathering zones (Kahraman, 2007). Fluid type and saturations in the pores can also have significant effects; Wyllie et al. (1958) found that, in ultrasonic frequency tests, when saturation is reduced from 100% to nearly 70%, a great decrease in P-wave velocity occurred. That study also concluded that velocities of fluid saturated rocks as a whole were dependent on the specific ratio between the velocity of the pore fluid and the velocity of the rock. In addition, fluid type is a big factor; Adam and Batzle (2007) reported observing attenuation (and thus dispersion- without modulus dispersion there is no attenuation) to have greatly increased when brine replaced a light hydrocarbon as the pore type fluid in their limestone samples.

This study has attempted to analyze acquired Vp and Vs data from core plug samples acquired through ultrasonic laboratory tests in order to possibly find an empirical relationship between Vp and Vs data in order for a robust Vs prediction method to be applied in future endeavors where similar rock characteristics exist.

Frequency Analysis

Differences in frequencies of the velocity measurement technique is another problem in determining accurate Vs where no *in situ* Vs measurements exist. Frequency is defined as the specific number of times a repeating event occurs per unit time, with an SI unit of hertz, and a

reciprocal known as the period which represents the duration (in SI units of seconds) of one cycle. A good way to compare between frequencies of waves of various known sources is by referencing the electromagnetic spectrum (seen in figure 2.7), which also gives a better perspective to our study's methods. Both the 1.25MHz and 20MHz frequencies examined in this study are considered ultrasonic, meaning they're above the ability of a human's hearing capability, and within the radio wave realm.

Frequency ranges of most interest and applicability to industry include 1) the seismic frequency at 1-100Hz, used by surface seismic techniques, 2) the sonic frequency around 10kHz, used by sonic logs, and 3) the ultrasonic frequency at 100kHz-30MHz, used by laboratory measurement techniques. It is evident how large the spread in frequencies used is, and much effort has been spent attempting to equalize their measurement effects on velocities of acoustic waves, in order for all three to be used in harmony and tandem to help characterize complex heterogeneous reservoirs, including carbonates.

Figure 2.7 The electromagnetic spectrum comparing wave types' frequencies and wavelengths. Image from Mayo (2015).
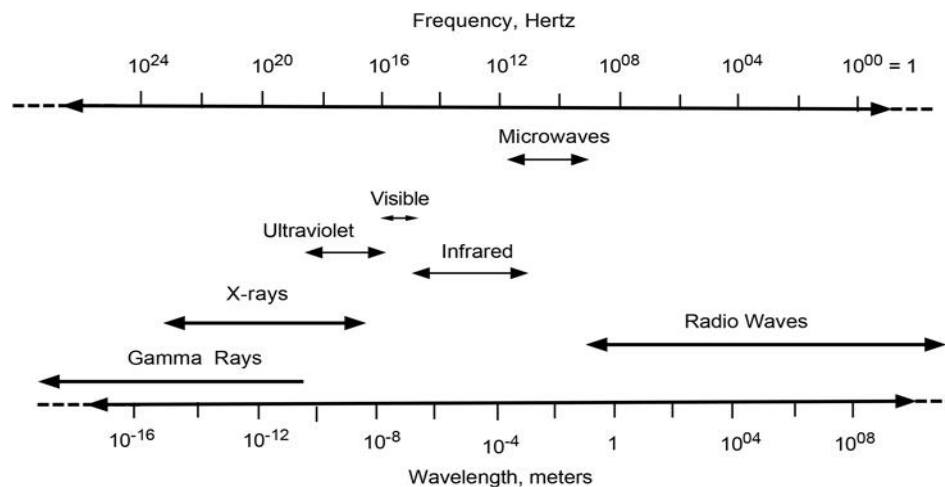
Velocity Dispersion

There exist both dispersive and non-dispersive mediums. In non-dispersive mediums, such as air without CO_2, the speed of sound is not dependent on frequency; at all sound frequencies the speed of the sound is the same while propagating through it. This can be thought of visually as a beam of white light traveling through space unimpeded. However, in dispersive mediums such as rocks, the speed of sound is dependent on the sound frequency, much like when a beam of light travels through a prism causing individual rainbow colors to separate due to changes in speed by which they propagate through the prism (called optical dispersion). Wang (2001) states that the true magnitude of (moduli and velocity) dispersion is still not known, making it a daunting issue in rock physics. The problem results from differences in frequencies used in different measurement techniques.

This effect does not occur in all kinds of solid materials. For instance, gypsum is a purely elastic material, thus having frequency independent elastic properties, however most rocks including carbonates are viscoelastic (Pimienta et al., 2014), and thus dispersive. A viscoelastic material is one which exhibits both elastic and viscous characteristics; a viscous material like honey will react differently and resist stress differently than a purely elastic material. In viscoelastic materials, typically as frequency of the measurement increases, so does the velocity due to the associated dispersion.

Assumption 2 of the Gassmann equations dealt with dispersion effects. Again, the higher the frequency of the measurement used, the greater the induction of stiffness in the rock from the passing waves causing a small amount of pore pressure to build up without allowing that induced pressure to equilibrate before the next wave passes. This then creates artificially higher measured velocities (Mavko et al., 1995). As an acoustic wave passes through a rock, fluids in the pore spaces become disturbed and consume part of the energy of that passing wave. This 'decoupling'

of the rock skeleton from the fluid in the pores causes dispersion to only occur in water-saturated rocks with high frequency measurements, regardless of rock type (Wang and Nur, 1990; Mavko and Jizba, 1991; Winkler, 1985; Batzle et al., 2001). Besides the fluid-skeleton decoupling mechanism, other potential factors can also create an artificially high velocity recording, including patchy saturation (Dutta and Ode, 1979), local fluid flow or squirt (Mavko and Jizba, 1991), and because ultrasonic laboratory tests are usually conducted on largely homogeneous, intact, competent core samples with minor fracturing; in comparison, conditions near the wellbore where sonic measurements take place can be areas high in induced fractures and naturally-occurring heterogeneities within various sections of the measured formations (Lin, 1985).

Interestingly, Adam and Batzle (2007) surprisingly found their dry ultrasonic samples to exhibit dispersion. Their conclusion was that a small amount of water in pores from humidity in the air was the cause, as their core samples were not oven dried. Contradictory observations to this rule have been described in the literature: Mavko et al. (1995) also found the effect of dispersion to be less when measurements were conducted at higher pressures, thus here also, the difference in measurements of differing frequency measurement techniques became less.

Poisson's Ratio

A possible remedy to the frequency and dispersion issues when attempting to acquire accurate Vs data with no *in situ* measurements is to develop an empirical or theoretical relationship which employs Poisson's ratio. As explained in earlier sections, Poisson's ratio is a ratio of Vp to Vs velocities. It is seen as a possible solution to the dispersion problem (therefore enabling the tying of ultrasonic to sonic frequency velocity measurements) because Poisson's Ratio values are less susceptible to the large potential variations between measurements of velocities between different frequency measurement techniques, being a ratio and not direct

measurements. Adam et al. (2006) stated that because the dispersion in their Vp and Vs measurements were similar for their samples, the subsequent dispersion in Poisson's ratio in negligible, allowing for a correction to be applied between their low and high frequency data.

Randi (2012) showed promising results in this respect with her Master's thesis, and this study has acquired complimentary data in an attempt to increase the confidence of those results. Mavko et al. (1998), Han (2004), Domenico (1984), and Assefa et al. (2003) also measured carbonates through ultrasonic methods and created empirical relations for Vs and Vp.

Many factors can affect Poisson's ratio values, including even the way it is measured, either dynamically or statically. The geophysics laboratory at Kansas State University and this study employ the use of the nondestructive pulse dynamic method. Because our core plug samples came from the Kansas Geological Survey, we were required not to damage them with any static techniques. Dynamic tests derive results from either the determination of pulse compressional and shear wave velocities in core samples, or through resonance frequencies of compressional and shear vibration measurements of bar-like cylindrical rock samples (Gercek, 2007; Siggins, 1993). It has been noted that large differences between these two techniques can exist (Fjaer et al., 1992; Siggins, 1993; Wang, 2000; Fjaer and Holt, 1994), with the static technique more widely used and accepted in engineering and rock mechanics, and the dynamic method more prone to error, some considerable, and usually through underestimations. Not only are Poisson's ratio values not in agreement between these methods, the other elastic moduli disagree as well, sometimes by up to 600%. This tendency has been documented well (Lin, 1985; Brace, 1964; Brace, 1965; Simmons and Brace, 1965; Heuze, 1980; Thill, 1983). Variations in results are primarily due to different amounts of stress applied (and thus strain generated on the samples), and how cracks within the samples act as a response. The static technique delivers

enough stress to physically damage the core sample often making it unrecoverable. When a very large stress is applied, cracks collapse and strain is not recoverable causing a variation in final values; steel, a crack-free material reports dynamic vs static Poisson's ratio values close to one (Wang, 2001; Bristow, 1960). Also, varying stress amounts between methods may create differences in the magnitude and behavior of mineral grain sliding and the subsequent influencing effects (Lin, 1985). In an effort to control for the difference between static and dynamic Poisson's ratio values, King (1983), Van Heerden (1987) and Eissa (1988) attempted empirical relationships, although conclusive evidence of successful attempts remains hidden.

Not only does the presence or absence of cracks potentially affect Poisson's ratio values, many other factors including changes in fluid content and saturation, the solid rock mineral composition (this being most influential at high effective pressures on rocks with less cracks), and clay contents in siliciclastics play important roles (Zhang and Bentley, 2005). Furthermore, combinations and more subtle characteristics of factors are influencers, including the aspect ratio of cracks (measured mathematically by dividing the length of the minor axis by the length of the major axis), the concentration of cracks, combinations of saturation and aspect ratio of cracks, the geometry, orientation, connectivity and distribution of pores, effective pressures, and proportion of different crack types among others (Walsh, 1993; Zhang and Bentley, 2005).

Typical Poisson's ratio values of intact rocks can be found in Table 4 of Gercek (2007), and include ranges from 0.1-0.35 in dolomites, and 0.1-0.33 in limestones. Furthermore, of all reservoir rocks, limestones have the highest Vp/Vs ratio on average, followed by dolomites, followed by unconsolidated sand at deep burial depths, followed by sandstones (Wang, 2001). This can be an important observation/ tool for lithology characterization and indirectly, pore fluid characterization as well.

Shear Wave Velocity Prediction Models

Shear wave velocity models determine shear wave velocities from Vp values through the use of empirical Vp/Vs relationships, or through other techniques. These are prominent in the literature and in industry due to a lack of dipole sonic log data in mature oilfields. Shear wave velocities are also required for AVO analyses. Many shear wave prediction models exist, so it is important to apply the most appropriate model to the unique set of subsurface formation characteristics that are of concern if the best results are desired. Empirical Vs prediction models have proven to be accurate methods (Jorstad et al., 1999), but validation from local shear logs when available is an advisable action, as large variations from established trends have been known to occur (Simm and Bacon, 2014). Although many other rock physics model types including fluid replacement models and the Gassmann equations require measurements of both Vp and Vs as initial inputs, shear wave velocity prediction models only require Vp information.

Mavko et al. (1995) developed two such methods: one which can operate on the P-wave modulus, which acts as a replacement to the rock and mineral bulk moduli requirements of Gassmann, and the other is able to decompose the measured P-wave modulus into shear and bulk moduli graphically, thus providing all necessary information for the Gassmann equations to be applied. Both methods were found to be very accurate on sandstones, although were not designed to be equipped to predict the effects of velocity dispersion in ultrasonic tests. Castagna et al. (1985) also provided a Vs prediction model intended for water-saturated clastic silicate rocks, known as the mudrock line. Other models include the Gregory-Pickett approach, the approach developed by Lee (2006), the Xu Paine method, the Greenberg/Castagna method, the Budiansky and O'Connell self-consistent approximation, Han's methods, the Modified Gassmann method, the Critical Porosity method, the Krief method, and others. Many other derived empirical relationships exist as well, all based on specific local conditions.

Gregory-Pickett

        The Gregory-Pickett approach from Gregory (1977) is a dry rock shear wave velocity prediction model. The method is also known as the 'dry rock Poisson's ratio' method, as it requires the dry rock Poisson's ratio as an important input. The dry rock Poisson's ratio can be calculated from the dry rock bulk modulus and the shear modulus as such: $\frac{3K_d-2u}{2u+6K_d}$, where K_d is the dry rock bulk modulus, and u is the shear modulus. This method will be used and results compared to the other rock physics models to compare for applicability. Steps for its exact calculation can be found in the methodology chapter.

Exploration Seismology

        Exploration seismology, reflection seismology, or seismic reflection, is the application of the principles of seismology to better understand subsurface Earth properties from reflected seismic waves, and requires both a seismic source and receivers. A main goal of rock physics studies is to link physical rock properties to reflection seismic observations, and creating a more meaningful and extremely important connection between the two. Seismic waves in exploration seismology provide subsurface rock and fluid information in the form of travel time, phase variations, and reflection amplitude. The three seismic properties of rocks are P-wave velocity, S-wave velocity and impedance, which depend mainly on the elasticity and density of the analyzed rocks (Simm and Bacon, 2014). This information, through analysis, can help give a clearer picture of spatial variations in subsurface porosity, pore fluid type and saturation, and lithology, all important aspects of 4D time-lapse efforts.

        It is important to understand that, in a reservoir or any other subsurface formation, two varieties of pressure exist: overburden or confining pressure, which is the pressure generated from the mass of the overburden above the particular area of interest, and reservoir or fluid or

pore pressure, which is the pressure exerted by the fluid mass pressing back against the pore walls from within the reservoir or subsurface formation of interest. The difference between these two pressures is known as the net overburden, or differential, or effective pressure. This effective pressure is important because it controls the rock seismic properties which are used in a large number of important applications, including 4D seismic and AVO analysis. Effective porosity is also important to define, being the porosity within a rock formation which is interconnected, and is thus the most important type in terms of CO_2 sequestration and EOR applications/ efforts.

Seismic properties of sedimentary rocks are not only affected by effective pressure, but also through many other factors in complex ways, including subsurface temperature, fluid-related factors (including fluid saturation, type, viscosity, phase, density, type ratios, and wettability), porosity, pore type and shape, fractures, pressure, compaction, age, lithology, consolidation history, cementation, clay content, texture (including roundness/ angularity, sorting and grain-to-grain contacts), bulk density, anisotropy, stress history, depositional environment, frequency of the measurement, and others (Wang, 2001). Of these, Wang (2001) determines pore shape to be the most significant, although hardest to quantify, although generally flatter pores generate lower seismic properties. Predicting and modeling the effects of fractures on seismic responses can prove difficult as well (Xu and Payne, 2009). Stiff rocks have also been observed to exhibit smaller seismic sensitivity to pore fluids compared with soft rocks (Jaiswal, 2014). These influencing factors are likely interrelated; if one changes properties of many others may also resultantly change. Therefore, in rock physics seismic studies, ideally one factor at a time should change for more accurate investigations.

The importance of integrating seismic reflection data into a rock characterization project has been demonstrated by Ohl and Raef (2014), who by using 3D seismic attributes successfully

characterized a Mississippian subsurface lithofacies and exposed subtle features to be used as valuable CO_2 plume time lapse tracking information. Furthermore, Raef et al. (2001) used seismic attributes to better characterize formations through the prediction of porosities in thin-bedded carbonates, and Raef et al. (2005) deployed the use of 4D seismic techniques during a CO_2 flood event to better understand carbonate reservoir characteristics. And, Wang (2000) successfully compared his Gassmann predicted results to the effect of fluid replacement on seismic properties, finding good agreement

Fluid substitution results are able to predict effects on 3D seismic attributes, thus this study integrates reflection seismology techniques through the use of an interactive spreadsheet employing the Gassmann method for potential use in large-scale CO_2 plume prediction and monitoring at the Wellington 1-32 well site.

4D Time Lapse Seismic

4D time-lapse monitoring using seismic techniques is a method used to study the evolution of subsurface processes through time, and is an important tool in areas outside the petroleum industry as well as within. The basic concept on which the tool is founded is that variations in the properties of the rock frame and the fluid within those pores change the characteristics of seismically-observed velocities and densities, providing a window through which to observe changing subsurface conditions without necessarily personally visiting. To understand time-lapse seismic data, Grochau and gurevich (2009) note that the combination of saturation effects (able to be determined from the Gassmann technique) and pressure effects on seismic wave propagation (able to be estimated through laboratory tests on core samples) need to be known, thus what this study has aimed to accomplish.

Although the Gassmann fluid substitution technique is a powerful tool for 4D interpretation (Xu and Payne, 2009), an important note is that monitoring injected CO_2 using seismic technologies is only possible if the rock physics-predicted, and more importantly, the actual CO_2-induced formation rock property changes are large enough to detect through current cost-effective methods (Sbar, 2000; Smith et al., 2003). These seismic changes include both velocity and amplitude (attenuation) of the propagating waves. Resolution of a seismic survey is important in this regard, and depends on a few key factors, including the frequency of the dominant wavelength used in the seismic survey, and the speed of the shear and compressional waves traveling through the subsurface area of interest. Knowing this information, and that seismic resolution is ¼ of the dominant wavelength, hypothetically given a surface seismic survey with 50Hz dominant wavelength with a Vp of 10,000$\frac{ft}{sec}$, the maximum resolution would be $\frac{10,000\frac{ft}{s}}{50\text{Hz}}$= 200ft, then $\frac{200\text{ft}}{4}$= 50 foot resolution. Indeed, CO_2 flood 4D seismic monitoring efforts depend most largely on the seismic measurement method, and the effect the CO_2 flood has on seismic properties of the formation rocks, including additional less significant factors such as reservoir depth and injection pressure (Wang et al., 1998).

Wang et al. (1998) observed modest though appreciable compressional wave velocity changes in their study of around -0.2% to -10% after CO_2 injection took place, which they attributed mostly to the compressibility contrast between the oil/ water mixture and the CO_2 in the reservoir. During geosequestration and enhanced oil recovery efforts, changes in subsurface fluid saturation and reservoir pressures both occur. These two changes may either reinforce or cancel each other out in terms of the velocity and impedance seismic responses, depending on the whether the wave is shear or compressional (Wang, 2001). If for instance, a specific procedure were to reduce reservoir pressure, decrease oil saturation, and increase water

saturation, the effects would have opposite influences on P-wave velocity and impedance, therefore generally cancelling out the individual effects. However, during that same procedure, Vs would not be expected to be significantly affected due to fluid saturation effects (apart from small bulk density changes or chemical-related effects), but it is expected to be sensitive to pore pressure changes (Wang et al., 1998). Therefore, differences between Vp and Vs values before and after a CO_2 flood may provide insight, revealing zones where CO_2 has either been swept with or without the buildup of pore pressure and thus providing good CO_2 plume spatial information (Wang et al., 1998). Castagna and Backus (1993), has also demonstrated the approximate feasibility of predicting and monitoring CO_2 flood plume zones, through various methods including high resolution surface seismic, crosswell techniques, and the Gassmann equations.

In addition to seismically-detectable velocity changes between pre- and post- fluid injection events, Adam and Batzle (2007) accumulated results on the attenuation/ amplitudes of waves in such a scenario. They determined the attenuation of waves to increase by a factor of 4 to 10 when the rock is brine- compared to butane-saturated at seismic frequencies in carbonate rocks (perhaps attributed to brine-softening of the matrix, or because of the heterogeneous nature of their samples), compared to fluid substitution velocity changes of only around a factor of 1.15. This suggests amplitude and attenuation of waves may be an additional important seismic feature to monitor in 4D CO_2 plume efforts.

Ideally, exploration seismology will eventually be able to map out exact spatial distributions of both different saturations of fluids and of different fluids within specific, detailed areas of subsurface interest. In order to achieve this noble goal, in part, seismic properties of those pore fluids need to be understood very well and under all conditions, as Batzle and Wang (1992) helped make more clear. Because rock physics has played significant roles in the

progression of seismic technologies including rock property inversions and 4D seismology, and has been underutilized in the interpretation of seismic data (Wang, 2001), this paper looks to in part remediate that insufficiency. A more all-inclusive perspective on likely future improvements and the current day state of 4D techniques can be found from Calvert (2005).

This study looks to apply a 4D CO_2 plume interactive Gassmann prediction and monitoring Excel spreadsheet which includes macro functions, provided by Dr. Abdelmoneam Raef from Kansas State University. Through Gassmann calculations, it will help determine the feasibility of 4D CO_2 plume monitoring at our study site through predictions of post fluid substitution effects on subsurface rock formations at the KGS 1-32 well site. Important seismic properties including changes in velocity, density, and acoustic impedance with changes in CO_2 saturation will be predicted and depicted graphically to determine the practicality of current seismic technology to observe subsurface fluid changes through time, indicating CO_2 plume migration. Acoustic impedance is a measurement of the resistance of a wave's travel within a system. Mathematically, it represents the seismic velocity of a wave penetrating a rock multiplied by that rock's density. It varies depending on factors including pore fluid type and saturation, among others. If spatial acoustic impedance contrasts are large enough, seismic techniques are able to observe them. Relating acoustic impedance to physical rock characteristics through rock physics models has been important for the seismic analysis of porosity and lithofacies (Jaiswal, 2014).

Chapter 3 - Geologic Setting

Study Area

The Wellington oil field is approximately two miles wide by three miles long, with an area of 22.6 km^2. It is located in Sumner County Kansas in the southern part of the state southwest of Wichita, at Section 32, Townships 31 South and 32 South, and Range 1 West, and at latitude 37.315444 and longitude -97.442414 (figures 3.1, 3.2). The field became a major oil producer after its discovery in 1929 at the drilling of the Peasel Well 1 lease; it has produced over 20 million barrels of oil from more than 250 wells drilled since. The producing zone is in the Mississippian formation within a nine-meter-thick zone between 3,670 and 3,700 feet measured depth (KGS, 2015). Initial production of wells ranged from 200 to 2,000 barrels of oil daily, though production was not particularly long-lived, and steadily declined as the reservoir became depleted (Cooperative Refinery Association, 1949). By 1953, wells were only producing 10 to 15 barrels daily on average, therefore water flooding secondary oil recovery efforts began which enhanced productivity (Cooperative Refinery Association, 1949). The field is currently continuing to be depleted after the application of nearly 50 years of water-flooding; 17 water-injection wells and 55 producing wells exist with yearly production in 2014 at 46,234 barrels of oil (KGS, 2015).

Figure 3.1 The left image is of Kansas with Sumner County highlighted in black. The right image is a close up of the Wellington Oil Field, highlighted in black, showing its location within Sumner County. Image 3.2 is modified from the Kansas Geological Survey website, (2015).
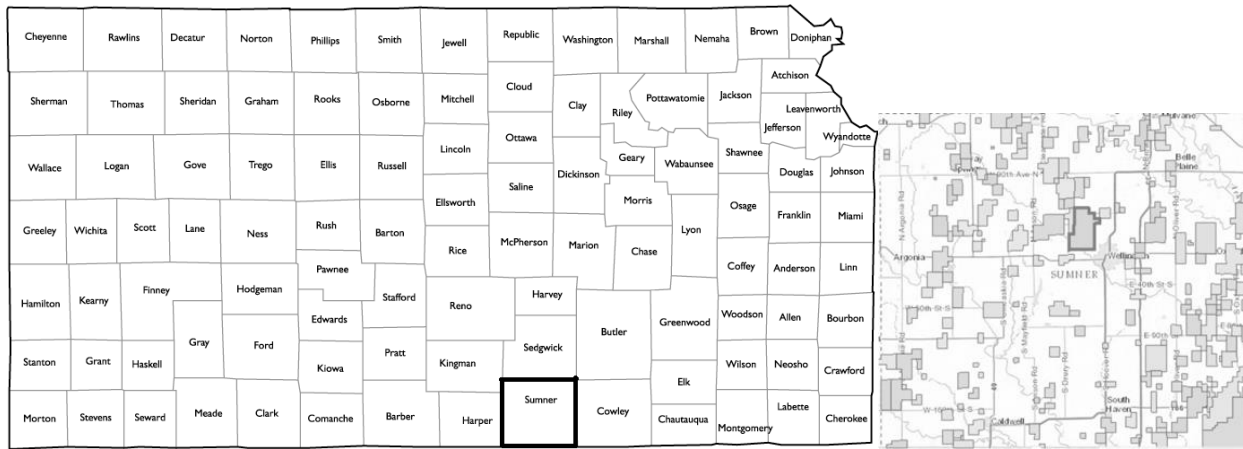
Figure 3.2 A close-up map showing the exact locations of the KGS 1-32 and 1-28 wells, both circled in black. Image modified from Huff (2014).
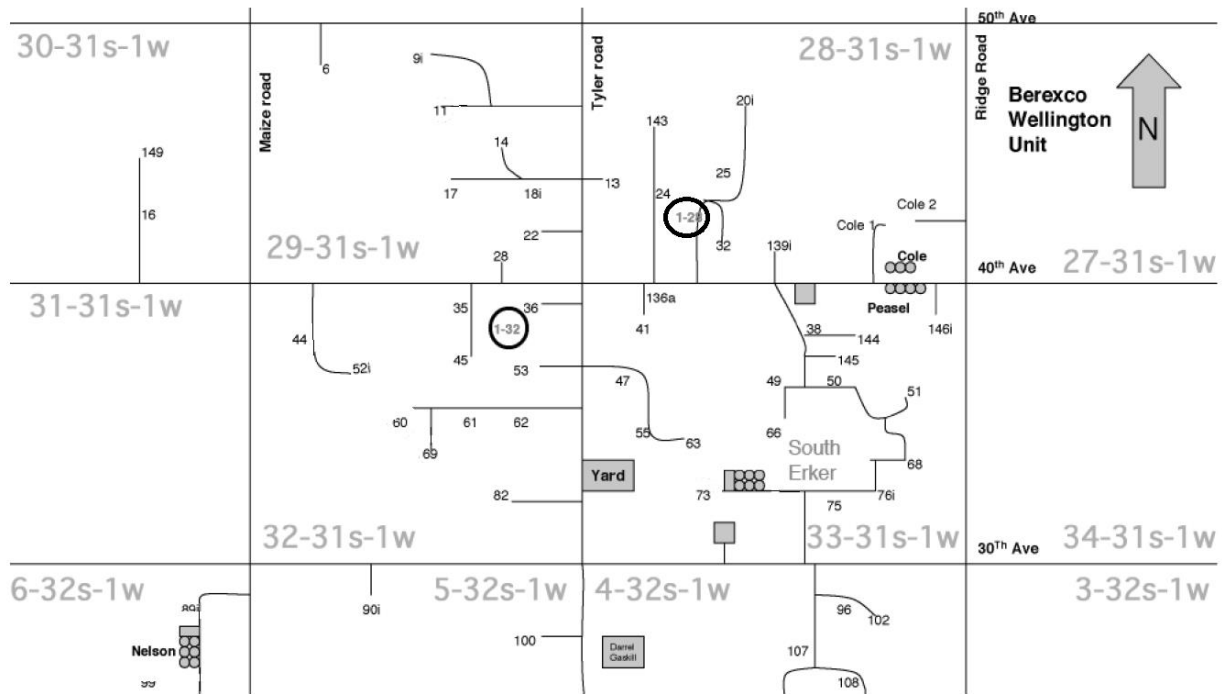
The well of interest is the KGS 1-32 well, API number 15191225910000, with X/Y coordinates 2307567.02680/ 237974.51742. It was drilled to a final depth of 5,250 feet measured

depth in 2011, and has provided 1,640 feet of core from 3,540 feet below groundsurface (within the Pennsylvanian Period) to 5,180 feet below groundsurface within the Precambrian and Proterozoic granite basement rocks. This 1,640-foot-long core from the Cherokee Shale to the granite basement was almost entirely continuous, with three breaks caused by the vuggy nature of the carbonates, and due to fractures in the reservoir which locked up the core shaft. During these vuggy sections, conventional drilling was used until coring could begin once again. The core was obtained in 60 foot units using a CT510 Core Bit with conventional split ring core catcher and aluminum casing, and then sent to Weatherford Labs in Houston, Texas for analysis. The core is currently kept at the Kansas Geological Survey core repository in Lawrence, Kansas.

The drilling of this well along with the associated KGS 1-28 (injector) well and related work was sanctioned by the United States Department of Energy (DOE) National Energy Technology Laboratory (NETL), under Grant Number DEFE0000002056, to determine the regional potential of carbon sequestration and enhanced oil recovery within the Wellington Oil Field. The project is currently managed by the Kansas Geological Survey and Dr. W.L. Watney. Funding is also partially supplied by cost-sharing partners.

The two areas of interest to this study are the limestone Mississippian depleting oil reservoir formation, and the underlying dolomite saline Arbuckle group aquifer.

Geologic History

Structural Geology

The structural framework of Kansas is relatively simple compared to other parts of the world. The basement is an extension of the large stable craton (the Canadian Shield), and therefore the sedimentary rocks above lie mostly parallel to one another (Merriam, 1963). It also was accreted by a series of orogenic events to the southern area of Laurentia. Although pre-

Mississippian features have undergone deformation since they were initially created due to relatively active tectonics (McBee, 2003), certain features have been identified and reconstructed. Important regional structural features in Kansas include the Ancestral Central Kansas Uplift, the Central Kansas Uplift, the Central Kansas Arch, the Chautauqua Arch, the Southwest Kansas Basin, the Pratt Anticline, the Sedgwick Basin, the Nemaha Anticline, and the Cherokee Basin (Merriam, 1963) (figure 3.3).

Kansas geology in the Ordovician and Devonian was largely determined through the influence of the Central Kansas Arch. Then, a change in the structural development of the area occurred at the closing of the Mississippian; this new structural regime helped determine the structural framework seen in Paleozoic beds (Merriam, 1963).

The Central Kansas Uplift is a large pre-Desmoinesian, post- Mississippian feature occupying 5,700 square miles, and which trends northwest and separates both the Sedgwick and Salina Basins on the east and the Hugoton Embayment on the west (Morgan, 1932). Sedimentary rocks are typically no thicker than 5,000 feet, with much associated information obtained through drilling to basement rocks.

The Chautauqua Arch is a pre-Mississippian broad westward-trending anticlinal feature which began rising while the North Kansas Basin started subsiding, and had stopped rising after Mississippian deposition and the subsequent post-Mississippian Cherokee Basin formed (Merriam, 1963). In some areas, Pennsylvanian rocks are even found lying on Cambrian rocks.

The Nemaha Anticline has been well studied and explored since oil was first found along its trend. It is a major narrow and southerly-plunging pre-Desmoinesian post-Mississippian feature reaching from Nebraska to Oklahoma, separating the Cherokee and Salina/ Sedgwick

Basins to the east and west respectively (Merriam, 1963). It is a basement block 'pop up'

structure with high relief, at the intersection of two wrench fault zones (McBee, 2003).

The Wellington Oil Field and Sumner County are positioned within the Sedgwick Basin,

which is surrounded by the Central Kansas Uplift and Pratt Anticline to the west, the Salina

Basin to the north, the Nemaha Anticline to the East and the Anadarko Basin to the south (figure

3.3). The Sedgwick Basin is a shelf-like southerly plunging, post-Mississippian pre-

Desmoinesian feature, and facies within the basin typically thicken southward towards the

Anadarko Basin in Oklahoma (Merriam, 1963). It is similar in many ways to the Hugoton

Embayment, and is composed of Cambrian-Ordovician, Silurian-Devonian, Mississippian and

Pennsylvanian-Permian rocks nearly 5,500 feet thick in its southern areas (Merriam, 1963). The

study area is in a location previously known as the Burlington shelf, located north of the

Anadarko basin and east of the Transcontinental Arch (Lane, 1978).

Figure 3.3 A map representing various major Kansas Post-Mississippian structural

features; Sumner County is highlighted in black. Image modified from Merriam (1963).
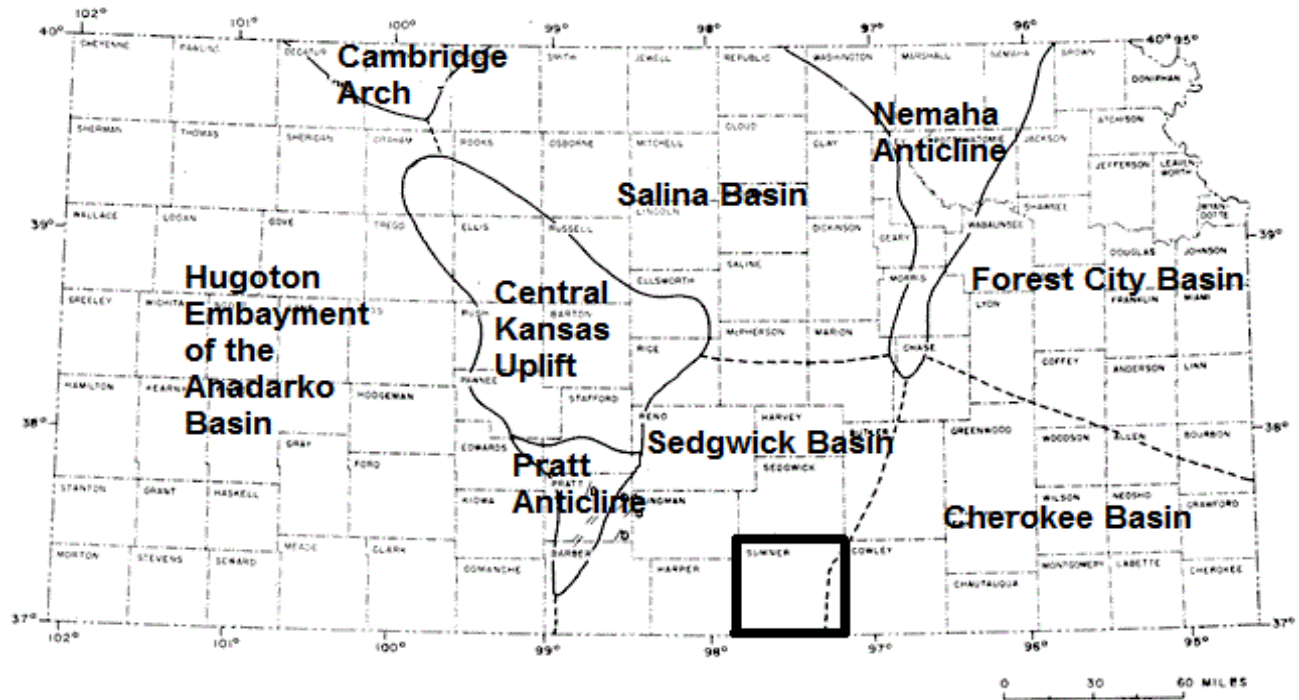
Stratigraphy

Lying beneath most of Kansas is the Western Interior Plains aquifer system (figure 3.4).

Near our study site, this system is composed of Arbuckle Group rocks (Ordovician and

Cambrian in age), Mississippian and Devonian shales known as the Chattanooga Shale,

Mississippian limestones, and capped by a large Pennsylvanian shale unit called the Cherokee

Shale. This entire area is being targeted for geologic carbon storage.

Figure 3.4 Two Paleozoic aquifer systems, the saltwater Western Interior Plains Aquifer

and the freshwater Ozark Plateaus Aquifer, and structural features are shown around the CO_2

sequestration evaluation area. Image modified from Carr et al. (2005).
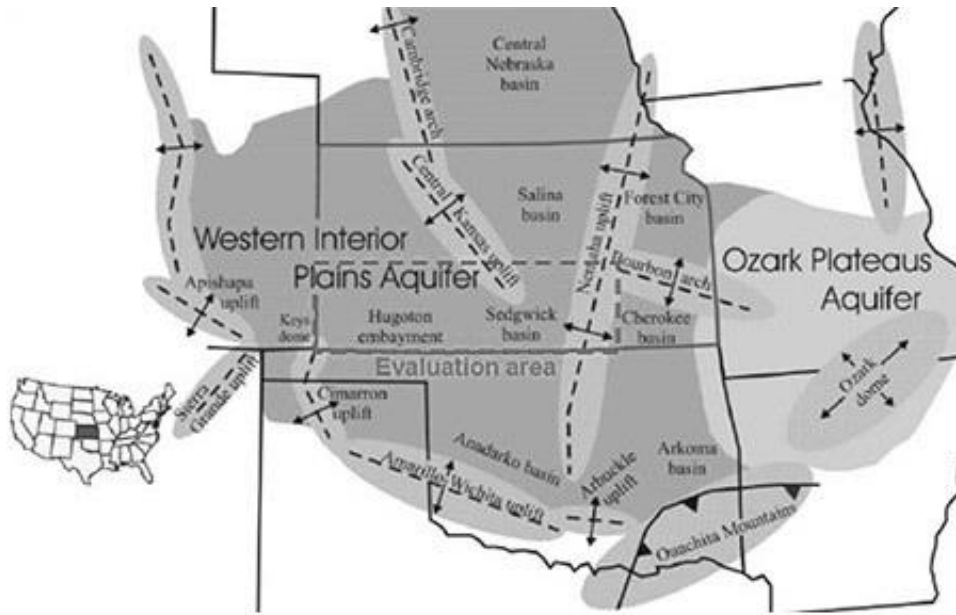
The relevant formations (in subsurface/ measured depth) at our study site, and seen in figures 3.5 and 3.6, include 1) the Arbuckle Group from 4,164 to 5,130 feet (with the proposed CO_2 injection zone from 4,900 to 5,050 feet, and with an observed baffle zone between 4,400 to 4,550 feet), serving as the CO_2 sequestration storage reservoir, 2) the Middle Ordovician Simpson Group composed of several sandstones and limestones from 4,070 to 4,157 feet and serving as part of the CO_2 reservoir lying between the CO_2 seal and reservoir facies, 3) the Upper Devonian Lower Mississippian Chattanooga Shale at around 4,060 feet and only 15cm thick at the KGS 1-32 well (this unit is quite variable across southern Kansas, ranging in thickness from approximately 1 to 150 feet), serving as the primary immediate CO_2 seal facies, 4) the Lower Mississippian Kinderhookian and Osagian Stages from 3,891 to 4,059 feet, including a low porosity section from 3,975 to 4,064 feet (Scheffer, 2012), which may act as a potential secondary seal, 5) the Upper Mississippian Series including the Meramecian and Chesterian Stages from 3,658 to 3,891 feet with the pay zone and thus enhanced oil recovery reservoir from 3,670 to 3,700 feet, 6) the thick Middle Pennsylvanian Cherokee Shale from 3,543 to 3,379 feet

serving as the secondary and regional seal, and 7) the Permian Sumner Group Evaporites from 606 to 1,197 feet, serving as the tertiary seal (KGS, 2012).

Figure 3.5 A stratigraphic column of Kansas, showing the respective locations of both formations of interest in this study, the Arbuckle and Mississippian. Image from Carr et al. (2005).
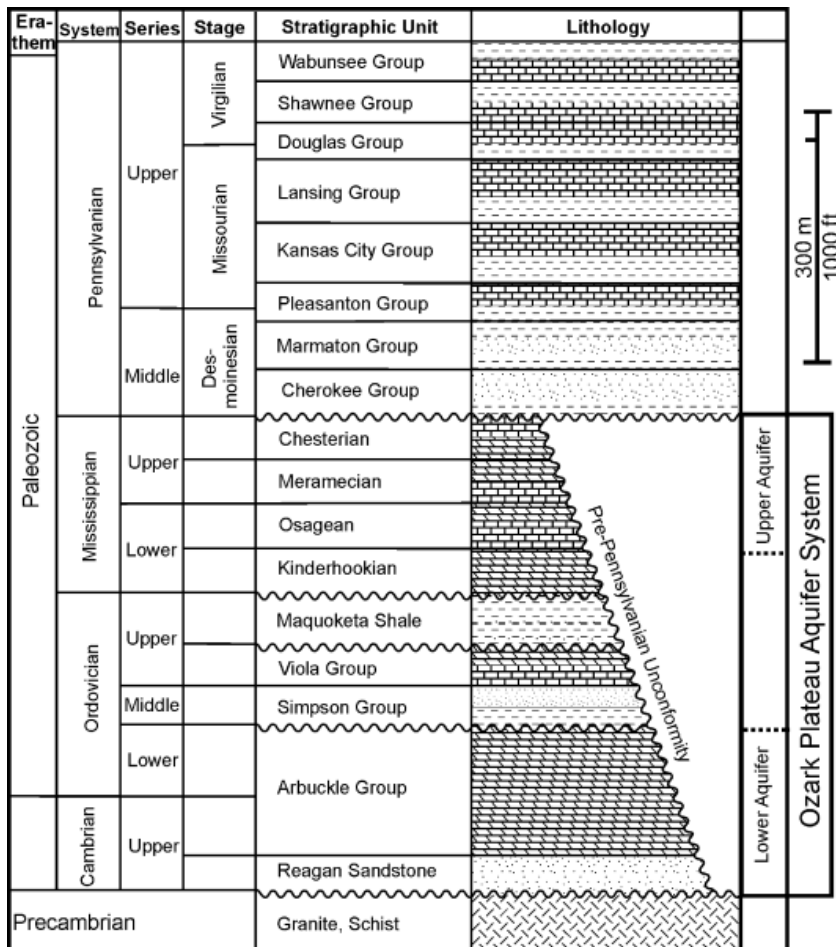
Figure 3.6 A stratigraphic column highlighting the purpose of each major lithologic formation within the KGS 1-32 well, and its associated CO_2 sequestration and CO_2-EOR purpose. Image modified from King (2013).

Sys.	Unit	Lithology	Purpose	
Perm.	Sumner Group		Tertiary Seal	590-1197ft
Penn.	Cherokee Group		Secondary Seal	3543-3658ft
Mississippian	Upper Mississippian Series		EOR Reservoir	3658-3891ft
Mississippian	Lower Mississippian Series		Primary Seal	3891-4063ft
D-M	Chattanooga Shale		Primary Seal	4063-4064ft
Cambrian-Ordovician	Simpson Group			4064-4165ft
Cambrian-Ordovician	Arbuckle Group		CO₂ Sequestration Reservoir	4165-5164ft
pЄ	Granite Basement			

* Not to scale

Core plug samples used in this study (figure 3.7) are located at the following subsurface/ measured depths from within both the Mississippian and Arbuckle formations: 1) core plug DM3716.7 at 3,716.7 feet, 2) core plug DM3716.8 at 3,716.8 feet, 3) core plug DM 3749.9 at 3,749.9 feet, 4) core plug DM 3829.4 at 3,829.4 feet, 5) core plug DM3829.5 at 3,829.5 feet, 6) core plug DA4300.3 at 4,300.3 feet, 7) core plug DA4300.4 at 4,300.4 feet, and 8) core plug DA4472.6 at 4,472.6 feet.

Figure 3.7 A picture of core plug DM3716.7. Additional core plug pictures can be found in Appendix A.

Mississippian Formation

Mississippian rocks in the study area can be divided into Upper and Lower Mississippian series; the upper series contains the oil-producing units of the Wellington oil field and thus targeted for CO_2 enhanced oil recovery efforts, and the lower series is planned to act as an alternative primary seal for the Arbuckle CO_2 sequestration. 230 feet (from 3658 to 3891 feet) of the upper series was collected by the KGS 1-32 core, and is composed of limestone and dolomite beds, including smaller beds of sandstone and shale and minor chert amounts (Zeller, 1968). 170 feet (from 3891 to 4061 feet) of the lower series was collected by the KGS 1-32 core. The two

series are distinguishable by an increase in carbonate and a decrease in argillaceous rocks in the upper series, and also by differences in porosity and permeability.

During the Carboniferous Period, the middle Mississippian reservoir rocks were deposited as part of a craton-scale depositional system, and bordered by deeper water to the south and west (Gutschlick and Sandberg, 1983). At this time, much of the central United States and the southern North American continent were covered by a broad carbonate shelf due to an epicontinental sea (figure 3.8); this shelf's outer shelf and shelf margin were located partially in southern Kansas (Witzke, 1990; Montgomery et al., 1998). The warm water shallow subtropical sea environment during that time created limestone deposition conditions, and because of the large coverage of this shelf, extensive laterally-continuous layers of carbonate and siliciclastic facies were deposited, and characterized by transgressive-regressive cycles of carbonate and silica- rich sediment deposits (Franseen, 2006). Biohermal buildups rich in sponge spicules reached nearly 50 meters in thickness on the shelf margin (Montgomery et al., 1998). The activity of the biota present during the depositional environment fluctuated depending on changes in water depth and associated oxygenation, and sediments were deposited below storm normal wave base (Mazzullo et al., 2011). Crinoids and bryozoans were the primary marine macroinvertebrates and carbonate mud producers, and the presence of framework organisms such as reefs were not present, as their population from the Silurian and Devonian Periods had collapsed by this time (Scoffin, 1986).

For carbonate depositional environments, basin fill changes are usually linked to changes in sea level fluctuations, called eustacy. Depending on the severity of sea level fluctuations, which can be controlled by factors such as tectonism, sediment supply, orbital variability and climatic changes, various kinds of cycles can be accumulated in the sediment record. First order

cycles usually influenced by tectonics span 80-90 million years; second order cycles last between 10-100 million years as a result of seafloor spreading; third order cycles range from 1-10 million years; fourth order cycles range from 0.2-0.5 million years and are driven by Earth's orbit, also known as Milankovitch cycles (Sloss, 1963). These sea level fluctuations and associated controlling mechanisms, especially climate, can often affect the depositional character of the sedimentary rocks, including continuity and geometry.

Figure 3.8 Land, shallow seas, and deep ocean locations during the late Mississippian period around 325ma, superimposed with modern territorial boundaries. Image modified from Blakey (2010).
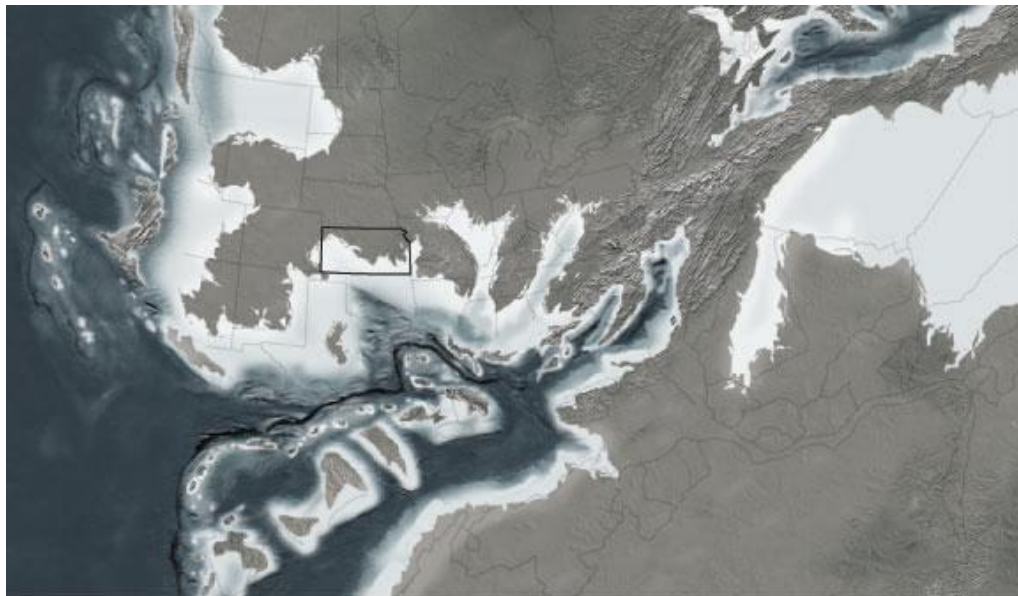
Diagenetic studies done in the area indicate many events have affected the Mississippian rock characteristics, including fracturing and dissolution events, which generated porosity and permeability conduits for fluids which later precipitated cements, reducing porosity (Young, 2010; Wojcik et al., 1992). Post Mississippian subaerial exposure resulted in an erosional

unconformity (figure 3.9). This and other influential diagenetic events created vuggy porosity,

sponge spicule dissolution and autobrecciation; carbonate dissolution, dolotimization and

silicification helped form cherty dolomites, vuggy cherts and microporosity (Watney et al., 2007;

Watney et al., 2001). As a result, today, porosity values in the Mississippian reservoir range from

three to 25 percent. According to King (2013), Mississippian facies in the KGS 1-32 core have

experienced nine known diagenetic events in its history: 1) carbonate dissolution creating vug

and cavern porosity increasing porosity by <5%, 2) brecciation and collapse features, 3)

megaquartz cement and reducing porosity by <5%, 4-7) chalcedony reducing porosity by <0.5%,

baroque dolomite reducing porosity by <0.5% and petroleum migration, 8-9) calcite cement

reducing porosity by <5% and anhydrite reducing porosity by <5%.

Figure 3.9 Distribution of Mississippian rocks (grey) in Kansas. Image modified from

Merriam (1963).
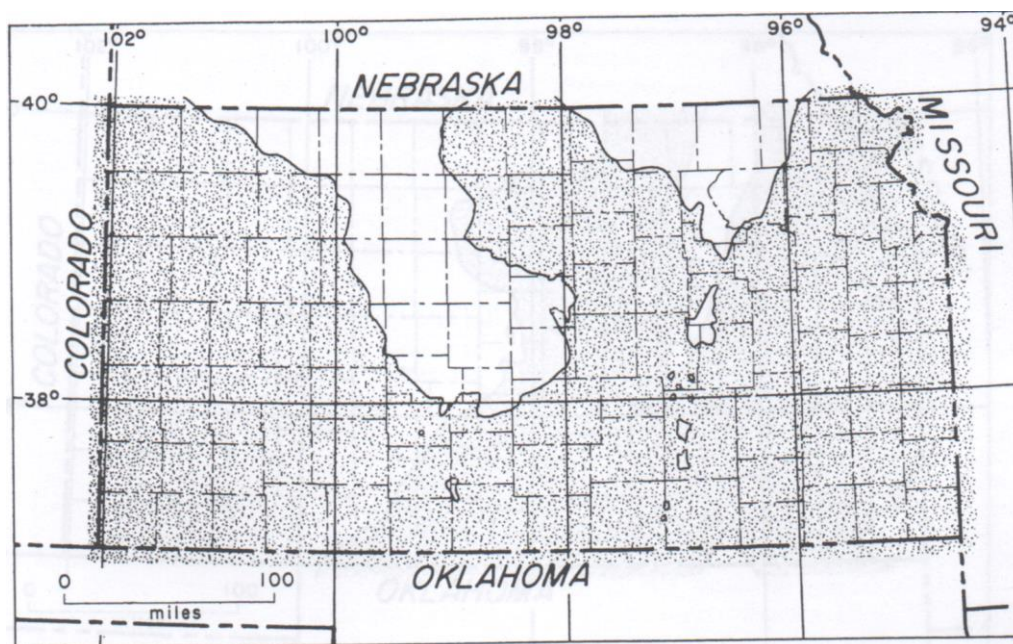
Arbuckle Formation

The Arbuckle Group is a deep saline aquifer included in the Ozark Plateau aquifer system, which dips gently southward with a westerly dip near the Nemaha anticline, and which is thickest in southeast Kansas (Franseen et al., 2004). The formation is present throughout most of Kansas, except where ancient uplifts have occurred (Franseen et al., 2004). Core descriptions of the unit from the KGS 1-32 well range from packstone to wackestone to grainstone, indicating the dominant depositional environment to be a subtidal to intertidal shallow carbonate shelf/ platform (Franseen et al., 2004). Deposition occurred in the Late Cambrian to Early Ordovician as carbonate strata in large packages within a shallow continental sea along and making up a large part of the 'Great American Bank,' which ran along the edge of the present North American Craton (figure 3.10) (Wilson et al., 1991). This sea contained high magnesium contents (Franseen et al, 2004) and fluctuated in depth, as the formation is currently largely dolotimized and bounded above and below by unconformities (figure 3.11). Dolomite formation requires a source of magnesium ions and a process by which to pump the dolomitizing fluid through the existing carbonate rocks (Tucker and Wright, 1990). Five types of dolomitization models currently exist, including the evaporative model, the seawater model, the mixing zone model, the burial model, and the seepage-reflux model.

Figure 3.10 Land, shallow seas, and deep ocean locations during the Cambrian period around 500ma, superimposed with modern territorial boundaries. Image modified from www2.nau.edu/rcb7/nam.html
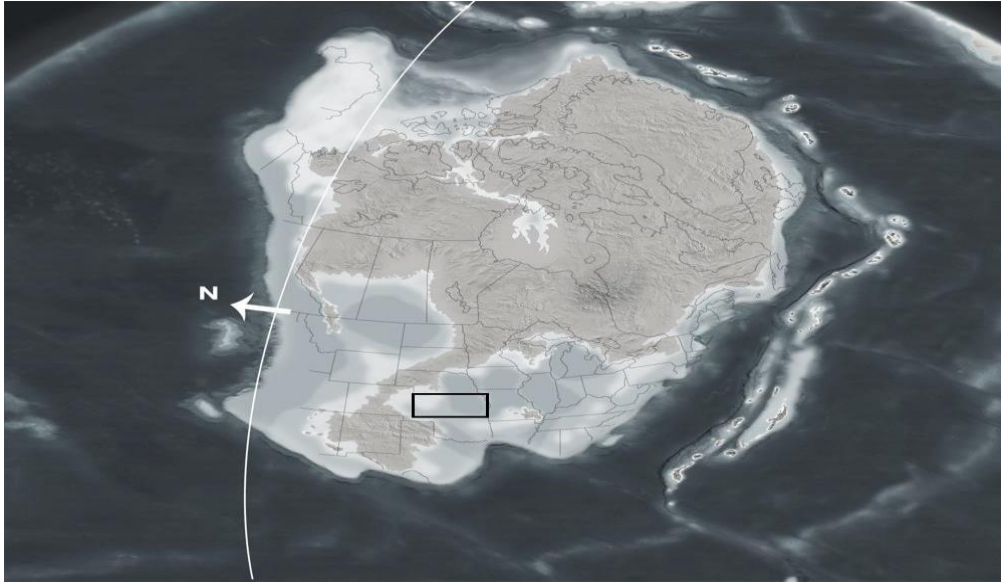
Figure 3.11 The distribution of Arbuckle rocks (grey) in Kansas Image modified from Merriam (1963).
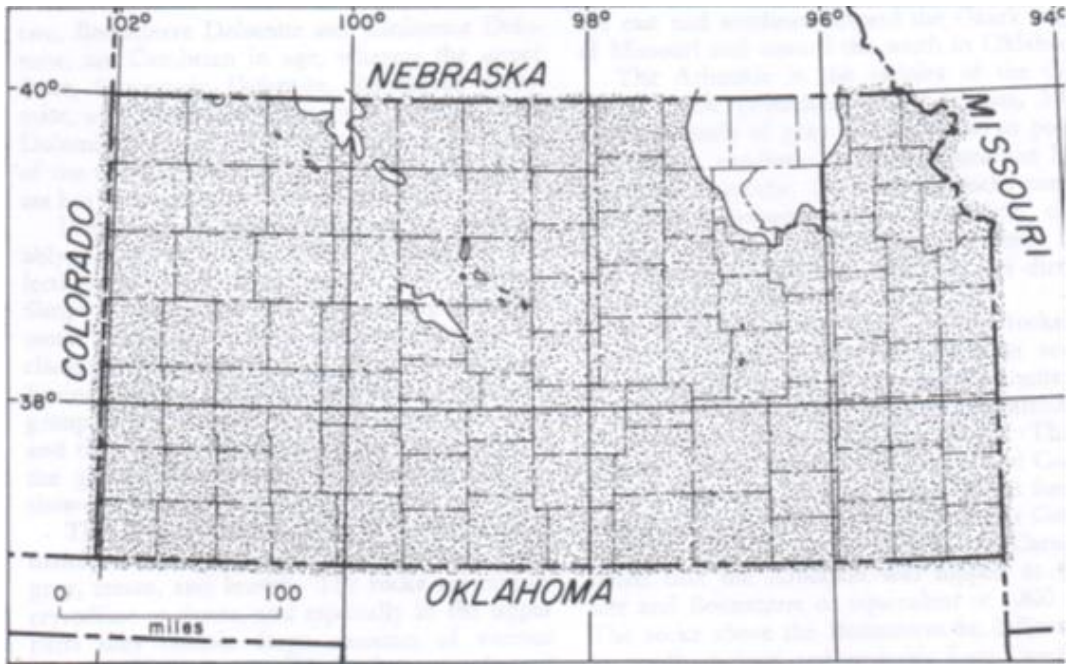
Five members exist within the Arbuckle Group: the Eminence dolomite, the Gasconade dolomite (4,908 to 5,157 feet), the Ruiobidoux dolomite (4,649 to 4,908 feet), the Jefferson City

dolomite (4,165 to 4,652 feet), and the Cotter dolomite. The Gasconade dolomite comes in direct contact with the igneous basement rocks unconformably; coring operations were unable to obtain a section of core from 4,997 to 5049 feet, indicating large vugs and fractures likely associated with that region. The Roubidoux dolomite also provided core extraction difficulties, as two sections from 4,655 to 4,680 feet and 4,818 to 4,899 feet were not recoverable, possibly also indicating the presence of large vugs. The Jefferson City-Cotter dolomite is a high impedance and thus dense and tight rock zone, according to core observations.

The Arbuckle mineral assemblage of the cored section in the KGS 1-32 well (4,163 to 5164 feet below ground surface) consists of baroque dolomite, calcite, megaquartz, galena and sphalerite, (Oliver, 1986; Garven, 1993; Sverjensky, 1986), and includes thrombolites and stromatolites, intraclastic conglomerate, minor shale and siltstone, coarse-grained skeletal, intraclastic, oolitic, peloidal packstones/ dolograinstones, and finer-grained mudstones (Franseen, et al., 2004). Both fenestral and interparticle primary porosity and vug and fracture secondary porosity exists; fractures appear common and are short, vertical, and unconnected (Scheffer, 2012); Carr et al. 1986), and Franseen et al. (2004) have determined through investigation that the Arbuckle Group is heterogeneous both laterally and vertically. Permeability variations that exist are likely due to changes in various depositional facies and associated grain size, pore size and shape, pore throat size, and how much cementation is present, largely due to the extensive dolomitizing effects. Also, a modern tight, dense, low permeability/ porosity 'baffle' zone from 4,400 to 4,550 feet was located by Scheffer (2012), which may help prohibit fluids from interacting between the upper and lower sections.

Due to subaerial exposure after deposition in the Early Ordovician, a large amount of weathering and secondary solution occurred in the upper regions (including a regionally

extensive karsting plain with caves and collapse breccias), which created enhanced permeability and porosity, ideal for a petroleum reservoir (Adler, 1971; Simo and Smith, 1997; Kupecz and Land, 1991). The uppermost portion of this group is an oil reservoir and rests above the saline aquifer (Franseen et al., 2004). Later, the unit was buried resulting in compaction, stylolitization and fracturing by structural deformation perhaps associated with both the Laramide and Ouachita orogenies (Franseen et al., 2004). King (2013) states that in all, 23 known major diagenetic events have affected this group, altering many of its characteristics including porosity, permeability and mineralogy; these occurred mainly as a series of dissolution and cementation events, with half occurring before burial and compaction, and with half occurring after burial and compaction. The diagenetic events King (2013) describes are 1) deposition, 2-4) early dissolution of carbonate strata, replacement dolomitization, and anhydrite, 5) early dolomite cements, 6) silicification, 7) chalcedony cement, 8) carbonate dissolution and karsting, 9) brecciation and collapse fractures, 10-11) middle dolomite cements and pyrite, 12) megaquartz, 13) internal sediment, 14-15) stylolitization, emanating fractures, and fracturing, 16-17) silica dissolution and carbonate dissolution, 18) megaquartz cement, 19) baroque dolomite cement, 20) petroleum migration, 21-23) galena, sphalerite, and calcite cement.

Chapter 4 - Methodology

Ult 100 Ultrasonic System

The basic synopsis of this Ult 100 Ultrasonic methodology section is as follows: to run velocity tests at varying ultrasonic frequencies and overburden pressures on eight air-humidified core plug samples from the Mississippian and Arbuckle formations, in order to estimate Vs, Vp, and the elastic moduli. Laboratory ultrasonic measurements are able to be conducted on short core plug samples because high frequency waves have short enough wavelengths to adequately sample the specimen: $wavelength = \frac{velocity}{frequency}$.

The Ult 100 Ultrasonic Velocity Measurement System, manufactured by GCTS Testing Systems, was an integral part of this work. The entire system ensemble contains an ULT controller and a Graphical Unser Interface (GUI) to the controller (known as the CATS Ultrasonics software), the CATS Ultrasonic software, and two platens. The GUI runs on a separate computer, and is able to interact with the ULT controller, which runs the program in real time and is only accessible through the CATS Ultrasonics software. The ULT controller performs the requested tests, saves data files, reads and writes to the boards, and controls the Ultrasonics Pulser, whereas the software handles the database and information aspect of the system. This setup can be seen in figure 4.1.

Figure 4.1 The Kansas State University geophysics laboratory, including the Ult 100 Ultrasonic Velocity Measurement System. Image from Randi (2012).

This system is non-destructive, and provides compressional (P) wave and shear (S) wave velocities and associated waveforms, both stored and viewable digitally. In order for the initial determination of Vp (compressional wave velocity) and Vs (shear wave velocity) to occur, it is necessary to locate the 'first arrival' of each tested wave either automatically through the software, or manually. This first arrival is the amount of time it takes for a wave pulse to travel through the core sample. These velocities are then used to calculate dynamic elastic constants including Bulk Modulus, Shear (Rigidity) Modulus, Young's Modulus, and Poisson's Ratio, allowing for subsequent application of these elastic properties. This system can be used in tandem with various laboratory set-ups, allowing core plugs to be tested either at *in situ* pressures, at lesser or greater pressures, or at no added pressure.

The basic experimental setup involves the two platens placed at both ends of each core plug sample; the platens each contain within them P-wave and S-wave piezoelectric crystals which determine the exact wave arrival times after a generated pulse propagates through the sample (figure 4.2). Pulses are initially generated when these piezoelectric crystals change shape in response to an applied voltage, causing the pulses, which propagate through the length of the specimen. Identical crystals are in the platen on the opposite side of the core sample, thus it doesn't matter which platen is on top or bottom; once the created pulse reaches the crystals on the opposite end, it is converted back to electrical energy, which then is processed. However, because the crystals are contained within the platens and not directly on the platen faces in contact with the core plug surfaces, an initial 'platen-to-platen' test must be conducted, where the platens are placed directly on top of each other with no substance except an acoustic couplant in between. This is to determine the amount of time it takes for the generated ultrasonic frequency pulse to propagate through the ultrasonic platens alone, and to ensure a strong and reliable signal is getting through. Once this time has been determined, it must be subtracted from any subsequent times recorded during the core plug tests, otherwise the travel time of the waves strictly through the core plug sample wouldn't be representative. Once these corrected P-wave and S-wave first arrival times have been determined, Vp and Vs can be calculated by dividing the core plug length by these first arrival times: $Velocity =$

$\dfrac{specimen\ height}{(arrival\ time - platen\ face\ to\ face\ arrival\ time)}$. Next, it is advisable to perform a test with the aluminum core sample provided by GCTS, to ensure the observation of strong signals and for the observer to understand what to look for once actual core plug testing begins; expected Vp and Vs aluminum values have been provided by the software manual, and velocities obtained from this test should be in agreement.

Figure 4.2 The Ult 100 System platens and an aluminum core in between. Image from Randi (2012).

Core plug samples are then tested. Before experimental testing begins, both ends of each core plug sample must be made perfectly smooth and flat, and an acoustic couplant needs to be applied between the faces of the platens and core plug. Both a perfectly smooth surface and the couplant provides the best coupling between the faces, thus maximizing the strength of the signal reaching the opposite platen, thus increasing the likelihood of an accurate and strong signal and first arrival time determination (Kahraman, 2007). The acoustic couplant used in this study was honey, which is of low viscosity and thus did not intrude into the pore structure of the specimen. Core plugs were originally cut perpendicularly to the original core axis at the Kansas Geological Survey, then were transferred to the Kansas State University geophysics laboratory where the

ends were made perfectly flat using both a water-cooling electric saw and sandpaper. The same technique for smoothing and flattening was used on every core plug as equally and similarly as possible. If core samples aren't perfectly flat and no acoustic couplant applied, air gaps may exist between the faces of the core sample and platens, which wouldn't allow the P- and S-waves to travel through, diminishing the signal strength.

Core plug samples were $1\frac{7}{16}$ inches in diameter and ranged from 6.5 to 8 centimeters in length. Core plugs were not oven-dried, but instead left air-humidified during testing, as a completely dry rock will cause velocity predictions to increase artificially (Clark et al., 1980; Grochau and Gurevich, 2009. Core plugs were tested in increasing pressure increments of 500lbf until appropriate *in situ* pressures were achieved. At each *in situ* pressure threshold, separate S- and P-wave waveforms were collected at both 1.25MHz and 20MHz. Pressure was applied and pressure measurements read from a 12-ton hydraulic jack and associated pressure sensor attached to one of the platens, respectively. *In situ* pressure for each core sample was determined from the assumption that overburden grain density averaged $2.3\frac{g}{cm^3}$, and that roughly one foot of overburden at our study area was equivalent to one pound per square inch (psi) of pressure. Conversion of pound force (lbf) to psi was accomplished by dividing the lbf measurement by the cross sectional area of the core plug in contact with the platen face: $psi = \frac{lbf}{\pi r^2}$, where the radius is the smoothed end of the core plug in inches. Although core plug diameters were $1\frac{7}{16}$ inches, the smoothing and flattening technique applied at best allowed for $1\frac{2.5}{16}$ of the diameter of each core plug face to be in direct contact with the platen faces during testing. Therefore, *in situ* pressure calculations were determined through this $1\frac{2.5}{16}$ inch diameter, and not the $1\frac{7}{16}$ inch diameter. All core plug samples were given for testing by the Kansas Geological Survey in

Lawrence, Kansas, under the condition that no samples would be subjected to destructive tests. Therefore, it was of importance to not exert any additional pressure greater than *in situ* pressure, for fear of cracking and destroying the core plugs. This was another reason great care was taken to make the core plug ends as smooth and flat as possible through the available techniques, as uneven pressure distributions caused by unevenness of core plug surfaces can easily damage or destroy the samples with too great of applied pressure. To test whether core plugs reached *in situ* pressures, P- or S-wave velocity and pressure applied were cross plotted. If these graphs exhibit velocity asymptotes as pressures increase, *in situ* pressures have been reached.

Before P-wave and S-wave tests could be initiated for each core plug, initial inputs relating to the physical nature of each specimen were also required, along with a general configuration of the software input board. It was necessary to choose the frequency of the sampling rate (this study utilized both 20MHz and 1.25MHz sampling rates), external manual gain (kept constant as off), input automatic gain (kept constant as 20), and energy output percent (kept constant at 100%). Specimen characteristic inputs were also required, including lithology type, height of the sample in millimeters, mass of the sample in grams, diameter of the sample in millimeters, and the type of platens used (NX platens was chosen consistently). From this information, density of each sample was determined. Core plug measurements were made on air-humidified samples. Sample characteristics including anisotropy and randomly oriented discontinuities can cause a weaker signal, and other factors such as heterogeneous lithologies, rock type, stress, water content and porosity may cause unexpected results. To minimize these undesirable affects, it is advised to reduce the energy output which minimizes excessive wave refraction, and also to perhaps to average the waveforms to decrease random noise.

The CATS Ultrasonics software provides both 'Ultrasonics Setup and Manual Execute' and 'Ultrasonics Plot' windows through which the analog waveforms can be visually seen and picked digitally. Typical compressional (figure 4.3) and shear (figure 4.4) waveforms displayed by the the Ult 100 system can be observed below. Both a cyan-colored vertical line and a vertically-oriented grey rectangle will appear superimposed over the waveform, representing the platen face to face arrival time and the expected arrival time range based on the core sample input parameters. In this study, the grey rectangle consistently occupied a range from 3,200-5,500$\frac{m}{s}$ for P-wave velocity, as determined by the software for limestones, after Rzhevsky and Novik (1971). An additional red line will appear, indicating the calculated first arrival time, and should lie within the grey rectangle, ideally.

Figure 4.3 A typical compressional wave waveform, as displayed by the Ult 100 system. Velocity and the elastic moduli are determined from a manually-determined wave first arrival time, the location of which as indicated by the vertical red line.
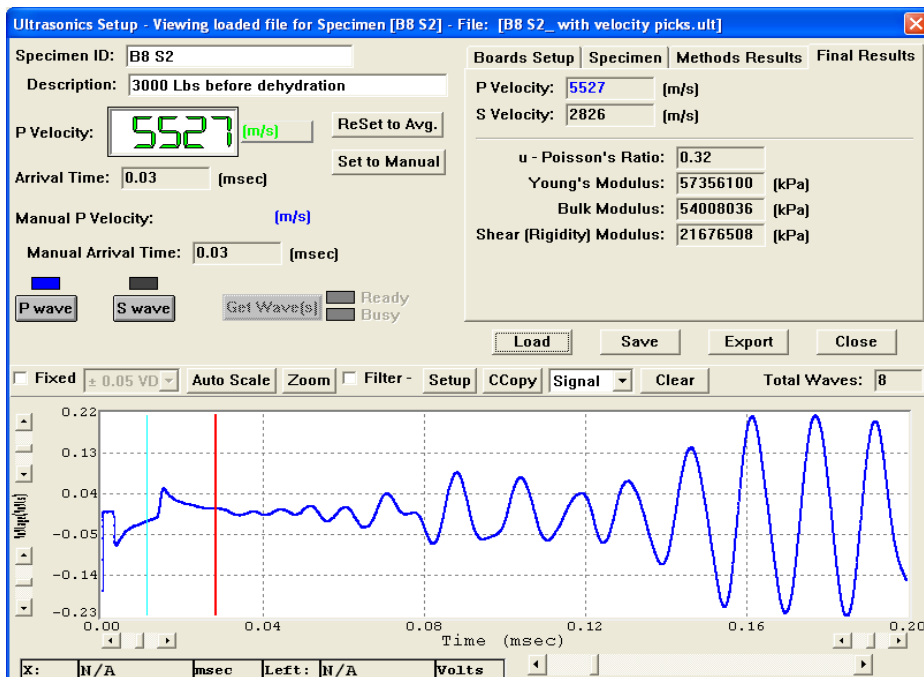
Figure 4.4 A typical shear wave waveform, as displayed by the Ult 100 system. Velocity and the elastic moduli are determined from a manually-determined wave first arrival time, the location of which as indicated by the vertical red line.
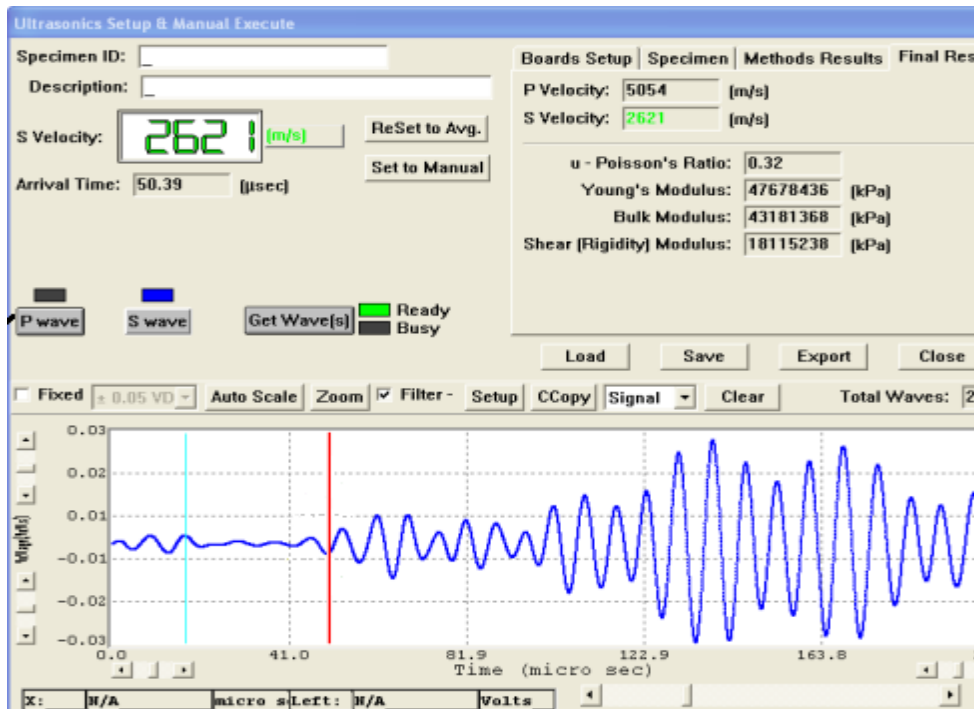
Through this waveform display, first arrival times can be determined; both manual and automatic first arrival determination methods are supplied by the software. Five automatic determination methods are provided: 1) the absolute threshold method, 2) the relative threshold method, 3) the relative of first peak method, 4) the first peak time method, and 5) the tangent of first peak method. Every automatic method was quickly determined ineffective and grossly inaccurate for this study's experimental setup, therefore the manual determination method was attempted. This is done by assessing the waveform and dragging the vertical red line (indicating first arrival times) to the exact position the observer sees as the first arrival, i.e. where only

random noise occurs before and where only the waveform occurs after. However, because of

relatively weak and low amplitude signals picked up from our core plug samples, even the

traditional manual determination could not consistently accurately determine the exact first

arrival times. Figure 4.5 shows the degree of difficulty present for picking the exact location for

S- and P-wave first arrivals. The most accurate method was finally determined instead through

acquiring and superimposing many different velocity measurements from the same sample at

different, increasing overburden pressures (figure 4.6). For each sample at each pressure, for

both frequencies tested, and for both S-waves and P-waves, all associated waveform data

generated by the software was exported to Microsoft Excel using the CATS software 'save to

clipboard' option. Data for each core plug was compiled into separate Excel spreadsheets, and

new graphs were generated from this data which were easier to manipulate and analyze. These

newly generated graphs of varying increasing pressures were then superimposed over each other

for the most accurate determination of first arrival times, based on the interpreter's opinion of

where the random noise ended and the actual waveform first began. This was determined to be a

very accurate process, though some signals were easier to pick than others, which could be quite

complex and subtle. With every core plug sample, a clear area of waveform departure from

random noise was able to be determined for S-waves and P-waves, indicating the exact location

and timing of first arrivals. All graphs were necessarily stretched on their X-axis the same

magnitude for better clarity of deviations.

Figure 4.5 Manually picking first arrival S- and P-waves was impossible using the

traditional manual approach. It could not reliably be determined exactly where random noise

ended and the waveform began (green arrow).
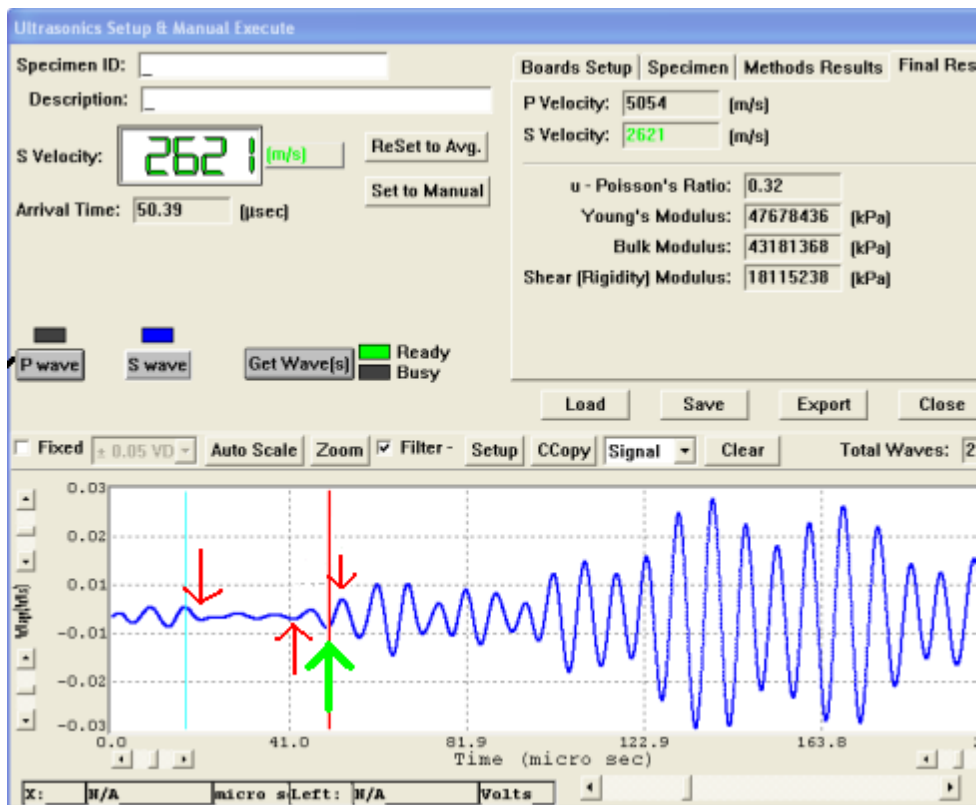
Figure 4.6 The correct s-wave pick location is represented again with the green arrow.

The top waveform is of a sample with only 500lbf of pressure applied, and the bottom waveform

shows the superimposition of all pressures applied to the same sample. It is evident how difficult

picking the correct first arrival times manually for a single pressure is without the superimposing

method. However, when waveforms are superimposed, it is much easier to see where waveforms

begin diverging from one another, thus indicating perfect first arrival times.
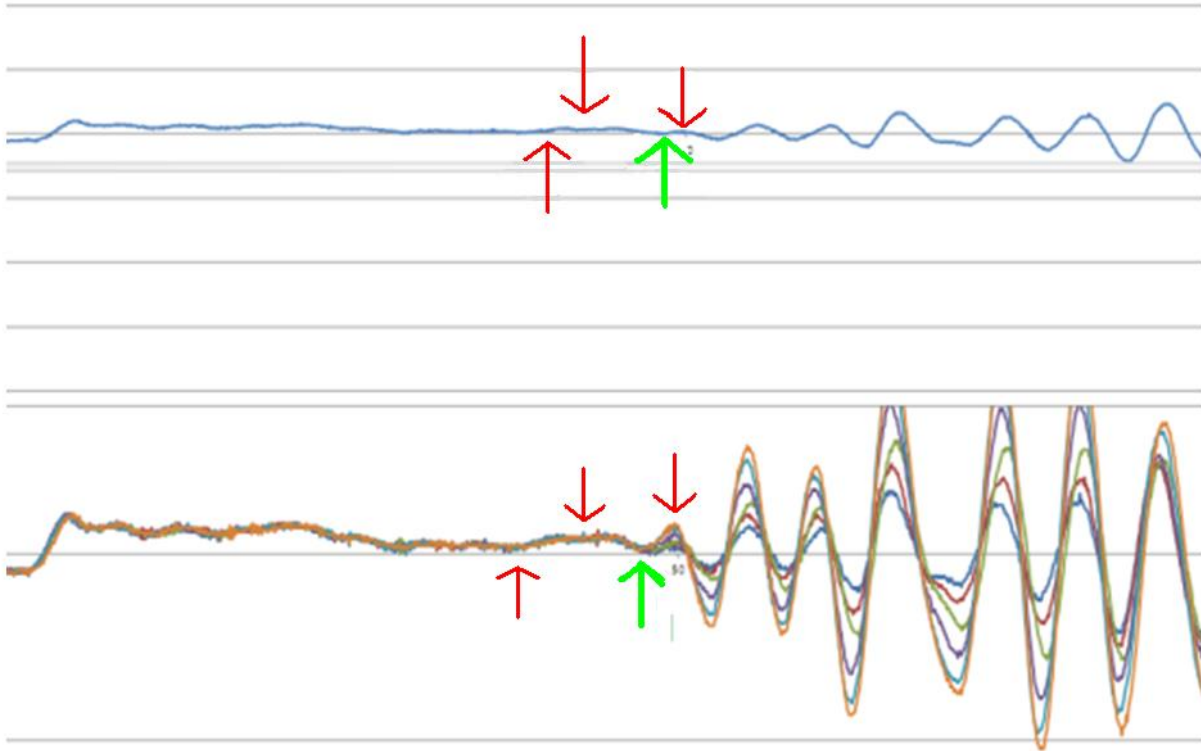
With the correct first arrival times and specimen densities determined, the CATS Ultrasonics software was able to calculate velocity of each wave, and thus elastic moduli in SI units of kilopascals (kPa) (or English units of psi depending on preference). Equations for the elastic moduli calculations are as follows: Bulk Modulus $K = \frac{p(3V_p^2 - 4V_s^2)}{3}$ where p is density, V_p is compressional wave velocity, and V_s is shear wave velocity. Shear Modulus $u = pV_s^2$ where p is density and V_s is shear wave velocity. Young's Modulus $E = \frac{pV_s^2(3V_p^2 - 4V_s^2)}{V_p^2 - V_s^2}$ where p is density, V_p is compressional wave velocity, and V_s is shear wave velocity. Poisson's Ratio $v = \frac{V_p^2 - 2V_s^2}{2(V_p^2 - V_s^2)}$ where V_p is the compressional wave velocity, and V_s is the shear wave velocity. An initial accurate determination of the first arrival times is paramount, as this heavily influences calculated velocities and elastic moduli which are then used throughout the rest of the study. This

velocity calculation is: $V = \frac{L}{Tf}$ where V is velocity, L is length of the sample, and T_f is the first

arrival time of the signal.

Well Log Data Extraction

Various pieces of information were extracted from log 1044564846 at the KGS 1-32

well; this well log's header is seen in figure 4.7. This information was compared to the

laboratory-acquired ultrasonic data, used in the validation of the rock physics models tested, and

in some cases used as inputs into rock physics models and an interactive Gassmann CO_2 plume

modeling spreadsheet. Specifically, information was collected at within 0.5 feet of each core

sample tested; information extracted from the well log includes depth, Poisson's ratio, P-wave

slowness, Fast Shear slowness, Slow Shear slowness, bulk density, and neutron porosity, which

are highlighted in yellow boxes in figure 4.7.

Figure 4.7 The complete 1044564846 KGS 1-32 well log header.

Well log units aren't always identical to laboratory-obtained values, so conversions of some units were required. Both the compressional wave and shear wave values from the well log are recorded in units of slowness ($\frac{us}{ft}$), not travel time or velocity. Therefore, the equation to convert this slowness time to velocity in $\frac{ft}{s}$ is, $velocity = \frac{1000000}{log\ slowness\ value}$, where the $log\ slowness\ value$ is in $\frac{us}{ft}$. From here, a simple conversion from $\frac{ft}{s}$ to $\frac{m}{s}$ is necessary, and comparable values are achieved.

Poisson's Ratio well log units also need to be converted for comparison. The value conversion equation from a well log value for a rock with porosity is $\frac{0.5*((log\ Poisson's\ ratio)^2-1)}{(log\ Poissons's\ ratio)^2-1}$.

Finally, for comparison to ultrasonic frequency velocity laboratory values, the shear modulus, bulk modulus and Young's modulus needed to be extracted from the well log data. Shear modulus values from log data for rocks with porosity can be found using $shear\ modulus = \frac{1000*density}{(S-wave\ slowness\ log\ value)^2}$, where $density$ is the well log bulk density value in $\frac{gm}{cc}$ and the $S-wave\ slowness\ log\ value$ is in $\frac{us}{ft}$. Also, the value of 1,000 is chosen if metric units are used, otherwise the value of 13,400 would be chosen for English units. Bulk modulus values from log data for rocks with porosity can be found using $bulk\ modulus =$ $1000 * density \left(\frac{1}{(P-wave\ slowness\ log\ value)^2}\right) - \frac{4}{3} * \left(\frac{1}{(S-wave\ slowness\ value)^2}\right)$, where $density$ is the well log bulk density value in $\frac{gm}{cc}$, and the value of 1,000 is applied when using metric units, otherwise the value of 13,400 would be used for English units. Young's modulus values from log data for rocks with porosity can be found using $Young's\ moduluss = 2 * shear\ modulus *$ $(1 + Poisson's\ ratio)$, where both the $shear\ modulus$ value and the $Poisson's\ ratio$ value

are those obtained from log values located previous to this computation. Equations were obtained from Crain (1978).

X-ray Diffraction

Sample preparation of X-ray diffraction samples began by cutting small sections of each core plug to be ground up into fine powders. A hammer was initially used to break these small pieces into pea-sized bits; a clean surface free of any other rock particles was worked on. Once pea-sized bits were obtained with the hammer, an agate mortar and pestle was used to grind the samples into fine powders. This was done one specimen at a time, with both the agate mortar and pestle washed thoroughly with water and acetone between samples. Power was ground to a size of 200 mesh, or 10 micrometers. To avoid preferentially including a disproportionate amount of softer grains for analysis, as much as possible of the sample was ground up, including the very hard grains. A 200 mesh sifter was used, and cleaned thoroughly between each individual sample (figure 4.8).

Once finished with this preparation, the mounds of fine powder were ready for X-ray diffraction analysis. The Geology Department at Kansas State University has a PANalytical EMPYREAN X-ray diffractometer, and it was used for sample analysis. For all samples, the scan axis was Gonio with a radius of 240mm, the start 2θ position was 20.0033 degrees, the end 2θ position was 69.99 degrees, the step size was 0.007, the scan type was continuous, and the anode material was copper (Cu).

Figure 4.8 Equipment used during the X-ray diffraction sample preparation process, including a 200 mesh sifter, acetone, an agate mortar and pestle, and hammers.

Rock Physics Models

Gassmann

The Gassmann procedure is a five step process as given by Avseth et al. (2006) and Berryman (2009).

The first step requires an initial set of densities and velocities (Vp and Vs) from a rock specimen which contains within it an initial set of fluids. Vp, Vs and density of eight core plugs, five from the Mississippian and three from the Arbuckle, were obtained from the ultrasonic frequency velocity laboratory tests, at both 1.25MHz and 20MHz. Density with the initially-saturating fluid of each core plug was determined from volumetric and mass measurements. From these, the dynamic bulk and shear modulus are extracted. The equation used to extract the bulk modulus is given as $K_{sat}^{(1)} = p((Vp^{(1)})^2 - \frac{4}{3}(Vs^{(1)})^2)$, where $K_{sat}^{(1)}$ is the bulk modulus of the rock specimen containing an initial fluid, p is the bulk density of the rock specimen with initial fluids, $Vp^{(1)}$ is the acquired compressional wave velocity with the initial fluid, and $Vs^{(1)}$ is the acquired shear wave velocity with the initial fluid. The equation used to extract the shear

modulus is given as $u_{sat}^{(1)} = p(Vs^{(1)})^2$, where $u_{sat}^{(1)}$ is the shear modulus of the rock specimen

containing an initial fluid, p is the density of the rock specimen with initial fluids, and $Vs^{(1)}$ is

the acquired shear wave velocity with the initial fluid. Both the bulk modulus and shear modulus

have been calculated in units of kilopascals, density in units of $\frac{g}{mm^3}$, and velocity in units of $\frac{m}{s}$.

The second step is to apply Gassmann's relation to transform the saturated bulk modulus.

The equation used for the transformation is $K_{sat}^{(2)} =$

$$\frac{K_{mineral}}{[\frac{K_{sat}^{(1)}}{K_{mineral}-K_{sat}^{(1)}} - \frac{K_{fluid}^{(1)}}{\Phi(K_{mineral}-K_{fluid}^{(1)})} + \frac{K_{fluid}^{(2)}}{\Phi(K_{mineral}-K_{fluid}^{(2)})}]^{-1}+1}$$, where $K_{sat}^{(2)}$ is the bulk modulus of the

rock with the second substituting pore fluid, $K_{mineral}$ is the bulk modulus of the minerals, $K_{fluid}^{(1)}$

is the bulk modulus of the initial saturating rock fluid, $K_{fluid}^{(2)}$ is the bulk modulus of the

substituting rock fluid, and Φ is the total porosity of the rock specimen. Both the bulk modulus

of the initial saturating fluid (air, at $1.42*10^5$ pascals) and substituting saturating fluid (brine, at

10^9 pascals) were used. Also, in order to determine the bulk modulus of the minerals for each

sample, it was necessary to consult the results from the X-ray diffraction technique. Knowing the

bulk modulus of each of the minerals making up each core plug sample, including quartz, calcite

and dolomite, and knowing each of their relative abundances in each core plug, it became

possible to determine the bulk modulus of the mineral assemblage of each core plug, i.e. the bulk

modulus of the minerals. Bulk modulus values of 37 Gpa for quartz, 77 Gpa for calcite, and 95

Gpa for dolomite were used, from Carmichael (1989). Total porosity in this step was also

determined through a combination of steps. Well log values weren't used because values

obtained by neutron porosity logs are effective, or connected, porosity. Because porosity is a

dimensionless volume ratio, it can be found for each core sample by dividing the volume taken

up by the pores by the total volume of the core plug. Knowing the original volume of each core plug, the mass of each core plug, and the densities, masses and percent abundance of each of the minerals occupying the core plugs, percent porosity was able to be found. For instance, if we know the density of dolomite is $2.84\frac{g}{cm^3}$, the density of calcite is $2.71\frac{g}{cm^3}$, and the density of quartz is $2.65\frac{g}{cm^3}$, plus each of these minerals' relative abundances, an average density can be found. The mass of the particular sample is then divided by this average density, and the volume of the mineral assemblage making up the rock, and thus the rock itself without the pore area (air weighs close to nothing) is determined. This volume of the pure rock mass is then divided by the total volume of the specimen as previously measured, and a percent porosity is obtained.

The third step is to leave the initially-obtained shear modulus unchanged, as rigidity is independent of fluid type. The equation used to signify this is, $u_{sat}^{(2)} = u_{sat}^{(1)}$, where $u_{sat}^{(1)}$ is the initial shear modulus with the initial pore fluid, and $u_{sat}^{(2)}$ is the shear modulus after the second fluid has been substituted into the rock.

The fourth step is to correct the bulk density for the effects of the substituting fluid. The equation used in this step is, $p^{(2)} = p^{(1)} + \Phi(p_{fluid}^{(2)} - p_{fluid}^{(1)})$, where $p^{(1)}$ is the bulk density of the rock specimen with the initial fluid, $p^{(2)}$ is the bulk density of the rock specimen with the substituting fluid, Φ is the total porosity of the rock specimen, $p_{fluid}^{(1)}$ is the density of the initial fluid, and $p_{fluid}^{(2)}$ is the density of the secondary substituting fluid. This step requires finding the density of air at STP and the density of brine, or saltwater; these values were found to be 1.2754 $\frac{kg}{m^3}$ and $1025\frac{kg}{m^3}$, respectively.

The fifth and final step is to recalculate the P-wave and S-wave velocities of the rock specimen with the secondary substituting fluid in place. The accompanying equations are, $V_p^{(2)} =$

$$\sqrt{\frac{K_{sat}^{(2)} + \frac{4}{3}u_{sat}^{(2)}}{p^{(2)}}}, \text{ and } V_s^{(2)} = \sqrt{\frac{u_{sat}^{(2)}}{p^{(2)}}}, \text{ where } V_p^{(2)} \text{ is the compressional wave velocity of the rock with}$$

substituting fluid, and $V_s^{(2)}$ is the shear wave velocity of the rock with substituting fluid.

Gregory-Pickett

This S-wave velocity prediction approach is also called the 'dry-rock Poisson's ratio' approach, because as an input to its equations, the dry rock Poisson's ratio values of each core sample are needed. Various equations are used to ultimately determine the shear wave velocity; initial inputs to these equations are density, in $\frac{g}{cm^3}$ (obtained from the KGS 1-32 well log), the bulk modulus of the minerals in units of Kpa (obtained from laboratory analysis), the dry rock Poisson's ratio (obtained from laboratory analysis), the KGS 1-32 Vp log value in units of $\frac{m}{s}$, the bulk modulus of the saturating fluid (brine) in units of Kpa, and the total porosity obtained from laboratory analysis. Equations now to be solved from Simm and Bacon (2014) are in order and as follows: $M = V_p^2 * p$, where M is a constant for later use, V_p is the compressional wave velocity, and p is the density of the rock sample. $S = \frac{3(1-\sigma_d)}{1+\sigma_d}$, where S is a constant for later use, and σ_d is the dry rock Poisson's ratio. $c = -\Phi(S - \frac{M}{K_o})(\frac{M}{K_{fl}} - 1)$, where c is a constant for later use, Φ is the total porosity, K_o is the bulk modulus of the minerals, and K_{fl} is the bulk modulus of the fluid. $b = \Phi S \left(\frac{K_o}{K_{fl}} - 1\right) - S + \frac{M}{K_o}$, where b is a constant for later use. $y = \frac{-b+(b^2-4ac)^{0.5}}{2a}$, where y is a constant for later use. $K_d = (1 - y) * K_o$, where K_d is the bulk modulus of the dry rock. $u = \frac{3K_d(1-2\sigma_d)}{2(1+\sigma_d)}$, where u is shear modulus. And, $V_s = \sqrt{\frac{u}{p}}$, where V_s is shear wave velocity.

Gassmann Interactive Spreadsheet

Fluid replacement models like Gassmann can be very beneficial for seismic reservoir monitoring, through predicting effects of varying effective fluid compositions and saturations on rock elastic moduli and thus seismic property information content. The interactive spreadsheet used in this study can be seen in figure 4.9.

Through a set of initial inputs, parameters are predicted using the Gassmann equation. Inputs required include the initially brine saturated Vp (from the KGS 1-32 well log), the initially-saturated Vs (fast shear value from the KGS 1-32 well log), the initially-saturated rock density (from the KGS 1-32 well log), the rock skeleton lithology (from laboratory assessment), the rock skeleton effective/connected porosity (from the Weatherford Labs analysis), the rock skeleton density (from the laboratory assessments), the initial rock skeleton bulk compressibility (inverse of the brine-saturated bulk modulus determined from the KGS 1-32 well log), the initial and substituting fluid type and saturations, the densities of the fluids involved (including brine, oil, CO_2 gas and CO_2 supercritical fluid) (determined through methods described below), and the bulk modulus and bulk compressibility of the fluids involved (determined through methods described below). From this information, the spreadsheet is able to calculate the initial saturated bulk modulus, the initial water saturation, the initial saturated Poisson's ratio, the rock skeleton bulk modulus, the bulk modulus of the initial fluid, the dry rock Vp, the dry rock Vs, the dry rock density, the dry rock bulk modulus, and the dry rock Poisson's ratio. From here, final values are calculated including Vp, Vs, density, bulk modulus, water saturation and Poisson's ratio with the selected substituting fluid and saturation amount in place.

Figure 4.9 The interactive Gassmann spreadsheet used in this study, provided by Dr. Abdelmoneam Raef from Kansas State University.

#	A	B	C	D	E	F	G	H	I
1	SACS: Calculation of the effect of CO2-saturation								
2	INITIAL SITUATION		NEW SITUATION		CONSTANTS				Units
3	Velocities from a rock with water saturation Sw and hydrocarbon saturation Shc are known		Velocities from the same rock with a new water saturation Sw2 and hydrocarbon saturation Shc2 are determined						
4	SAT ROCK		SAT ROCK (GASSMAN)						
5	Vp(Sw)	5076.7	Vp(Sw2)	4884					m/s
6	Vs(Sw)	3173	Vs(Sw2)	3173					m/s
7	RHO(Sw)	2632	RHO(Sw2)	2632					kg/m3
8	K(Sw)	3.251E+10	K(Sw2)	2.745E+10					Pa
9	Sw	1.00	Sw2	0.94					
10	Poisson(Sw)	0.180	Poisson(S	0.135					
11	ROCK SKELETON				SANDSTONE	SHALE	OTHER		
12	Lithology	OTHER			SS	SH	OTHER		
13	POR	0.0140							
14	RHOs	2670			2650	2700	2670		kg/m3
15	COMPs	2.326E-11			2.710E-11	2.530E-11	2.326E-11		1/Pa
16	Ko	4.300E+10			3.690E+10	3.953E+10	4.300E+10		Pa
17	INITIAL HYDROCARBON		NEW HYDROCARBON		WATER	OIL	GAS		
18	Hydrocarbon	WATER	Hydrocarb	Fluid	water	oil	gas	Fluid	
19	Shc	0.00	Shc2	0.06					
20	RHOhc	1090	RHOhc2	850	1090	850	660	870.06	kg/m3
21	COMPhc	4.200E-10	COMPhc2	3.509E-09	4.200E-10	6.300E-10	1.286E-08	3.51E-09	1/Pa
22	fractional Saturation				2.000E-01	3.000E-01	6.000E-01		
23	TOTAL FLUID (water + hc)		TOTAL FLUID 2 (water + hc2)						
24	COMPfl	4.200E-10	COMPfl2	6.053E-10					1/Pa
25	Kfl	2.381E+09	Kfl2	1.652E+09					Pa
26	DRY ROCK (GASSMAN)								
27	Vp(dry)	14684							m/s
28	Vs(dry)	3182							m/s
29	RHO(dry)	2617			CALCULATION OF VELOCITIES AFTER FLUID SUBSTITUTION				kg/m3
30	K(dry)	5.289E+11							Pa
31	Poisson(dry)	0.475							
32									

A certain number of these inputs are not constant values to be used unchangingly with every core plug sample, but change due to variations in *in situ* pressures and temperatures. At each core plug location, *in situ* temperature was determined from Holubnyak et al. (2013), and *in situ* pressure was determined from the psi measurements determined earlier. From this information, the density of CO_2 at those specific conditions was calculated. Furthermore, because the bulk modulus (and thus the bulk compressibility) of CO_2 also changes with changes in pressure and temperature, these values were determined individually with assistance from Yam and Schmitt (2011).

Figure 4.10 Changes in the bulk modulus (left) and density (right) of CO_2 with changing pressures and temperatures. Image from Yam and Schmitt (2011).

Bulk Modulus of CO$_2$ (MPa)

Density of CO$_2$ (kg/m^3)
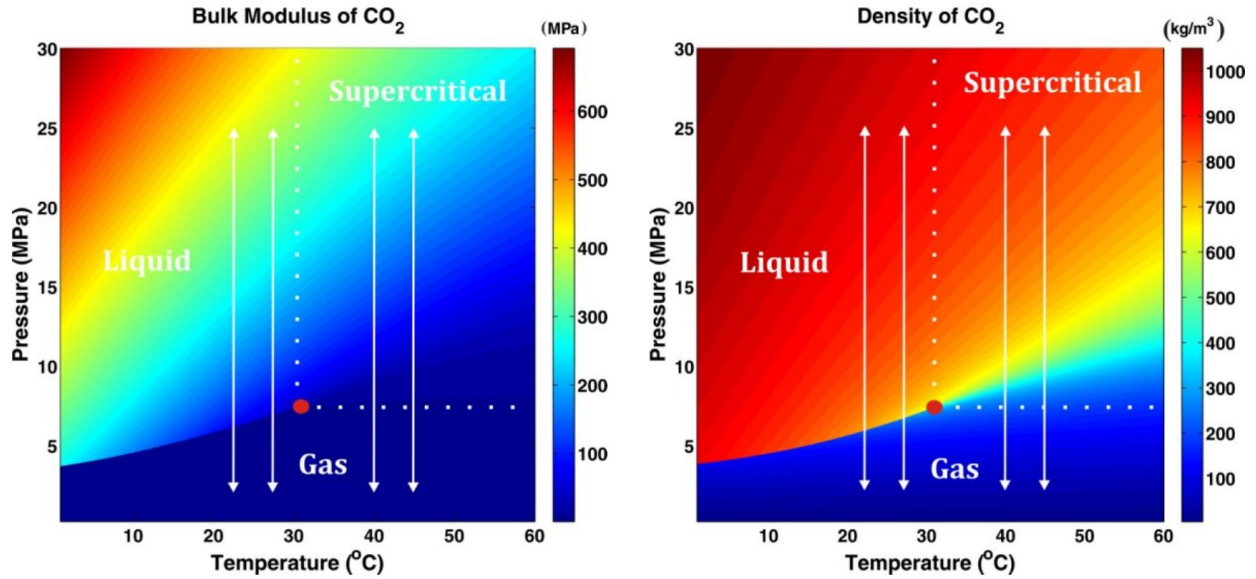
The spreadsheet is used on every core plug sample in the study with supercritical CO_2 saturation from 0% to 100% in increments of 5%, and data was plotted in tables and graphed for easier interpretation of the results. Data tables include variations in Vp, density and impedance with variations in CO_2 saturation, along with changes in Vp, density and impedance in the form of percentage difference from the initial respective value; graphed are the delta Vp, delta density and delta impedance values, seen in the results section.

Chapter 5 - Results and Discussion

Dry Core Plug Data

Dry core plug data for each core sample is composed of 1) 1.25MHz and 20MHz frequency data with 500lbf of incremental pressure applied and associated P-wave first arrival times, S-wave first arrival times, P-wave velocity, S-wave velocity, Poisson's ratio, Young's modulus, bulk modulus, and shear modulus (table 5.1, 5.2), 2) Vp and Vs versus pressure cross plots at 1.25MHz and 20MHz frequencies, and 3) P-wave and S-wave first arrival Ult-100 waveform charts at 1.25MHz and 20MHz frequencies.

Table 5.1 Core plug DM3716.7 lab export data at 20MHz.

20MHz Ultrasonic Velocity Lab Test								
Lbf	p-wave first arrival time	s-wave first arrival time	P-wave Velocity	S-wave Velocity	Poisson's Ratio	Young's Modulus	Bulk Modulus	Shear Modulus
500	28.5	44.45	5118	3193	0.181372082	63353452.17	33138680.29	26813504.87
1000	28.4	44.45	5148	3193	0.187389934	63676171.54	33948667.69	26813504.87
1500	28.35	44.45	5163	3193	0.190327112	63833683.64	34355436.64	26813504.87
2000	28.35	44.45	5163	3193	0.190327112	63833683.64	34355436.64	26813504.87
2500	28.3	44.4	5179	3199	0.191544202	64139324.54	34656140.32	26914370.63
3000	28.25	44.4	5194	3199	0.194410547	64293616.28	35065355.17	26914370.63
3500	28.25	44.4	5194	3199	0.194410547	64293616.28	35065355.17	26914370.63
3900	28.25	44.4	5194	3199	0.194410547	64293616.28	35065355.17	26914370.63

Table 5.2 Core plug DM3716.7 lab export data at 1.25MHz.

1.25MHz								
Lbf	p-wave first arrival time	s-wave first arrival time	P-wave Velocity	S-wave Velocity	Poisson's ratio	Young's modulus	Bulk modulus	shear modulus
500	28.7	47.05	5058	2915	0.25134157	55929216.38	37487311.65	22347701.75
1000	28.7	47.05	5058	2915	0.25134157	55929216.38	37487311.65	22347701.75
1500	28.65	47.05	5073	2915	0.253533654	56027192.48	37886979.6	22347701.75
2000	28.65	47	5073	2919	0.252521759	56135709.16	37805148.03	22409075.43
2500	28.65	47	5073	2919	0.252521759	56135709.16	37805148.03	22409075.43
3000	28.6	47	5088	2919	0.254693637	56233048.7	38205999.48	22409075.43
3500	28.6	46.95	5088	2924	0.253437773	56369380.12	38103552.21	22485910.88
3900	28.6	46.95	5088	2924	0.253437773	56369380.12	38103552.21	22485910.88

An unusual Vs vs pressure chart shape occurs in figure 5.1, likely because a total of only $6\frac{m}{s}$ of velocity increase is achieved, making any small Vs increase look dramatic. All graphs are

expected to exhibit an asymptotic shape with initial steeply increasing velocities, and an eventual exponential-like leveling off in velocity increases through time, confirming *in situ* pressure levels have been achieved. The 1.25MHz Vs increase is similarly small to the 20MHz increase, only showing a $10\frac{m}{s}$ increase, thus accounting for its slightly unusual shape as well.

Figure 5.1 Core plug DM3716.7 pressure vs velocity cross plots at 20MHz.
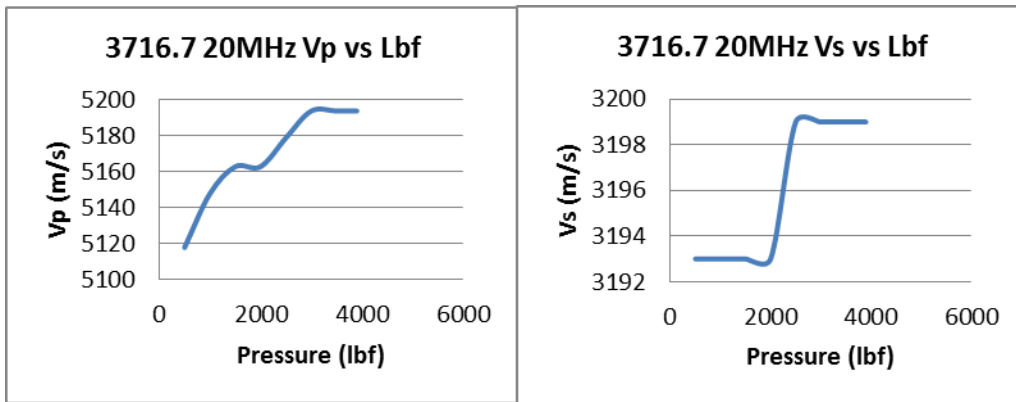
Figure 5.2 Core plug DM3716.7 pressure vs velocity cross plots at 1.25MHz.
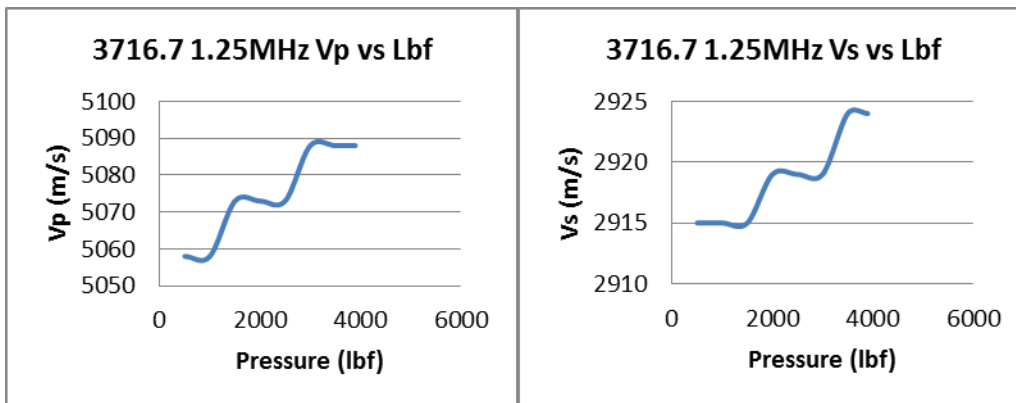
Interpreting the waveform charts became much easier when every tested pressure was stacked together. In this way, variations in first arrival times were much easier to pick out. Even

so, the process is still somewhat subjective where signal strength is not the strongest. Time and care must be taken to determine first arrivals.

Figure 5.3 Core plug DM3716.7 P-wave first arrival 20MHz stacked waveforms. Values at the top of the figure correspond to the first arrival times at each pressure tested.

28.25, 28.25, 28.25, 28.30,
28.35, 28.35, 28.4, 28.5

3900lbf 28.25us
↓

↑
500lbf 28.5us

30

Figure 5.4 The 20MHz Vp waveform from core plug sample 3716.7.

Figure 5.5 Core plug DM3716.7 P-wave first arrival 1.25MHz stacked waveforms.

Values at the top of the figure correspond to the first arrival times at each pressure tested.

28.6, 28.6, 28.6, 28.65,
28.65, 28.65, 28.7, 28.7

3900lbf 28.6us

500lbf 28.7us

30

Figure 5.6 The 1.25MHz Vp waveform from core plug sample 3716.7.
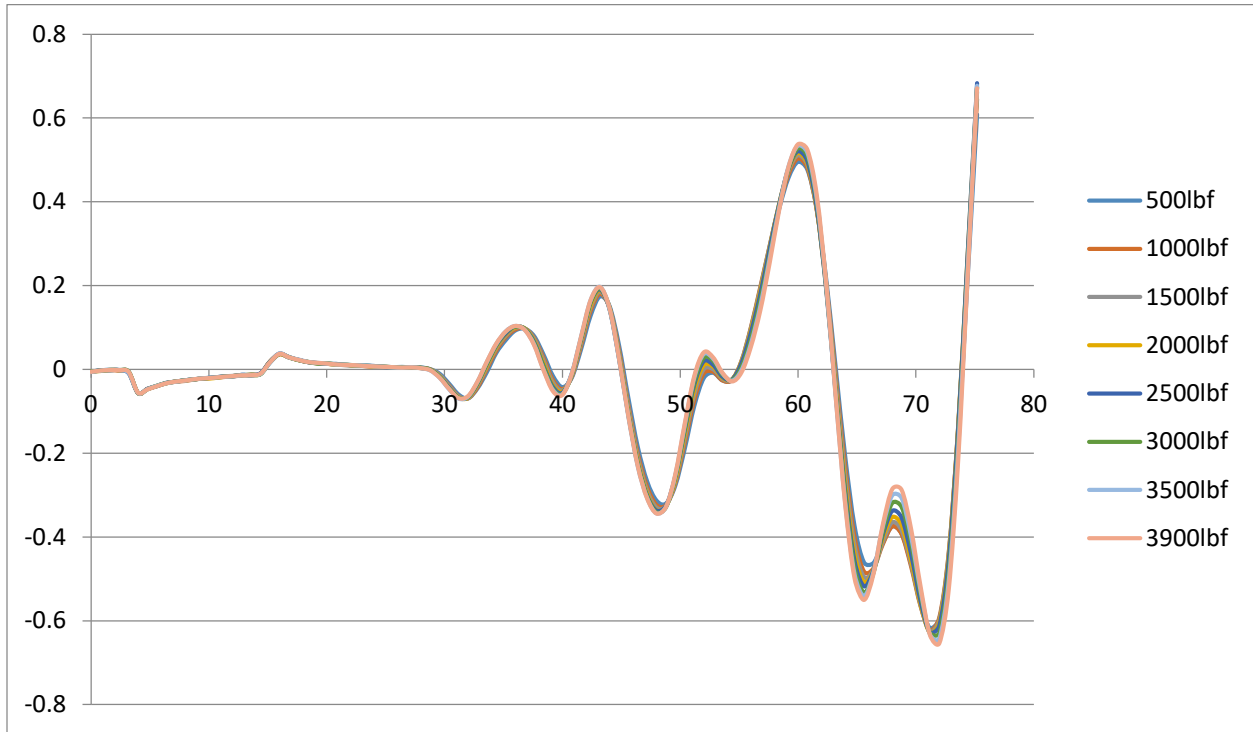
Both figures 5.6 and 5.7 confirm the small Vs increases at both 20MHz and 1.25MHz frequencies, as the first arrival times from 500lbf to 3900lbf are seen to be nearly identical. The reason for this absence of Vs increase with pressure is unknown.

Figure 5.7 Core plug DM3716.7 S-wave first arrival 20MHz stacked waveforms. Values at the top of the figure correspond to the first arrival times at each pressure tested.

44.4, 44.4, 44.4, 44.4,
44.45, 44.45, 44.45, 44.45

3900lbf 44.4us

500lbf 44.45us

Figure 5.8 The 20MHz Vs waveform from core plug sample 3716.7.

Figure 5.9 Core plug DM3716.7 S-wave first arrival 1.25MHz stacked waveforms.

Values at the top of the figure correspond to the first arrival times at each pressure tested.
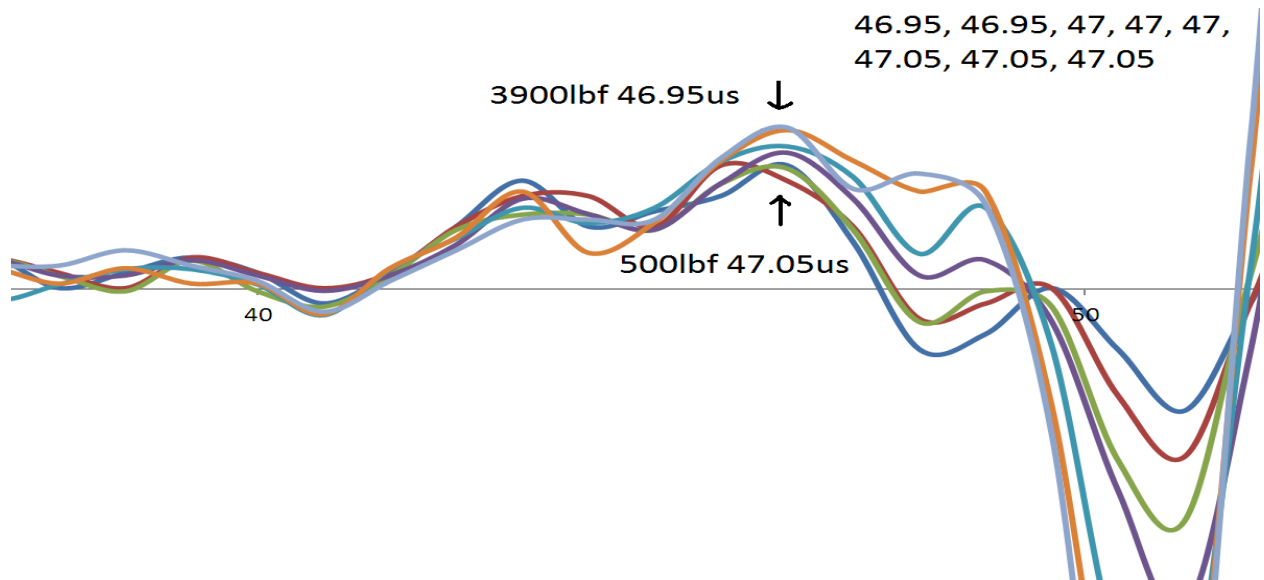
Figure 5.10 The 1.25MHz Vs waveform from core plug sample 3716.7.

Table 5.3 Core plug DM3716.8 lab export data at 20MHz.

20MHz Ultrasonic Velocity Lab Test								
Lbf	p-wave first arrival time	s-wave first arrival time	P-wave Velocity	S-wave Velocity	Poisson's Ratio	Young's Modulus	Bulk Modulus	Shear Modulus
500	28.8	48.7	4971	2730	0.233627009	49764364.03	38411466.6	19377540
1000	28.8	48.2	4971	2774	0.223375201	50973694.8	37571923.13	20007197.6
1500	28.8	48.2	4971	2774	0.223375201	50973694.8	37571923.13	20007197.6
2000	28.75	47.95	4986	2797	0.219914021	51680953.96	37516051.73	20340343.4
2500	28.7	47.9	5000	2801	0.220826254	51866361.65	37801916.53	20398562.6
3000	28.6	47.65	5029	2824	0.219235183	52655152.43	38109603.13	20734937.6
3500	28.55	47.45	5044	2843	0.216737685	53259930.91	38129183.73	21014887.4
3900	28.35	47.4	5104	2848	0.223425552	53731674.35	39613627.73	21088870.4

Table 5.4 Core plug DM3716.8 lab export data at 1.25MHz.

1.25MHz								
Lbf	p-wave first arrival time	s-wave first arrival time	P-wave Velocity	S-wave Velocity	Poisson's Ratio	young's modulus	bulk modulus	shear modulus
500	29.4	48.9	4804	2713	0.21542371	48449517.88	34487935.73	19136959.4
1000	29.3	48.75	4831	2726	0.215981223	48936810.48	34919195.13	19320797.6
1500	29.25	48.6	4845	2739	0.214718812	49354659.86	35025112.2	19505514.6
2000	29.2	48.5	4859	2748	0.21445038	49668820.99	35207143.4	19633910.4
2500	29.05	48.15	4900	2779	0.212529077	50717167.83	35653484.53	20079386.6
3000	29	48.1	4914	2783	0.213496459	50902992.2	35933587.73	20137231.4
3500	28.95	47.95	4928	2797	0.212009038	51354707.81	36021020.53	20340343.4
3900	28.95	47.9	4928	2801	0.211025934	51460709.54	35943394.93	20398562.6

An unusual 'inverted asymptote' shape is seen in the Vp chart of figure 5.11, exhibiting almost the opposite of what would normally be expected. The reason for this is not known.

Figure 5.11 Core plug DM3716.8 pressure vs velocity cross plots at 20MHz.
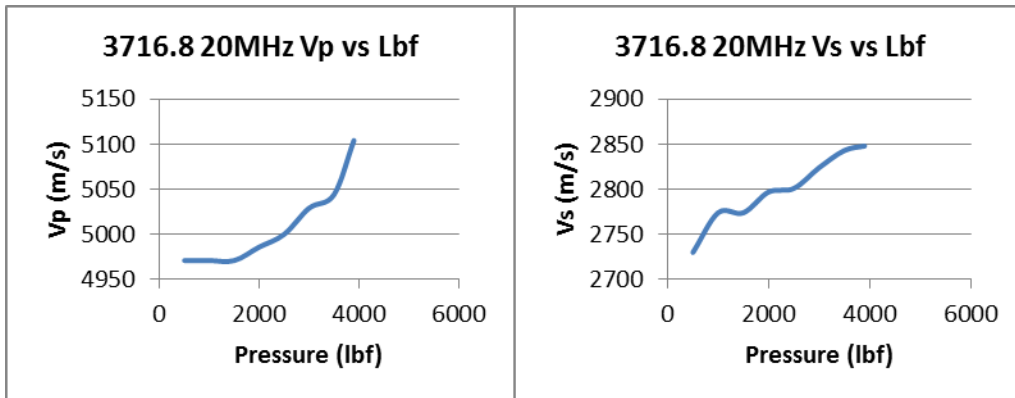
Figure 5.12 Core plug DM3716.8 pressure vs velocity cross plots at 1.25MHz.
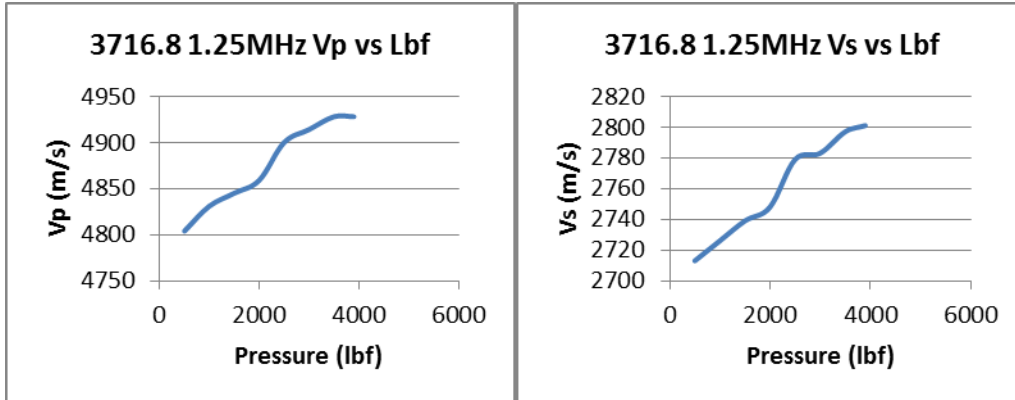
Figure 5.13 Core plug DM3716.8 P-wave first arrival 20MHz stacked waveforms.

Values at the top of the figure correspond to the first arrival times at each pressure tested.

28.35, 28.55, 28.6, 28.7,
28.75, 28.8, 28.8, 28.8

3900lbf 28.35us

30

500lbf 28.8us

Figure 5.14 The 20MHz Vp waveform from core plug sample 3716.8.

Figure 5.15 Core plug DM3716.8 P-wave first arrival 1.25MHz stacked waveforms.

Values at the top of the figure correspond to the first arrival times at each pressure tested.

28.95, 28.95, 29, 29.05,
29.2, 29.25, 29.3, 29.4
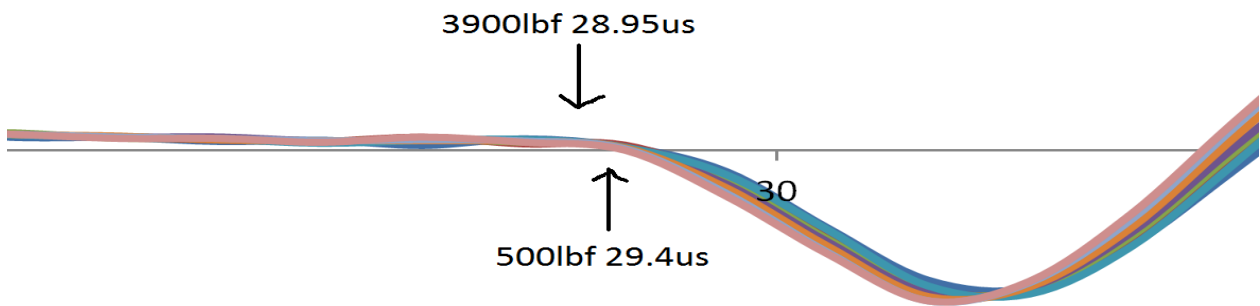
Figure 5.16 The 1.25MHz Vp waveform from core plug sample 3716.8.

Figure 5.17 Core plug DM3716.8 S-wave first arrival 20MHz stacked waveforms.

Values at the top of the figure correspond to the first arrival times at each pressure tested.

Figure 5.18 The 20MHz Vs waveform from core plug sample 3716.8.

Figure 5.19 Core plug DM3716.8 S-wave first arrival 1.25MHz stacked waveforms.

Values at the top of the figure correspond to the first arrival times at each pressure tested.

47.9, 47.95, 48.1, 48.15,
48.5, 48.6, 48.75, 48.9

3900lbf 47.9us

500lbf 48.9us
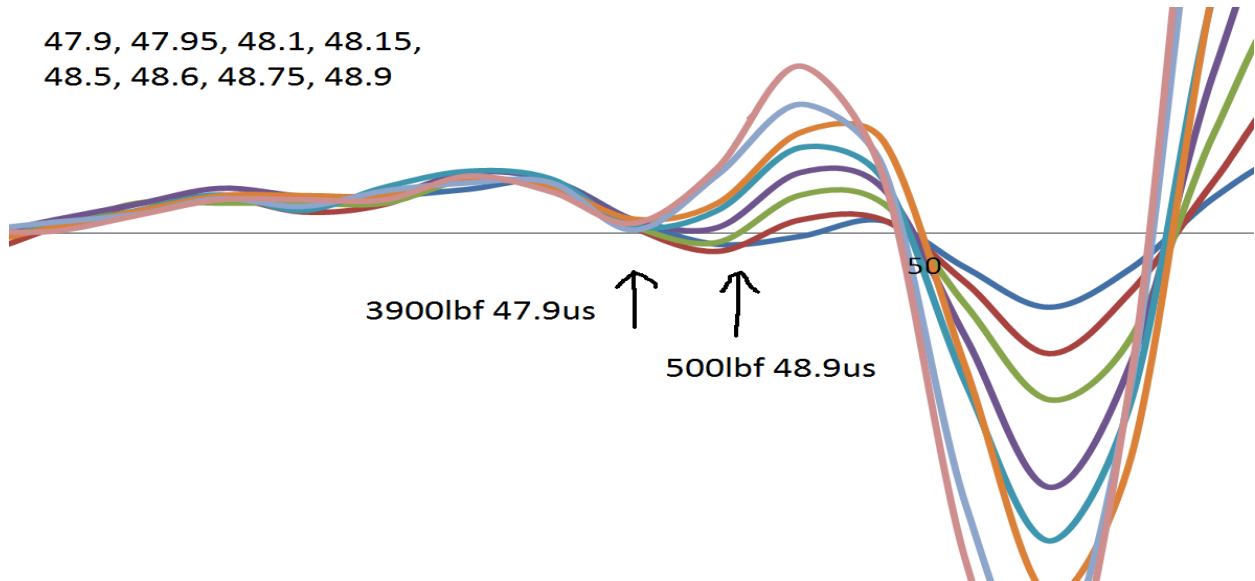
Figure 5.20 The 1.25MHz Vs waveform from core plug sample 3716.8.
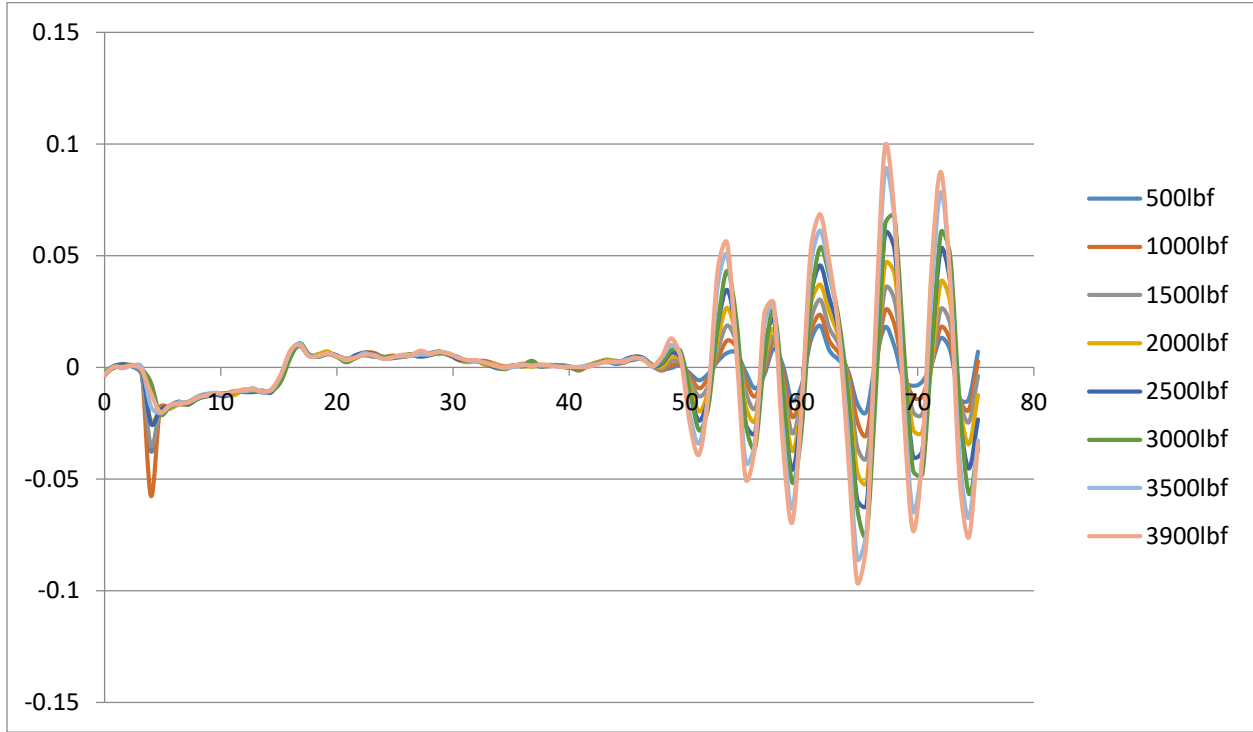
Table 5.5 Core plug DM3749.9 lab export data at 20MHz.

20MHz Ultrasonic Velocity Lab Test								
Lbf	p-wave first arrival time	s-wave first arrival time	P-wave Velocity	S-wave Velocity	Poisson's Ratio	Young's Modulus	Bulk Modulus	Shear Modulus
500	28	46.35	5273	2985	0.2642087	60151810.37	42517691.43	23790300.75
1000	27.9	46.25	5305	2995	0.266076644	60644987.06	43208587.75	23949966.75
1500	27.9	46.15	5305	3005	0.263772694	60939540.77	42994987.75	24110166.75
2000	27.9	46.05	5305	3016	0.261212624	61262150.85	42759205.39	24287003.52
2500	27.8	45.85	5337	3036	0.260791929	62056633.44	43237555.47	24610180.32
3000	27.8	45.8	5337	3042	0.259390072	62232886.04	43107729.39	24707549.88
3500	27.8	45.75	5337	3047	0.258215664	62379408.63	42999345.19	24788838.03
3940	27.8	45.75	5337	3047	0.258215664	62379408.63	42999345.19	24788838.03

Table 5.6 Core plug DM3749.9 lab export data at 1.25MHz.

1.25MHz								
Lbf	p-wave first arrival time	s-wave first arrival time	P-wave Velocity	S-wave Velocity	Poisson's Ratio	young's modulus	bulk modulus	shear modulus
500	28.65	47.05	5073	2914	0.253785984	56851740.15	38483958.67	22672027.32
1000	28.6	47	5088	2919	0.254693637	57088304.19	38787079.32	22749897.87
1500	28.6	46.9	5088	2930	0.251922285	57392331.52	38558032.48	22921683
2000	28.6	46.4	5088	2979	0.23919112	58724666.1	37527266.52	23694757.47
2500	28.6	46.3	5088	2990	0.236243575	59018433.91	37293520.48	23870067
3000	28.55	46.25	5103	2995	0.237266604	59264988.07	37595137.03	23949966.75
3500	28.55	46.25	5103	2995	0.237266604	59264988.07	37595137.03	23949966.75
3940	28.55	46.2	5103	3000	0.235924931	59398552.18	37488426.03	24030000

Figure 5.21 Core plug DM3749.9 pressure vs velocity cross plots at 20MHz.

Figure 5.22 Core plug DM3749.9 pressure vs velocity cross plots at 1.25MHz.

Figure 5.23 Core plug DM3749.9 P-wave first arrival 20MHz stacked waveforms.

Values at the top of the figure correspond to the first arrival times at each pressure tested.

27.8, 27.8, 27.8, 27.8,
27.9, 27.9, 27.9, 28

3940lbf 27.8us

500lbf 28us

30

Figure 5.24 The 20MHz Vp waveform from core plug sample 3749.9.

Figure 5.25 Core plug DM3749.9 P-wave first arrival 1.25MHz stacked waveforms.

Values at the top of the figure correspond to the first arrival times at each pressure tested.

28.55, 28.55, 28.55, 28.6,
28.6, 28.6, 28.65

3940lbf 28.55us

30

500lbf 28.65us

Figure 5.26 The 1.25MHz Vp waveform from core plug sample 3749.9.

Initially the 20MHz Vs first arrival time waveforms in figure 5.27 were difficult to interpret, especially at low pressures, and thus multiple options of where first arrival times were located were identified. However, after then analyzing figure 5.29, the picture became much clearer as to the likely 20MHz first arrival locations.

Figure 5.27 Core plug DM3749.9 S-wave first arrival 20MHz stacked waveforms. Values at the top of the figure correspond to the first arrival times at each pressure tested.

Figure 5.28 The 20MHz Vs waveform from core plug sample 3749.9.

Figure 5.29 Core plug DM3749.9 S-wave first arrival 1.25MHz stacked waveforms.

Values at the top of the figure correspond to the first arrival times at each pressure tested.
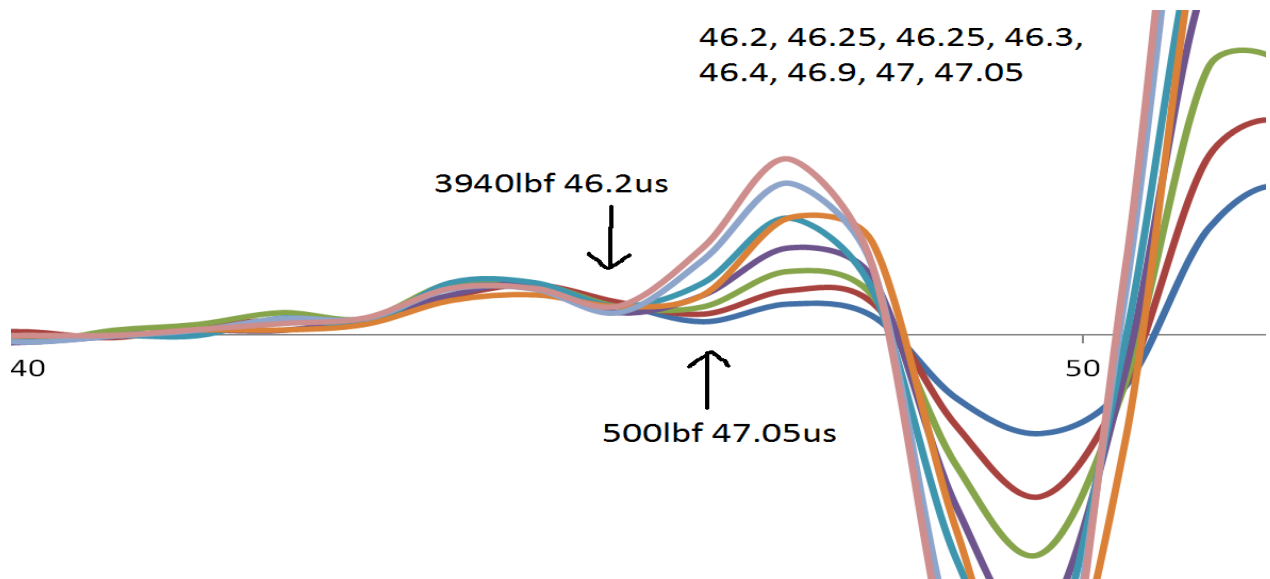
Figure 5.30 The 1.25MHz Vs waveform from core plug sample 3749.9.
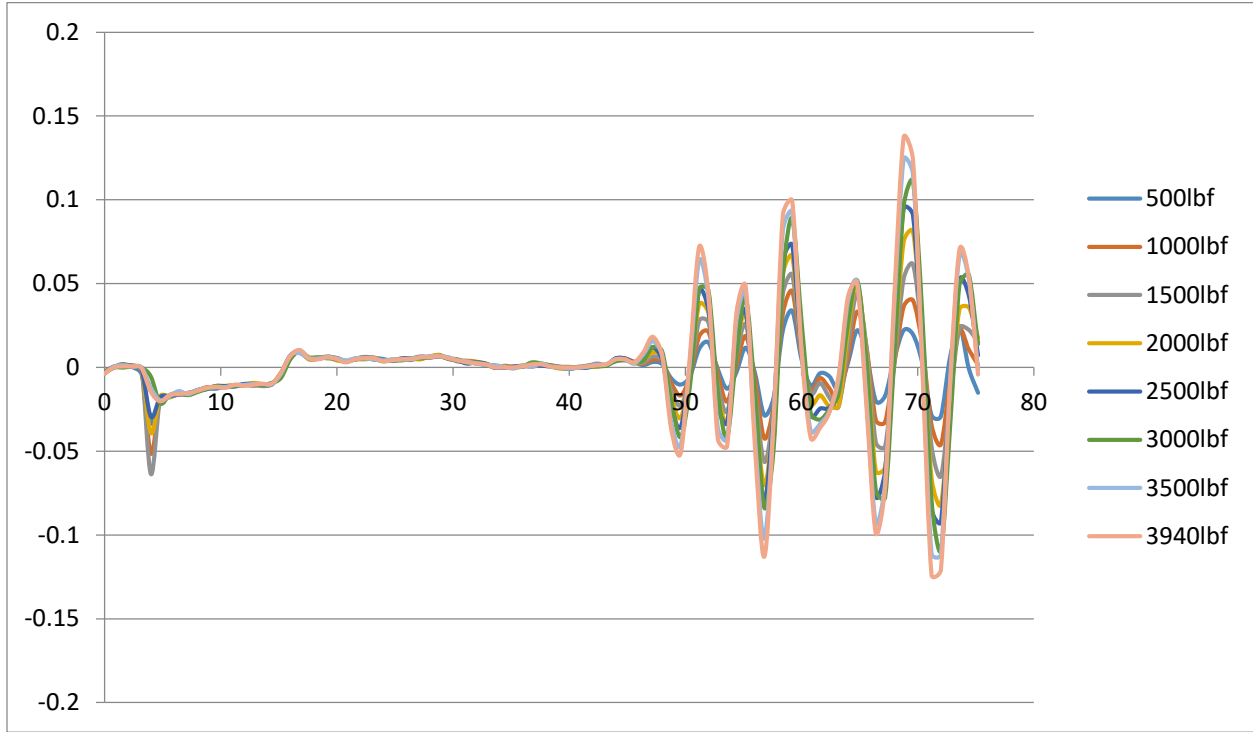
Table 5.7 Core plug DM3829.4 lab export data at 20MHz.

20MHz Ultrasonic Velocity Lab Test								
Lbf	p-wave first arrival time	s-wave first arrival time	P-wave Velocity	S-wave Velocity	Poisson's Ratio	Young's Modulus	Bulk Modulus	Shear Modulus
500	30.65	50.25	4281	2481	0.247142487	39764851.34	26210315.67	15942384.99
1000	30.6	50.1	4294	2492	0.246079691	40084055.38	26310128.23	16084065.76
1500	30.55	49.8	4305	2516	0.240622149	40680901.06	26140050.7	16395363.04
2000	30.3	49.45	4361	2543	0.242386829	41617819.16	26925266.18	16749138.91
2500	30.1	49.25	4409	2559	0.246001761	42265789.68	27733650.07	16960565.79
3000	30.1	49	4409	2578	0.24024929	42697709	27396594.38	17213357.56
3500	30.05	48.95	4422	2583	0.241042229	42890897.27	27604820.88	17280192.51
4020	30	48.9	4432	2587	0.24160075	43043203.21	27762724.55	17333753.71

Table 5.8 Core plug DM3829.4 lab export data at 1.25MHz.

1.25MHz								
Lbf	p-wave first arrival time	s-wave first arrival time	P-wave Velocity	S-wave Velocity	Poisson's Ratio	young's modulus	bulk modulus	shear modulus
500	31.1	51.1	4184	2419	0.248952596	37857109.54	25132776.39	15155542.99
1000	31.1	50.3	4184	2477	0.230195578	39098125.35	24152140.23	15891020.11
1500	31.05	50.25	4195	2481	0.231034617	39251255.62	24322371.43	15942384.99
2000	31	50.15	4206	2488	0.230870138	39467784.41	24441598.63	16032472.96
2500	30.6	50.1	4293	2492	0.245901258	40078315.52	26287887.9	16084065.76
3000	30.6	50.1	4293	2492	0.245901258	40078315.52	26287887.9	16084065.76
3500	30.55	49.5	4304	2539	0.233127296	41177793.62	25716251.59	16696489.39
4020	30.55	49.3	4304	2555	0.227917129	41522225.86	25434791.11	16907584.75

An unusually late increase in velocities exists in the Vs chart of figure 5.32. It appeared as though an asymptote shape had been achieved, and then a large increase in velocities occurred again. Because a rather substantial total increase in around $100\frac{m}{s}$ occurred instead of only a few $\frac{m}{s}$ as in cases before, the reason for this anomaly is unknown.

Figure 5.31 Core plug DM3829.4 pressure vs velocity cross plots at 20MHz.

Figure 5.32 Core plug DM3829.4 pressure vs velocity cross plots at 1.25MHz.
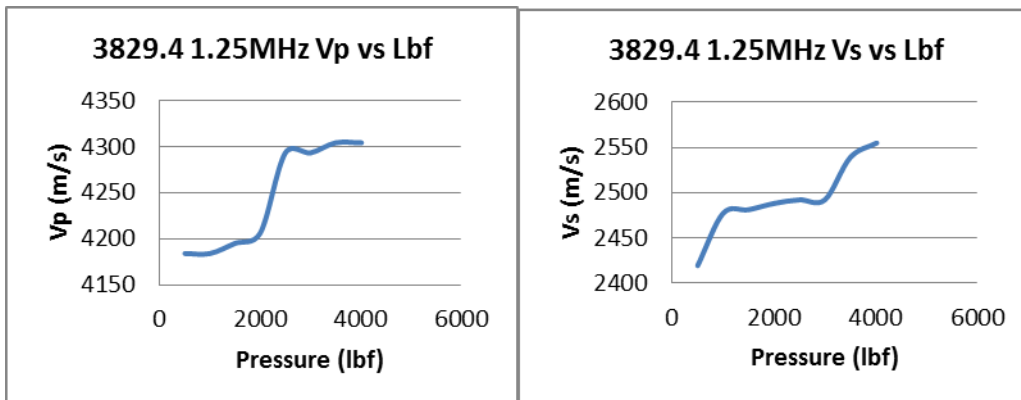
Figure 5.33 Core plug DM3829.4 P-wave first arrival 20MHz stacked waveforms.

Values at the top of the figure correspond to the first arrival times at each pressure tested.

30, 30.05, 30.1, 30.1,
30.3, 30.55, 30.6, 30.65

4020lbf 30us   4020lbf 30.65us

30

Figure 5.34 The 20MHz Vp waveform from core plug sample 3829.4.

500lbf
1000lbf
1500lbf
2000lbf
2500lbf
3000lbf
3500lbf
4020lbf

Figure 5.35 Core plug DM3829.4 P-wave first arrival 1.25MHz stacked waveforms.

Values at the top of the figure correspond to the first arrival times at each pressure tested.

30.55, 30.55, 30.6, 30.6, 31, 31.05, 31.1, 31.1

4020lbf 30.55us

30

500lbf 31.1us

Figure 5.36 The 1.25MHz Vp waveform from core plug sample 3829.4.

Figure 5.37 Core plug DM3829.4 S-wave first arrival 20MHz stacked waveforms.

Values at the top of the figure correspond to the first arrival times at each pressure tested.

48.9, 48.95, 49, 49.25,
49.45, 49.8, 50.1, 50.25

4020lbf 48.9us

50

500lbf 50.25us

Figure 5.38 The 20MHz Vs waveform from core plug sample 3829.4.

Figure 5.39 Core plug DM3829.4 S-wave first arrival 1.25MHz stacked waveforms.

Values at the top of the figure correspond to the first arrival times at each pressure tested.

49.3, 49.5, 50.1, 50.1,
50.15, 50.25, 50.3, 51.1

50

4020lbf 49.3us

500lbf 51.1us
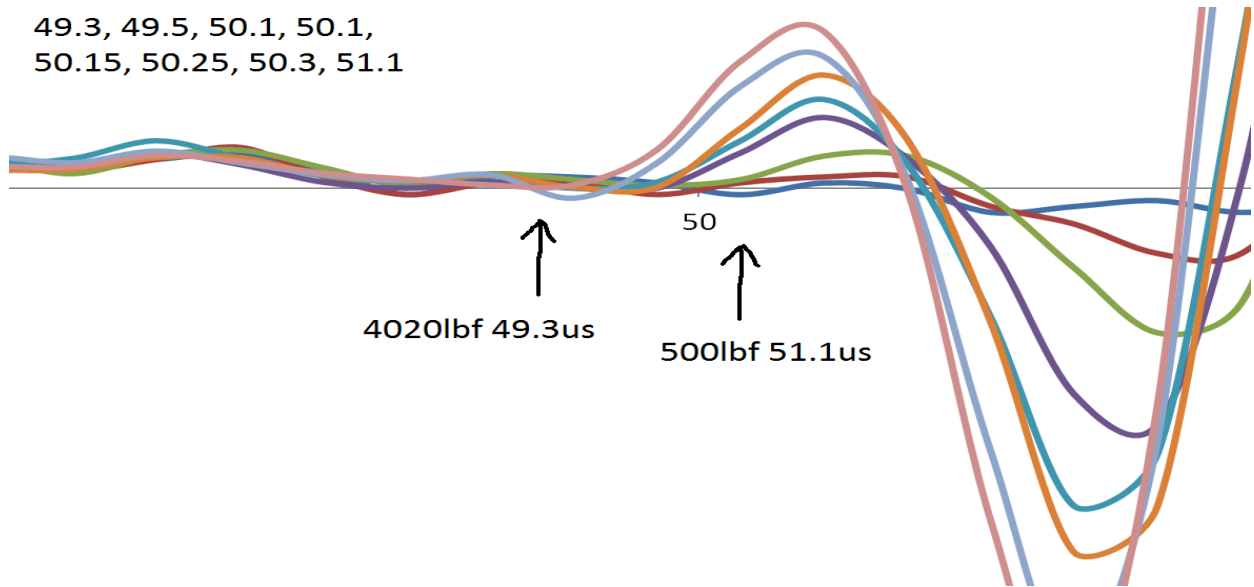
Figure 5.40 The 1.25MHz Vs waveform from core plug sample 3829.4.
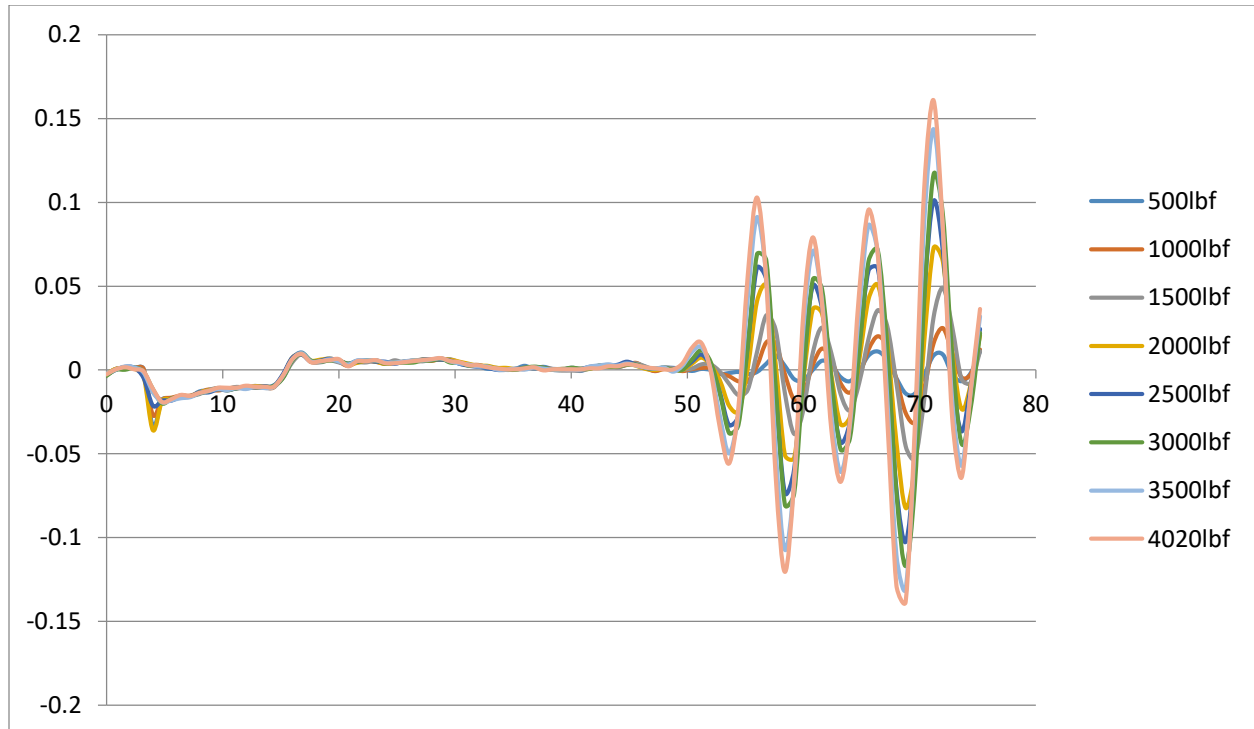
Table 5.9 Core plug DM3829.5 lab export data at 20MHz.

| 20MHz Ultrasonic Velocity Lab Test | | | | | | | | |
Lbf	p-wave first arrival time	s-wave first arrival time	P-wave Velocity	S-wave Velocity	Poisson's Ratio	Young's Modulus	Bulk Modulus	Shear Modulus
500	29.95	49.45	4390	2512	0.256589823	41549336.73	28449465.63	16532577.28
1000	29.9	49.4	4402	2516	0.257412158	41709042.08	28655628.19	16585270.72
1500	29.8	49.2	4426	2531	0.257046546	42195577.63	28946270.03	16783617.82
2000	29.75	49.1	4438	2539	0.256722627	42451801.33	29083264.59	16889885.02
2500	29.75	48.85	4438	2559	0.250958386	42925436.65	28727084.32	17157020.22
3000	29.7	48.75	4451	2567	0.250811796	43189183.4	28886589.05	17264461.18
3500	29.6	48.65	4475	2575	0.252496267	43517325.25	29304154.17	17372237.5
4020	29.55	48.55	4488	2584	0.25206044	43806806.99	29447234.99	17493886.72

Table 5.10 Core plug DM3829.5 lab export data at 1.25MHz.

| 1.25MHz | | | | | | | | |
Lbf	p-wave first arrival time	s-wave first arrival time	P-wave Velocity	S-wave Velocity	Poisson's Ratio	young's modulus	bulk modulus	shear modulus
500	30.5	49.85	4263	2481	0.243906668	40121079.65	26110975.02	16127045.82
1000	30.35	49.55	4297	2504	0.24290976	40835655.8	26472971.69	16427441.92
1500	30.2	49.55	4332	2504	0.249123254	41039799.41	27264250.99	16427441.92
2000	30.15	49.5	4343	2508	0.249830113	41194319.73	27444230.14	16479967.68
2500	30.1	49.4	4355	2516	0.249510457	41446938.4	27577291.21	16585270.72
3000	30.1	49.4	4355	2516	0.249510457	41446938.4	27577291.21	16585270.72
3500	30.05	49.35	4367	2520	0.25038303	41607865.74	27781141.18	16638048
4020	30	49.35	4378	2520	0.252256547	41670209.08	28033172.08	16638048

It is unusual that, although figure 5.41 shows nearly linear charts at 20MHz, whereas figure 5.42 shows good representations of velocity asymptotes, even though the same sample was tested. Reasons for this could stem from the subjective nature of the first arrival location picks.

Figure 5.41 Core plug DM3829.5 pressure vs velocity cross plots at 20MHz.
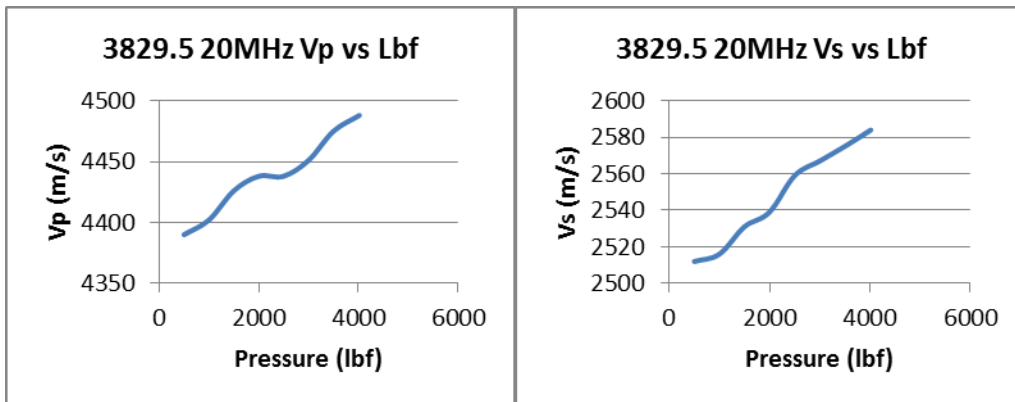
Figure 5.42 Core plug DM3829.5 pressure vs velocity cross plots at 1.25MHz.

3829.5 1.25MHz Vp vs Lbf

3829.5 1.25MHz Vs vs Lbf
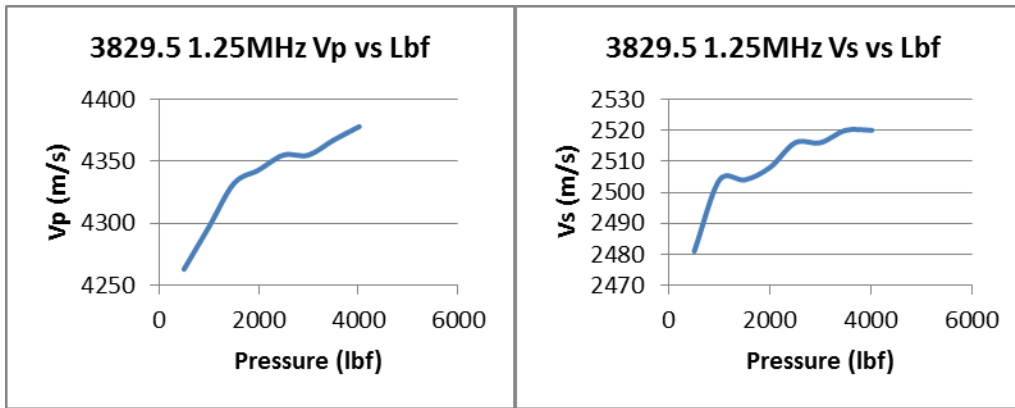
Figure 5.43 Core plug DM3829.5 P-wave first arrival 20MHz stacked waveforms.

Values at the top of the figure correspond to the first arrival times at each pressure tested.

29.55, 29.6, 29.7, 29.75,
29.75, 29.8, 29.9, 29.95
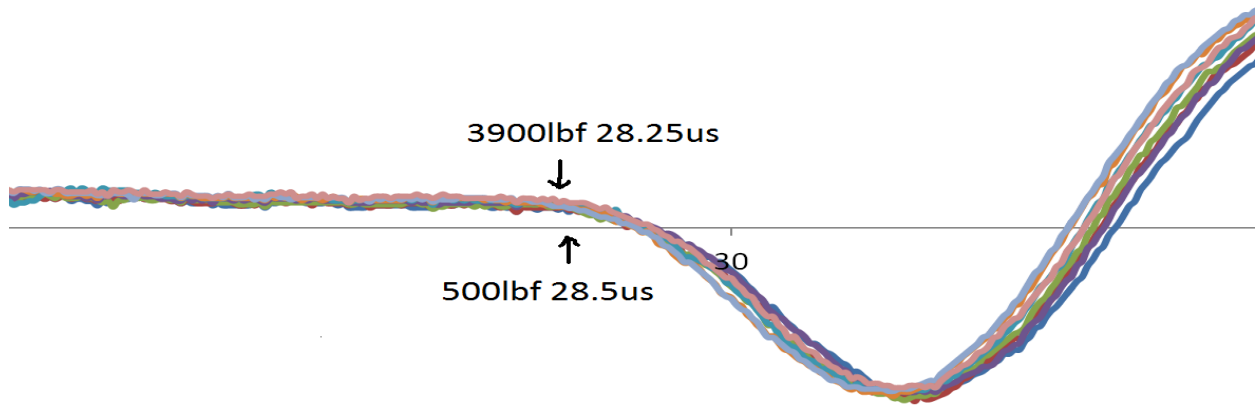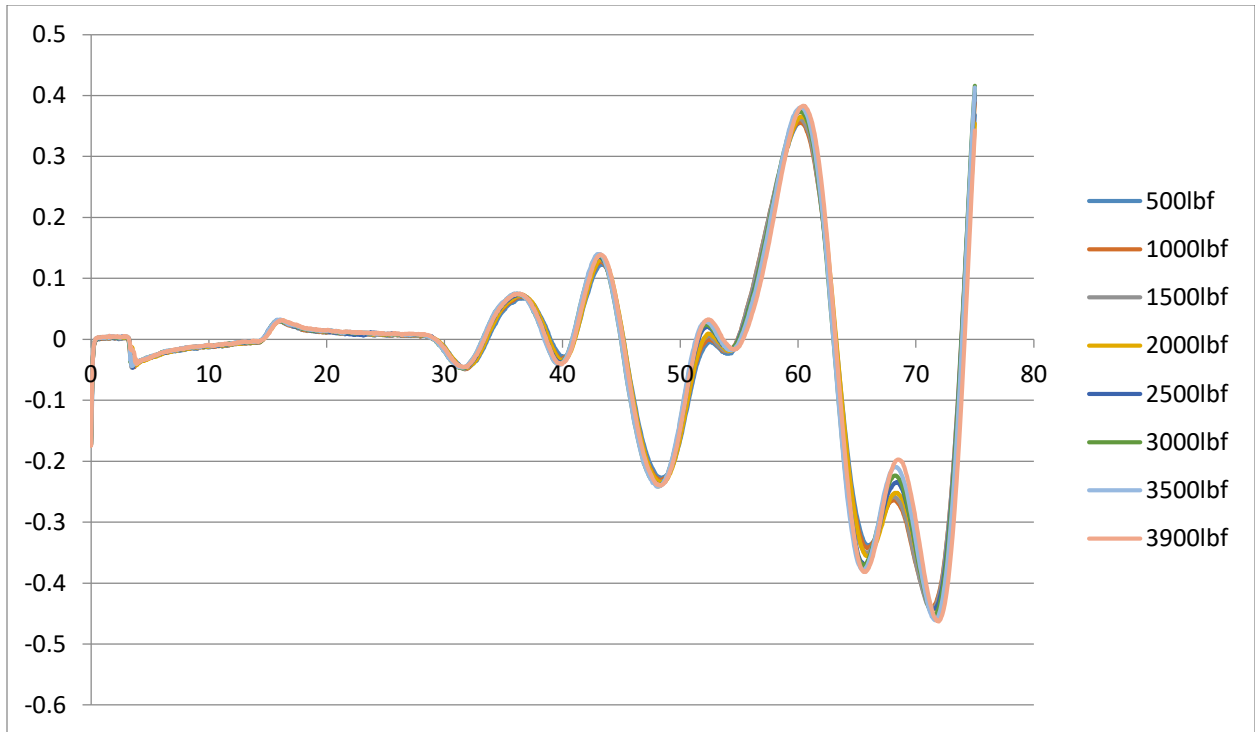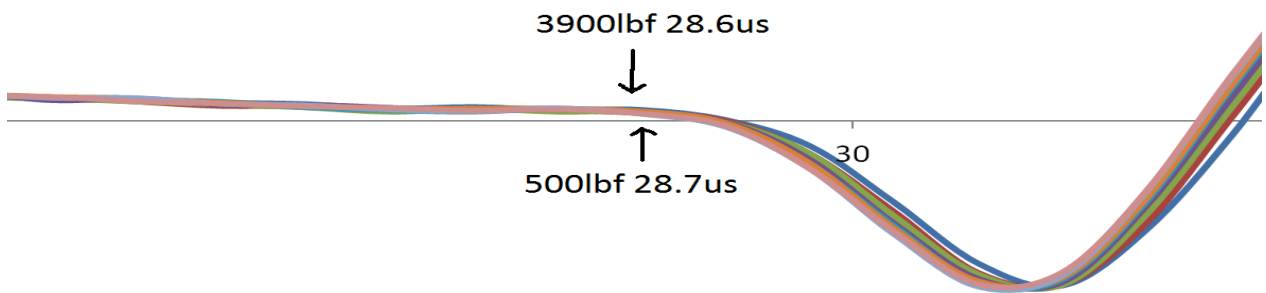
500lbf 29.95us

4020lbf 29.55us

30
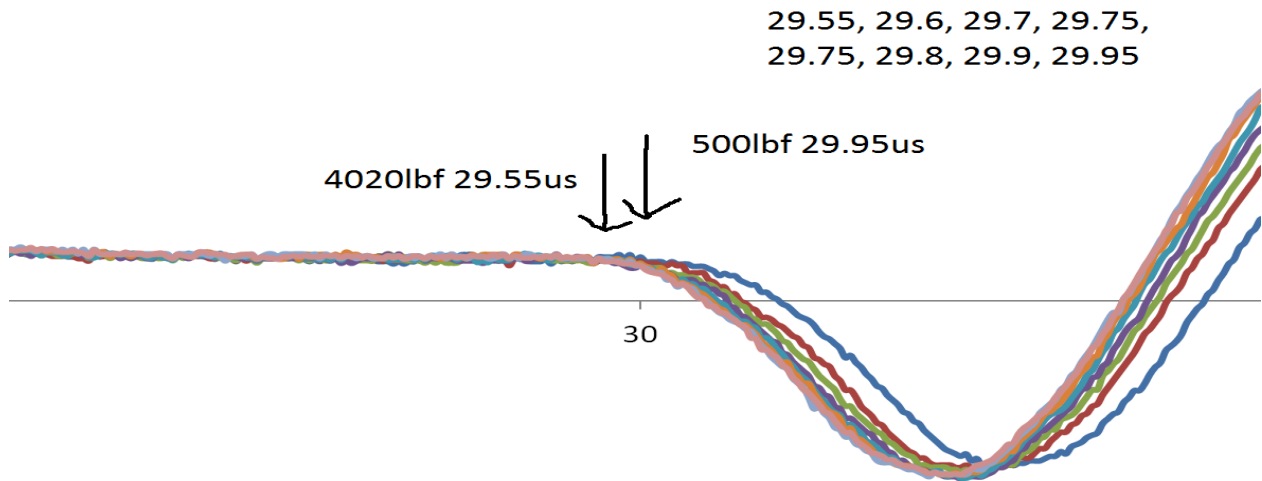
Figure 5.44 The 20MHz Vp waveform from core plug sample 3829.5.
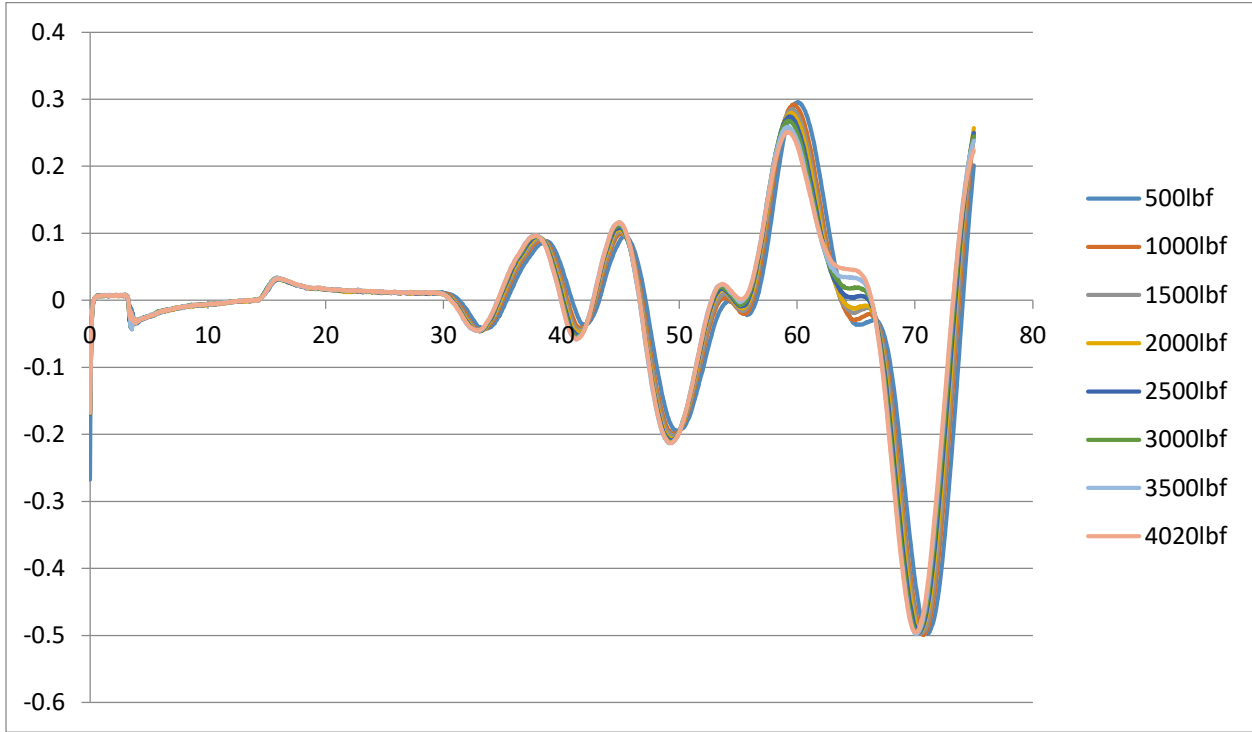
Figure 5.45 Core plug DM3829.5 P-wave first arrival 1.25MHz stacked waveforms.

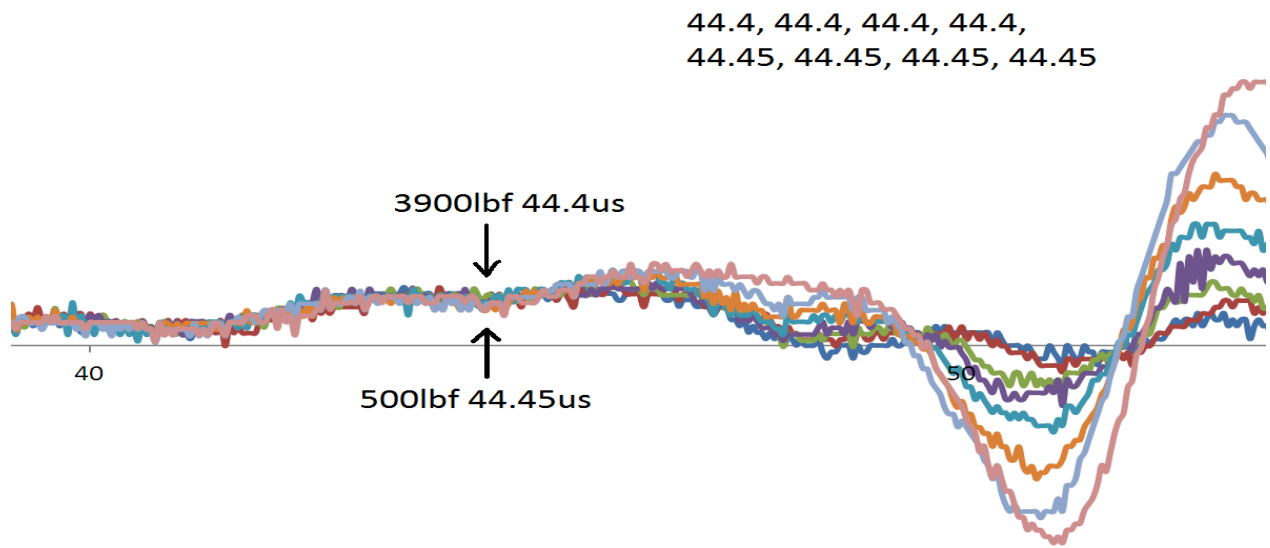Values at the top of the figure correspond to the first arrival times at each pressure tested.

30, 30.05, 30.1, 30.1, 30.15, 30.2, 30.35, 30.5

500lbf 30.5us

30

4020lbf 30us
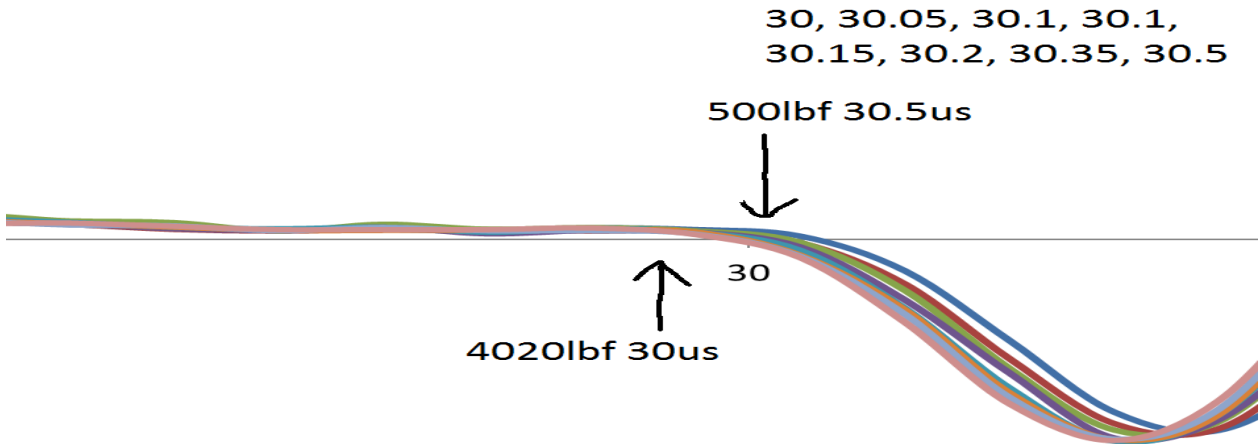
Figure 5.46 The 1.25MHz Vp waveform from core plug sample 3829.5.
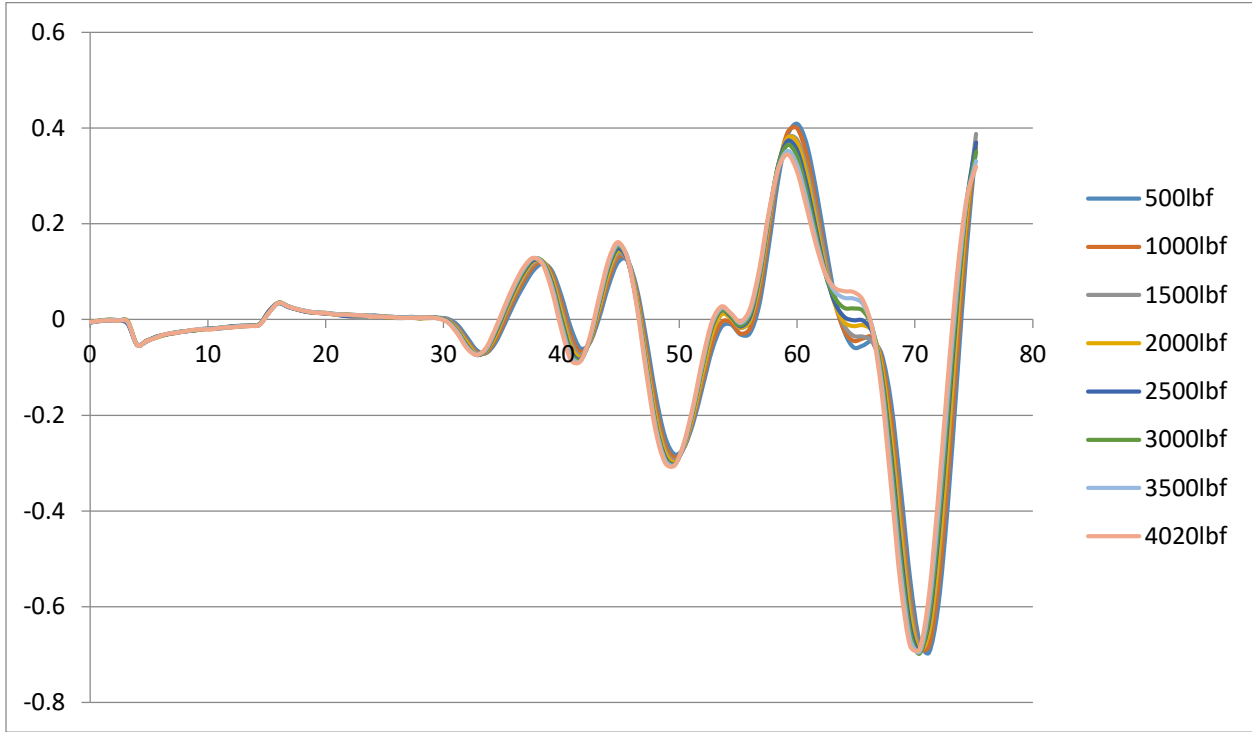
Figure 5.47 Core plug DM3829.5 S-wave first arrival 20MHz stacked waveforms.

Values at the top of the figure correspond to the first arrival times at each pressure tested.
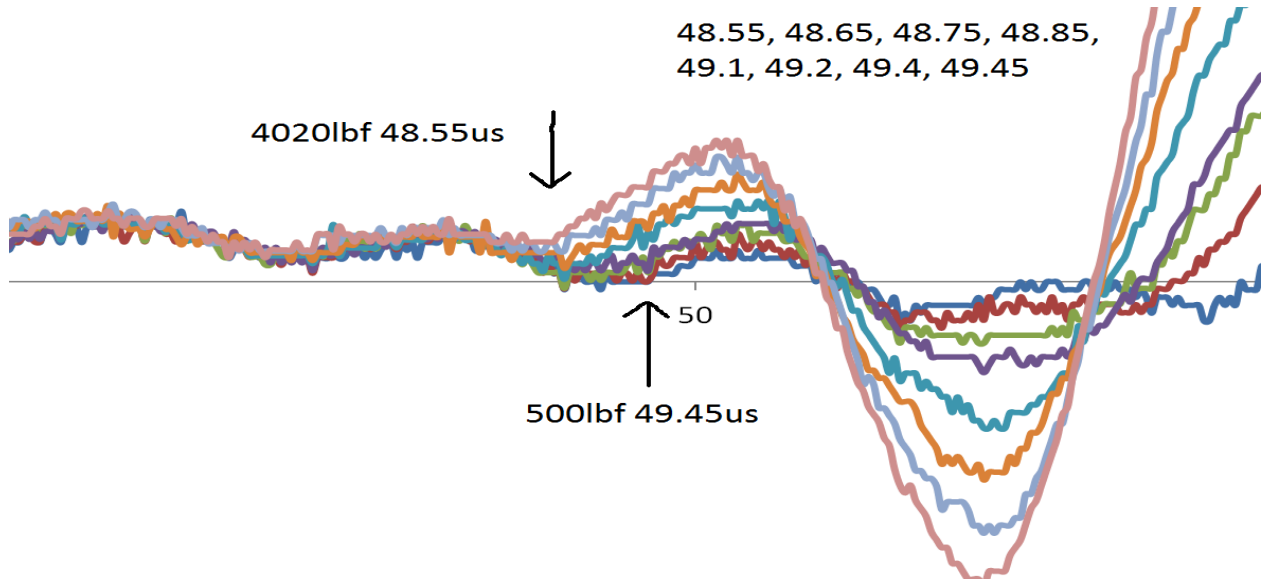
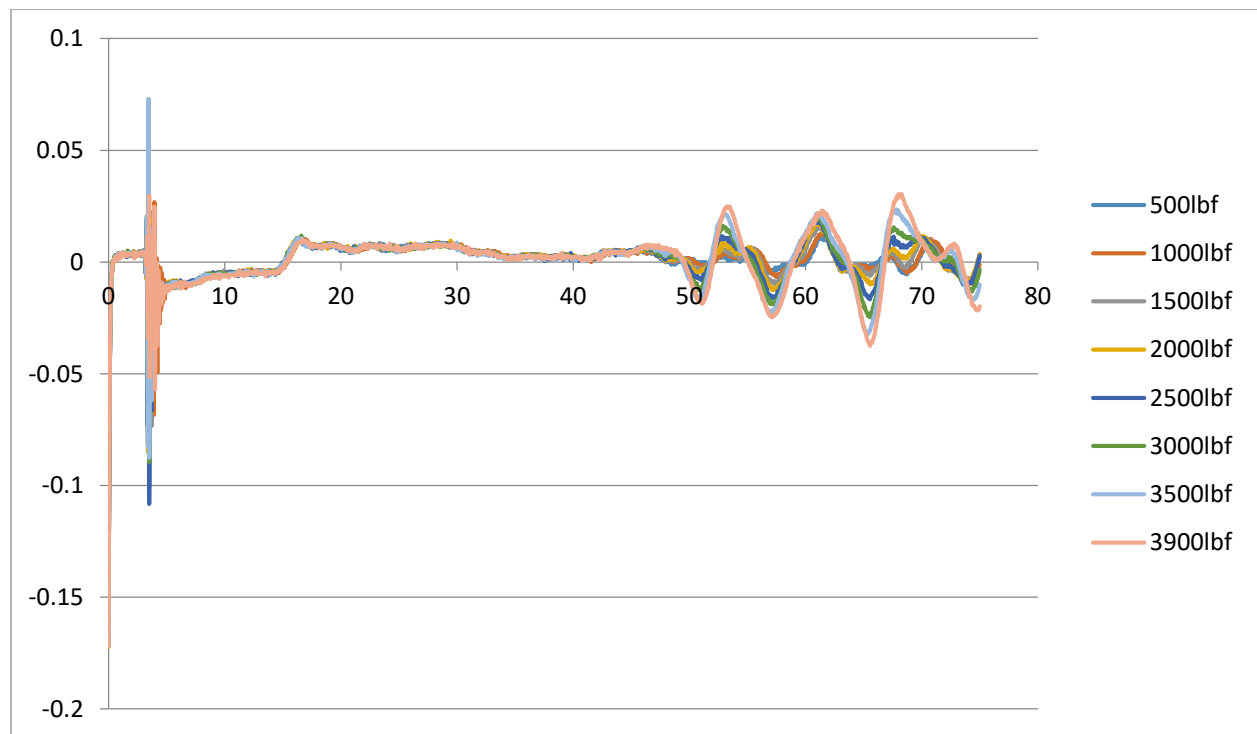**Figure 5.48** The 20MHz Vs waveform from core plug sample 3829.5.
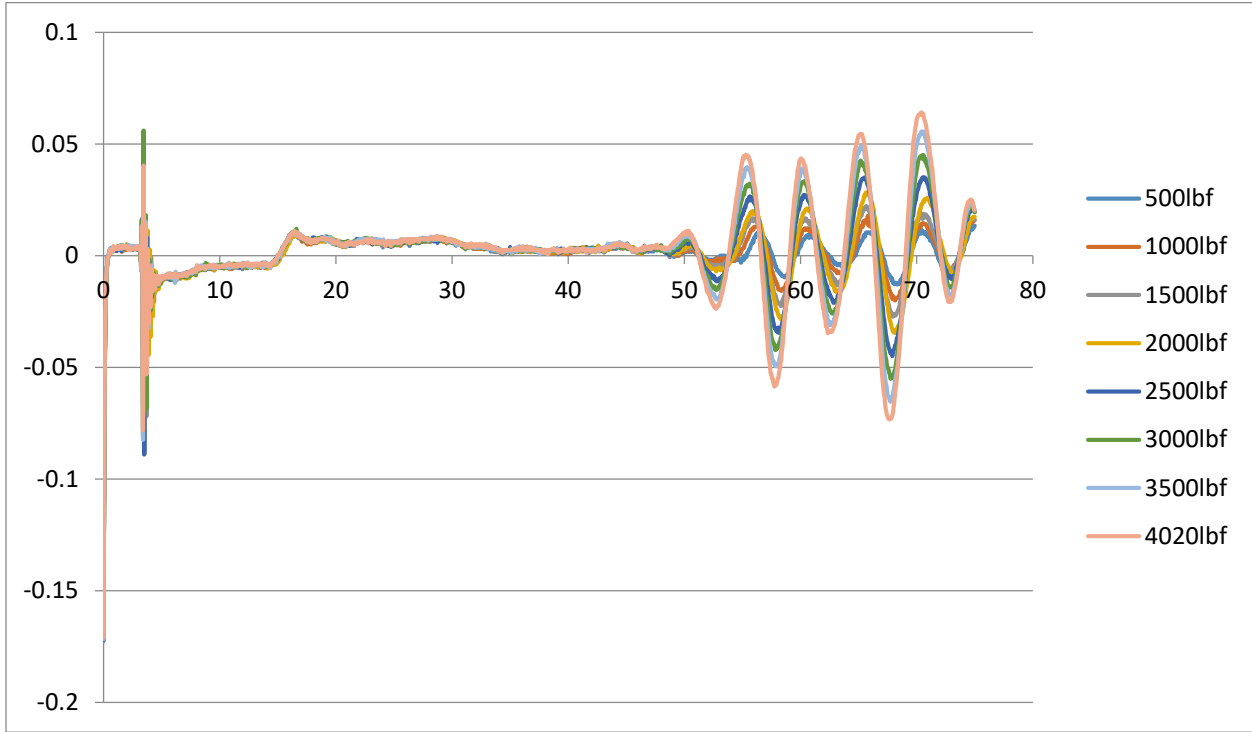
Figure 5.49 Core plug DM3829.5 S-wave first arrival 1.25MHz stacked waveforms.

Values at the top of the figure correspond to the first arrival times at each pressure tested.

49.35, 49.35, 49.35, 49.4, 49.4,
49.5, 49.55, 49.55, 49.85

4020lbf 49.35us

50

500lbf 49.85us
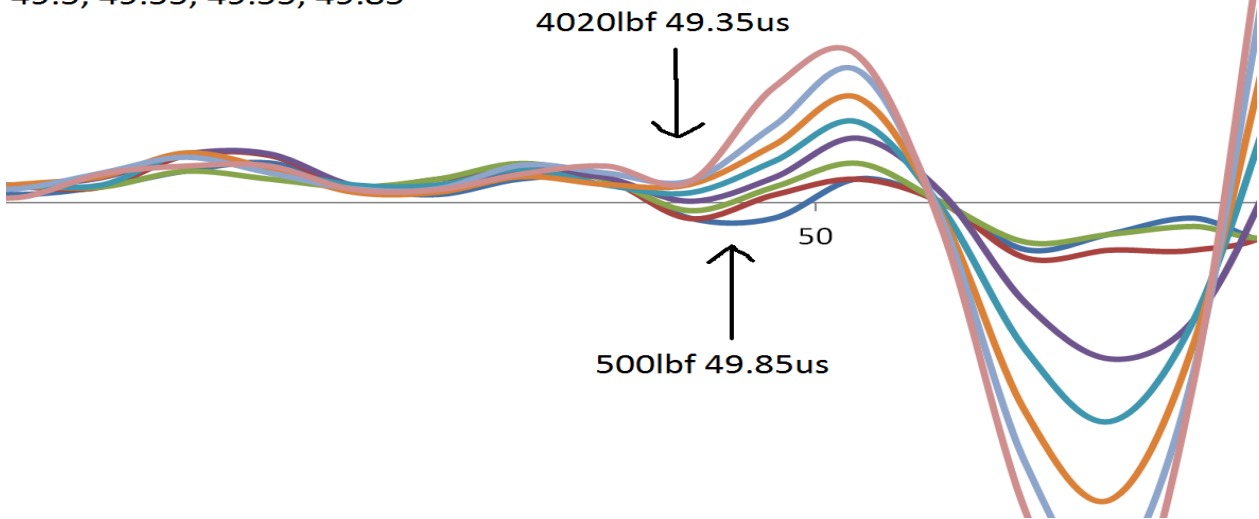
Figure 5.50 The 1.25MHz Vs waveform from core plug sample 3829.5.
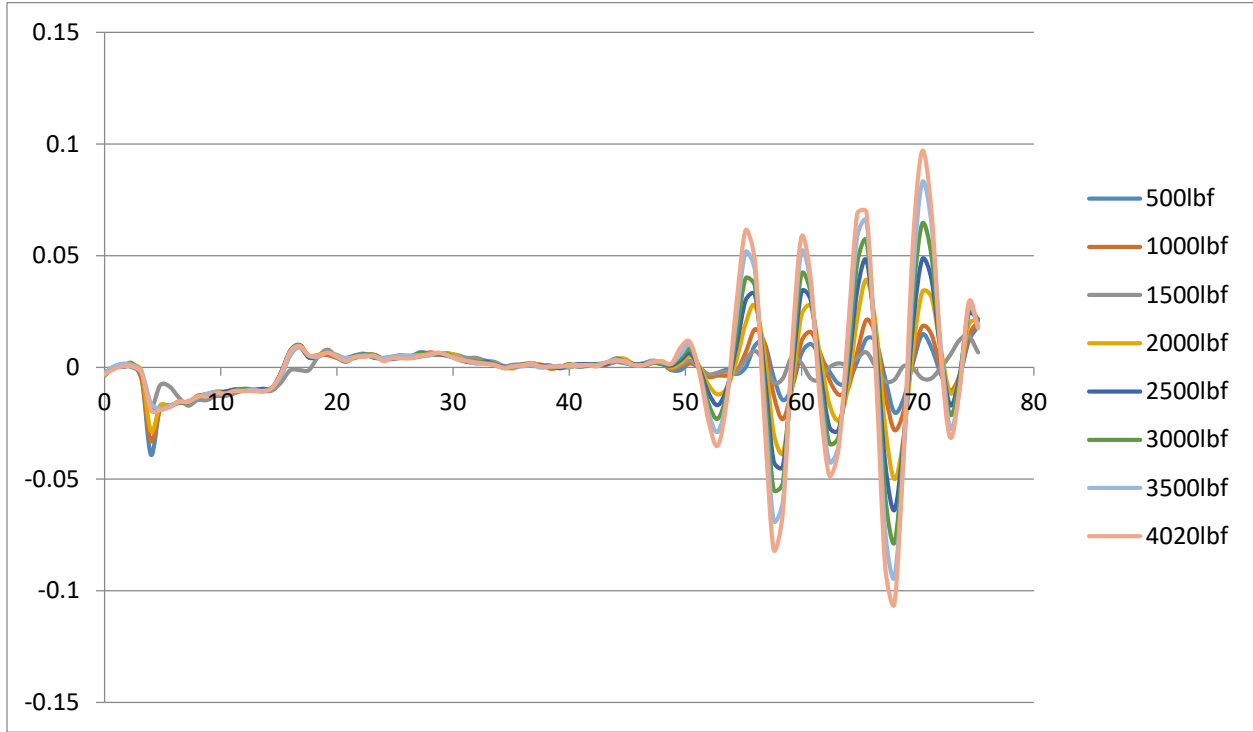
Table 5.11 Core plug DA4300.3 lab export data at 20MHz.

20MHz Ultrasonic Velocity Lab Test								
Lbf	P-wave first arrival time	S-wave first arrival time	P-wave Velocity	S-wave Velocity	Poisson's Ratio	Young's Modulus	Bulk Modulus	Shear Modulus
500	31.05	54.2	4475	2365	0.220709348	39014148.55	33556537.75	14933910.75
1000	30.7	52.65	4557	2469	0.206460116	42065373.63	33744263.67	16276215.87
1500	30.4	51.05	4629	2585	0.188159444	45439316.98	33423080.47	17841540.75
2000	29.65	50.05	4821	2664	0.194662316	48516881.28	36791299.71	18948712.32
2500	29.55	49.7	4846	2692	0.191418397	49411439.94	36902685.88	19349126.88
3000	29.25	49.45	4931	2713	0.197297418	50425000.27	38717498.23	19652185.23
3500	29.2	49.2	4943	2734	0.194083597	51076130.71	38626643.47	19957598.52
4000	29.15	49.05	4957	2747	0.192909313	51513822.17	38743044.79	20147844.03
4515	28.9	48.75	5028	2774	0.195624556	52647195.69	40105222.72	20545852.92

Table 5.12 Core plug DA4300.3 lab export data at 1.25MHz.

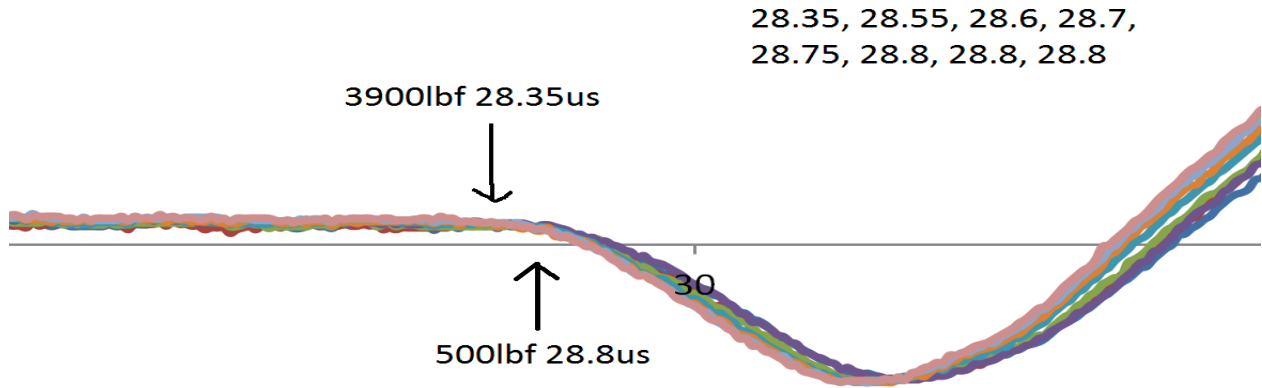| 1.25MHz								
Lbf	P wave first arrival time	S-wave first arrival time	P-wave Velocity	S-wave Velocity	Poisson's Ratio	Young's Modulus	Bulk Modulus	Shear Modulus
500	31.65	53.6	4342	2404	0.193470356	39470505.15	29763404.92	15430506.72
1000	31.05	53.05	4475	2440	0.202712616	40963000.28	32273602.75	15896112
1500	30.4	52.75	4629	2462	0.217132045	42168104.98	35633060.83	16184055.48
2000	30.2	50.2	4680	2651	0.179140463	47427151.89	33460436.44	18764228.67
2500	29.9	49.8	4756	2684	0.181529889	48714564.59	34748433.76	19234295.52
3000	29.6	49.75	4835	2688	0.190933236	49245116.38	36694966.11	19291668.48
3500	29.55	49.45	4849	2713	0.186972519	50001412.9	36576265.03	19652185.23
4000	29.45	49.35	4874	2721	0.1883456	50354136.08	37070514.96	19768255.47
4515	29.4	49.05	4888	2747	0.184177788	51142734.56	36929300.44	20147844.03

Interestingly, two Arbuckle samples, core plug 4300.3 and 4300.4 showed much more pronounced asymptotic chart shapes, and much more clear and easy to interpret waveform first arrival times than any of the other core plugs, as can be seen below. It is hypothesized that the waveforms and asymptote charts exhibit different characteristics because of the presence or lack of microcracks closing with increased applied pressure.

Figure 5.51 Core plug DA4300.3 pressure vs velocity cross plots at 20MHz.
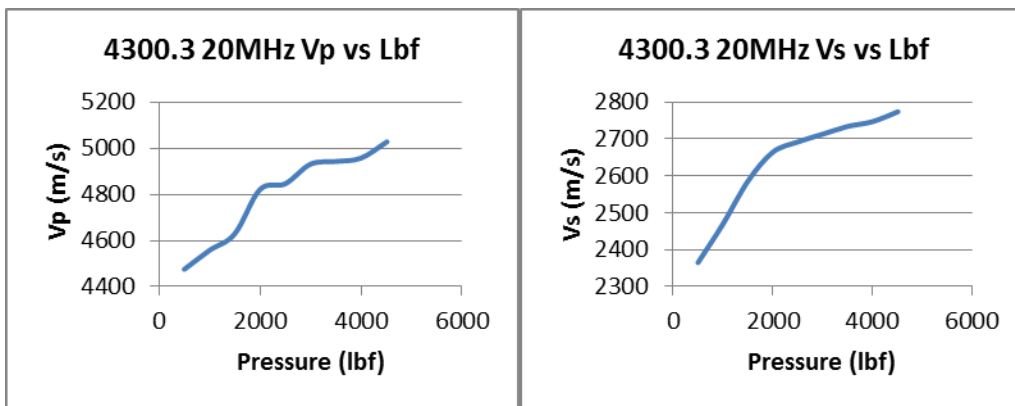
Figure 5.52 Core plug DA4300.3 pressure vs velocity cross plots at 1.25MHz.
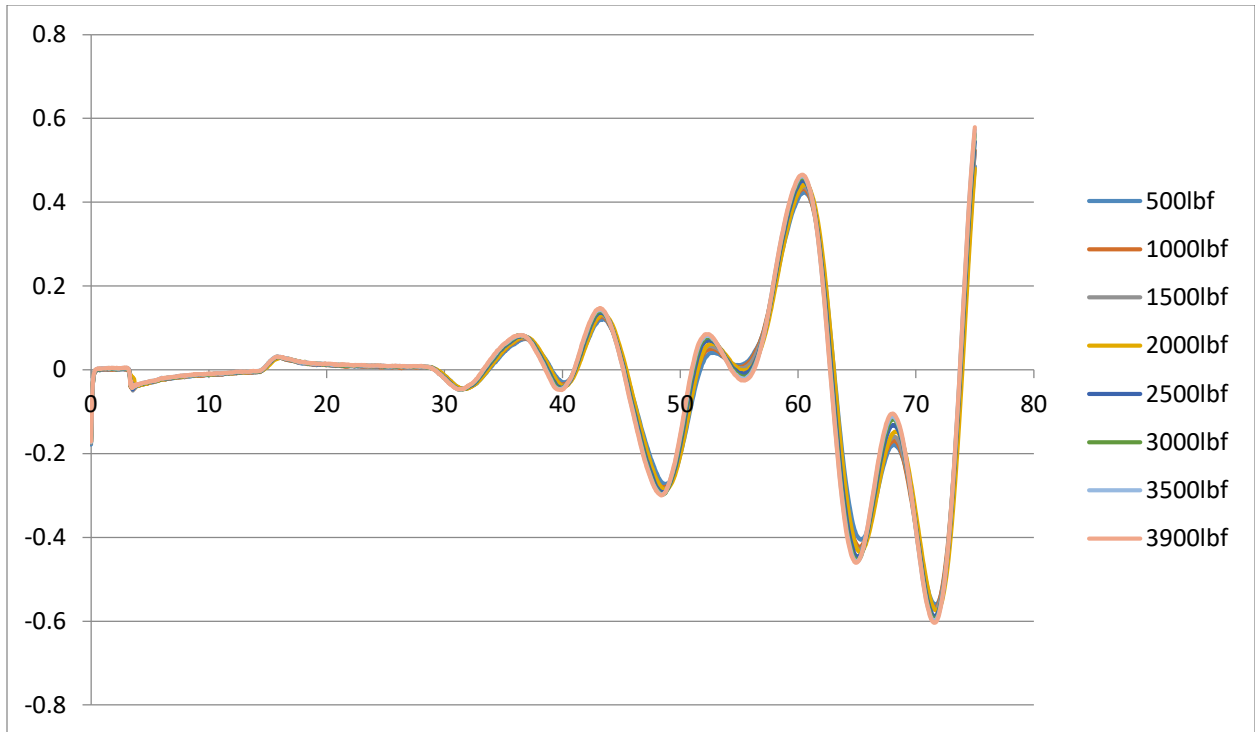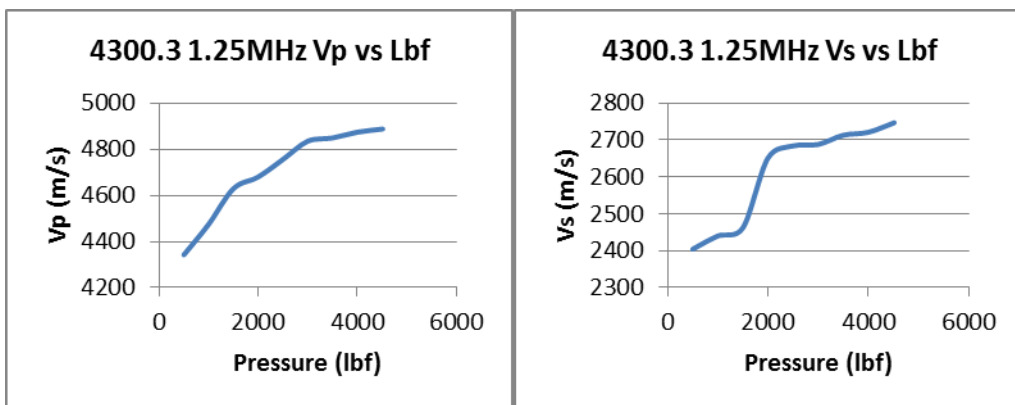
Figure 5.53 Core plug DA4300.3 P-wave first arrival 20MHz stacked waveforms. Values at the top of the figure correspond to the first arrival times at each pressure tested.

28.9, 29.15, 29.2, 29.25,
29.55, 29.65, 30.4, 30.7,
31.05

4515lbf 28.9us

500lbf 31.05us
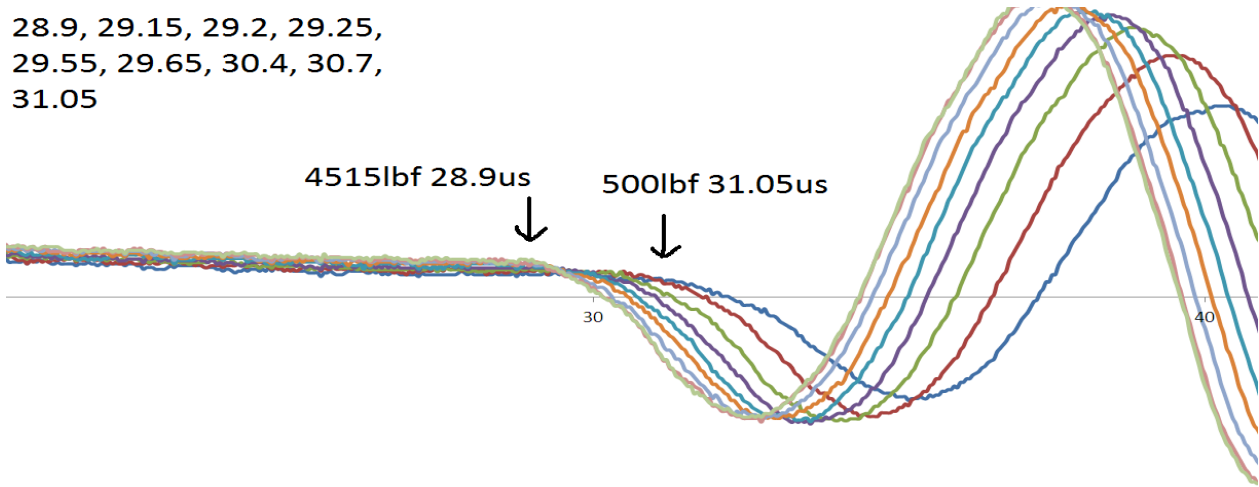
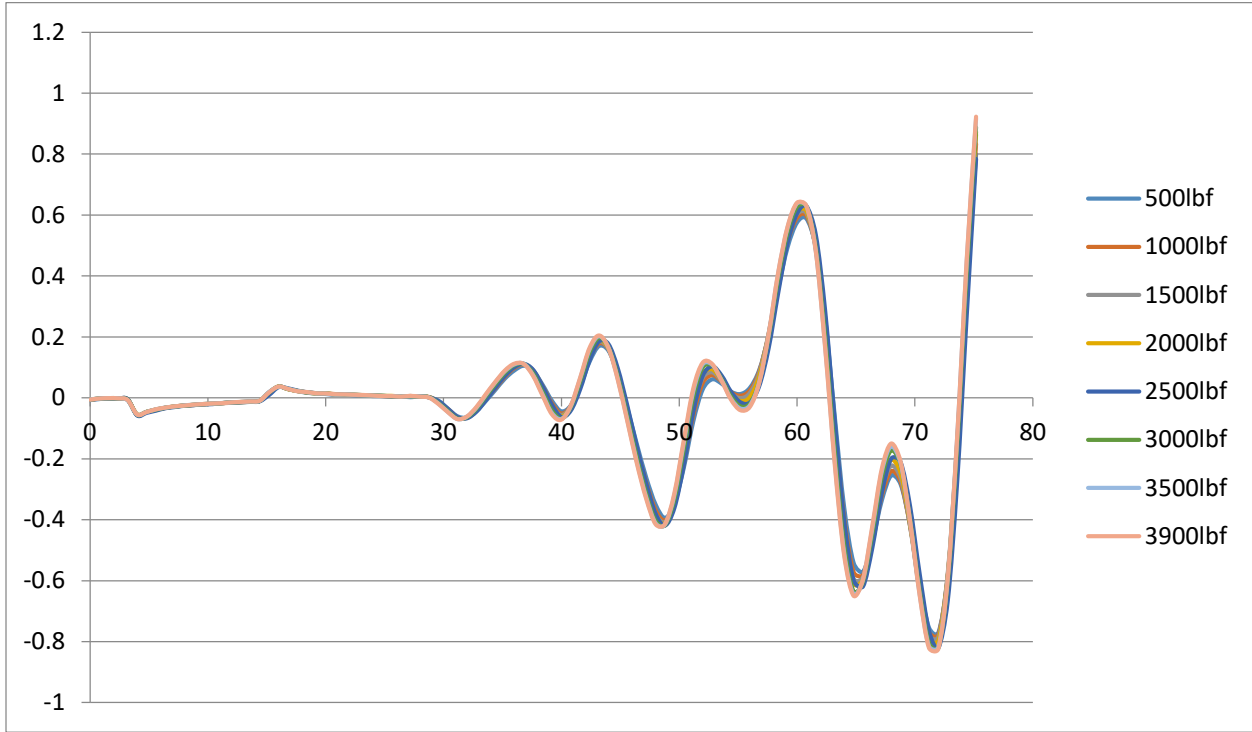**Figure 5.54** The 20MHz Vp waveform from core plug sample 4300.3.
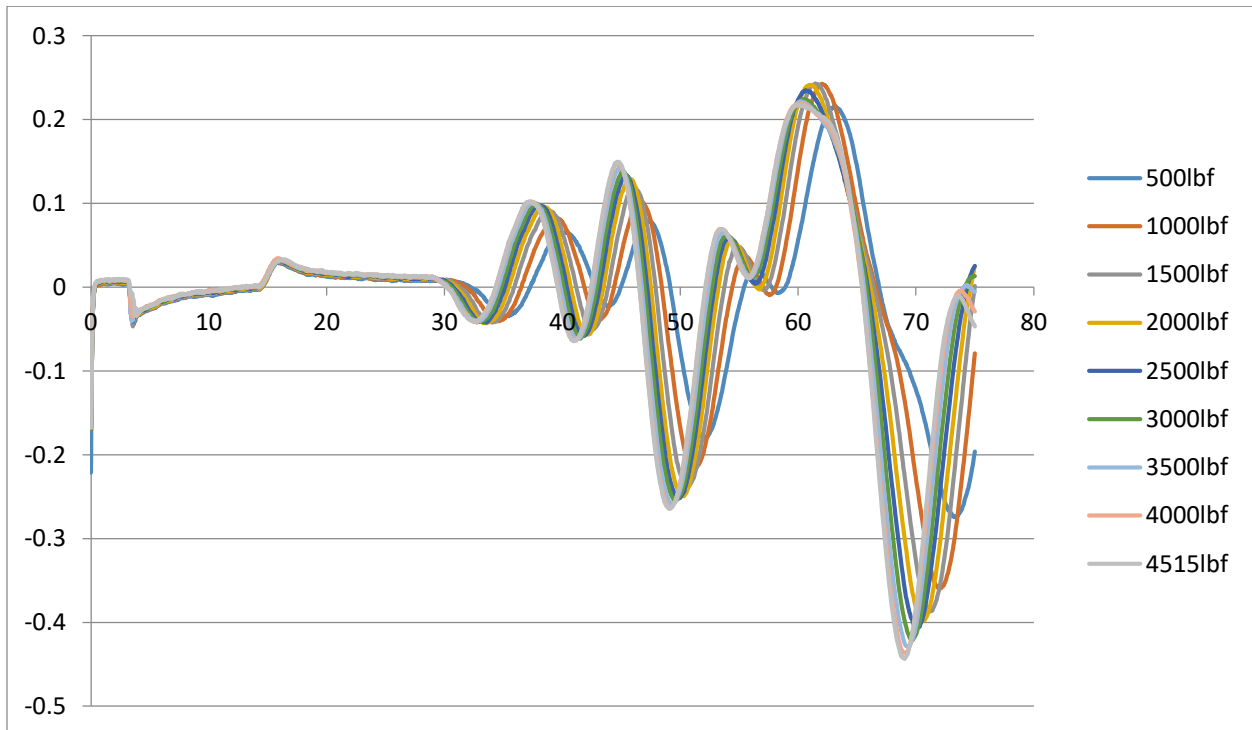
Figure 5.55 Core plug DA4300.3 P-wave first arrival 1.25MHz stacked waveforms.

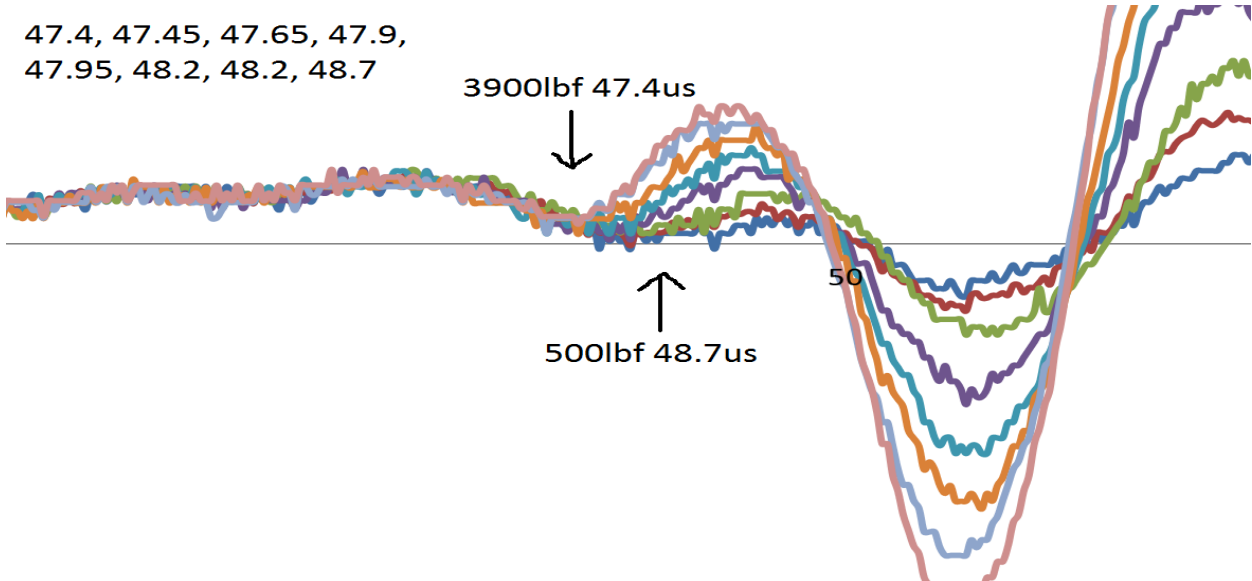Values at the top of the figure correspond to the first arrival times at each pressure tested.

29.4, 29.45, 29.55, 29.6, 29.9, 30.2, 30.4, 31.05, 31.65

500lbf 31.65us

4515lbf 29.4us
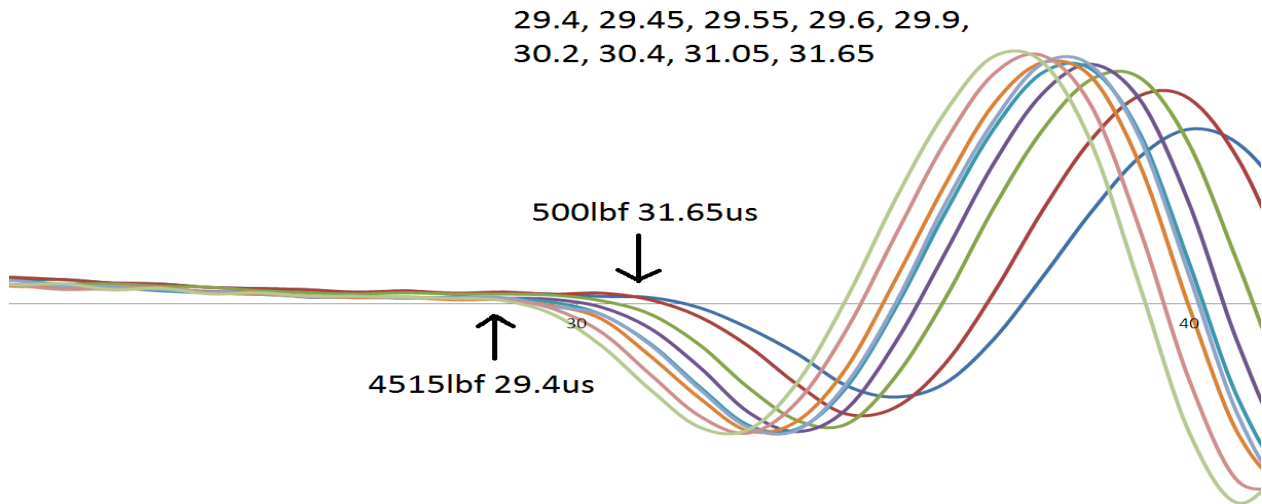
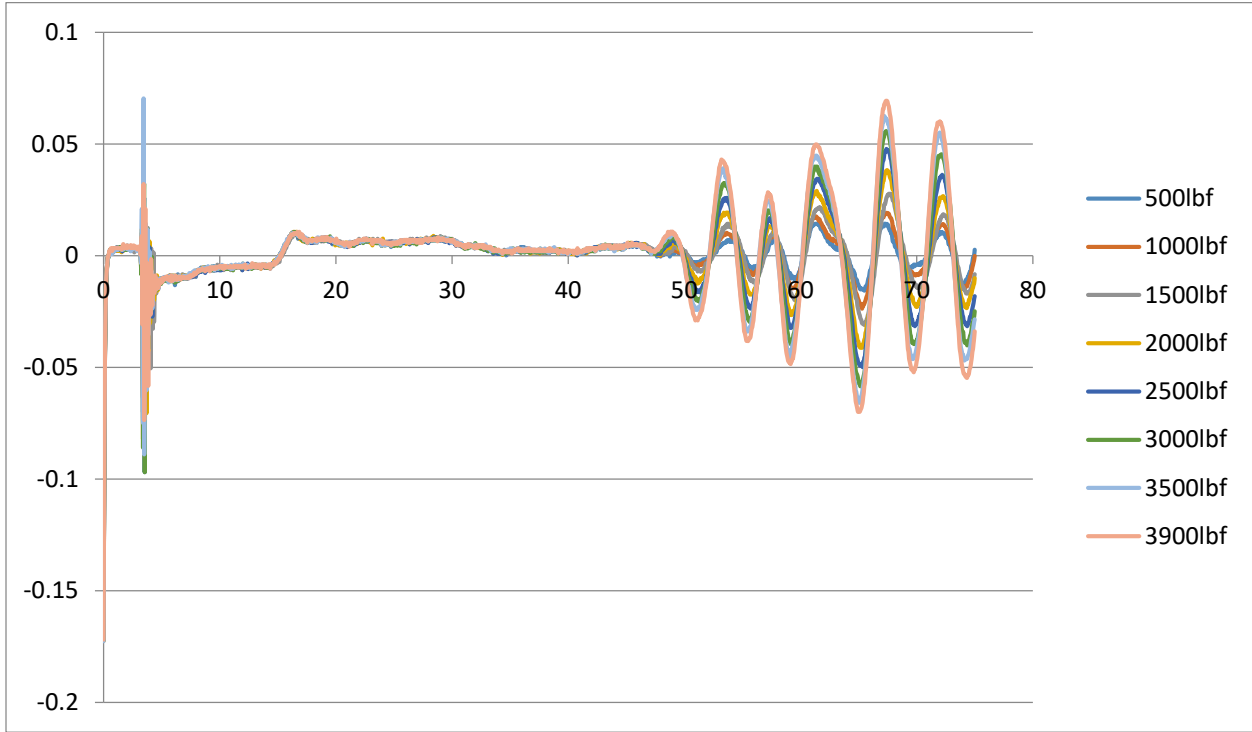**Figure 5.56** The 1.25MHz Vp waveform from core plug sample 4300.3.
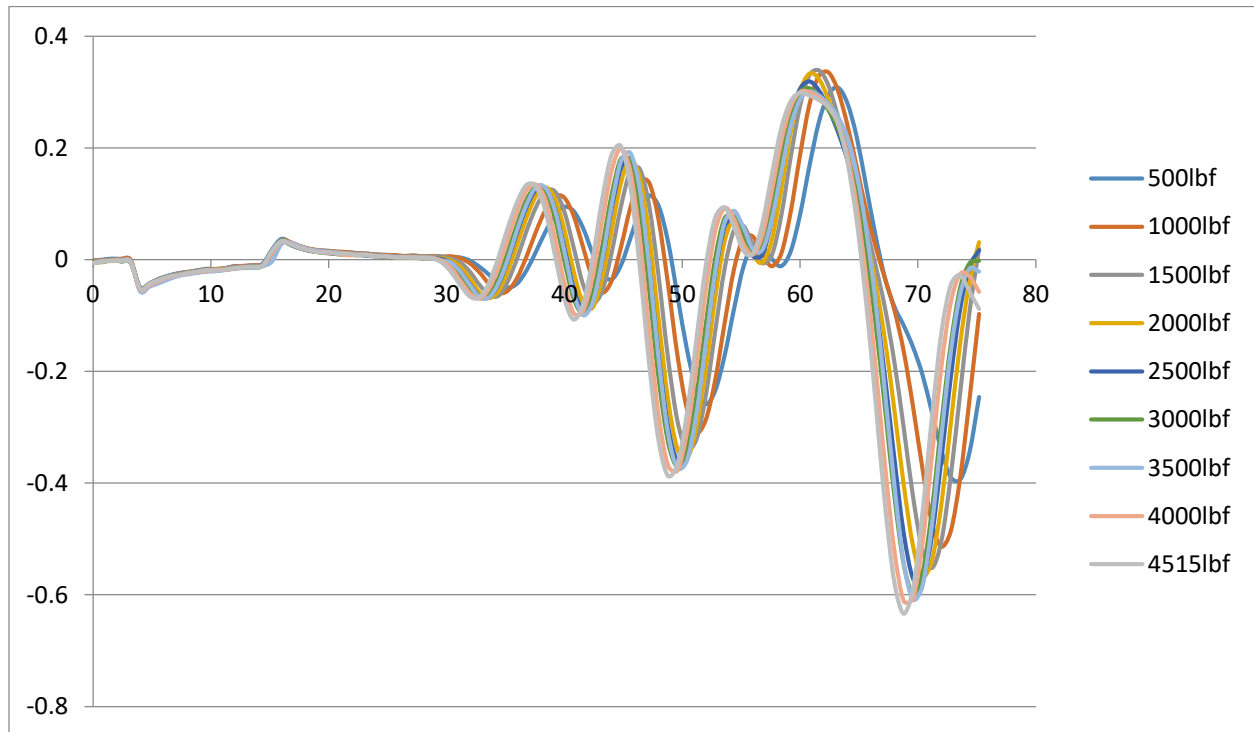
Figure 5.57 Core plug DA4300.3 S-wave first arrival 20MHz stacked waveforms. Values at the top of the figure correspond to the first arrival times at each pressure tested.

48.75, 49.05, 49.2, 49.45, 49.7, 50.05, 51.05, 52.65, 54.2

4515lbf 48.75us

50

500lbf 54.2us
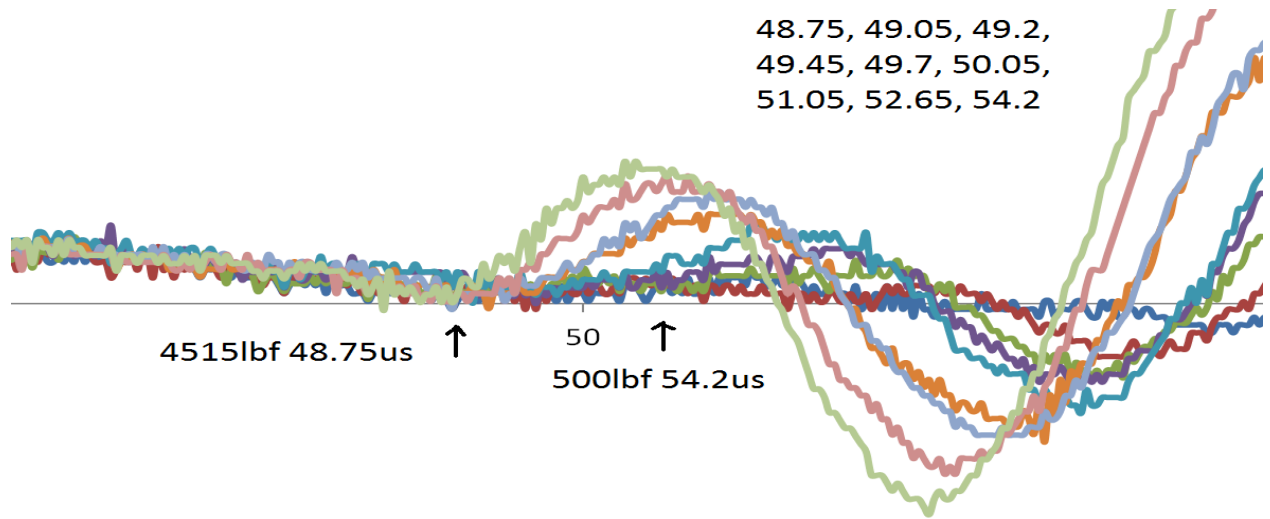
Figure 5.58 The 20MHz Vs waveform from core plug sample 4300.3.

- 500lbf
- 1000lbf
- 1500lbf
- 2000lbf
- 2500lbf
- 3000lbf
- 3500lbf
- 4000lbf
- 4515lbf
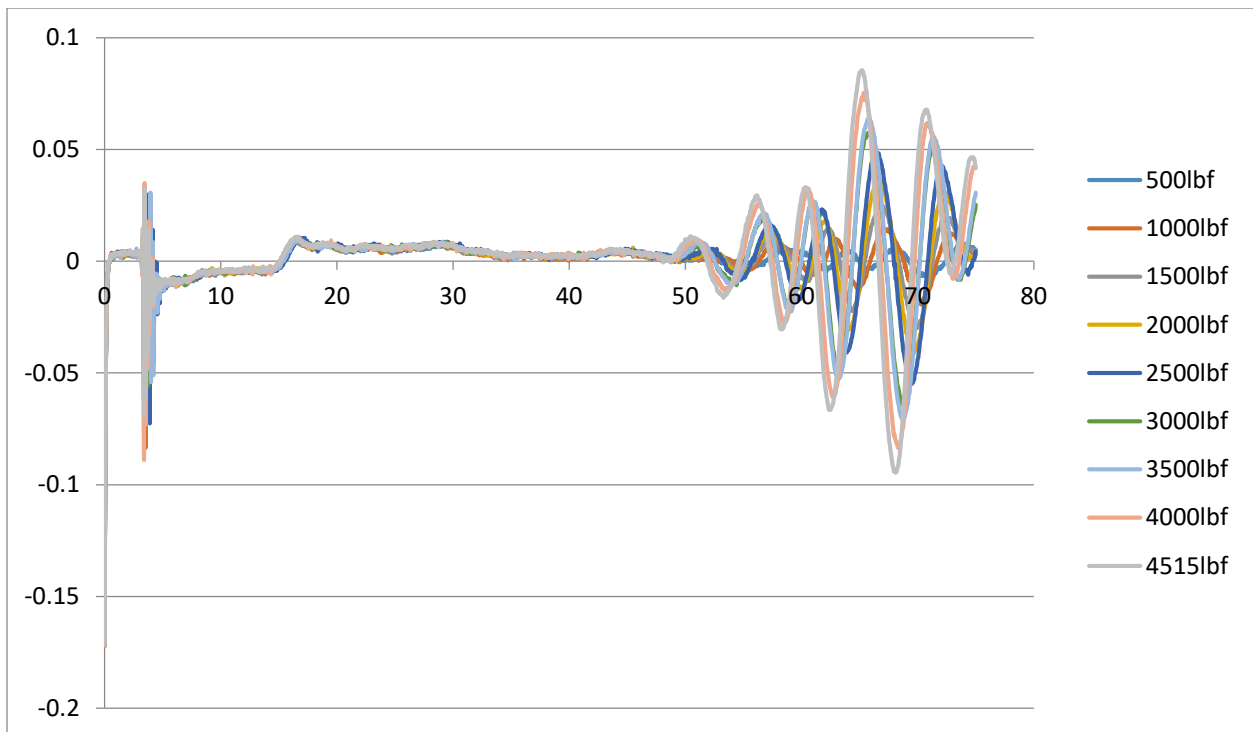
Figure 5.59 Core plug DA4300.3 S-wave first arrival 1.25MHz stacked waveforms.

Values at the top of the figure correspond to the first arrival times at each pressure tested.

49.05, 49.35, 49.45,
49.75, 49.8, 50.2, 52.75,
53.05, 53.6

500lbf 53.6us

50

4515lbf 49.05us
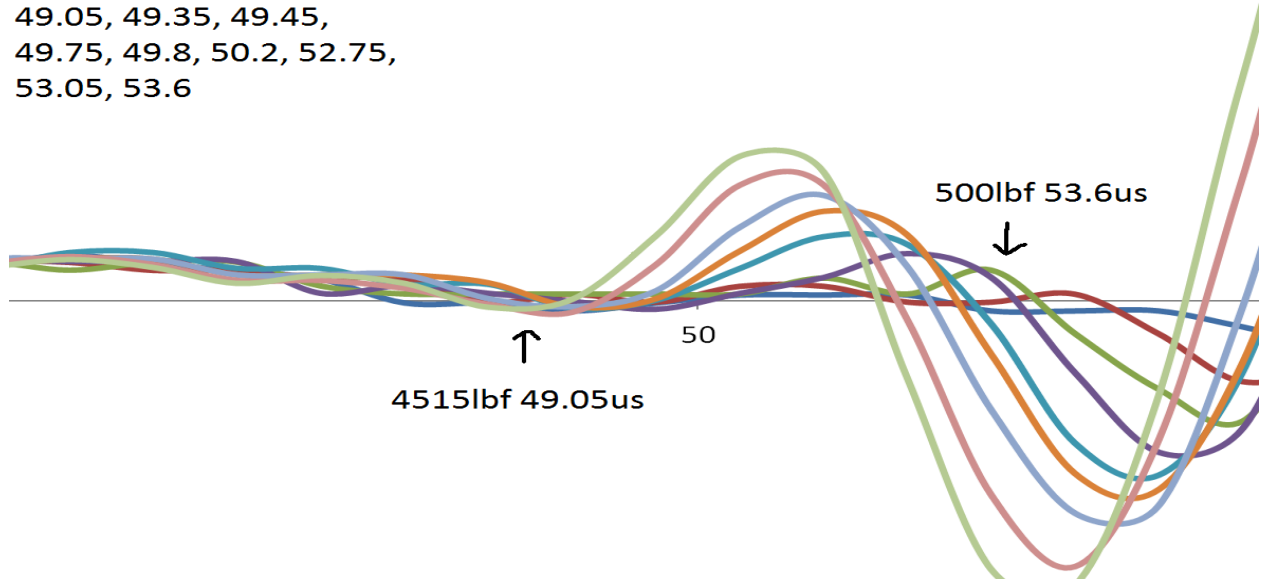
Figure 5.60 The 1.25MHz Vs waveform from core plug sample 4300.3.
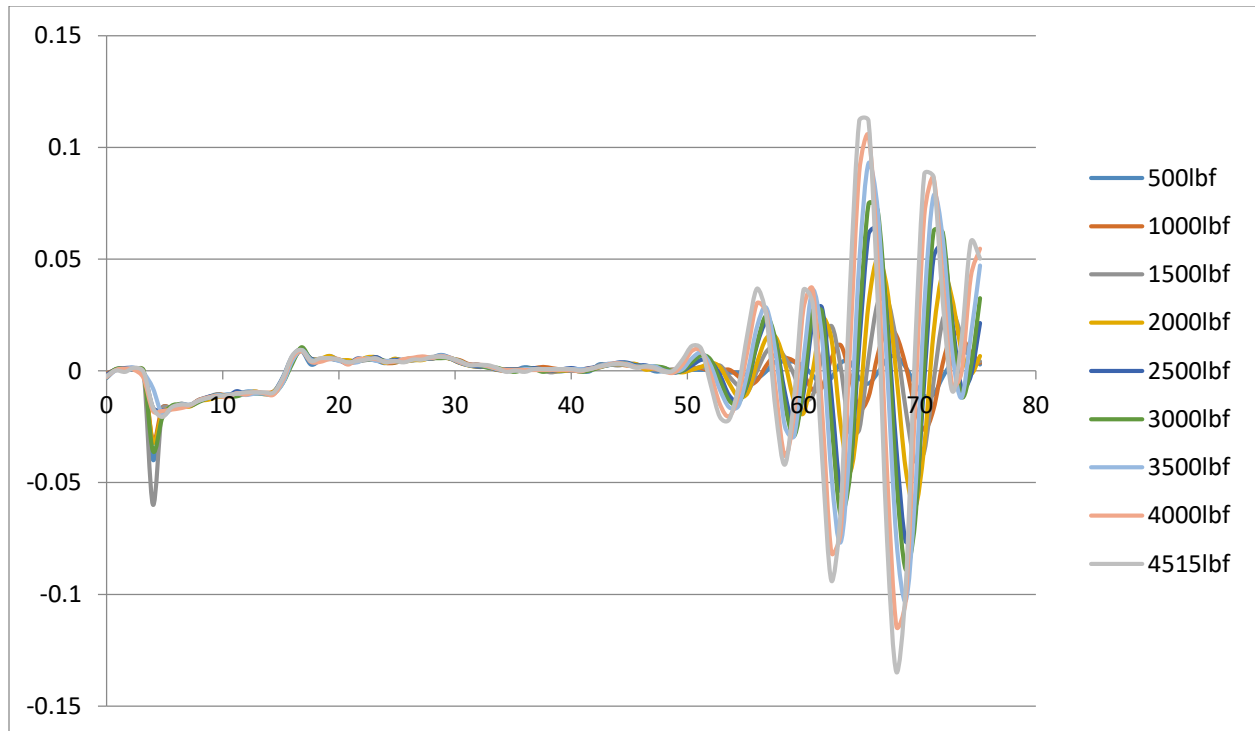
Table 5.13 Core plug DA4300.4 lab export data at 20MHz.

20MHz Ultrasonic Velocity Lab Test								
Lbf	p-wave first arrival time	s-wave first arrival time	P-wave Velocity	S-wave Velocity	Poisson's Ratio	Young's Modulus	Bulk Modulus	Shear Modulus
500	31.3	51.75	4091	2345	0.205130692	36448080.28	24827213.84	14517426
1000	30.8	51.3	4196	2375	0.213888872	37654075.58	26625938.24	14891250
1500	29.9	50.85	4401	2407	0.236204289	39357948.98	30739990.16	15295233.36
2000	29.35	49.65	4537	2496	0.23253103	42203363.72	32413077.84	16447242.24
2500	29.2	49.25	4576	2527	0.230133508	43178220.6	32803242.56	16858324.56
3000	28.9	48.85	4655	2559	0.233002539	44376800.21	34155572.88	17287989.84
3500	28.5	48.4	4766	2597	0.238488133	45896419.96	36226636.16	17805239.76
4000	28.45	48.2	4780	2613	0.236508649	46393795.24	36286029.12	18025310.16
4515	28.4	48.1	4792	2621	0.236167875	46666180.27	36441880.64	18135852.24

Table 5.14 Core plug DA4300.4 lab export data at 1.25MHz.

1.25MHz								
Lbf	p-wave first arrival time	s-wave first arrival time	P-wave Velocity	S-wave Velocity	Poisson's Ratio	Young's Modulus	Bulk Modulus	Shear Modulus
500	31.7	52.4	4009	2301	0.204207398	35066459.25	23793298.32	13977746.64
1000	30.6	51.8	4241	2341	0.230406219	37063696.4	28192664.72	14467941.84
1500	30.35	51	4297	2396	0.223889512	38628961.3	28537839.44	15155754.24
2000	29.75	50.15	4439	2459	0.228139362	40822476.42	30736146.32	15963237.84
2500	29.65	49.7	4462	2492	0.222837788	41751887.16	30701506.88	16394568.96
3000	29.35	49.25	4539	2527	0.22490573	43002752.6	31912889.36	16858324.56
3500	29.2	48.65	4576	2575	0.217837156	44403090.69	31941208.64	17504850
4000	29.15	48.2	4590	2613	0.209937451	45433388.82	31586037.12	18025310.16
4515	29	48.15	4628	2617	0.214543433	45742606.55	32437148.48	18080538.96

Figure 5.61 Core plug DA4300.4 pressure vs velocity cross plots at 20MHz.
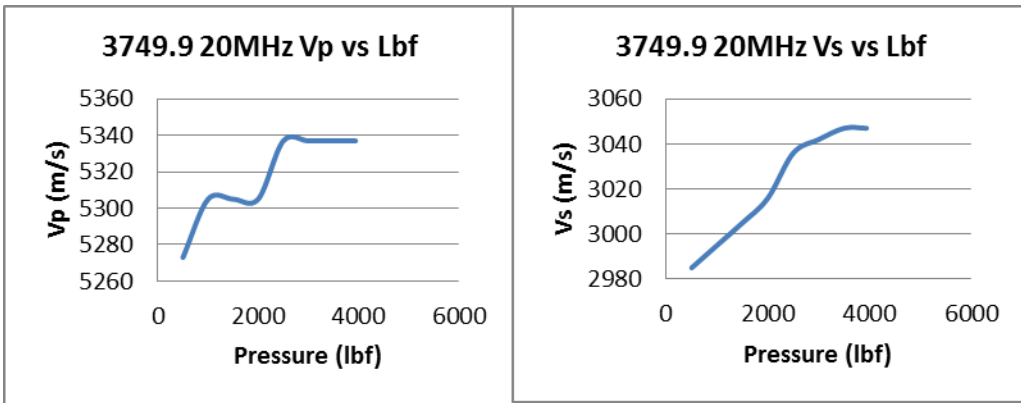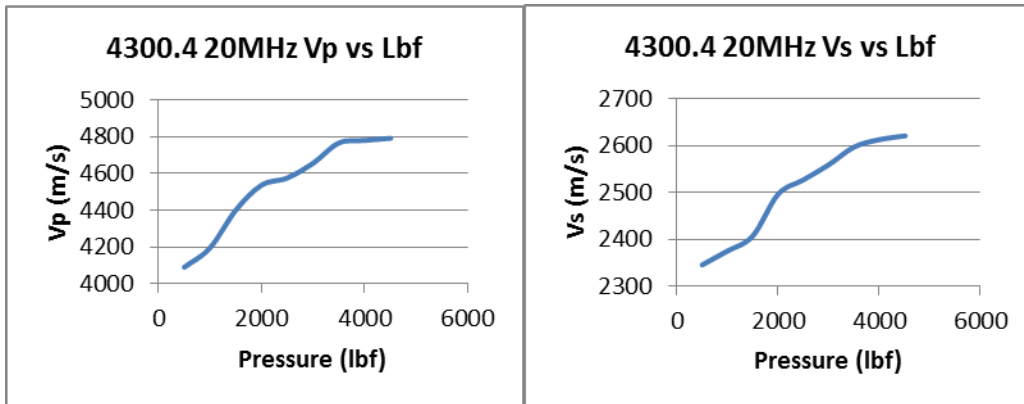

Figure 5.62 Core plug DA4300.4 pressure vs velocity cross plots at 1.25MHz.
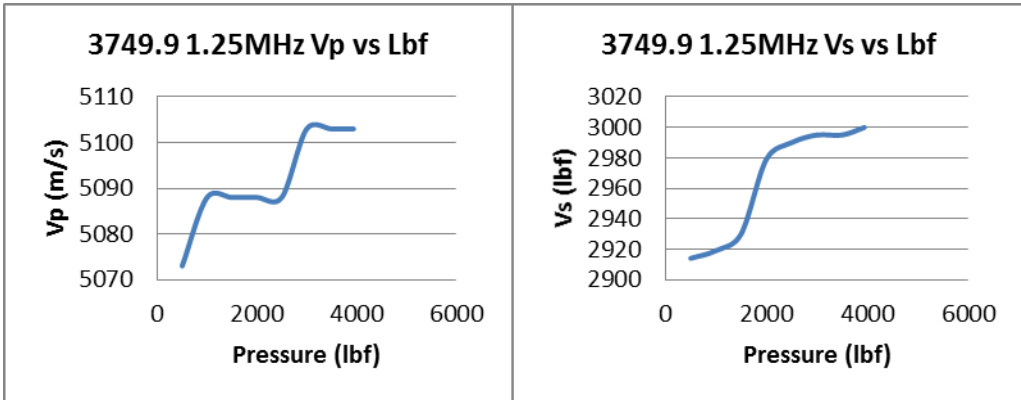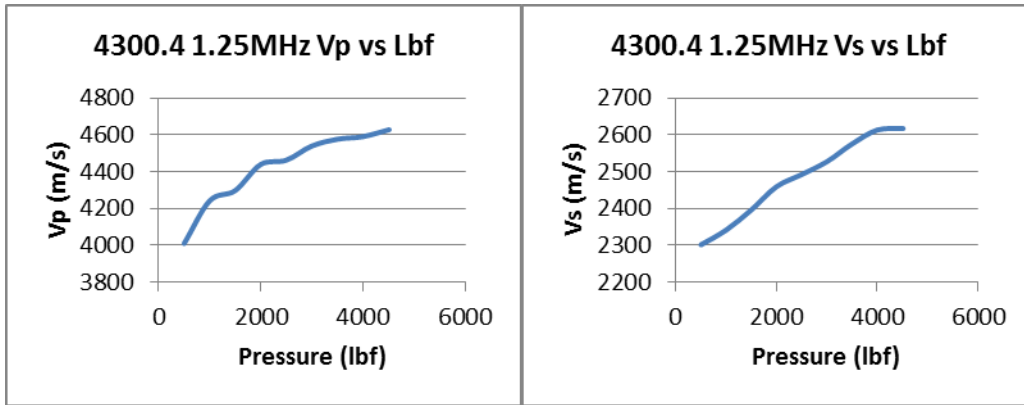
Figure 5.63 Core plug DA4300.4 P-wave first arrival 20MHz stacked waveforms. Values

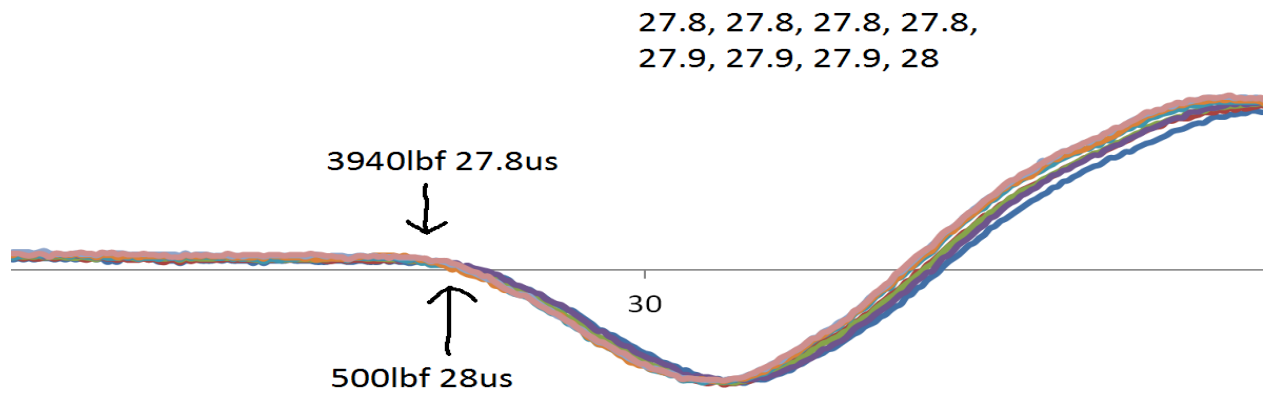at the top of the figure correspond to the first arrival times at each pressure tested.
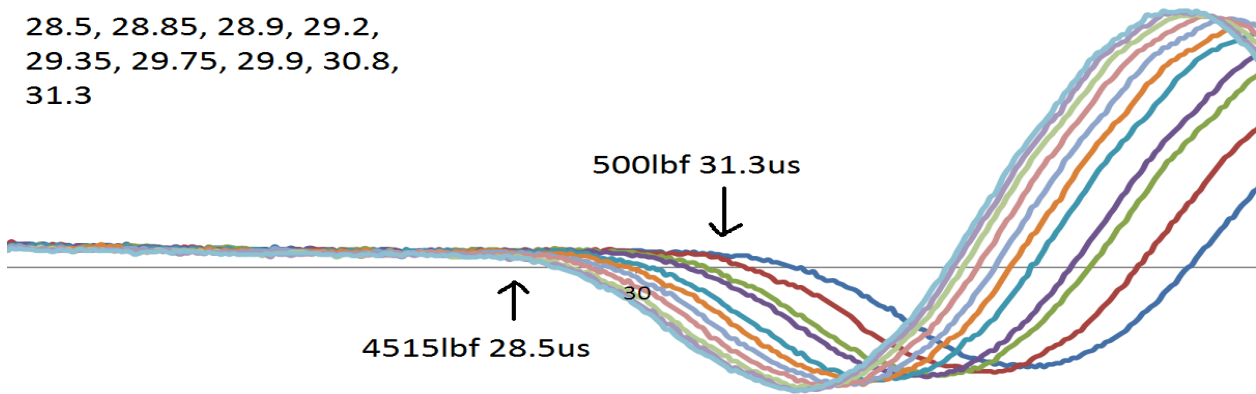
Figure 5.64 The 20MHz Vp waveform from core plug sample 4300.4.
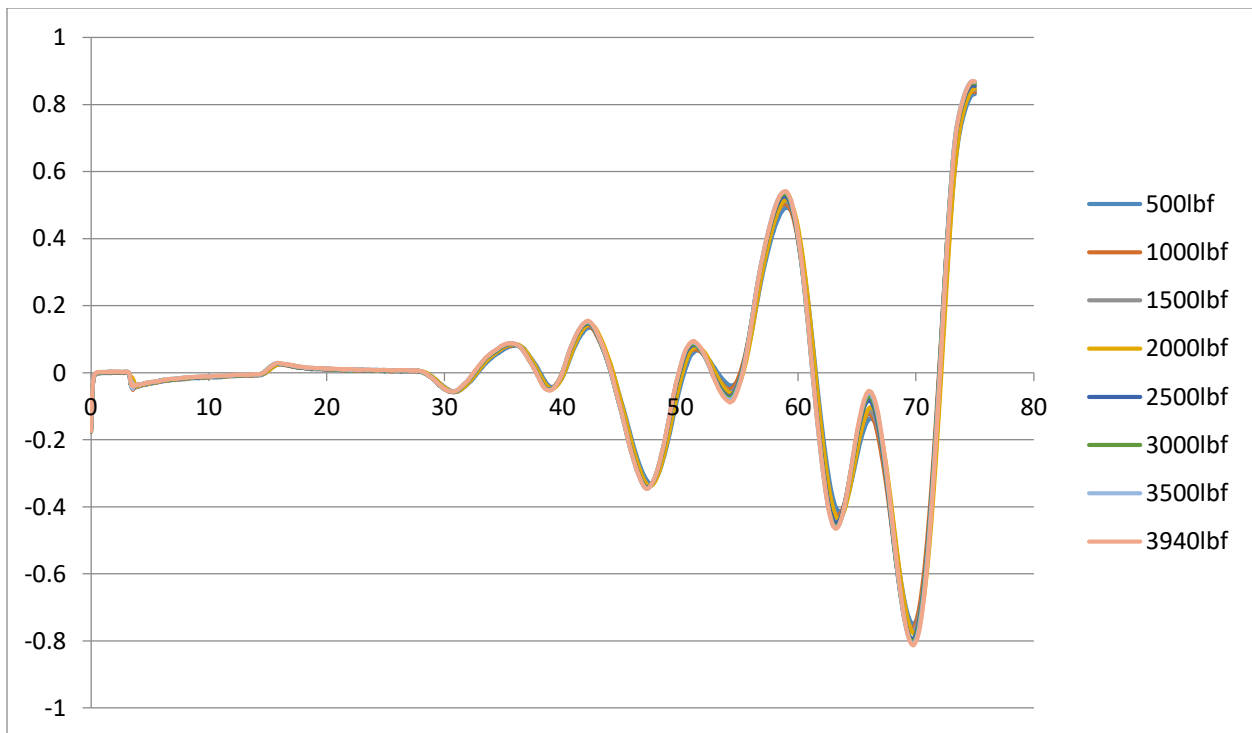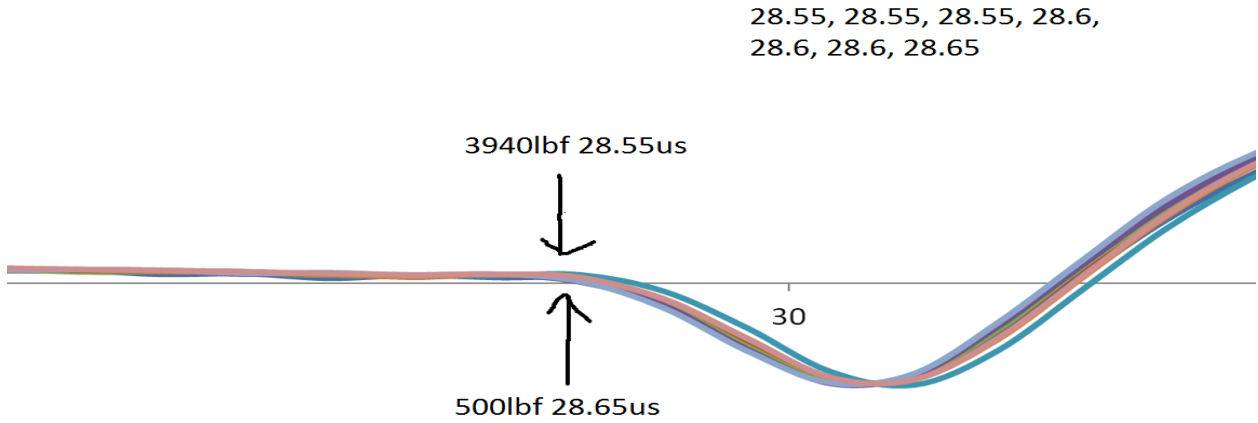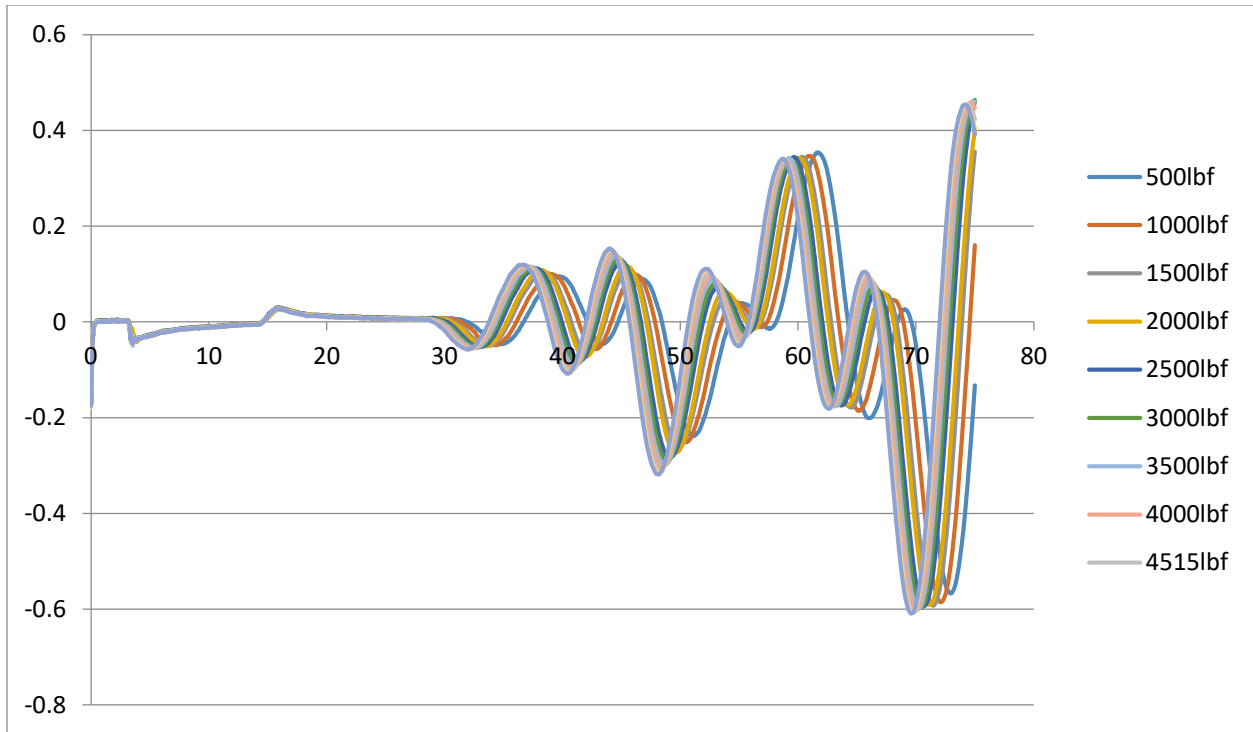
Figure 5.65 Core plug DA4300.4 P-wave first arrival 1.25MHz stacked waveforms.

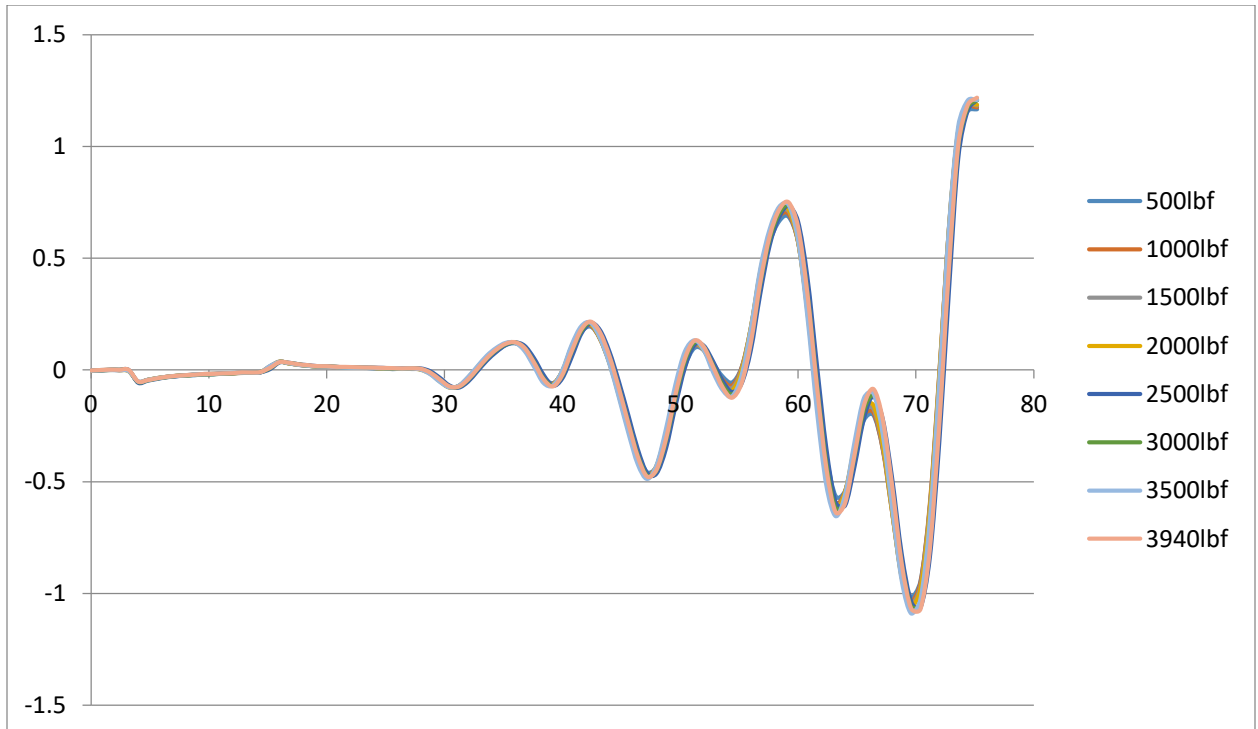Values at the top of the figure correspond to the first arrival times at each pressure tested.

29.2, 29.25, 29.35,
29.65, 29.75, 30, 30.35,
30.6, 31.7

500lbf 31.7us

4515lbf 29.2us
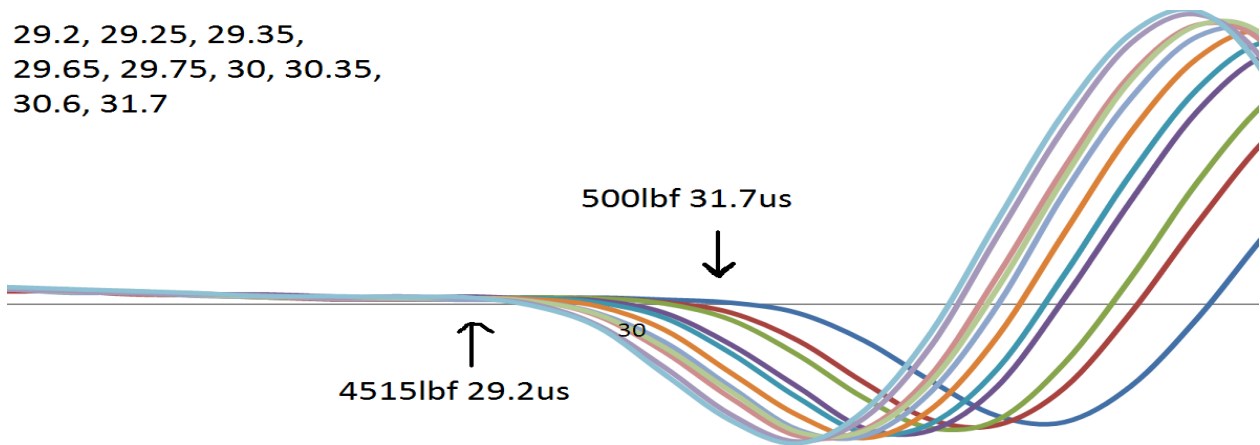
Figure 5.66 The 1.25MHz Vp waveform from core plug sample 4300.4.
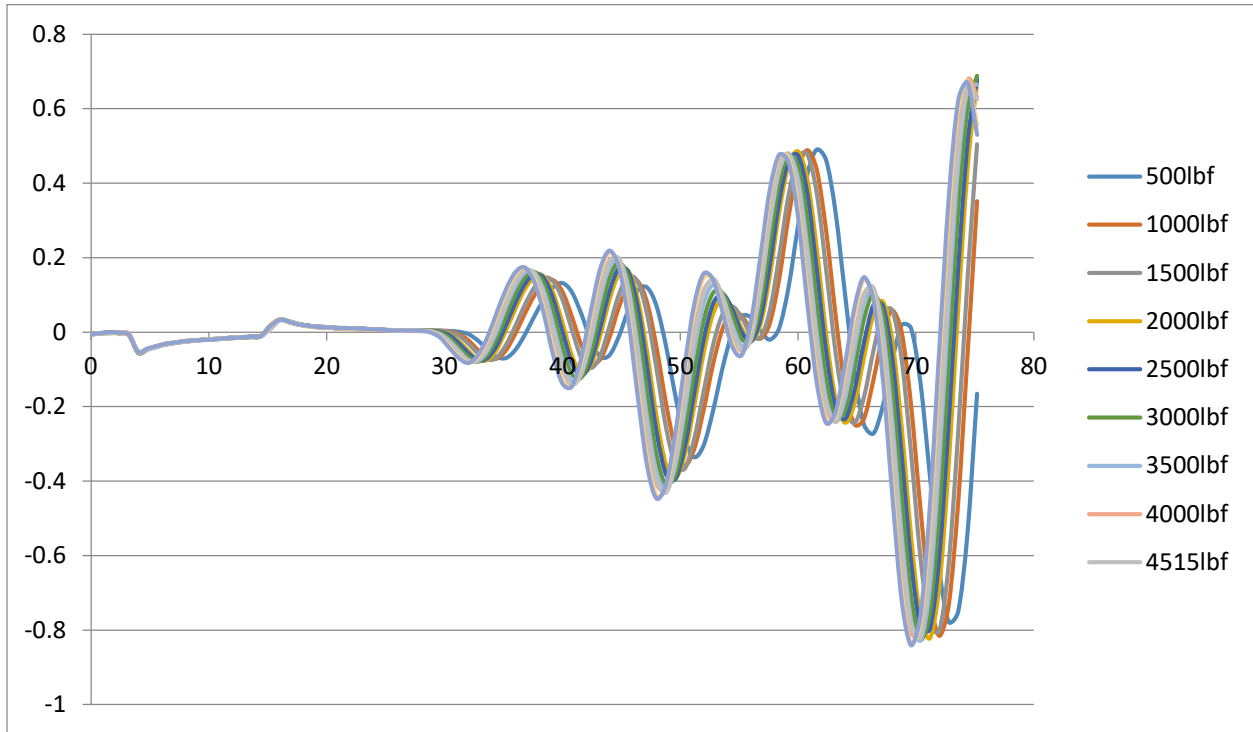
Figure 5.67 Core plug DA4300.4 S-wave first arrival 20MHz stacked waveforms. Values at the top of the figure correspond to the first arrival times at each pressure tested.
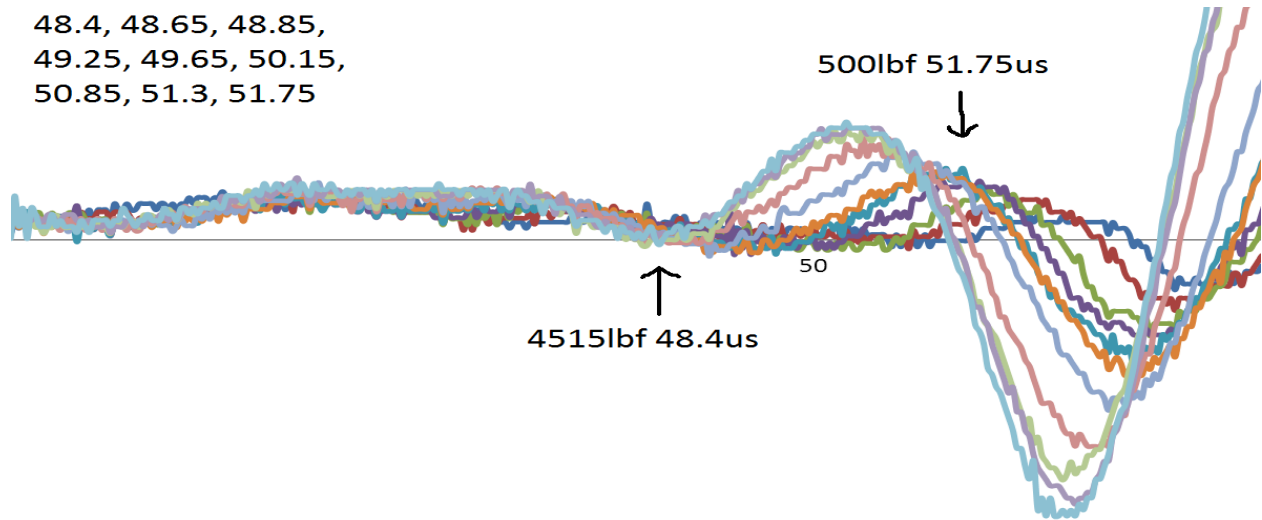
Figure 5.68 The 20MHz Vs waveform from core plug sample 4300.4.
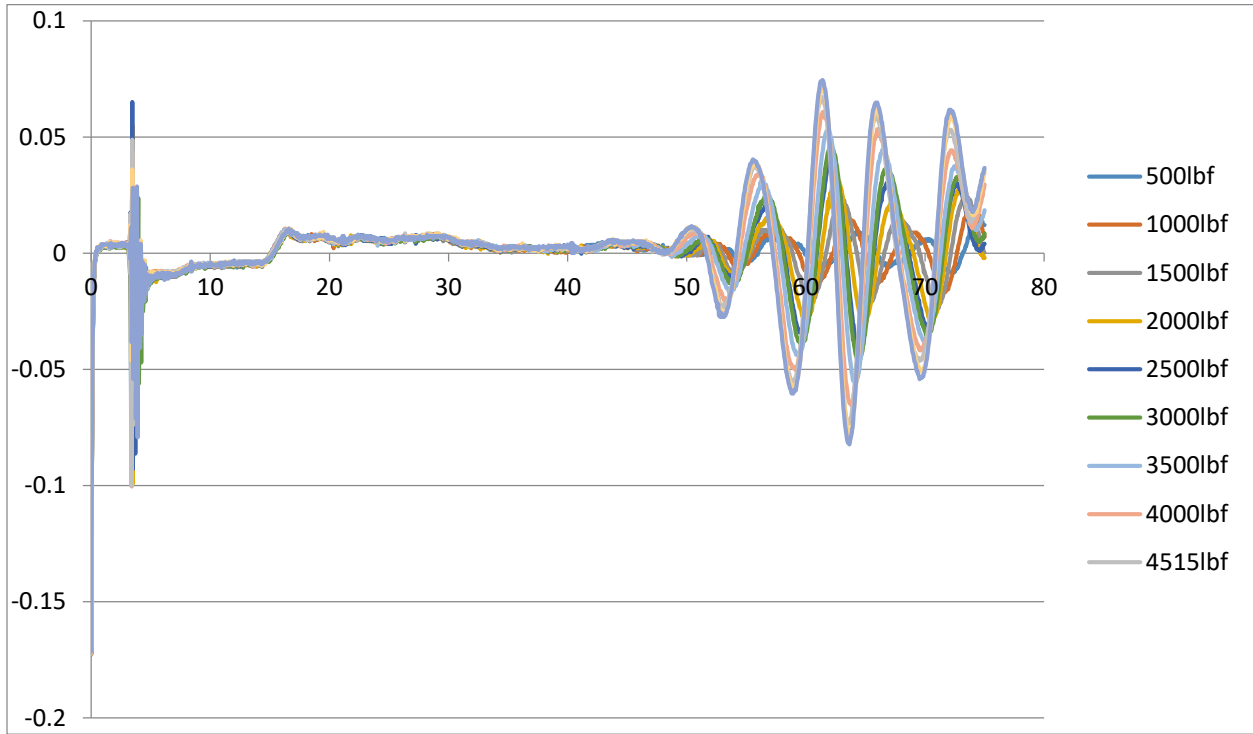
Figure 5.69 Core plug DA4300.4 S-wave first arrival 1.25MHz stacked waveforms.

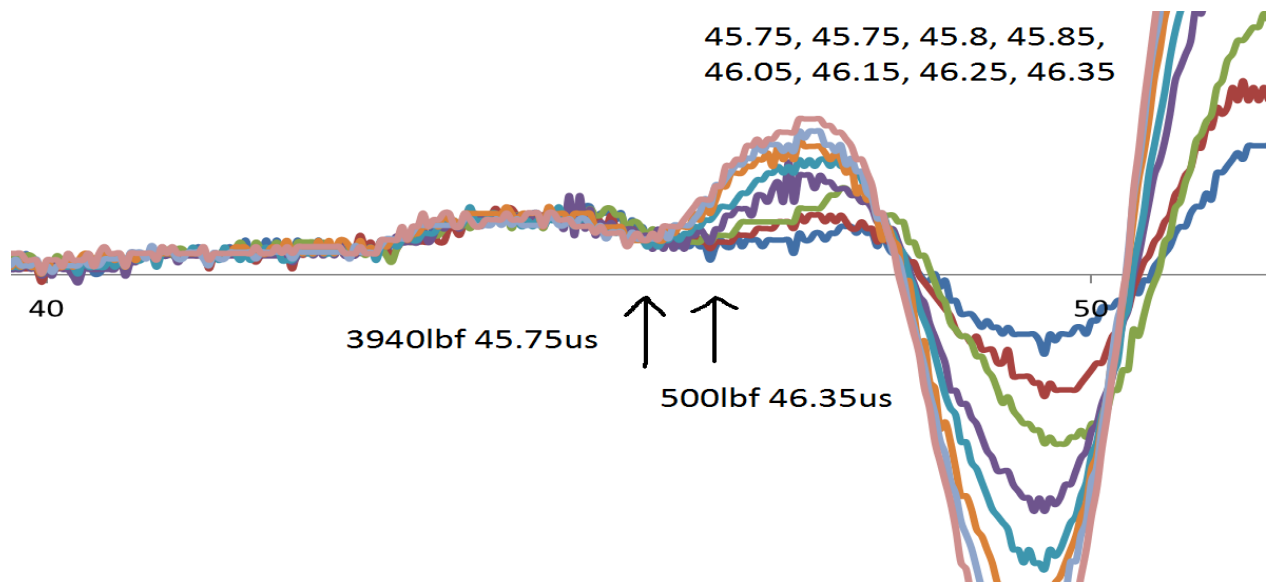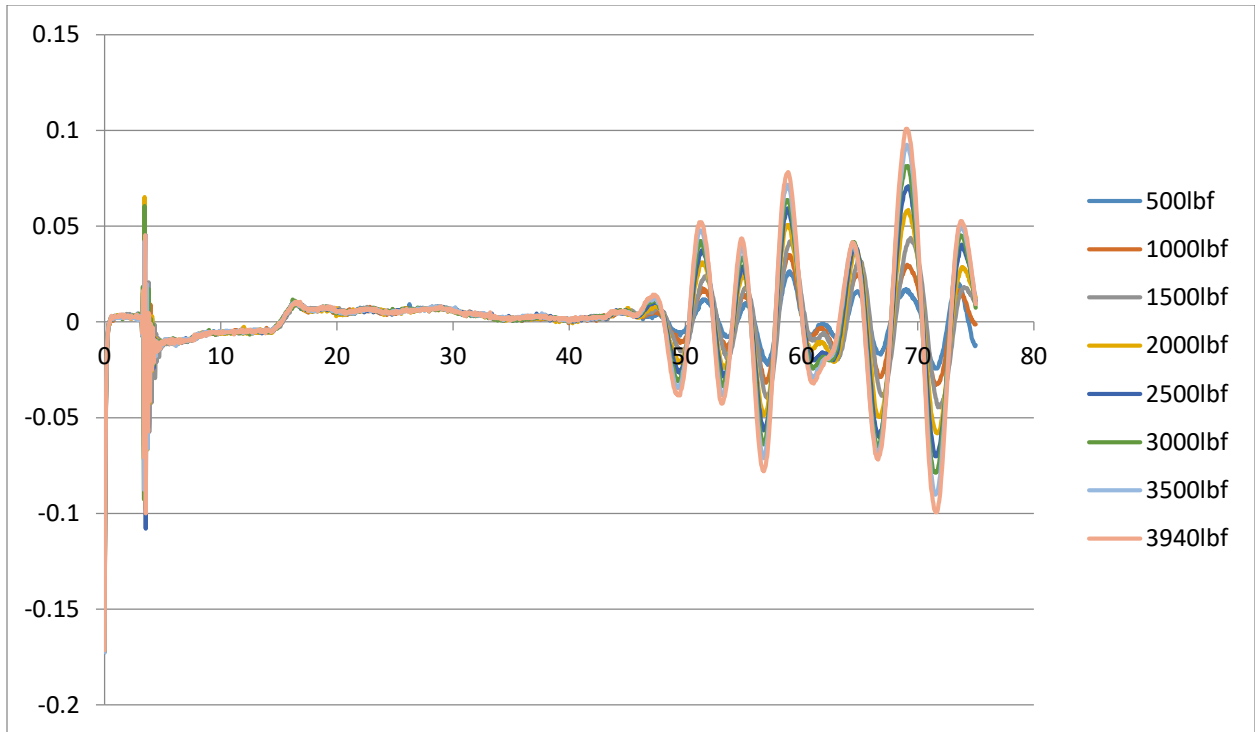Values at the top of the figure correspond to the first arrival times at each pressure tested.

48.65, 49.2, 49.25, 49.7,
50.15, 50.9, 51, 51.8, 52.4

500lbf 52.4us

4515lbf 48.65us
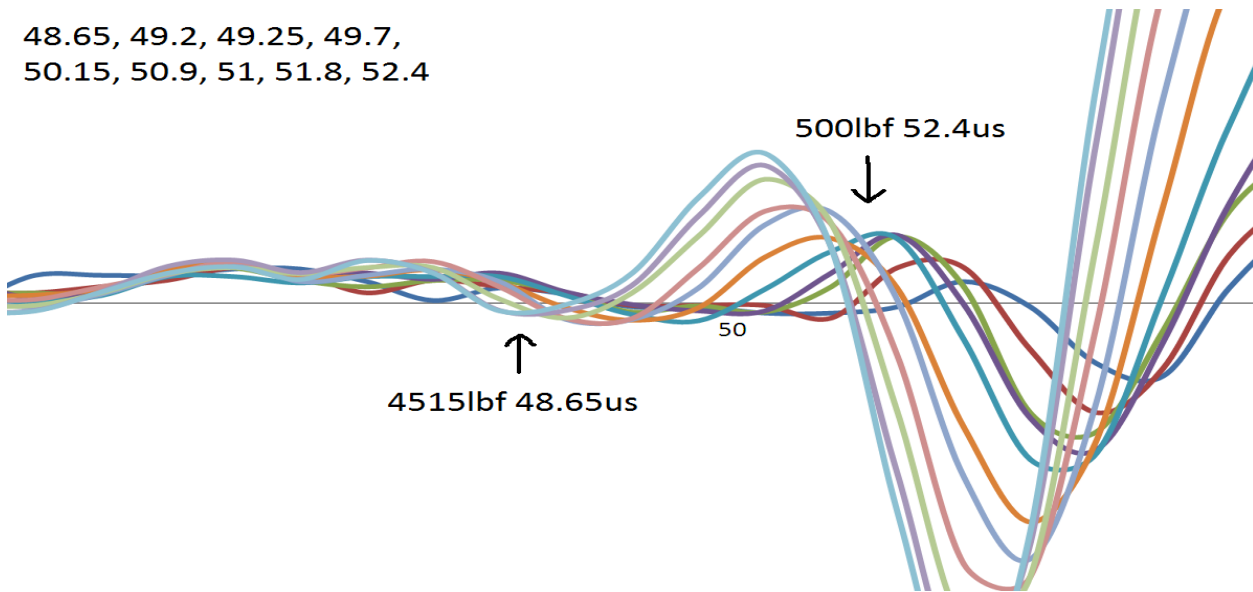
Figure 5.70 The 1.25MHz Vs waveform from core plug sample 4300.4.
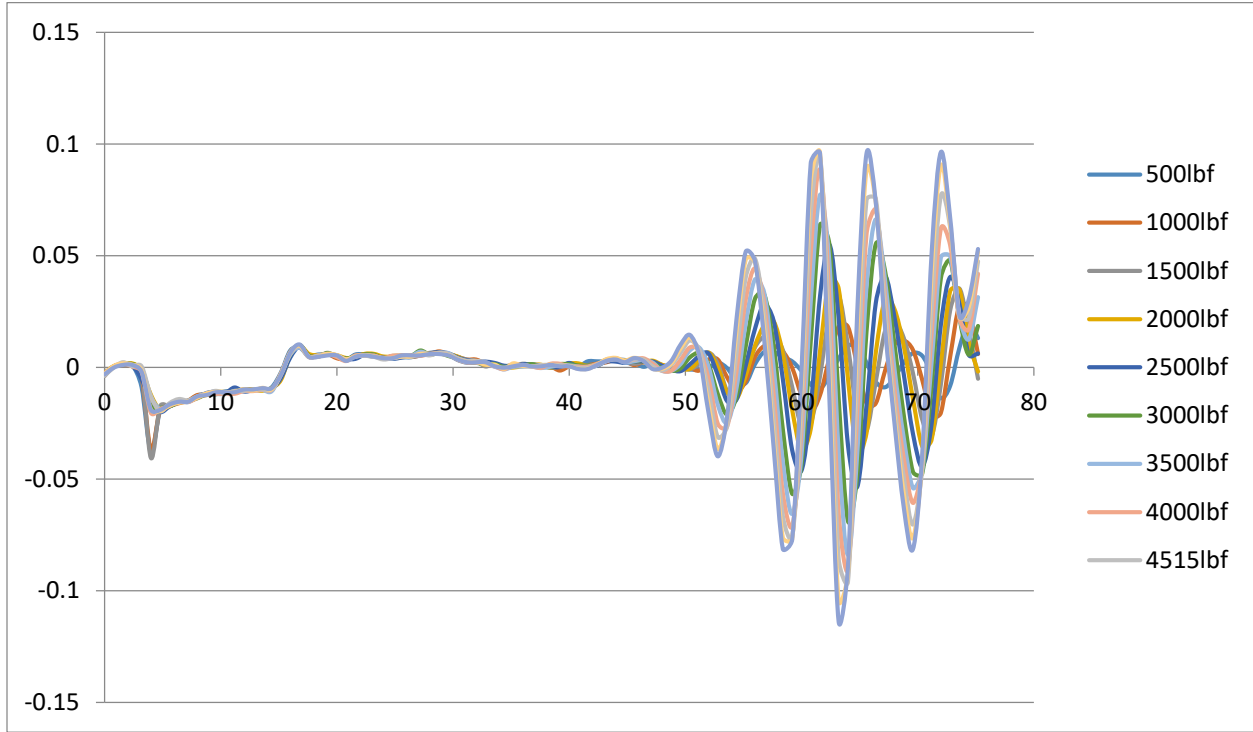
Table 5.15 Core plug DA4472.6 lab export data at 20MHz.

20MHz Ultrasonic Velocity Lab Test								
Lbf	p-wave first arrival time	s-wave first arrival time	P-wave Velocity	S-wave Velocity	Poisson's Ratio	Young's Modulus	Bulk Modulus	Shear Modulus
500	27.15	48.55	5368	2679	0.334159489	51898220.04	52156757.56	19449781.11
1000	27.05	48.3	5402	2701	0.333333333	52721431.23	52721431.23	19770536.71
1500	26.8	48.1	5490	2718	0.337655218	53560223.33	54986084.28	20020190.04
2000	26.75	47.8	5509	2745	0.334860031	54515464.08	55019452.51	20419917.75
2500	26.7	47.6	5527	2763	0.33341373	55172921.22	55199548.27	20688597.99
3000	26.6	47.55	5562	2768	0.335399643	55455255.93	56151413.19	20763543.04
3500	26.55	47.5	5582	2772	0.336335056	55654604.38	56675346.52	20823596.64
4000	26.45	47.3	5618	2791	0.33616016	56412776.83	57386100.03	21110035.51
4500	26.4	47.25	5637	2795	0.337003245	56610289.06	57884883.66	21170587.75
4700	26.35	47.2	5657	2800	0.337759418	56845143.39	58395935.46	21246400

Table 5.16 Core plug DA4472.6 lab export data at 1.25MHz.

1.25MHz								
Lbf	p-wave first arrival time	s-wave first arrival time	P-wave Velocity	S-wave Velocity	Poisson's Ratio	Young's Modulus	Bulk Modulus	Shear Modulus
500	28.15	48.65	5045	2671	0.305264627	50471432.5	43196596.94	19333793.11
1000	27.6	48.6	5218	2675	0.321750174	51262081.36	47930931.71	19391743.75
1500	27.45	48.5	5267	2684	0.324616445	51719516.02	49148960.18	19522449.76
2000	27.45	48.4	5267	2692	0.323199138	51972619.57	48993557.94	19639001.44
2500	27.4	47.6	5282	2763	0.311644824	54272184.95	48022912.72	20688597.99
3000	27.4	47.55	5282	2768	0.310704181	54429725.34	47922985.99	20763543.04
3500	26.95	47	5435	2819	0.315982998	56681288.8	51337003.34	21535722.31
4000	26.25	46.85	5657	2833	0.33262493	57969608.75	57724256.54	21750159.19
4500	26.2	46.8	5677	2838	0.333411606	58208753.55	58236103.27	21827001.24
4700	26.2	46.75	5677	2843	0.332627431	58379685.95	58133466.54	21903978.79

Figure 5.71 Core plug DA4472.6 pressure vs velocity cross plots at 20MHz.
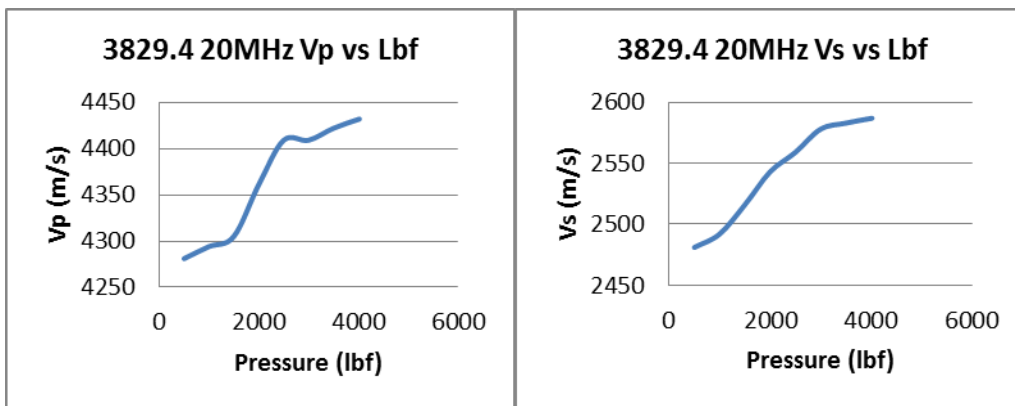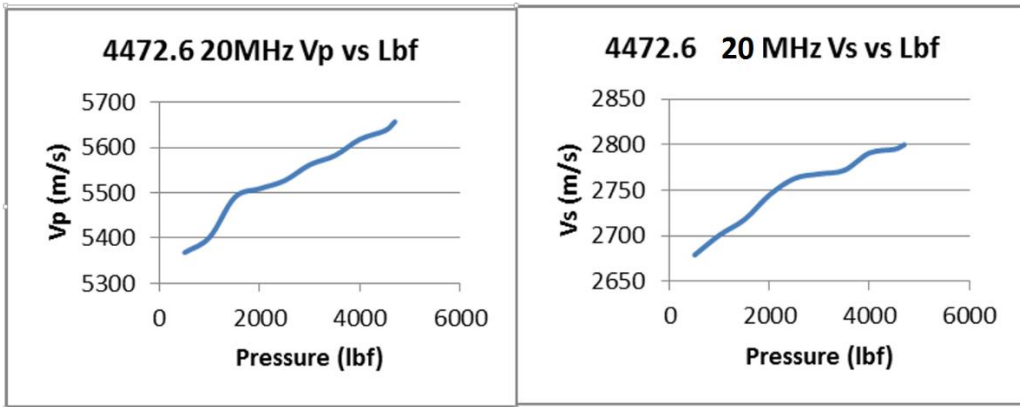

**Figure 5.72** Core plug DA4472.6 pressure vs velocity cross plots at 1.25MHz.
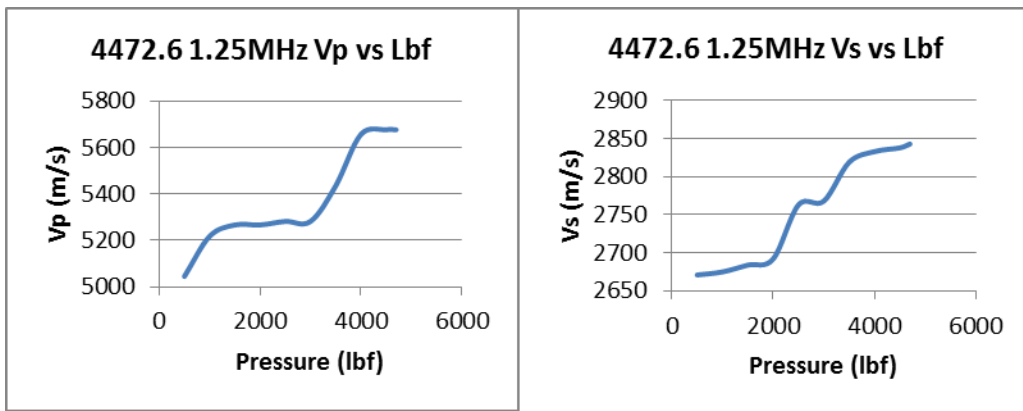
Figure 5.73 Core plug DA4472.6 P-wave first arrival 20MHz stacked waveforms. Values at the top of the figure correspond to the first arrival times at each pressure tested.

26.35, 26.4, 26.45,
26.55, 26.6, 26.7, 26.75,
26.8, 27.05, 27.15

4700lbf 26.35us

500lbf 27.15us

30
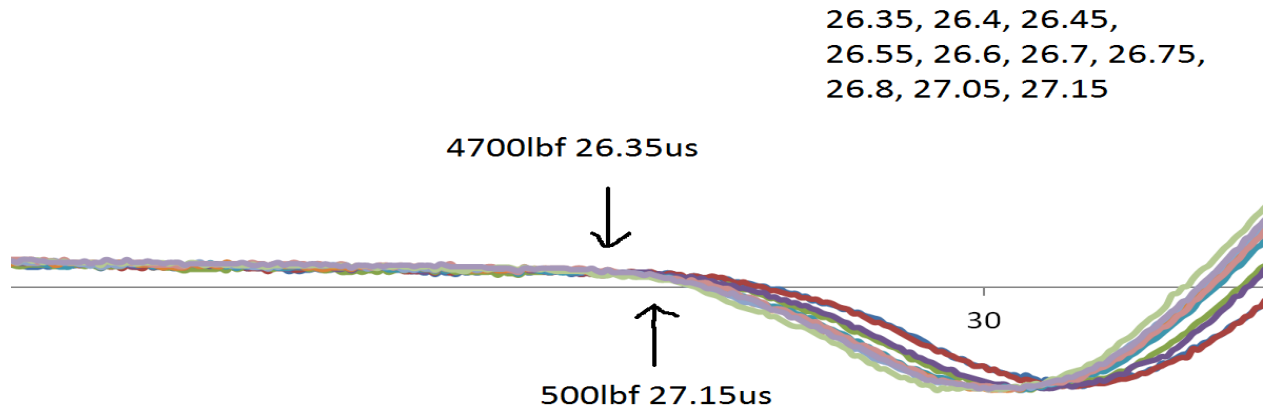
Figure 5.74 The 20MHz Vp waveform from core plug sample 4472.6.
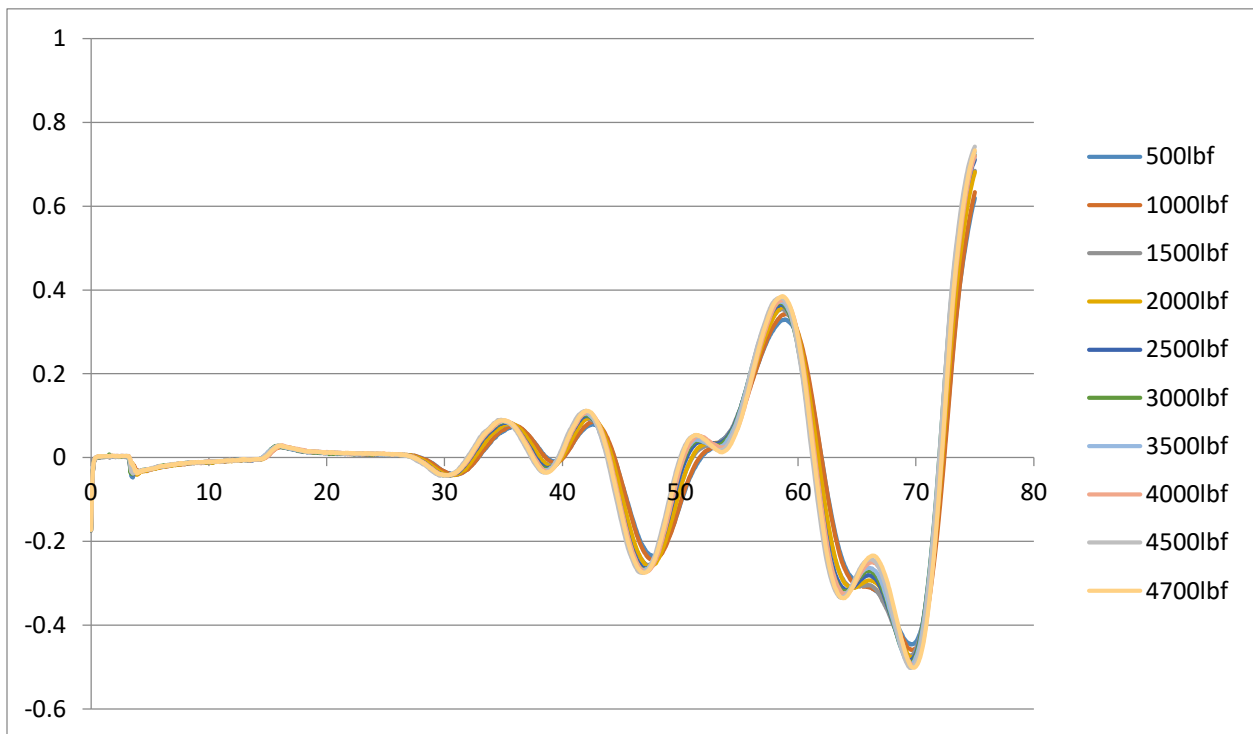
Figure 5.75 Core plug DA4472.6 P-wave first arrival 1.25MHz stacked waveforms.

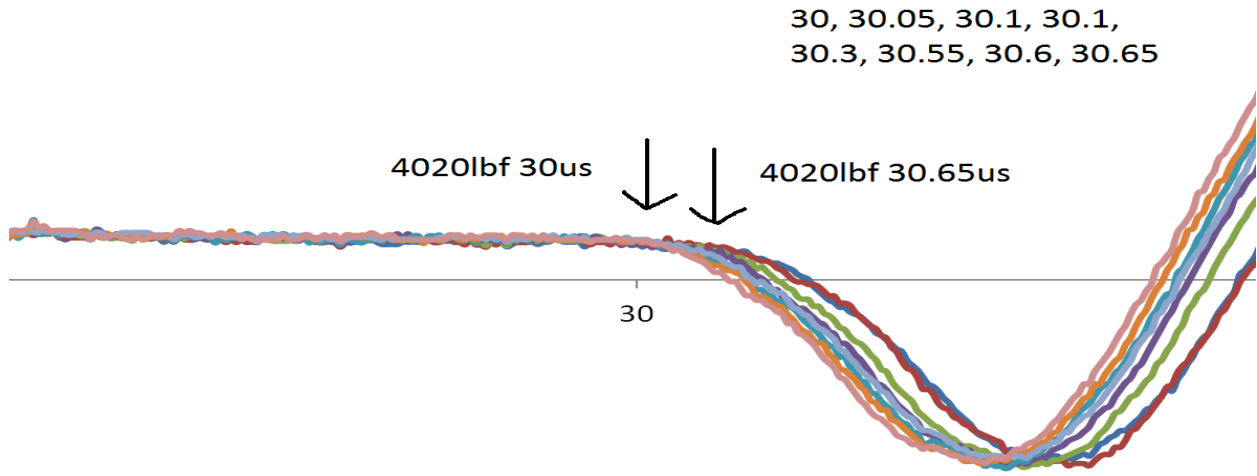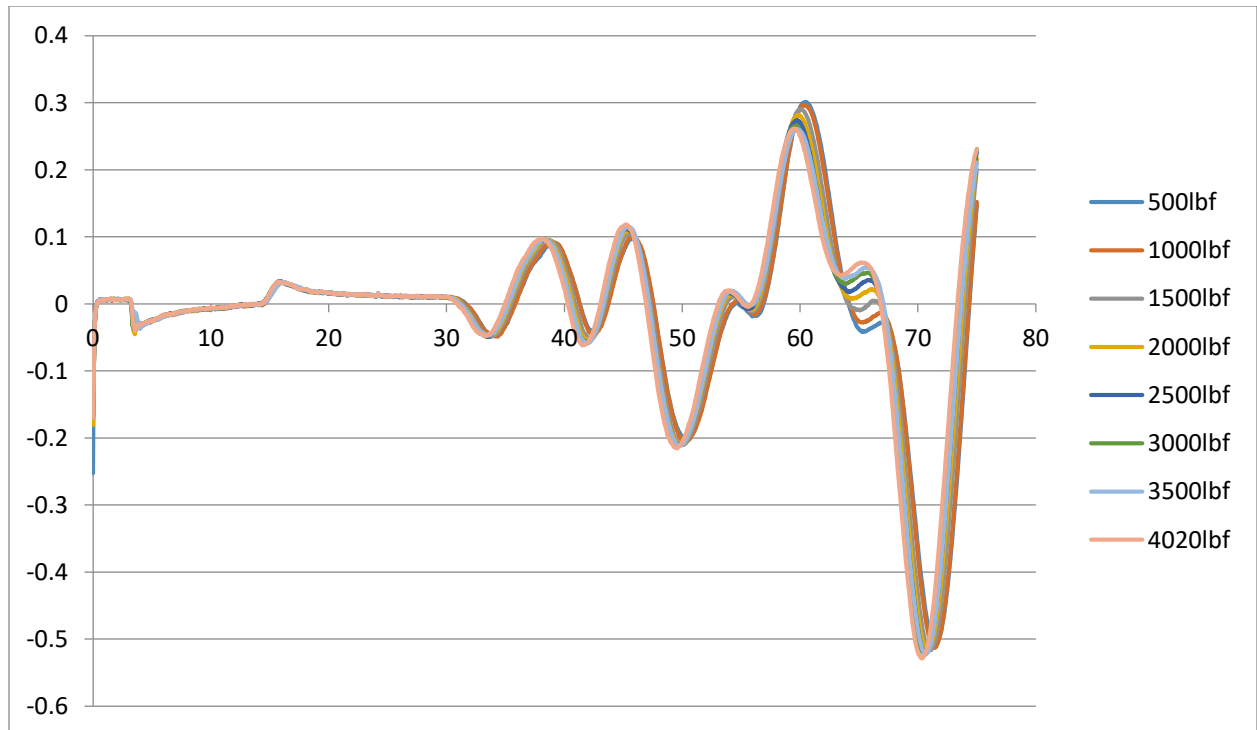Values at the top of the figure correspond to the first arrival times at each pressure tested.

26.2, 26.2, 26.25, 26.95,
27.4, 27.4, 27.45, 27.45,
27.6, 28.15

4700lbf 26.2us

500lbf 28.15us

30
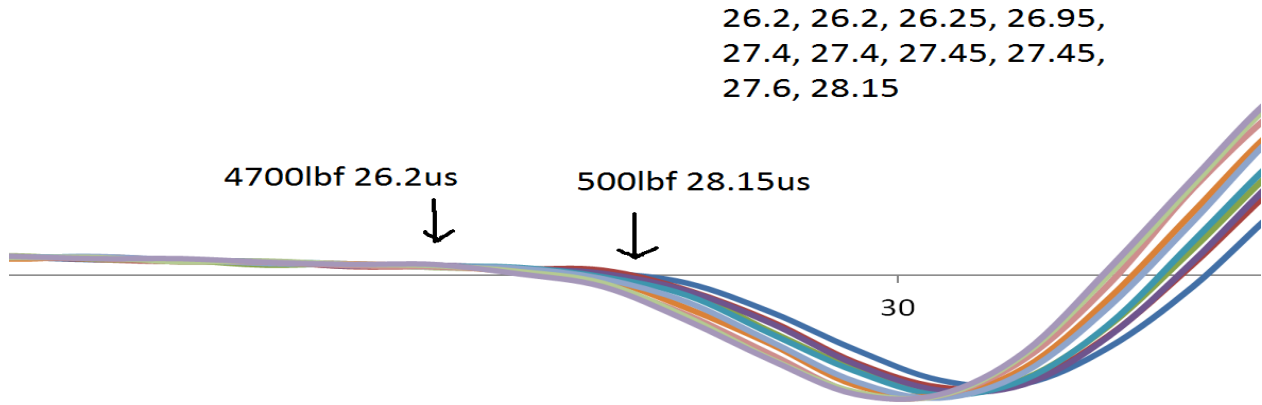
Figure 5.76 The 1.25MHz Vp waveform from core plug sample 4472.6.
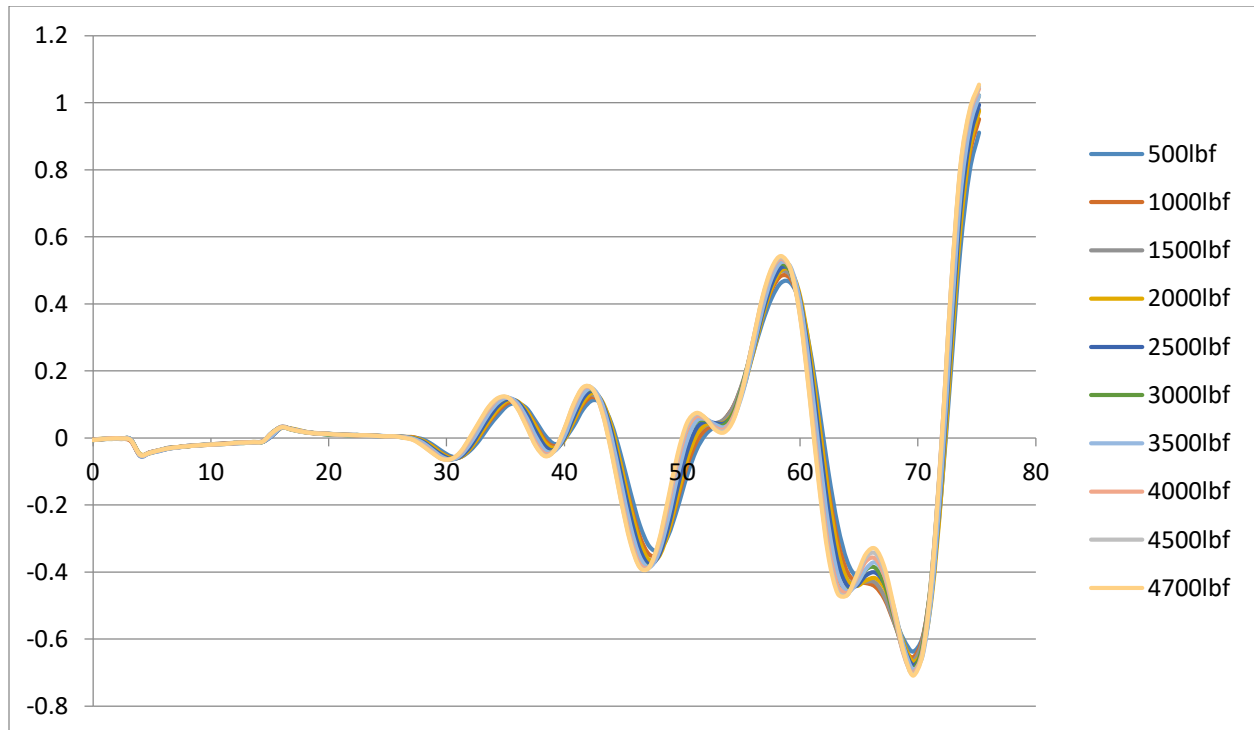
Figure 5.77 Core plug DA4472.6 S-wave first arrival 20MHz stacked waveforms. Values at the top of the figure correspond to the first arrival times at each pressure tested.
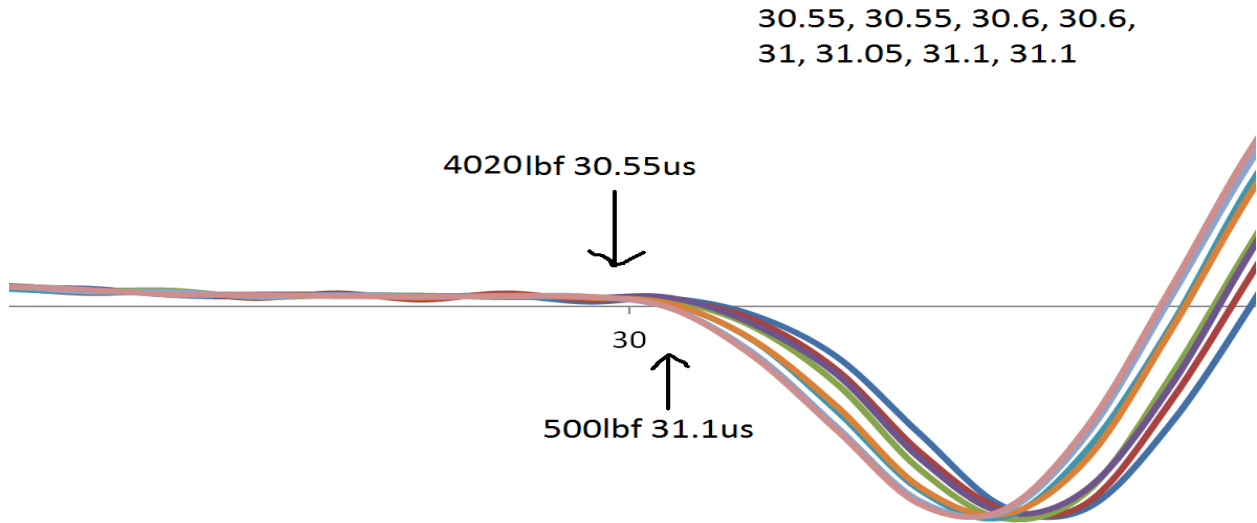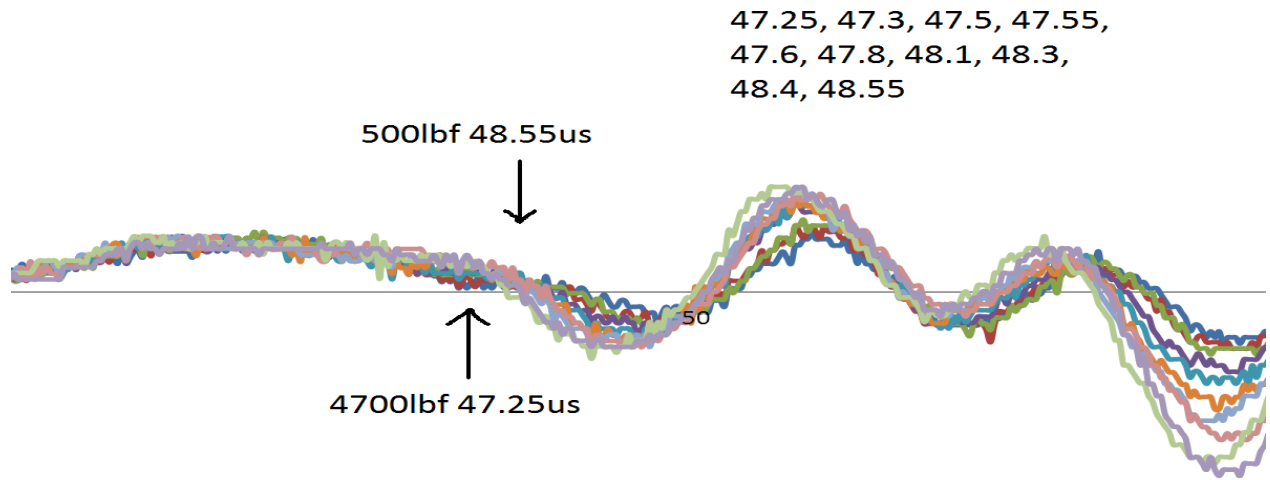
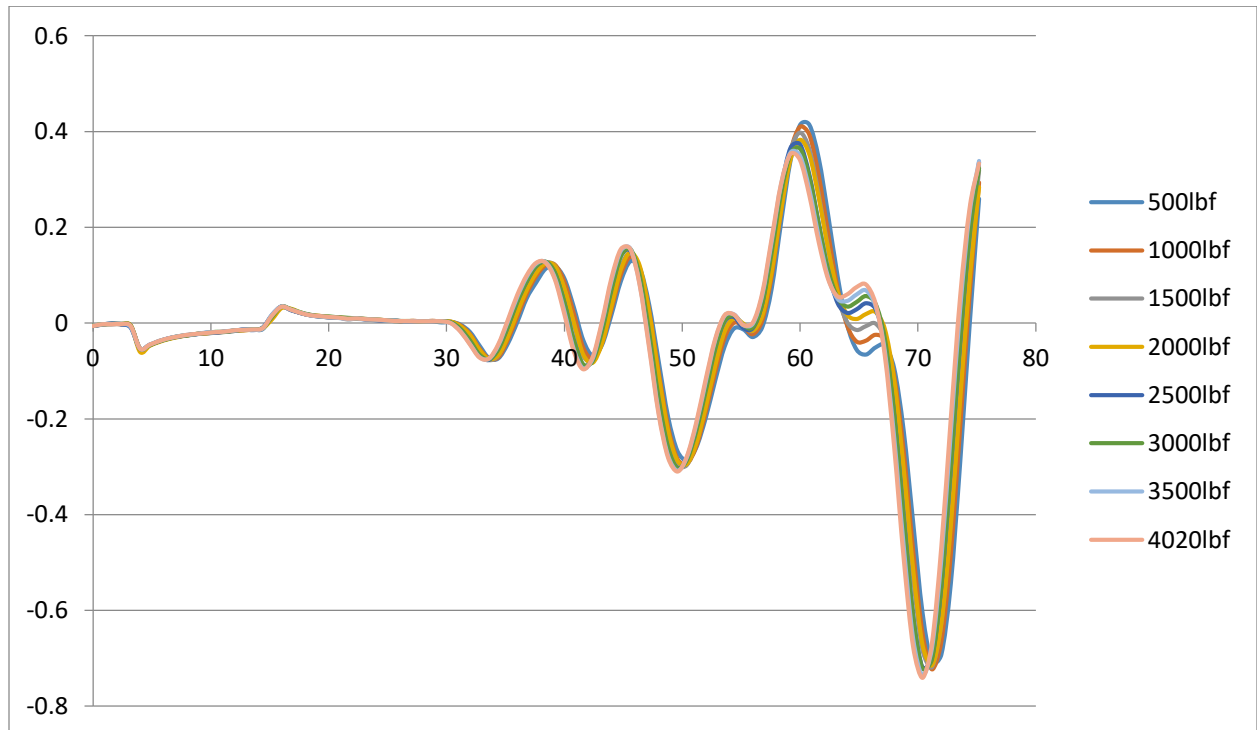**Figure 5.78** The 20MHz Vs waveform from core plug sample 4472.6.
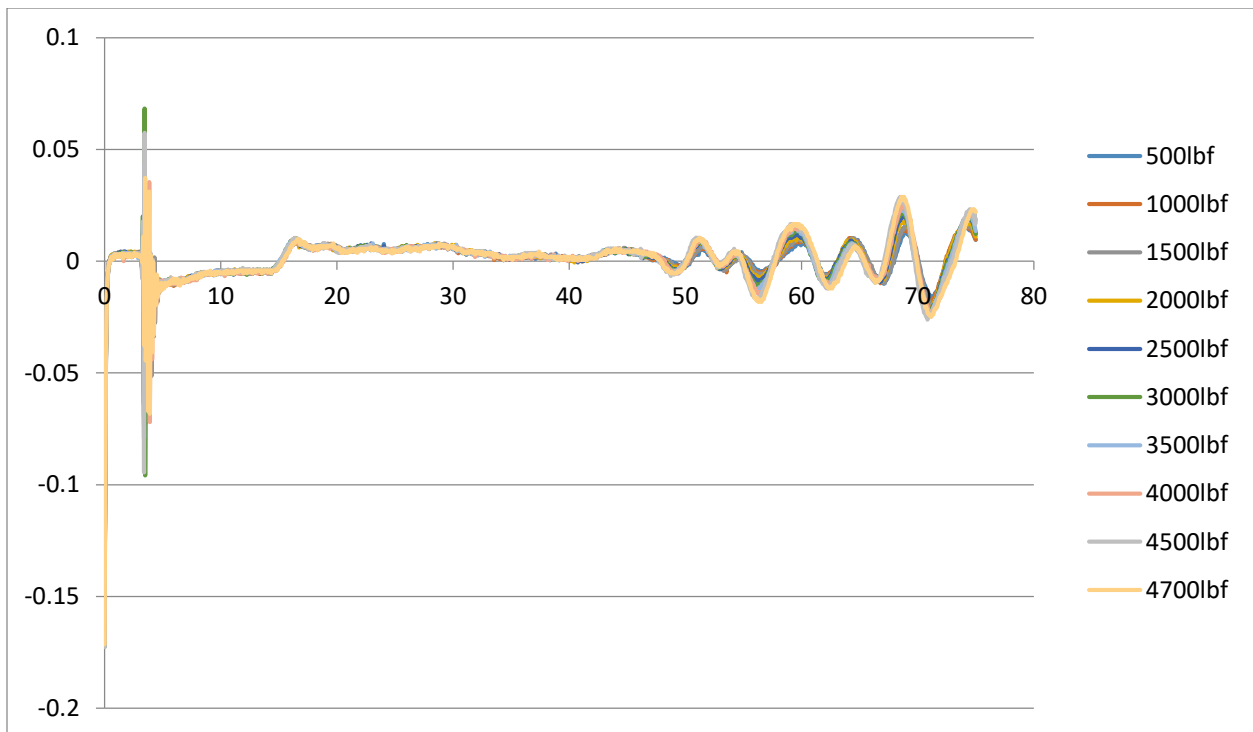
Figure 5.79 Core plug DA4472.6 S-wave first arrival 1.25MHz stacked waveforms.

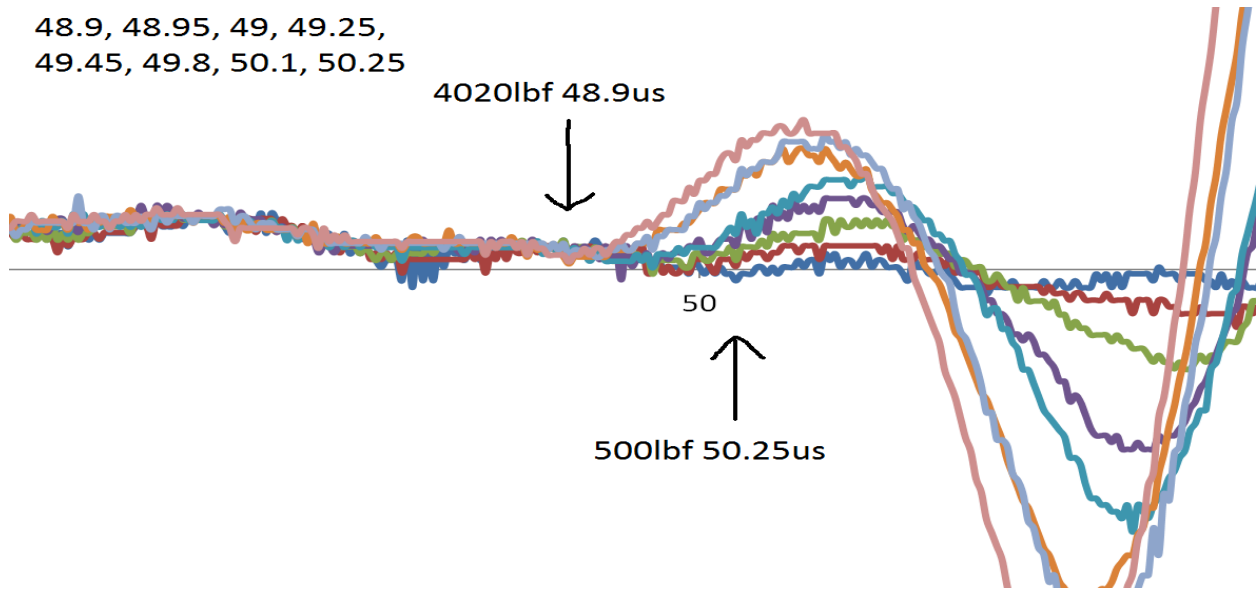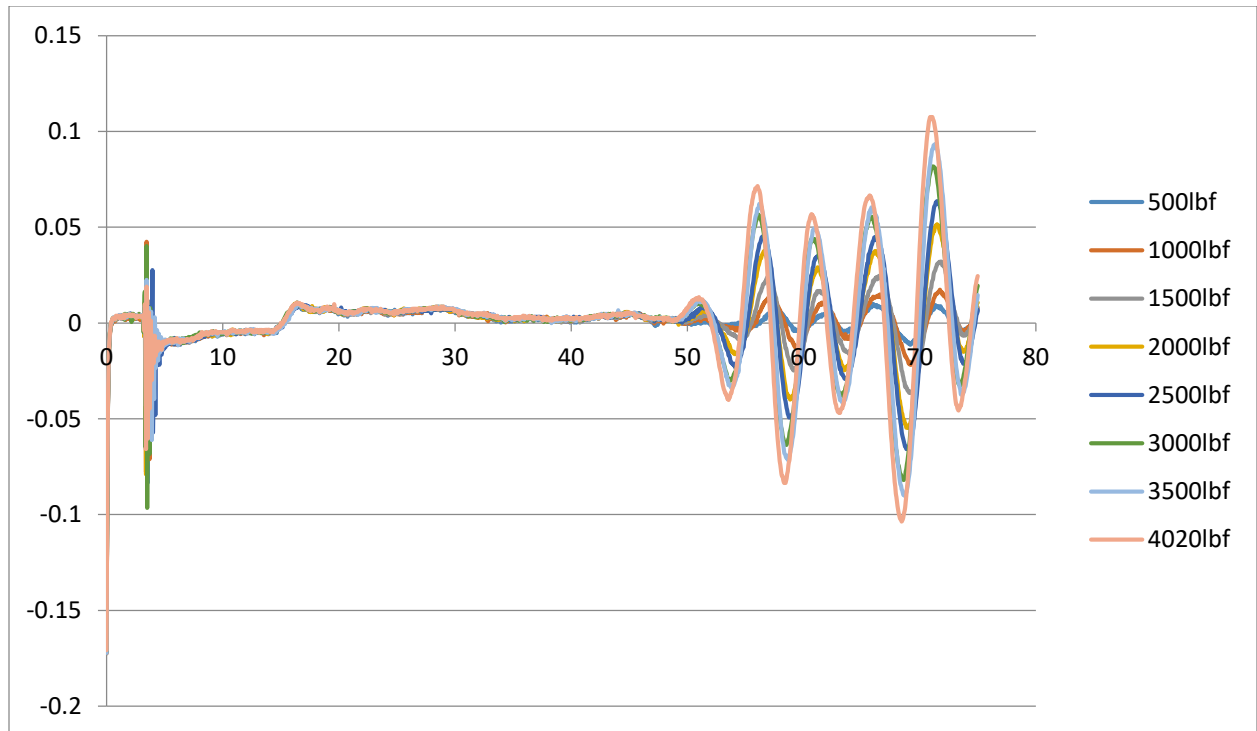Values at the top of the figure correspond to the first arrival times at each pressure tested.

46.75, 46.8, 46.85, 47,
47.55, 47.6, 48.4, 48.5,
48.6, 48.65

4700lbf 46.75us

500lbf 48.65us

40

50
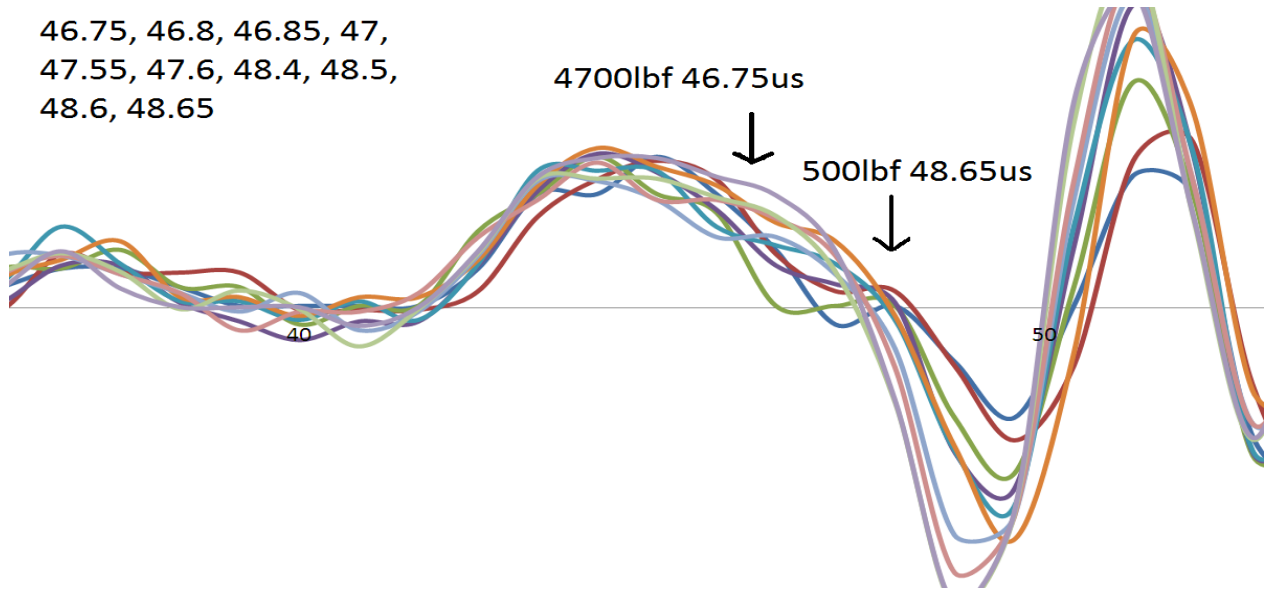
Figure 5.80 The 1.25MHz Vs waveform from core plug sample 4472.6.

500lbf
1000lbf
1500lbf
2000lbf
2500lbf
3000lbf
3500lbf
4000lbf
4500lbf
4700lbf
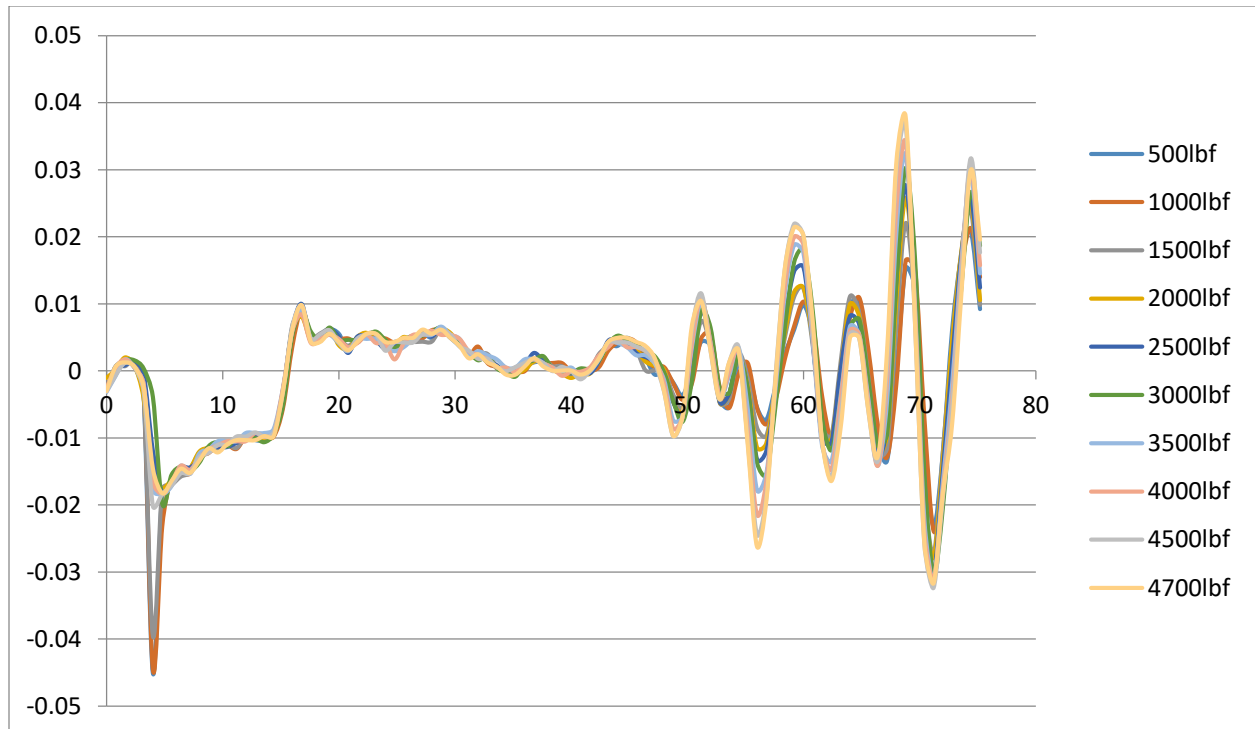
X-ray Diffraction

Collected X-ray diffraction data consists of, for each core plug, diffractograms, mineral count lists, and a pattern list of analyzed samples. Furthermore, table 5.17 shows XRD results compared between each core plug sample. This information was compiled and used as an input into the Gassmann fluid replacement modeling demonstrated in earlier chapters. An example of the diffractograms, lists, and patterns can be seen in figure 5.81 and tables 5.18 and 5.19 respectively, with the complete mineralogy datasets found in Appendix B.

Table 5.17 A composite of XRD-derived mineralogy data for all core plugs.

Core #	Total Counts	Dolomite Counts	% of total	Quartz Counts	% of total	Calcite Counts	% of total
3716.7	161364	92290	57	49471	30.6	19603	12.1
3716.8	106120	52708	49.7	39524	37.2	13888	13.1
3749.9	157264	74584	47.4	58344	37.1	24336	15.5
3829.4	111201	57805	51.9	53396	48.1	insignificant	0
3829.5	135224	79723	58.9	53396	48.1	insignificant	0
4300.3	203551	203551	100	insignificant	0	insignificant	0
4300.4	423770	378750	89.4	45020	10.6	insignificant	0
4472.6	245789	188839	76.8	56950	23.2	insignificant	0

Figure 5.81 Diffractogram for core plug sample DM3716.7.
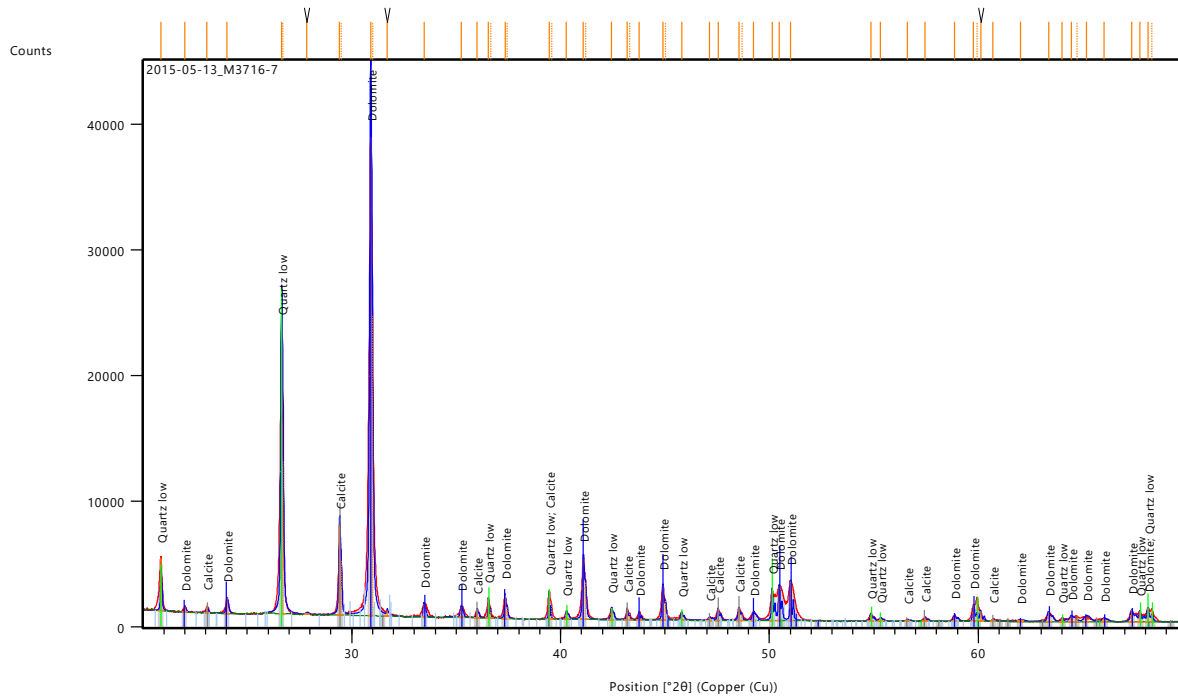
Table 5.18 Mineral count list for core plug sample DM3716.7.

Pos. [°2θ]	Height [cts]	FWHM Left [°2θ]	d-spacing [Å]	Rel. Int. [%]
20.8687	4197.24	0.0551	4.25677	11.02
22.0186	422.07	0.0827	4.03699	1.11
23.0683	559.19	0.0689	3.85562	1.47
24.0361	1223.27	0.1102	3.70252	3.21
26.6430	22569.74	0.0924	3.34310	59.26
26.7128	12106.51	0.0504	3.34281	31.79
27.8552	119.31	0.2016	3.20030	0.31
29.4211	7169.35	0.0840	3.03343	18.82
29.4962	4409.71	0.0336	3.03340	11.58
30.9020	38086.79	0.1092	2.89136	100.00
30.9937	23832.12	0.0588	2.89018	62.57
31.7030	447.62	0.0504	2.82011	1.18
33.4582	1079.64	0.0840	2.67607	2.83
35.2380	850.78	0.1008	2.54488	2.23
36.0075	675.36	0.0756	2.49224	1.77
36.5468	1575.95	0.0504	2.45669	4.14
36.6486	806.57	0.0588	2.45619	2.12
37.3474	1878.96	0.0756	2.40585	4.93
37.4412	993.51	0.0504	2.40599	2.61
39.4429	2229.04	0.0420	2.28272	5.85
39.5623	1273.98	0.0504	2.28176	3.34

40.2811	635.52	0.1008	2.23713	1.67
41.0919	4891.04	0.1008	2.19485	12.84
41.2042	2974.10	0.0672	2.19456	7.81
42.4415	935.71	0.1008	2.12812	2.46
43.1847	929.67	0.0672	2.09320	2.44
43.3133	533.64	0.0672	2.09247	1.40
43.7541	644.94	0.0588	2.06727	1.69
44.9047	2755.12	0.0924	2.01694	7.23
45.0227	1554.66	0.0672	2.01693	4.08
45.7929	608.95	0.1008	1.97986	1.60
47.1348	259.39	0.1008	1.92658	0.68
47.5387	939.41	0.0840	1.91115	2.47
48.5381	994.02	0.1008	1.87411	2.61
48.6854	578.38	0.0672	1.87343	1.52
49.2443	657.72	0.1344	1.84887	1.73
50.1267	2484.76	0.0756	1.81837	6.52
50.4661	2738.06	0.0840	1.80694	7.19
51.0060	3111.25	0.0588	1.78907	8.17
54.8616	586.80	0.1008	1.67210	1.54
55.3153	258.80	0.1344	1.65946	0.68
56.6130	150.82	0.1008	1.62446	0.40
57.4519	329.24	0.0840	1.60272	0.86
58.8645	508.36	0.1176	1.56758	1.33
59.7732	1310.17	0.1008	1.54590	3.44
59.9504	1865.05	0.0504	1.54558	4.90
60.1146	811.75	0.0840	1.53794	2.13
60.7051	197.29	0.1008	1.52438	0.52
62.0138	111.77	0.3360	1.49532	0.29
63.3717	770.41	0.1512	1.46651	2.02

Table 5.19 Mineral pattern list for core plug sample DM3716.7.

Visible	Ref. Code	Score	Compound Name	Displacement [°2Th.]	Scale Factor	Chemical Formula
*	98-017-1508	66	Dolomite	-0.070	0.955	C2 Ca1 Mg1 O6
*	98-003-1228	65	Quartz low	-0.008	0.574	O2 Si1
*	98-005-2151	65	Calcite	0.039	0.196	C1 Ca1 O3

Rock Physics Models

Gassmann

Results and data from the Gassmann fluid replacement model includes 1) a comparison between initial air humidified sample velocities with Gassmann model velocities (table 5.20, figure 5.82), 2) eight charts (figures 5.83- 5.90) which compare the Gassmann results with data of other published literature to see how well it fits, and 3) six charts (figures 5.91- 5.96) which compare Gassmann estimated Vp, Vs, bulk modulus, shear modulus, Poisson's ratio and Young's modulus to the corresponding *in situ* KGS 1-32 well log values, in order to determine accuracy and robustness of the model.

Although Gassmann predicts no change in the shear modulus (and thus shear velocity) with fluid substitutions, our study shows slight Vs deviations on the order of 1-2%. This unexpected behavior has occurred for other studies as well, including Baechle et al. (2005), Adam et al. (2006) and Clark et al. (1984); the term 'shear weakening effect' has been attributed to the accumulation of similar observations. Although this study's shear weakening effect is quite small, the effect has been known to be largest in dynamic measurements in carbonates with particular microstructures; higher Vp/Vs ratios have been attributed to this effect as well. A potential cause could include either rock frame strengthening or weakening as a response to fluid substitutions.

Carbonates with significant microporosity and complex pore structures generally exhibit low velocities at any given porosity amount, according to Weger et al. (2009). Also, for rocks with low porosities such as ours, estimated Gassmann P-wave velocities are known in some cases to differ substantially from measured values (Kahraman, 2007); particularly, dry-to-saturation effects have been known to exaggerate Vp values with low porosity samples when

compared to high porosity samples (Gregory, 1977), and soft rocks with compliant pores (Wang, 2001). These factors may be a cause of some of the variability in our Vp results. A more systematic analysis of porosity effects on velocity in carbonates can be found in Eberli (2003).

Furthermore, laboratory tests require competent core samples to conduct *in situ* pressure tests; these may not be representative of the lithology in that section of the formation, since macroscopic features such as vugs and joints would be excluded in core samples. Thus, variability in results may occur, as strength of core samples would be slightly higher than the average of the entire formation, and thus velocity measures would be slightly higher as well. Heterogeneities within individual core samples may also cause preferential high velocity pathways for ultrasonic waves, increasing velocity measurements in these cases (Adam and Batzle, 2007). Heterogeneities combined with patchy saturations within samples can lead to significant velocity dispersion, although additional research needs to be conducted in this regard (Ba et al., 2013).

Because $wavelength = \frac{velocity}{frequency}$, wavelengths on the order of 0.025cm are sampling the core plugs. Scattering of these waves by heterogeneities comparable in size or larger may cause a loss in wave energy, causing multiple reflections, resulting in lower moduli and thus velocities (Adam et al., 2006). Evidence for low wave energy was provided by the weak signals in the Ult 100 tests, and Gassmann predicted velocities in the Arbuckle samples are lower (sometimes significantly) than well log measurements; therefore, our Arbuckle samples may contain more heterogeneities than the Mississippian samples.

Permeability can also be an important aspect to consider. According to the whole core analysis by Weatherford on the KGS 1-32 core, permeability varied significantly in our samples: Kmax is 0.04md in samples 3716.7 and 3716.8, 0.13md in sample 3749.9, 0.03md in sample

3829.5, 9.57md in sample 3829.4, 0.24md in sample 4300.3, 2.94md in sample 4300.4, and 223.55md in sample 4472.6. Adam and Batzle (2007) concluded that dispersion was positively correlated with permeability, suggesting dispersion in our samples is greatest in samples 4300.4, 4472.6, 3829.4 and 4300.3.

A likely solution for many potential discrepancies and anomalies in the results is to collect and analyze many more samples to find better averages. Scaling up in this way is a well-known method to increase accuracy of results in laboratory studies such as this one.

Table 5.20 A comparison between initial dry-rock and Gassmann brine-saturated velocities at 20MHz and 1.25MHz.

	Dry rock 20MHz Vp (m/s)	Dry rock 20MHz Vs (m/s)	Gassmann 20MHz Vp (m/s)	Gassmann 20MHz Vs (m/s)
3716.7	5194	3199	5528.3	3170.9
3716.8	5104	2848	5301.5	2818.3
3749.9	5337	3047	5594.5	3029.4
3829.4	4432	2587	4812.2	2557.7
3829.5	4488	2584	4923.4	2559.3
4300.3	5028	2774	5384.3	2756.8
4300.4	4792	2621	5124.5	2588.9
4472.6	5657	2800	5785.4	2784.1
	Dry rock 1.25MHz Vp (m/s)	Dry rock 1.25MHz Vs (m/s)	Gassmann 1.25MHz Vp (m/s)	Gassmann 1.25MHz Vs (m/s)
3716.7	5088	2924	5382.5	2898.4
3716.8	4928	2801	5189.9	2771.8
3749.9	5103	3000	5477.6	2982.7
3829.4	4304	2555	4740.9	2526.1
3829.5	4378	2520	4852.4	2495.9
4300.3	4888	2747	5308.5	2736.5
4300.4	4628	2617	5029.4	2584.9
4472.6	5677	2843	5808	2826.9

Figure 5.82 Graphical representations of the same information found in table 5.20.
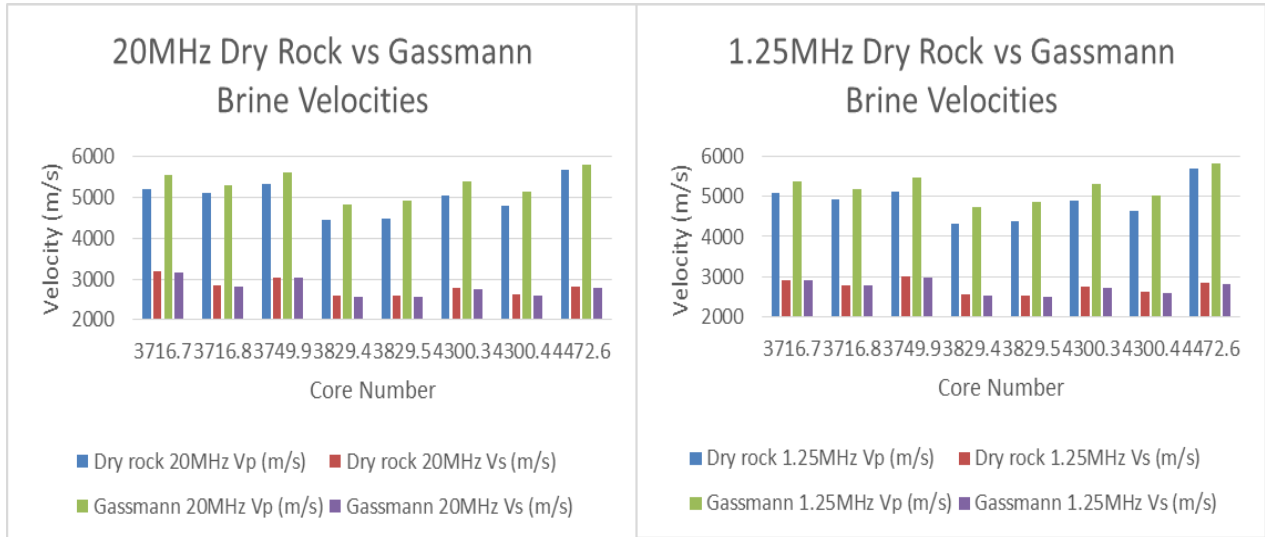
Gardner's relations, an empirical model, was used to compare this study's ultrasonic Gassmann results to the Gardner et al. (1974) log data and associated relations. Higher velocity and higher bulk density are often correlated in rocks, although different rock types have different density-velocity relationships. The dolomite and limestone relationships, represented as curves in the relations, are used to validate the Gassmann technique using ultrasonic frequencies at our study site and with our study characteristics. The Gardner et al. (1974) relations are in the form $p_b = dV_p^f$, where p_b is bulk density ($\frac{g}{cc}$), V_p is the compressional wave velocity ($\frac{km}{s}$), and where f and d are constants which change depending on the lithology tested. This study's Gassmann results (table 5.21) were superimposed over a chart showing Gardner's relations (figure 5.83), and plots between the Gardner limestone, dolomite, and shale lithology lines. This shows an accurate fit to our carbonate data.

Table 5.21 This study's 20MHz and 1.25MHz Gassmann brine saturated Vp, KGS 1-32

log Vp results and KGS 1-32 bulk density values for each core plug sample and/or the

corresponding depth. Data is averaged in figure 5.83.

	20MHz Vp (ft/s)	1.25MHz Vp (ft/s)	Log Vp (ft/s)	Bulk Density (g/cc)
3716.7	18137.73	17659.05	16285.76	2.621
3716.8	17393.74	17026.9	16233.27	2.626
3749.9	18354.66	17971.19	16655.84	2.6319
3829.4	15788.25	15554.36	15187.66	2.61
3829.5	16152.8	15919.8	15217.8	2.5953
4300.3	17664.99	17416.31	17848.57	2.72
4300.4	16812.59	16500.59	18498.36	2.7415
4772.6	18980.97	19055.12	18975.7	2.6605

Figure 5.83 Brine saturated bulk density vs brine saturated Vp, with Gardner's relations

plotted as lines corresponding to various lithologies. Superimposed are this study's averaged

Gassmann ultrasonic data and the KGS 1-32 well log data, represented as a black triangle for the

Arbuckle formation and a black circle for the Mississippian formation. Image modified from

Simm and Bacon (2014).
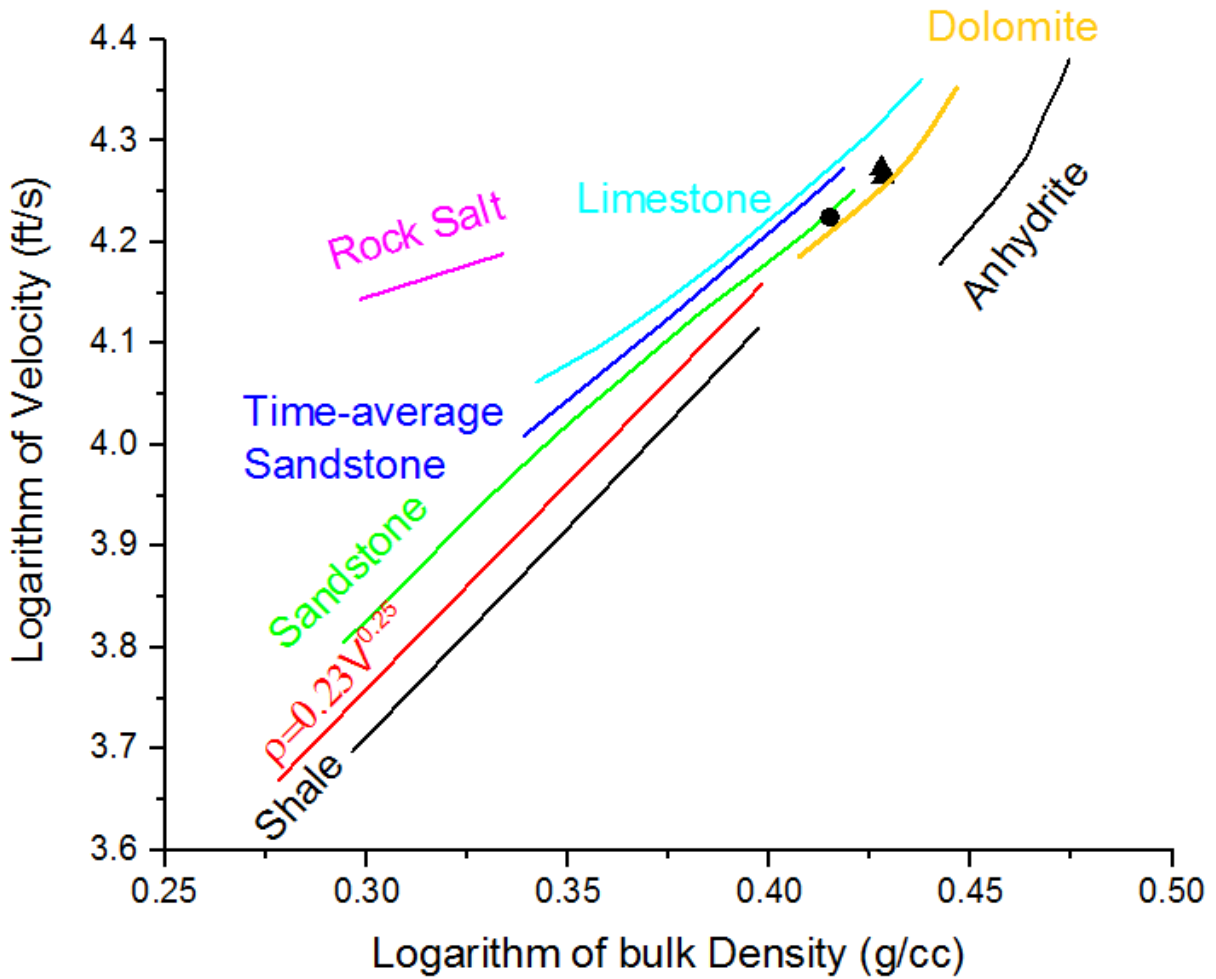
The time average equation from Wyllie et al. (1958) is a derived relationship comparing velocity and porosity, and used for sandstones and limestones. The time average equation is $t = \Phi t_{fl} + (1 - \Phi)t_o$, where t is the interval transit time through the measured rock, t_{fl} is the interval transit time through the fluid, t_o is the interval transit time through the mineral matrix, and Φ is porosity. Carbonates are known to fit the model well due to mineralogy and associated stiffness of this rock type. Data from this study in table 5.22 was superimposed over a Wyllie's time average plot including data from other authors for comparison; results show our core plug

samples have a good fit to other data points, and show porosity to likely be either microporosity, densely cemented porosity, or interparticle/ crystalline porosity.

Both figures 5.84 and 5.90 give porosity type information, suggesting pores in our carbonate samples are mostly elongated, densely cemented, microporosity, and crystalline/ interparticle. Wang and Nur (1992) and Xu and Payne (2009) suggest that the Gassmann equations may be more applicable in carbonates with homogeneous pore systems in both type and spatial distribution, with round shaped pores considered more applicable. Because our core plug data points cluster relatively well in both figures, and with the exception of one core plug sample all plot relatively close to the 'reference line' in figure 5.90, we might initially be able to determine that the Gassmann equations are not necessarily applicable or not applicable to our subsurface formations of interest. Gassmann may not be considered applicable where fractures are common because in these situations, pore fluid may not have time to reach equilibrium between passing measurement waves. Additionally, Xu and Payne (2009) found that Gassmann tends to underestimate Vp in carbonate samples with microcracks, with large differences between 100% rounded and 100% crack-shaped pores, again, because the small microcrack size creates low local permeability and restricts the ability of the pore pressure to relax within a half cycle of the measurement wave, violating a fundamental Gassmann assumption. However, it is also known that at high pressures, cracks and microcracks are known to close, thus theoretically allowing the Gassmann model to perform more accurately; Wang (2000) demonstrated in ultrasonic laboratory carbonate samples that Gassmann was most accurate at predicting velocities at the highest measured pressures. Porosity amount and also type are determined to be among the most important P- and S-wave velocity determinants in carbonates, with velocities in rock specimens with equal porosity known to vary by 2,500m/s, caused mostly by pore type and

not mineralogy (as in siliciclastics) (Eberli et al., 2003). Thus these are important aspects to hone in on for interpreting this study's results; future studies may need to conduct an analysis on fluid substitution models which take into account pore type.

Table 5.22 This study's 20MHz and 1.25MHz Gassmann brine saturated Vp at a pressure of 8MPa results, and porosity data averaged from the whole core Weatherford analysis and the KGS 1-32 neutron porosity well log, for each core plug sample and/or the corresponding depth. Data are averaged in figure 5.84.

	20MHz Vp (m/s)	1.25MHz Vp (m/s)	Porosity (%)
3716.7	5508.2	5367.6	7.1
3716.8	5205.6	5121.5	7.1
3749.9	5562.7	5440.7	3.03
3829.4	4722.7	4664.6	7.7
3829.5	4869.2	4818.9	7.7
4300.3	5087.2	5045.3	6.43
4300.4	4793.2	4771.2	6.1
4772.6	5647.2	5530.1	4.05

Figure 5.84 Porosity vs Vp of brine saturated carbonates at 8MPa effective pressure and various pore types. Colored data points are those from Eberli et al. (2003) with yellow circles indicating microporosity, dark green circles indicating interparticle/ crystalline porosity, red circles indicating moldic porosity, light green indicating densely cemented porosity, and purple circles indicating intraframe porosity. The black line is the time average equation. Superimposed are this study's averaged Gassmann ultrasonic data; plotted black triangles represent the Arbuckle formation and plotted black circles represent the Mississippian formation. Image modified from Simm and Bacon (2014).
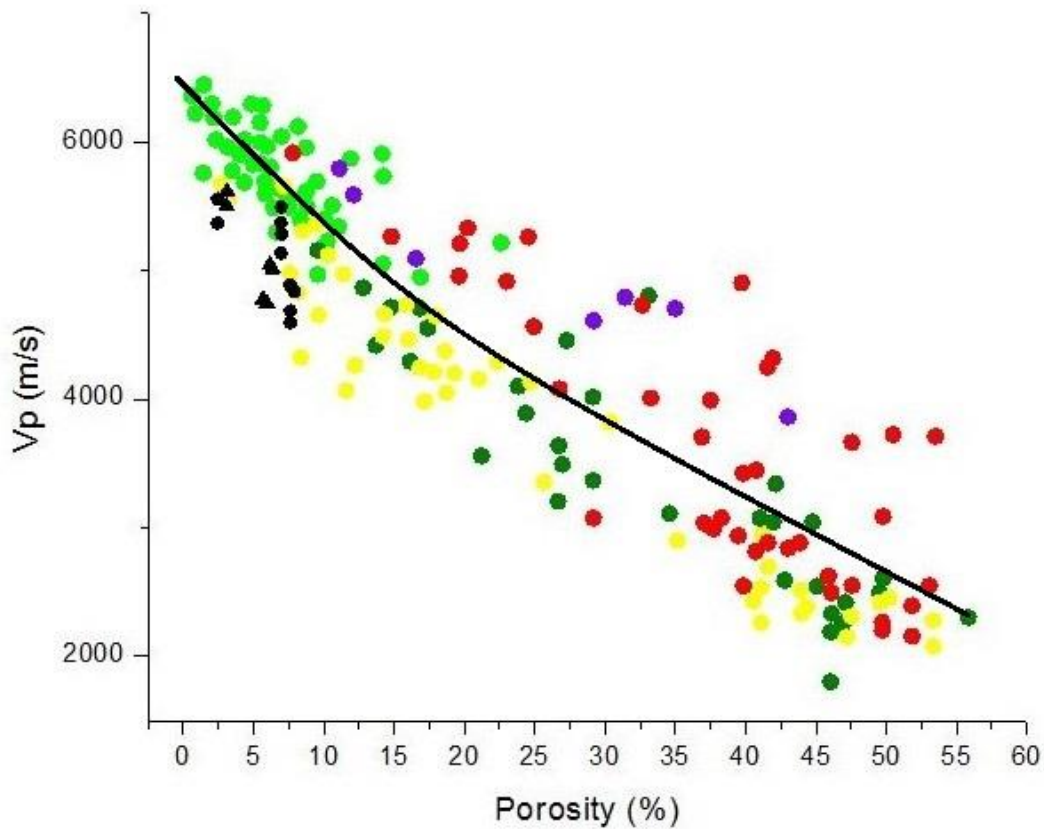
Porosity values between the whole core Weatherford analysis and the KGS 1-32 well were averaged in hopes for a more accurate value, as Grochau and Gurevich (2009) suggest that log porosities have been known to be systematically higher than other forms of measurement, potentially due to fractures created near the well bore area of log porosity measurement.

For situations where dipole sonic shear wave log data aren't available, the Greenberg-Castagna (Greenberg and Castagna, 1992) empirical relations may provide accurate predictions based on available Vp well log data. These relations showed a large lithology-dependent, mostly pressure independent correlation between Vs and Vp. Four main trends found for common lithologies include 1) $sandstone\ V_s = 0.8042V_p - 0.8559$, 2) $limestone\ V_s = 0.0551V_p^2 +$

$1.016V_p - 1.0305$, 3) $dolomite\ V_s = 0.58321V_p - 0.07775$, and 4) $shale\ V_s = 0.7697V_p -$

0.86735, where V_s is shear wave velocity and V_p is compressional wave velocity. Gassmann

fluid replacement results from this study were superimposed over the Greenberg-Castagna

relations in figure 5.85 using data from table 5.23, and results show good agreement. All data

points are confined between the limestone and dolomite Greenberg-Castagna lines. Similar

results can be seen in figure 5.86, another plot representing the Greenberg-Castagna relations.

This is an indication that the Gassmann equations may be valid at our study site despite using

ultrasonic frequencies.

Table 5.23 This study's 20MHz and 1.25MHz Gassmann brine saturated Vp and Vs

results, and the KGS 1-32 Vp and Vs log data for each core plug sample and/or corresponding

depth. Log Vs fast and Vs slow data are averaged. Data is averaged in figure 5.85.

	20MHz Vp (m/s)	1.25MHz Vp (m/s)	Log Vp (m/s)	20MHz Vs (m/s)	1.25MHz Vs (m/s)	Log Vs (m/s)
3716.7	5528.38	5382.4	4963.9	3170.98	2898.4	2771.5
3716.8	5301.53	5189.8	4947.9	2818.29	2771.7	2778.4
3749.9	5594.5	5477.62	5076.7	3029.45	2982.7	3070.5
3829.4	4812.26	4740.97	4629.2	2557.69	2526.05	2603.4
3829.5	4923.37	4852.37	4638.4	2559.3	2495.92	2618.2
4300.3	5384.29	5308.5	5440.3	2756.8	2736.5	3116.5
4300.4	5124.4	5029.4	5638.3	2588.9	2584.97	3133.15
4772.6	5785.4	5808.02	5783.8	2784.1	2826.93	3212.3

Figure 5.85 Brine saturated Vs vs Vp as seen in relation to the Greenberg-Castagna

lithology trends. The black line is limestone, purple is dolomite, orange is shale, and grey

represents sand. Superimposed are this study's averaged Gassmann ultrasonic and KGS 1-32

well log data. Plotted black triangles represent the Arbuckle formation, and plotted black circles

represent the Mississippian formation. Image modified from Simm and Bacon (2014).
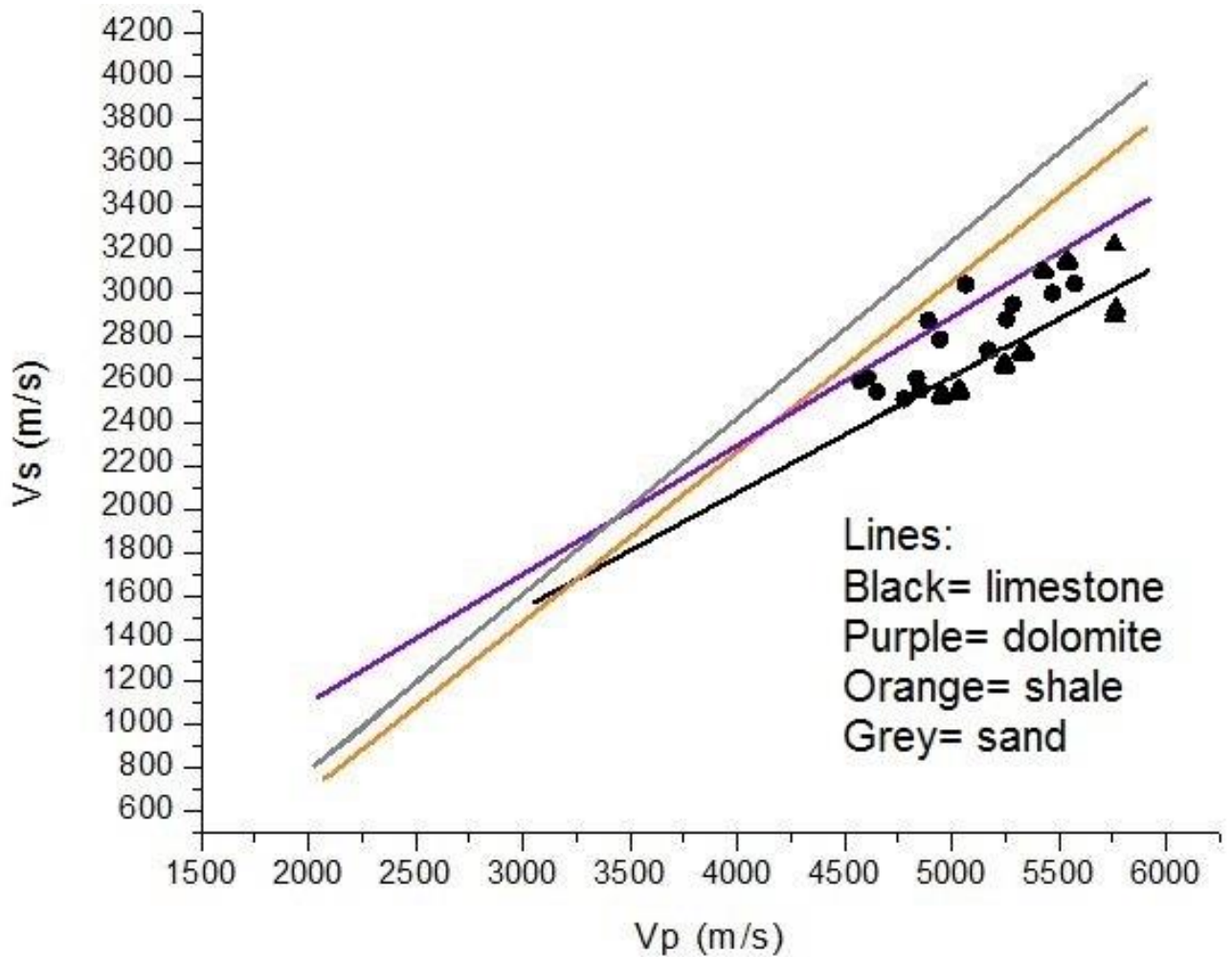
Table 5.24 This study's 20MHz and 1.25MHz Gassmann brine saturated Vp and Vs results, and the KGS 1-32 log Vp and Vs data for each core plug sample and/or corresponding depth. Log Vs data is averaged between fast and slow shear. Data is averaged in figure 5.86.

	20MHz Vp (m/s)	1.25MHz Vp (m/s)	Log Vp (m/s)	20MHz Vs (m/s)	1.25MHz Vs (m/s)	Log Vs (m/s)
3716.7	5528.38	5382.4	4963.9	3170.98	2898.4	2771.5
3716.8	5301.53	5189.8	4947.9	2818.29	2771.7	2778.4
3749.9	5594.5	5477.62	5076.7	3029.45	2982.7	3070.5
3829.4	4812.26	4740.97	4629.2	2557.69	2526.05	2603.4
3829.5	4923.37	4852.37	4638.4	2559.3	2495.92	2618.2
4300.3	5384.29	5308.5	5440.3	2756.8	2736.5	3116.5
4300.4	5124.4	5029.4	5638.3	2588.9	2584.97	3133.15
4772.6	5785.4	5808.02	5783.8	2784.1	2826.93	3212.3

Figure 5.86 Brine saturated Vs vs Vp data, with the Castagna-Greenberg (1992) dolomite and limestone trends, and with original data points plotted from Rafavich et al. (1984) along with the North Sea as brine saturated carbonates and chalks. The upper grey line represents the Castagna limestone, and the lower purple line represents the Castagna dolomite. White circles indicate chalk data from the North Sea, and dark green circles represent dolomite data from Rafavich et al. (1984). Superimposed are this study's averaged Gassmann ultrasonic and KGS 1-32 well log data. Plotted black triangles represent the Arbuckle formation, and plotted black circles represent the Mississippian formation. Image modified from Simm and Bacon (2014).
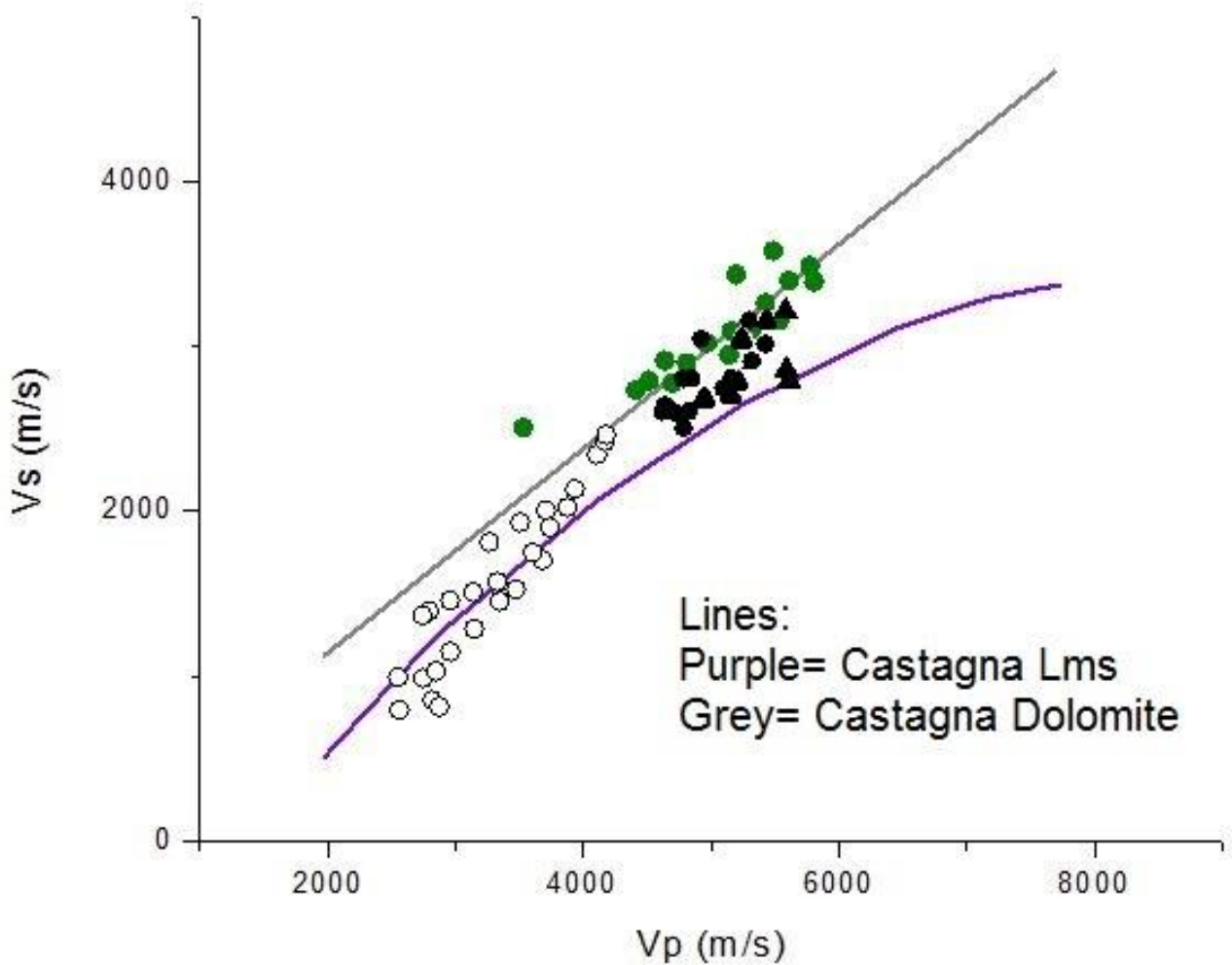
This study's Gassmann results are also in good agreement with data plotted from Rafavich et al. (1984) in figures 5.87 and 5.88, where porosity is cross plotted against dry rock bulk modulus and shear modulus respectively. These comparisons again indicate the Gassmann equations may be valid at our study site despite using ultrasonic frequencies.

Table 5.25 This study's 20MHz and 1.25MHz Gassmann dry bulk modulus results (taken at *in situ* pressures), and porosity data averaged from the KGS 1-32 neutron porosity log and the Weatherford whole core analysis for each core plug sample and/or corresponding depth. Data is averaged in figure 5.87.

	20MHz Kd (Gpa)	1.25MHz Kd (Gpa)	Porosity (%)
3716.7	35.065	38.1	6.86
3716.8	39.613	35.94	7.12
3749.9	42.99	37.48	2.93
3829.4	27.76	25.4	8.01
3829.5	29.44	28.03	7.72
4300.3	40.11	36.92	6.34
4300.4	36.44	32.44	6.12
4772.6	58.39	58.13	4.05

Figure 5.87 Dry bulk modulus (Kd) vs porosity for carbonates, with original data plotted from Rafavich et al. (1984) and the North Sea. Original white data points represent chalks from the North Sea, original light green data points represent dolomite data from Rafavich et al. (1984), yellow data points represent anhydrite data from Rafavich et al. (1984), and pink data points represent limestone data from Rafavich et al. (1984). Superimposed are this study's averaged Gassmann ultrasonic data. Plotted black triangles represent the Arbuckle formation, and plotted black circles represent the Mississippian formation. Image modified from Simm and Bacon (2014).
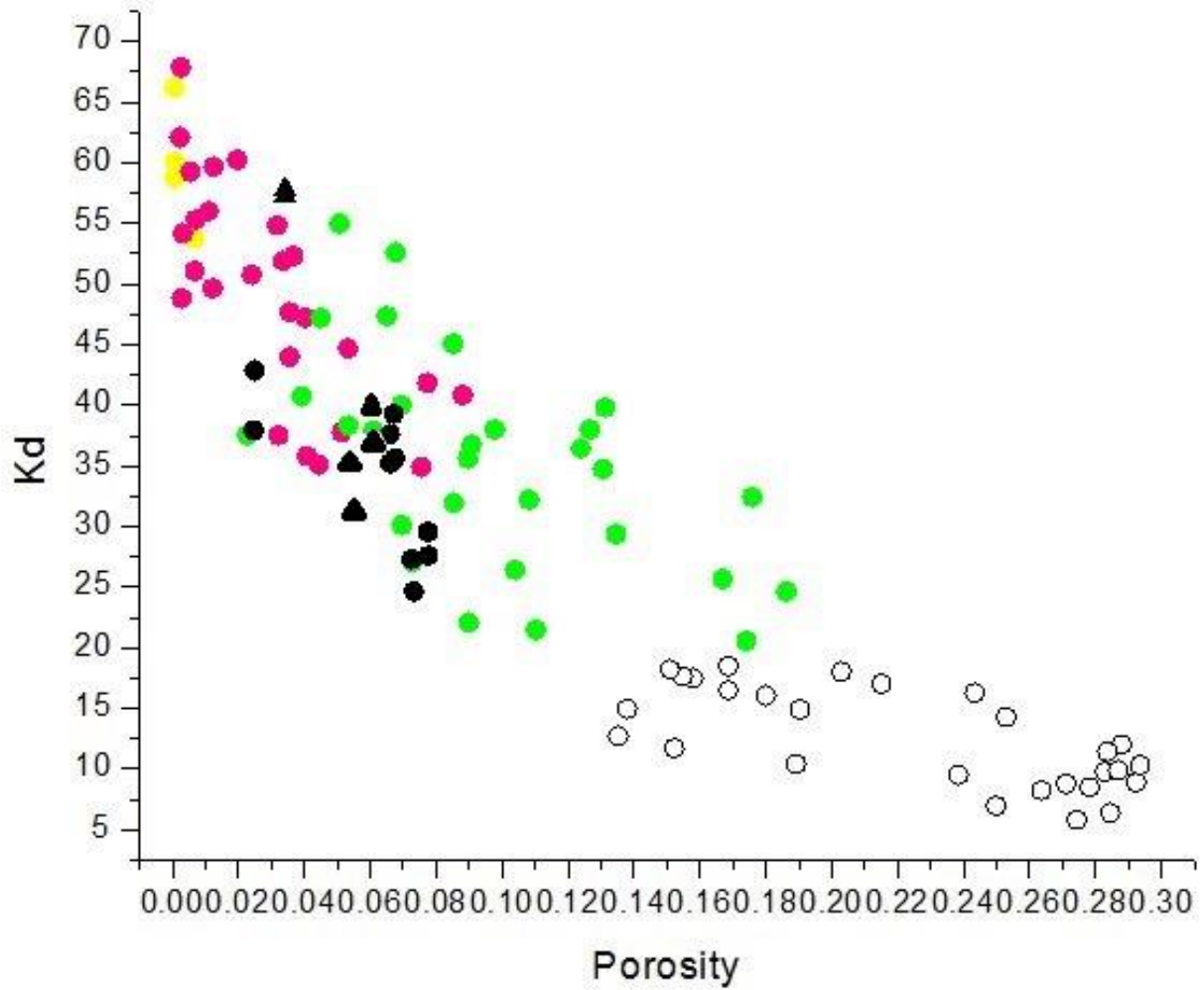
Table 5.26 This study's 20MHz and 1.25MHz Gassmann shear modulus results at *in situ* pressures, and porosity data averaged from the KGS 1-32 neutron porosity log and the Weatherford whole core analysis for each core plug sample and/or corresponding depth. Data is averaged in figure 5.88.

	20MHz u (Gpa)	1.25MHz u (Gpa)	Porosity (%)
3716.7	26.9	22.48	6.86
3716.8	21.08	20.39	7.12
3749.9	24.78	24.03	2.93
3829.4	17.33	16.91	8.01
3829.5	17.49	16.64	7.72
4300.3	20.54	20.15	6.34
4300.4	18.13	18.08	6.12
4772.6	21.24	21.9	4.05

Figure 5.88 Shear modulus (u) vs porosity for carbonates, with original data plotted from Rafavich et al. (1984) and the North Sea. Original white data points represent chalks from the North Sea, original dark green data points represent dolomite data from Rafavich et al. (1984), original pink data points represent limestone data from Rafavich et al. (1984), and original yellow data points represent anhydrite data from Rafavich et al. (1984). Superimposed are this study's averaged Gassmann ultrasonic data. Plotted black triangles represent the Arbuckle formation, and plotted black circles represent the Mississippian formation. Image modified from Simm and Bacon (2014).
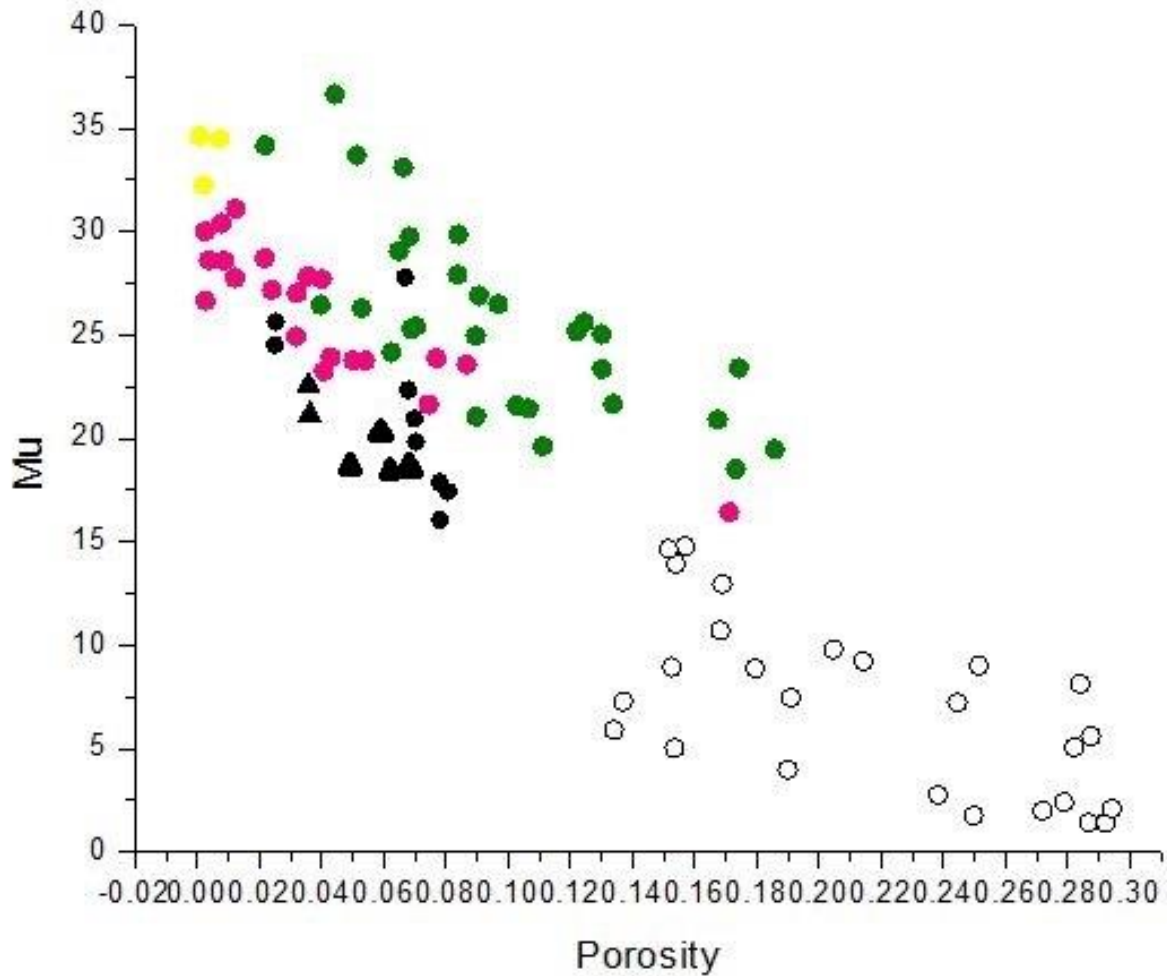
Inclusion models imagine rocks as elastic solids containing inclusions (pores), and can relate acoustic velocities to porosity including pore aspect ratios. The Xu-Payne model (Xu and Payne, 2009) is an inclusion model which splits porosity into clay-related, interparticle, microcrack (low aspect ratio), and stiff/ rounded/ moldic or vuggy types. From porosity amount and Vp data, the type of porosity is predicted. Data from this study's Gassmann results found in table 5.28 were superimposed over a chart representing the Xu-Payne model (figure 5.90). Results show every core plug lying below the 'reference line,' indicating low aspect ratio pores

similar to the shape of cracks. Core plug sample 3749.9 lies the closest to the '100% crack' line, indicating that its pores have the lowest aspect ratio of this study's samples.

Table 5.27 This study's 20MHz and 1.25MHz Gassmann brine saturated Vp results, the KGS 1-32 log Vp data, and porosity data averaged from the KGS 1-32 neutron porosity log and the Weatherford whole core analysis for each core plug sample and/or corresponding depth. Data is averaged in figure 5.89.

	20MHz Vp (km/s)	1.25MHz Vp (km/s)	Log Vp (km/s)	Porosity (%)
3716.7	5.528	5.38	4.964	6.86
3716.8	5.301	5.19	4.948	7.12
3749.9	5.595	5.48	5.07	2.93
3829.4	4.81	4.74	4.63	8.01
3829.5	4.92	4.85	4.64	7.72
4300.3	5.38	5.31	5.44	6.34
4300.4	5.12	5.03	5.64	6.12
4772.6	5.79	5.81	5.78	4.05

Figure 5.89 Brine saturated carbonate Vp vs porosity with reference lines of various aspect ratios of pores, indicating different pore types, as derived from Xu and Payne (2009). Pore shapes below the reference line are non-circular, and mostly resemble shapes similar to cracks. Superimposed are this study's averaged Gassmann ultrasonic and the KGS 1-32 well log data. Plotted black triangles represent the Arbuckle formation, and plotted black circles represent the Mississippian formation. Image modified from Simm and Bacon (2014).

$\alpha_{Ref}=0.15, \alpha_{Crack}=0.02, \alpha_{StiffPore}=0.8$
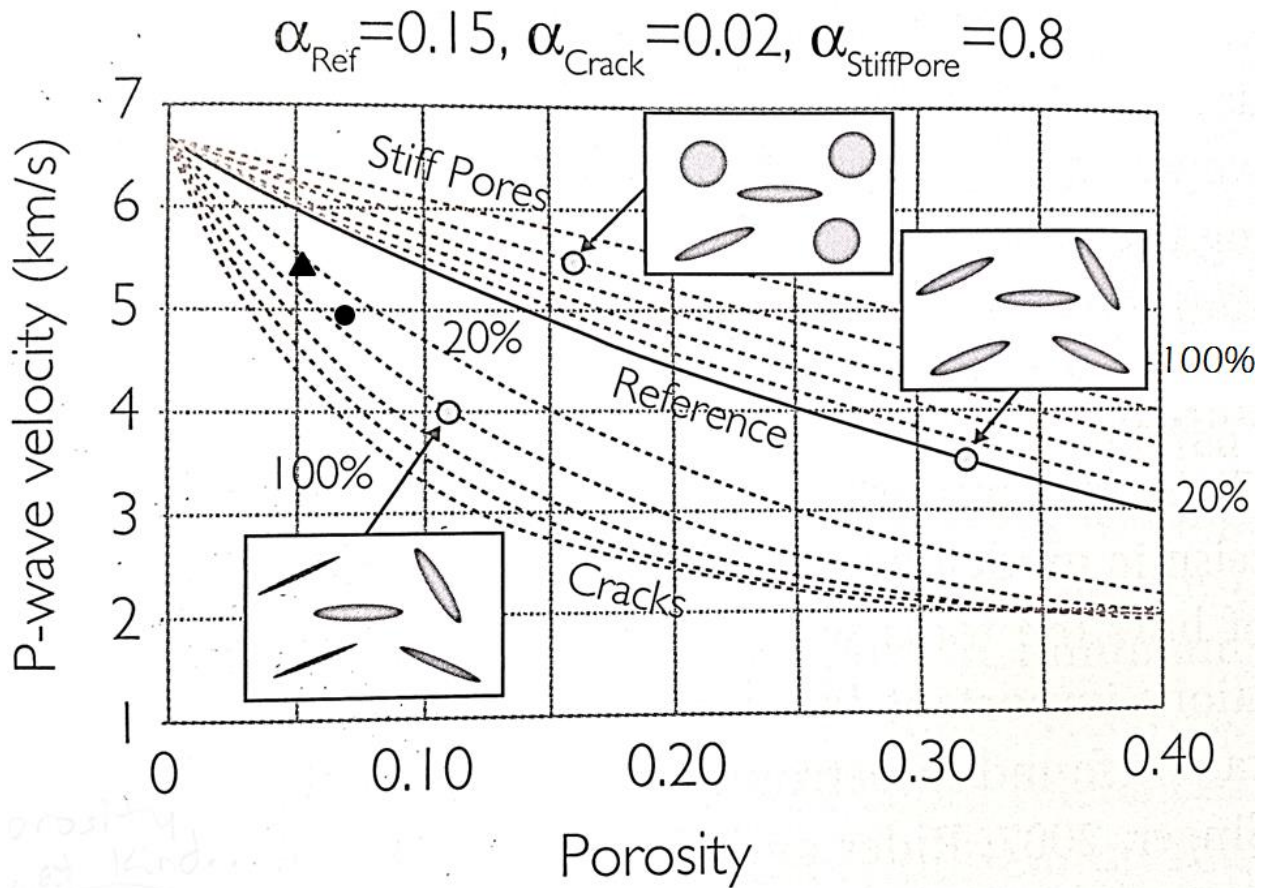
To further test the validity of the Gassmann fluid replacement model at our study site using ultrasonic frequencies, Gassmann Vp, Vs, bulk modulus, shear modulus, Poisson's ratio and Young's modulus values were directly compared to identical *in situ* KGS 1-32 well log data. Figure 5.90 shows an overestimation of Vp by Gassmann in the Mississippian by about $300\frac{m}{s}$, and an underestimation in the Arbuckle by about $200\frac{m}{s}$. Figure 5.91 shows Gassmann predicting Vs perfectly for Mississippian samples, but underestimating Vs in the Arbuckle by $400\text{-}500\frac{m}{s}$. Figure 5.92 indicates an overestimation by the Gassmann technique in Poisson's ratio for both the Mississippian and Arbuckle samples, although the Mississippian values are in better agreement, and specifically the Mississippian data points comparing the log Poisson's ratio

calculated with fast shear value and Gassmann calculated using 1.25MH, or the log Poisson's

ratio calculated with the slow shear value and Gassmann calculated using 20MHz; here,

Gassmann Poisson's ratio values were only overestimated by 0.2. Figure 5.93, comparing

Gassmann estimated and log shear modulus, mimics almost exactly the Vs comparisons. The

bulk modulus was compared in figure 5.94; Gassmann overestimated both Mississippian and

Arbuckle core plug values, although the Arbuckle in this case was most closely representative of

log values. Specifically, the points which were closest to equal were with the log bulk modulus

calculated using the slow shear log value compared to both 1.25MHz and 20MHz Gassmann

results; here Gassmann only overestimated the bulk modulus by 1-3Gpa. Finally, Young's

modulus was compared in figure 5.95. Oddly, this comparison greatly resembles both those of

Vs and the shear modulus, with only a slight overestimation of Gassmann values for about half

of the Mississippian values. From this analysis, it can be preliminarily remarked that Gassmann

appears best to predict Mississippian rather than Arbuckle rock properties at our site, and it does

a particularly good job in its predictions for Vs, shear modulus, and Young's modulus.

Both 'fast' and 'slow' shear waves exist in the KGS 1-32 well log measurements because

the rock medium in this area is anisotropic. Anisotropy is when a given value (such as velocity)

differs in a predictable way due to the direction in which that value is measured. For instance, a

velocity wave will travel at the same speed regardless of which direction through a material that

has perfectly randomly oriented constituents which make it up. However, if that same velocity

wave were to travel through a shale formation showing highly preferential orientation of mineral

alignment (parallel to the compressional force of the overburden), it would have different

velocities depending on which angle it intercepted that shale. This anisotropy causes what's

known as shear wave splitting, or seismic birefringence, where the shear wave splits into two

polarized shear waves, one moving faster than the other. Oftentimes shear wave splitting is a first

indication that anisotropy in rocks exist, and it can also provide fracture density information. In

order to determine the most accurate ultrasonic velocities of anisotropic specimens, traditionally

core plugs are drilled from the original core in the direction with the most anisotropic

characteristics in that core (Lin, 1985). Our core samples were drilled perpendicular to the long

axis of the core.

Figure 5.90 Ultrasonic brine-saturated Gassmann Vp vs *in situ* log Vp in the

Mississippian and Arbuckle formations.
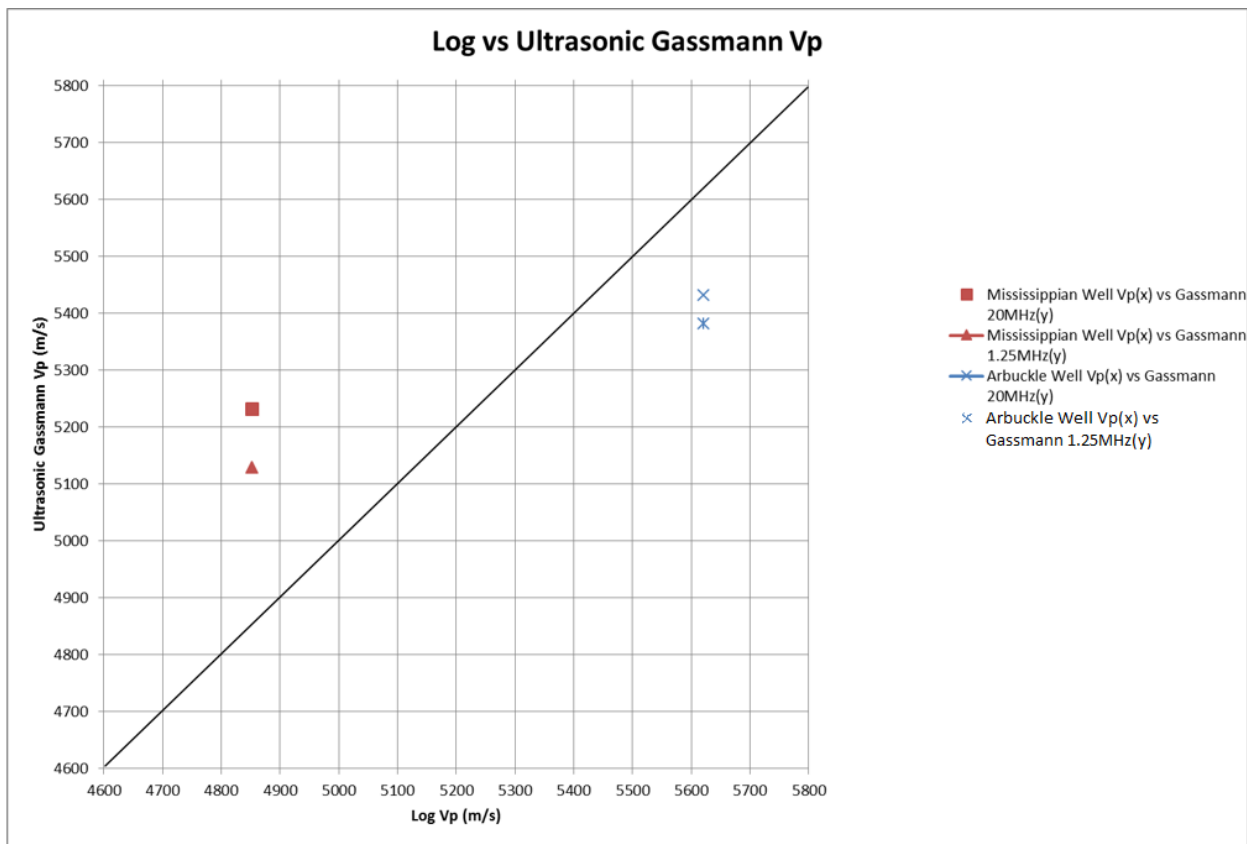
Figure 5.91 Ultrasonic brine-saturated Gassmann Vs vs *in situ* log Vs in the Mississippian and Arbuckle formations. Fast shear and slow shear values were analyzed and compared separately.
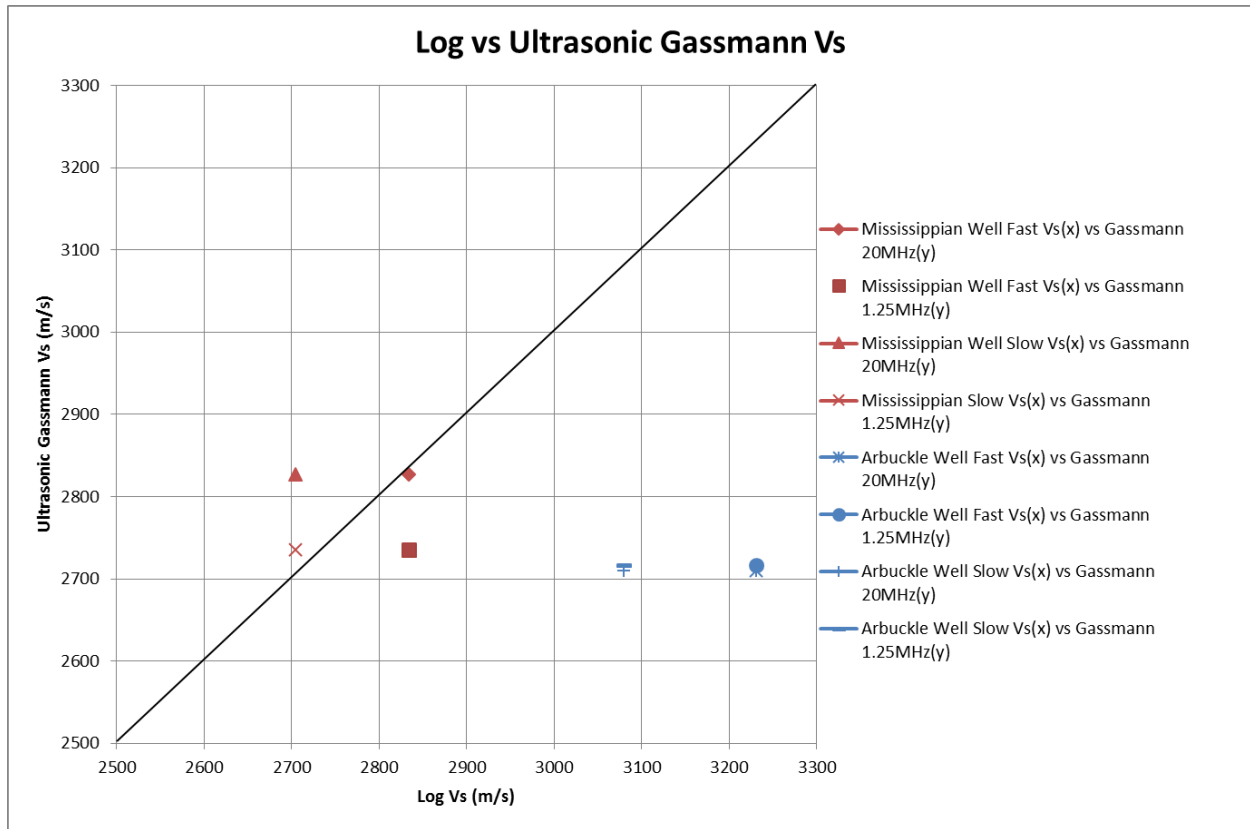
Figure 5.92 Ultrasonic brine-saturated Gassmann Poisson's ratio (sigma) vs *in situ* log Poisson's ratio in the Mississippian and Arbuckle formations. The given log 'VPVS' Poisson's ratio value was converted and used in calculations for separate analysis and comparison, along with manually-calculated Poisson's ratios using both fast shear and slow shear log values.
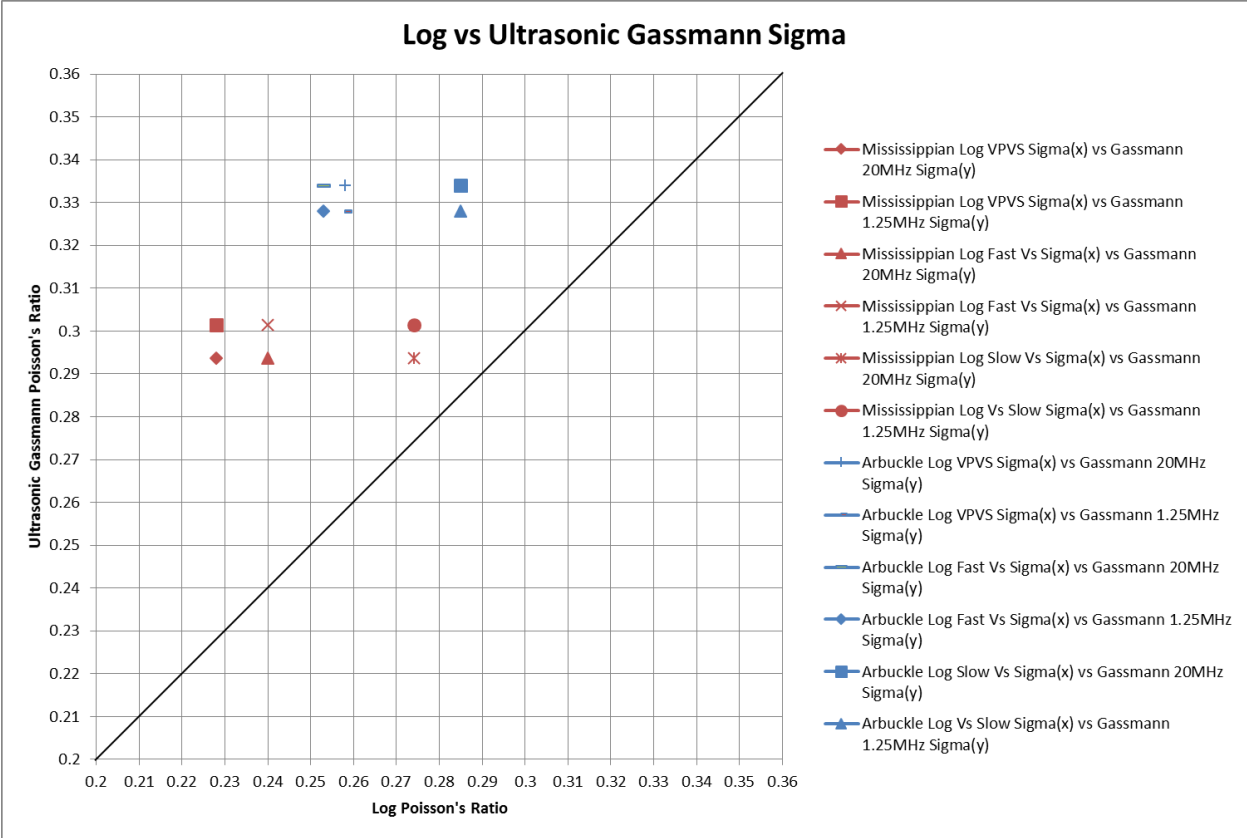
Figure 5.93 Ultrasonic brine-saturated Gassmann shear modulus vs *in situ* log shear

modulus in the Mississippian and Arbuckle formations. Fast and slow shear log values were used

in calculations for separate analysis and comparison.
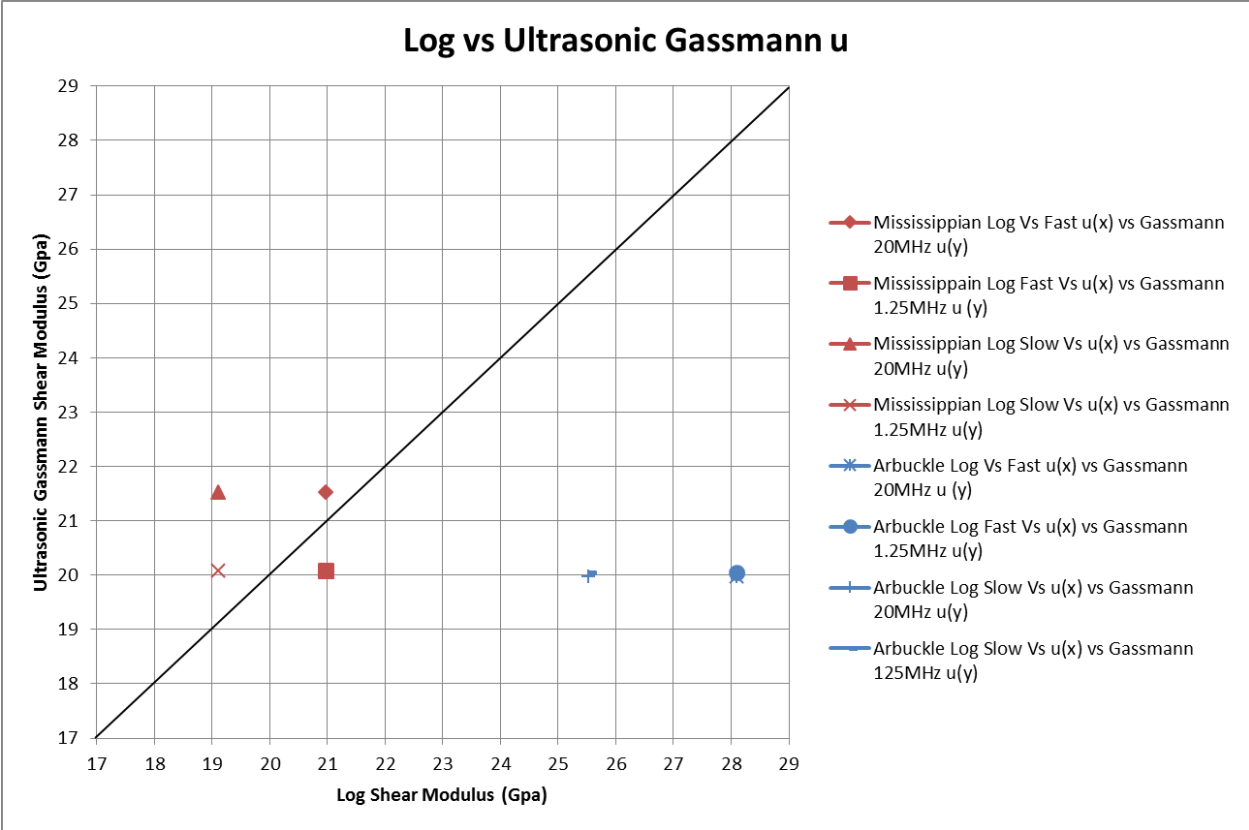
Figure 5.94 Ultrasonic brine-saturated Gassmann bulk modulus vs *in situ* log bulk modulus in the Mississippian and Arbuckle formations. Values for both fast and slow shear log values were used in calculations for separate analysis and comparison.
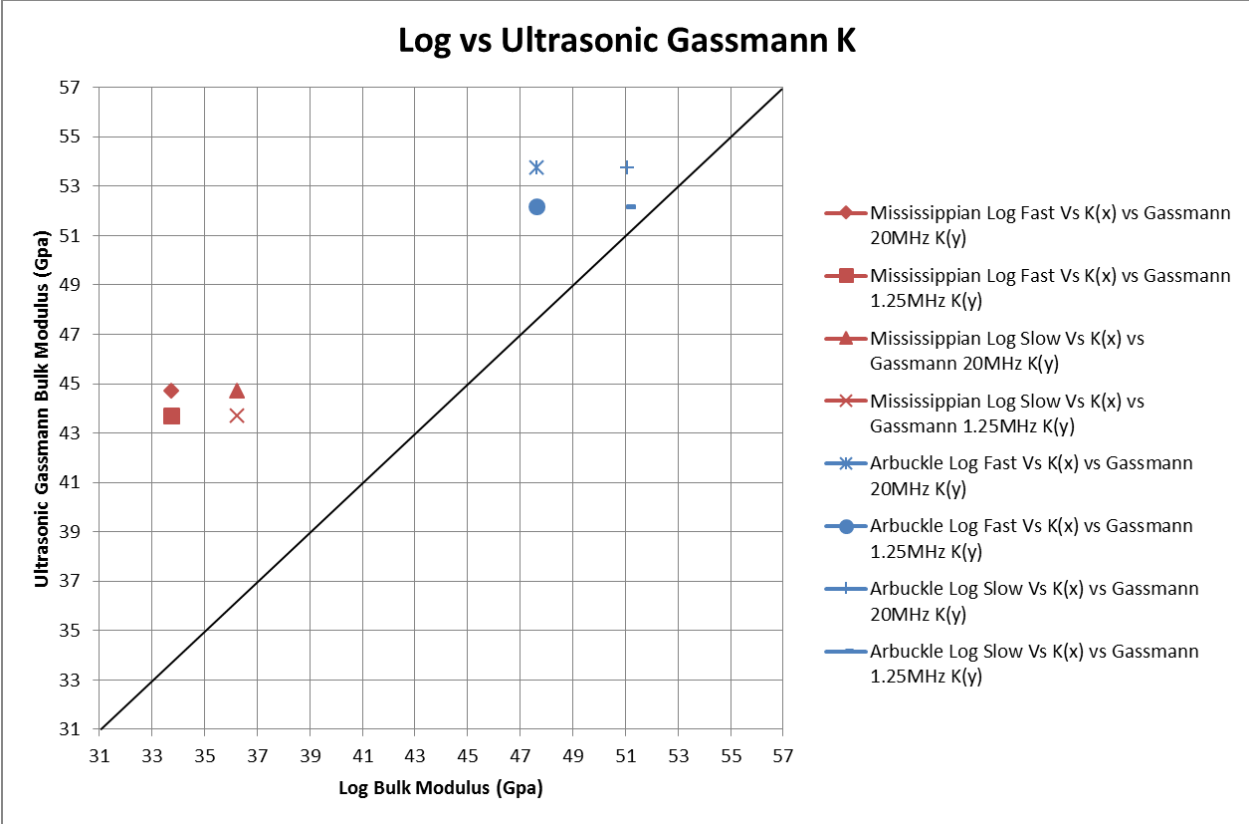
Figure 5.95 Ultrasonic brine-saturated Gassmann Young's modulus vs *in situ* Young's modulus in the Mississippian and Arbuckle formations. Values for both fast and slow shear log values were used in calculations for separate analysis and comparison.

Log vs Ultrasonic Gassmann Y

Legend:
- Mississippian Log VPVS Sigma Fast u Y(x) vs Gassmann 20MHz Y(y)
- Mississippian Log VPVS Sigma Fast u Y(x) vs Gassmann 1.25MHz Y(y)
- Mississippian Log VPVS Sigma Slow u Y(x) vs Gassmann 20MHz Y(y)
- Mississippian Log VPVS Sigma Slow u Y(x) vs Gassmann 1.25MHz Y(y)
- Mississippian Log Fast Sigma Fast u Y(x) vs Gassmann 20MHz Y(y)
- Mississippian Log Fast Sigma Fast u Y(x) vs Gassmann 1.25MHz Y(y)
- Mississippian Log Fast Sigma Slow u Y(y) vs Gassmann 20MHz Y(y)
- Mississippian Log Fast Sigma Slow u Y(x) vs Gassmann 1.25MHz Y(y)
- Mississippian Log Slow Sigma Fast u Y(x) vs Gassmann 20MHz Y(y)
- Mississippian Log Slow Sigma Fast u Y(x) vs Gassmann 1.25MHz Y(y)
- Mississippian Log Slow Sigma Slow u Y(x) vs Gassmann 20MHz Y(y)
- Mississippian Log Slow Sigma Slow u Y(x) vs Gassmann 1.25MHz Y(y)
- Arbuckle Log VPVS Sigma Fast u Y(x) vs Gassmann 20MHz Y(y)
- Arbuckle Log VPVS Sigma Fast u Y(x) vs Gassmann 1.25MHz Y(y)
- Arbuckle Log VPVS Sigma Slow u Y(x0 vs Gassmann 20MHz Y(y)
- Arbuckle Log VPVS Sigma Slow u Y(x) vs Gassmann 1.25MHz Y(y)
- Arbuckle Log Fast Sigma Fast u Y(x) vs Gassmann 20MHz Y(y)
- Arbuckle Log Fast Sigma Fast u Y(x) vs Gassmann 1.25MHz Y(y)
- Arbuckle Log Fast Sigma Slow u Y(x) vs Gassmann 20MHz Y(y)
- Arbuckle Log Fast Sigma Slow u Y (x) vs Gassmann 1.25MHz Y(y)
- Arbuckle Log Slow Sigma Fast u Y(x) vs Gassmann 20MHz Y(y)
- Arbuckle Log Slow Sigma Fast u Y(x) vs Gassmann 1.25MHz Y(y)
- Arbuckle Log Slow Sigma Slow u Y(x) vs Gassmann 20MHz Y(y)
- Arbuckle Log Slow Sigma Slow u Y(x) vs Gassmann 1.25MHz Y(y)

Gregory-Pickett

The Gregory-Pickett model was used to compare between the other rock physics models tested, to determine which was more accurate and applicable in our study area. Results from both figures 5.96 and 5.97 show quite conclusively that this approach is not as accurate in predicting shear wave velocities as the Gassmann model. This study does not place much emphasis in this model, because in a direct comparison with its Vs prediction results to those of the Gassmann model (and the KGS 1-32 well log data), it performs relatively poorly. Regardless of frequency as seen in figures 5.96 and 5.97, the Gregory-Pickett model was more accurate than Gassmann in two of eight core plugs.

154

Figure 5.96 A comparison between 20MHz Gassmann Vs results, 20MHz Gregory-Pickett Vs results, and *in situ* log Vs data.
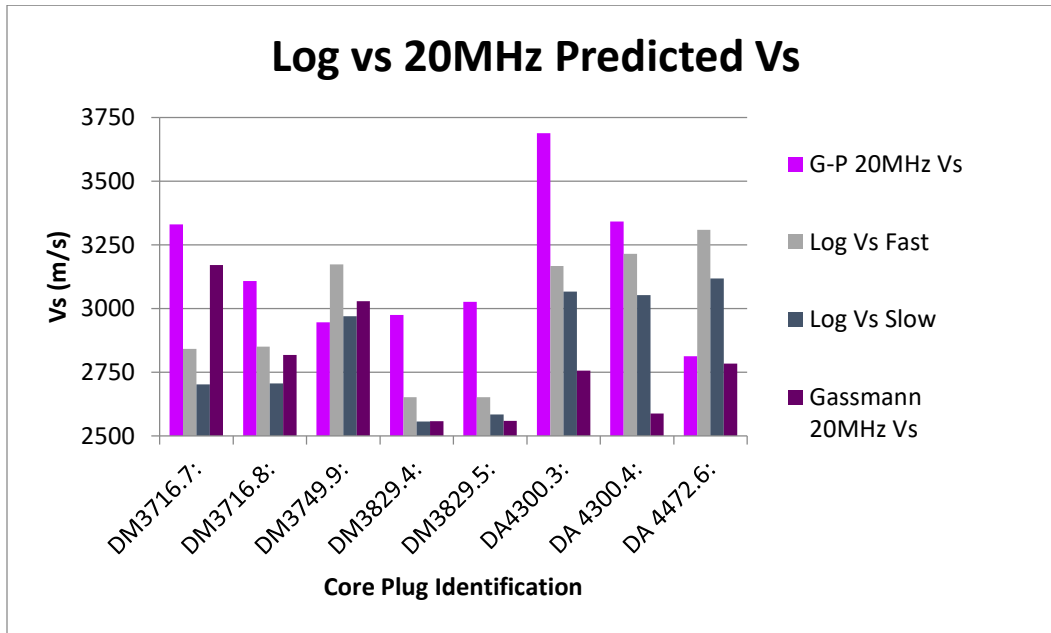
Figure 5.97 A comparison between 1.25MHz Gassmann Vs results, 1.25MHz Gregory-Pickett Vs results, and *in situ* log Vs data.
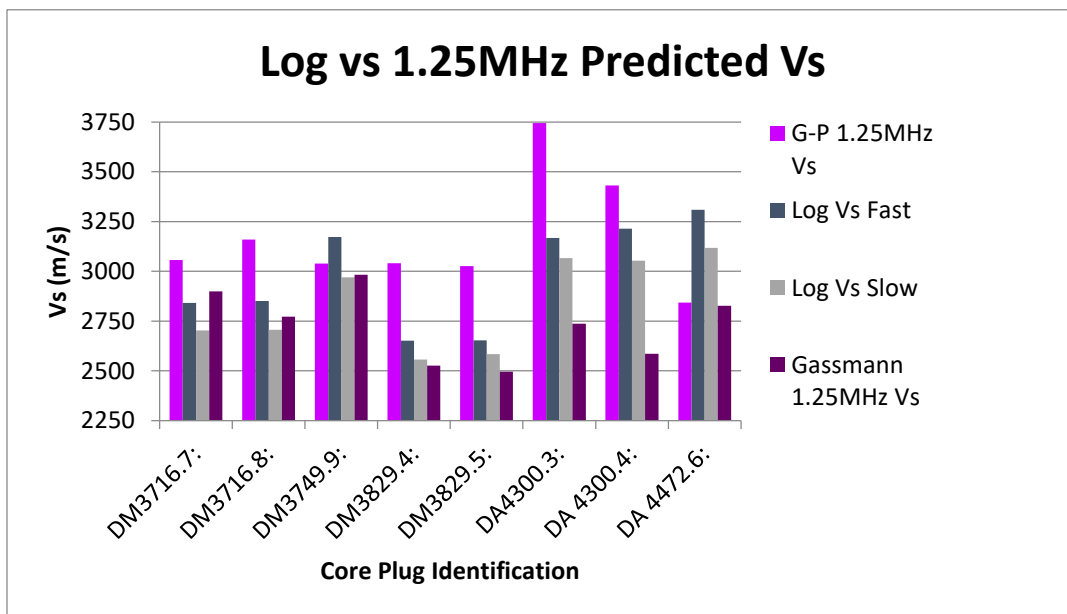
Ultrasonic To Sonic Vs Transformation

An attempt was made to accurately transform ultrasonic to sonic frequency Vs data using multiple observations including Poisson's ratio. Dry rock ultrasonic laboratory Vp (figures 5.98 and 5.100), Vs (figures 5.99 and 5.101), and Poisson's ratios (figures 5.102 and 5.103) were compared with sonic frequency log Vp, Vs, and Poisson's ratios to determine broad trends in order to possibly create a transformation, or calibration between datasets, allowing for an accurate prediction of each value using only laboratory data at our study site (under applicable conditions). When comparing ultrasonic Gassmann to *in situ* well log Vp (figure 5.98 and 5.100), a very robust relationship exists between datasets, as broad trends are generally seen to be in agreement, with the exception of core plug 4300.4 where a large deviation exists. Gassmann overestimates well log Vp in the upper Mississippian and underestimates well log Vp in the lower Mississippian and Arbuckle, with one particularly large underestimation being core plug 4300.4. Analyzing the comparison between Vs values (figure 5.99 and 5.101), the same general tend exists, where Gassmann overestimates upper Mississippian log values and increasingly underestimates velocities with depth, again, with the largest deviation from core plug 4300.3.

Figures 5.102 and 5.103 compare log and laboratory Poisson's ratio values. Log Poisson's ratios were mostly larger than those measured in the laboratory, with no clear trends evident. Differences in measurements in each case were less than 0.1.

Figure 5.98 A comparison between laboratory dry core 20MHz and 1.25MHz Vp values to log Vp values for each core plug used in the study.
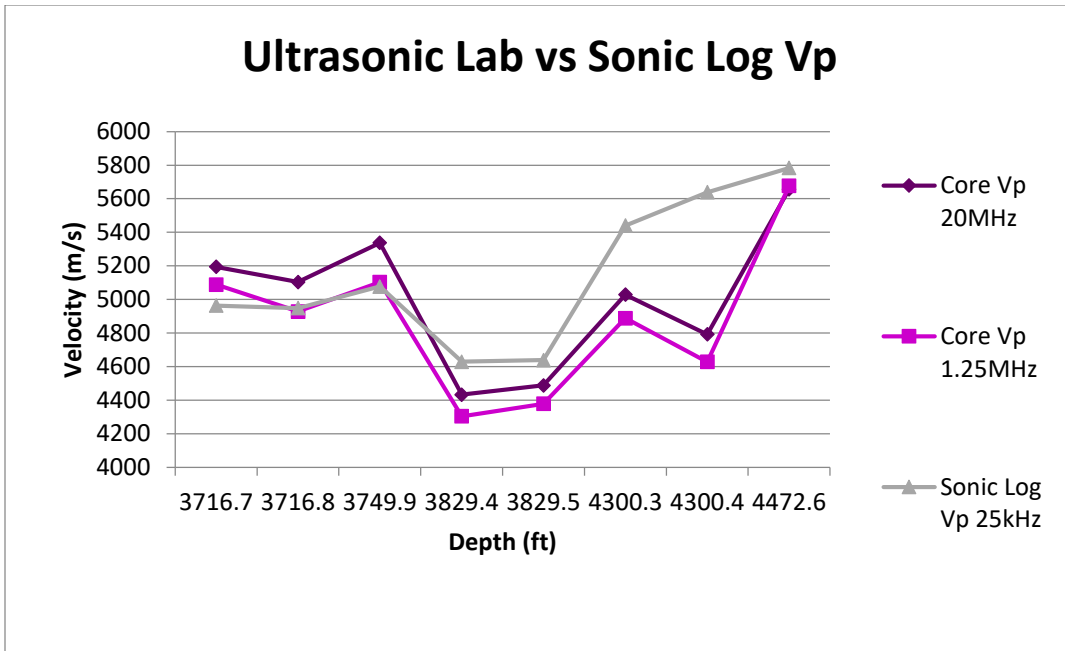
Figure 5.99 A comparison between laboratory dry core 20MHz and 1.25MHz Vs values to log Vs values for each core plug used in the study.
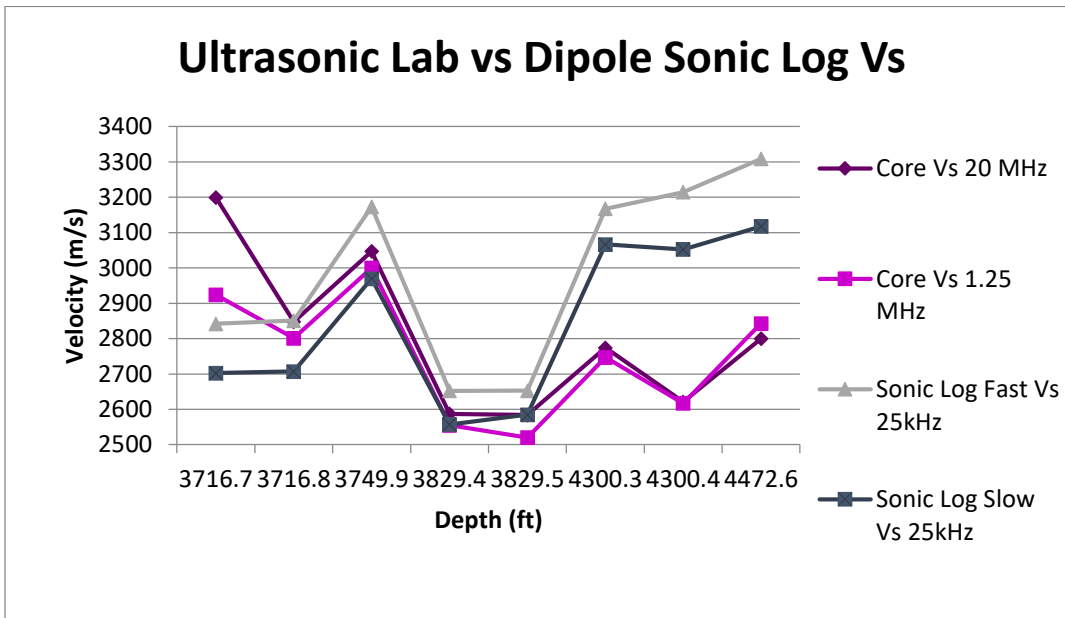
Figure 5.100 Compressional wave velocity deviations between laboratory ultrasonic and well log measurement methods.
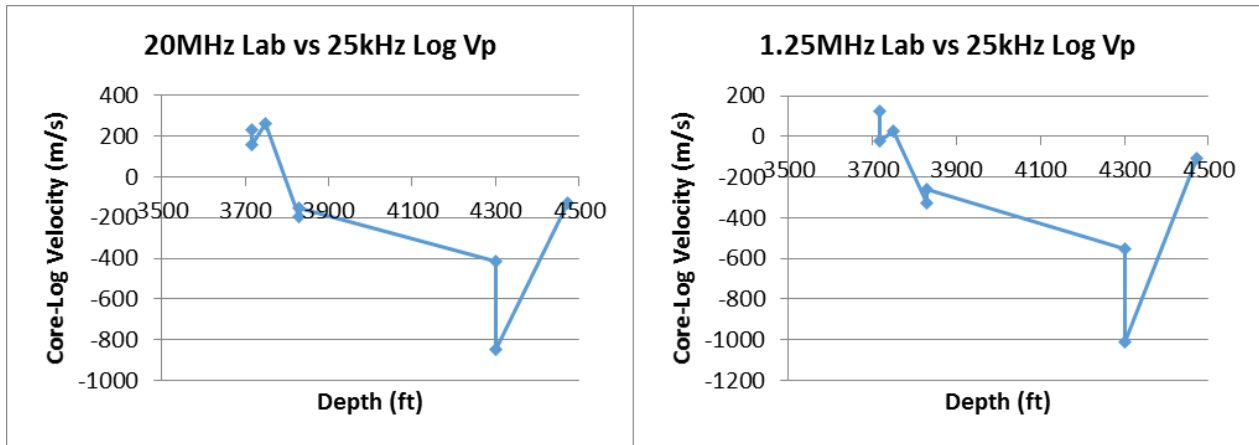
Figure 5.101 Shear wave velocity deviations between laboratory ultrasonic and well log measurement methods for each core used in this study.
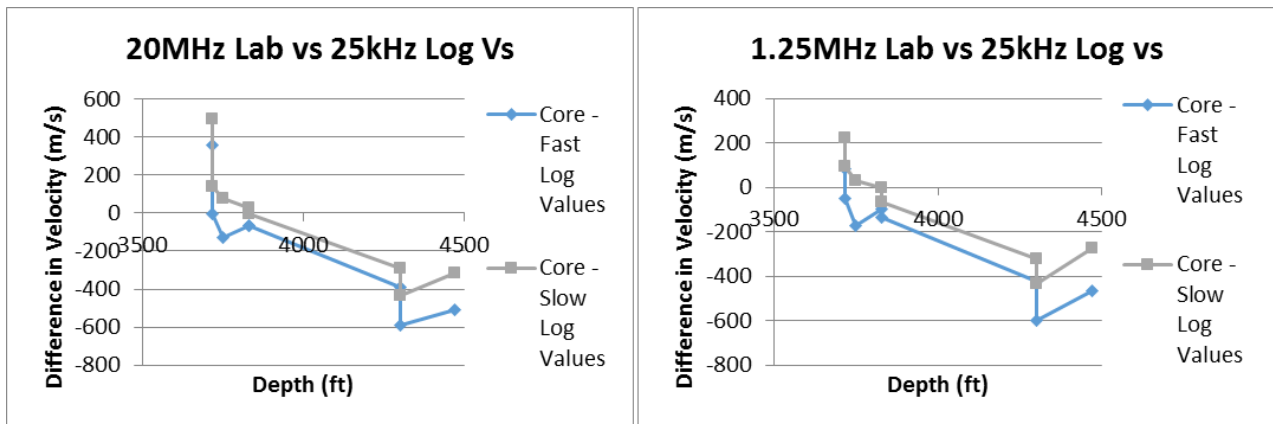
Figure 5.102 A comparison between laboratory dry core 20MHz and 1.25MHz Poisson's ratio values to log Poisson's ratio values for each core plug used in the study.
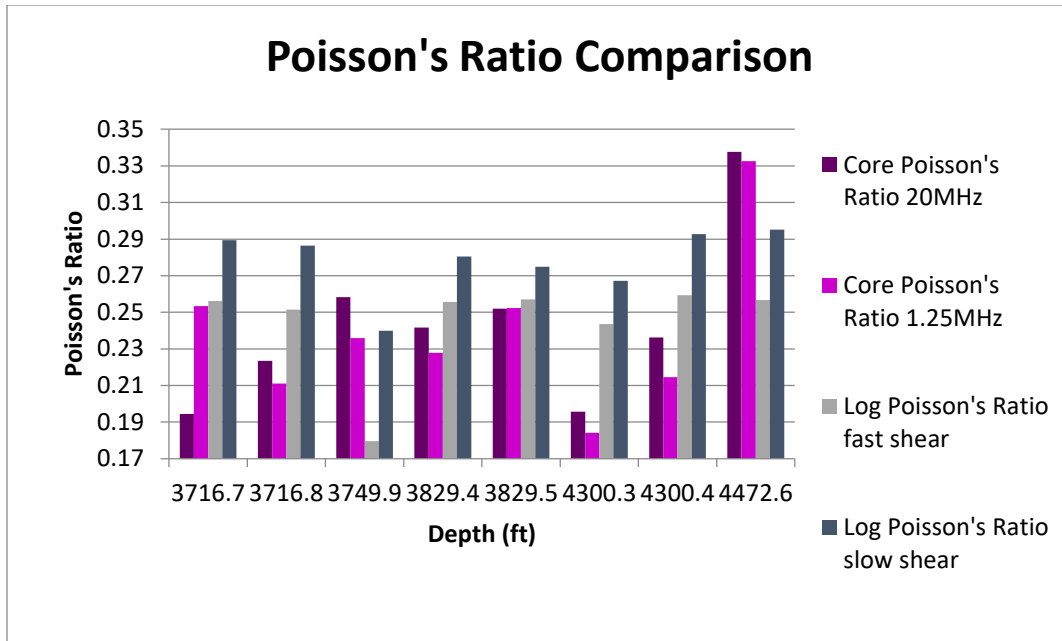
Figure 5.103 Poisson's ratio value deviations between laboratory ultrasonic and well log measurement methods for each core used in this study.
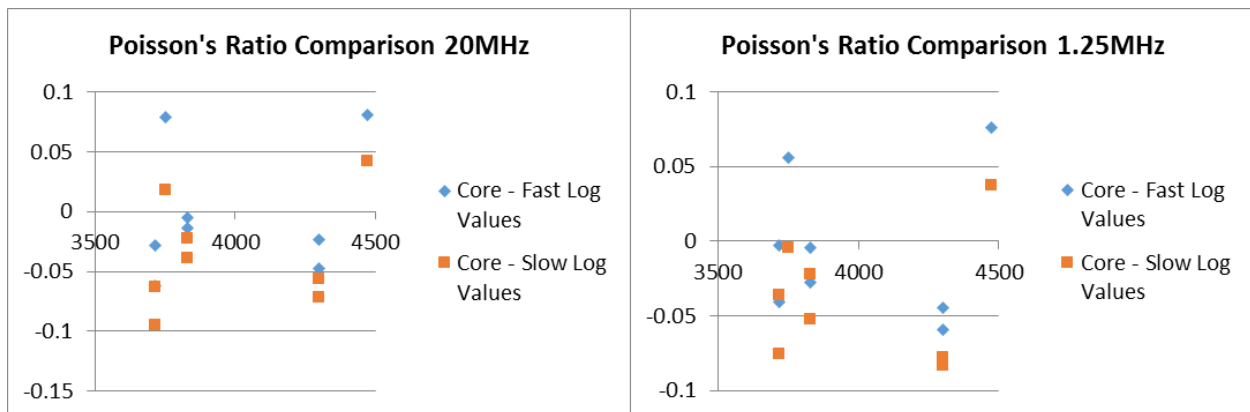
Gassmann Interactive Spreadsheet

Of the eight core plugs, samples 3749.9 and 4300.4 display the most optimistic results suggesting exploration geophysics techniques may be able to detect physical changes in the subsurface formations of interest as a result of CO_2 sequestration and CO_2-EOR efforts. These

samples both show nearly a 3.5% increase in Vp and impedance due to increases in CO_2

concentrations substituting in for brine. The other six samples show little or no substantial

change in Vp, impedance or density with any hypothetical saturation of CO_2. Seismic techniques

including high-resolution crosswell tomography have been known to resolve as small as a 1%

change in velocity (Harris et al., 1995). As discussed above, many possible factors could be

attributed to this observed difference, as many physical characteristics and specific combinations

of them may cause a multiplicity of different results to the seismic response. It is generally

known that shallower reservoirs are better candidates for seismic monitoring since Vp and Vs are

known to be more sensitive to changes in pore fluids under these conditions—relative changes in

formation pressure are larger at shallower depths where overburden pressures are less. Porosity

and permeability appear to be large factors in determining saturation effects on velocity, density

and impedance because of larger pore pressure buildup potential; however, both samples 3749.9

and 4300.4 had unimpressive porosities lower than many of the other specimens. Permeability

was also low and not significantly different from the average value across the eight specimens.

Although only two of eight samples showed responses in characteristics that can be more

easily detected through exploration geophysics techniques, perhaps other areas within these large

formations could show detectable changes as well. If these areas are thick enough when

compared to the resolution of the seismic techniques applied, they may be useful in monitoring

CO_2 plume movement. Furthermore, Daley et al. (2006), McCrank and Lawton (2009), Raef et

al. (2004) and Wang et al. (1998) all have demonstrated that Gassmann model predictions of

time-lapse seismic effects can be less than the actual observed effects, suggesting the same may

be true in this case. It is possible that closer to the surface, faults, joints and fractures are more

abundant creating this discrepancy, as laboratory and field measurements are known to match

better at greater depths where these discontinuities are closed and less prevalent (Lin, 1985).

Another potential reason for this observed difference between modeled results and reality, at

least in carbonates, is chemical dissolution effects of calcite which can increase porosity and

permeability within affected zones. The possibility thus exists that an alternative fluid

replacement model may work better for the Mississippian and Arbuckle formations of interest,

such as one which takes into consideration chemical effects of substituting fluids, or the Biot

model (Biot, 1956), which takes into consideration frequency effects. The Biot model could be

tested for applicability in future studies.

Table 5.28 Varying Vp, density and impedance with varying saturations of CO_2

replacing brine, predicting responses of hypothetical sequestration at core plug sample 3716.7.

Vp	Density	SatCO2	Detlta_Vel	Delta_Density	Impedance	Delta_Impedance
4964	2621	0	0	0	13010381.9	
4964	2620	0.05	0	0.038153377	13005680	0.0361396
4965	2619	0.1	-0.0201455	0.076306753	13003335	0.054163668
4966	2618	0.15	-0.0402909	0.11446013	13000988	0.072203107
4967	2617	0.2	-0.0604364	0.152613506	12998639	0.090257919
4968	2616	0.25	-0.0805818	0.190766883	12996288	0.108328104
4969	2615	0.3	-0.1007273	0.228920259	12993935	0.12641366
4970	2614	0.35	-0.1208727	0.267073636	12991580	0.14451459
4971	2613	0.4	-0.1410182	0.305227013	12989223	0.162630891
4972	2612	0.45	-0.1611636	0.343380389	12986864	0.180762565
4973	2610	0.5	-0.1813091	0.419687142	12979530	0.237132932
4974	2609	0.55	-0.2014545	0.457840519	12977166	0.255303036
4975	2608	0.6	-0.2216	0.495993895	12974800	0.273488513
4976	2607	0.65	-0.2417454	0.534147272	12972432	0.291689362
4977	2606	0.7	-0.2618909	0.572300649	12970062	0.309905584
4978	2605	0.75	-0.2820363	0.610454025	12967690	0.328137178
4979	2604	0.8	-0.3021818	0.648607402	12965316	0.346384144
4980	2603	0.85	-0.3223272	0.686760778	12962940	0.364646483
4981	2602	0.9	-0.3424727	0.724914155	12960562	0.382924194
4982	2601	0.95	-0.3626181	0.763067531	12958182	0.401217277
4983	2600	1	-0.3827636	0.801220908	12955800	0.419525733

Figure 5.104 Percent change in Vp, density and impedance with increasing CO_2

saturation replacing brine in a hypothetical sequestration event at core plug sample 3716.7.

Core plug 3716.7 change in impedance, density and Vp with change in CO2 saturation

Figure 5.105 resembles very closely and represents well the six core plug samples which didn't show significant changes in properties with increasing CO_2 concentrations. In these cases, instead of an increase in Vp with increasing CO_2 saturation, Vp decreases slightly, and density increases slightly (which occurs in all eight samples). Because impedance is the product of velocity and density, it is nearly constant throughout.

Table 5.29 Varying Vp, density and impedance with varying saturations of CO_2 replacing brine, predicting responses of hypothetical sequestration at core plug sample 3716.8.

Vp	Density	SatCO2	Detlta_Vel	Delta_Density	Impedance	Delta_Impedance
4948	2626	0	0	0	12993185	
4946	2625	0.05	0.0404212	0.038080731	12983250	0.076466237
4945	2624	0.1	0.0606318	0.076161462	12975680	0.134727547
4945	2623	0.15	0.0606318	0.114242193	12970735	0.172785959
4946	2622	0.2	0.0404212	0.152322925	12968412	0.190664562
4946	2621	0.25	0.0404212	0.190403656	12963466	0.22873067
4947	2620	0.3	0.0202106	0.228484387	12961140	0.246632362
4947	2619	0.35	0.0202106	0.266565118	12956193	0.284706166
4948	2618	0.4	0	0.304645849	12953864	0.302630947
4949	2616	0.45	-0.020211	0.380807312	12946584	0.358660317
4950	2615	0.5	-0.040421	0.418888043	12944250	0.37662358
4950	2614	0.55	-0.040421	0.456968774	12939300	0.414720473
4951	2613	0.6	-0.060632	0.495049505	12936963	0.432706825
4952	2612	0.65	-0.080842	0.533130236	12934624	0.450708569
4953	2611	0.7	-0.101053	0.571210967	12932283	0.468725706
4954	2610	0.75	-0.121264	0.609291698	12929940	0.486758236
4955	2609	0.8	-0.141474	0.64737243	12927595	0.504806158
4956	2608	0.85	-0.161685	0.685453161	12925248	0.522869473
4957	2607	0.9	-0.181895	0.723533892	12922899	0.54094818
4958	2606	0.95	-0.202106	0.761614623	12920548	0.559042281
4959	2605	1	-0.222317	0.799695354	12918195	0.577151774

Figure 5.105 Percent change in Vp, density and impedance with increasing CO_2

saturation replacing brine in a hypothetical sequestration event at core plug sample 3716.8.

Table 5.30 Varying Vp, density and impedance with varying saturations of CO_2

replacing brine, predicting responses of hypothetical sequestration at core plug sample 3749.9.

Vp	Density	SatCO2	Detlta_Vel	Delta_Density	Impedance	Delta_Impedance
5077	2632	0	0	0	13361366.7	
5038	2631	0.05	0.7682156	0.037995365	13254978	0.796241374
5012	2631	0.1	1.2803593	0.037995365	13186572	1.308209957
4994	2630	0.15	1.6349203	0.075990729	13134220	1.700026162
4981	2630	0.2	1.8909922	0.075990729	13100030	1.955913158
4971	2629	0.25	2.0879705	0.113986094	13068759	2.189953587
4963	2629	0.3	2.2455532	0.113986094	13047727	2.347362634
4956	2628	0.35	2.3834381	0.151981458	13024368	2.522187564
4951	2628	0.4	2.4819272	0.151981458	13011228	2.620530797
4947	2627	0.45	2.5607186	0.189976823	12995769	2.736230038
4943	2627	0.5	2.6395099	0.189976823	12985261	2.814874688
4940	2626	0.55	2.6986034	0.227972187	12972440	2.91083044
4937	2626	0.6	2.7576969	0.227972187	12964562	2.969791474
4935	2625	0.65	2.7970926	0.265967552	12954375	3.046033675
4933	2625	0.7	2.8364883	0.265967552	12949125	3.085326062
4931	2624	0.75	2.8758839	0.303962917	12938944	3.161523357
4930	2624	0.8	2.8955818	0.303962917	12936320	3.181162067
4928	2623	0.85	2.9349774	0.341958281	12926144	3.25732194
4927	2622	0.9	2.9546753	0.379953646	12918594	3.313828136
4926	2622	0.95	2.9743731	0.379953646	12915972	3.333451877
4925	2621	1	2.994071	0.41794901	12908425	3.389935619

Figure 5.106 Percent change in Vp, density and impedance with increasing CO_2

saturation replacing brine in a hypothetical sequestration event at core plug sample 3749.9.
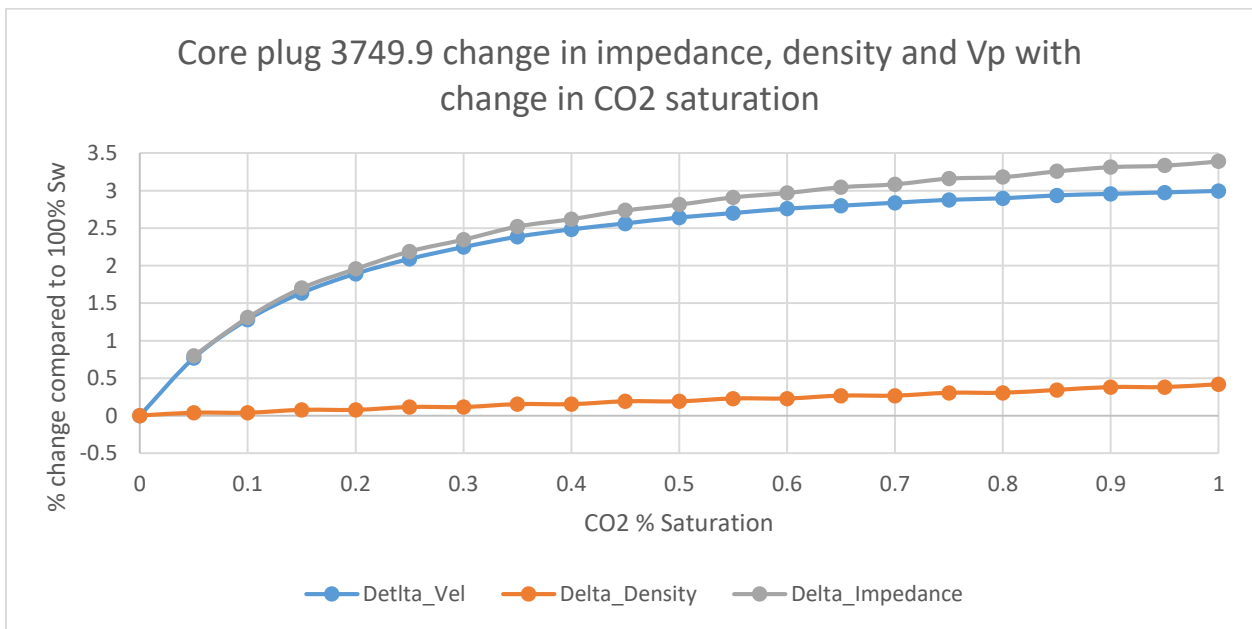
Figure 5.107 is one of two examples where Vp does noticeably change with changing CO_2 saturation. A dramatic increase in Vp occurs from 0% to 30% CO_2 saturation, and then levels off afterwards in an asymptote-like fashion. Again, because impedance is the product of density and velocity, it too resembles an asymptote-like shape, and closely follows the Vp changes. The exact difference of behavior in responses between samples is not known.

Table 5.31 Varying Vp, density and impedance with varying saturations of CO_2 replacing brine, predicting responses of hypothetical sequestration at core plug sample 3829.4.

Vp	Density	SatCO2	Detlta_Vel	Delta_Density	Impedance	Delta_Impedance
4629	2610	0	0	0	12082212	
4626	2609	0.05	0.064806	0.038314176	12069234	0.107414106
4624	2607	0.1	0.10801	0.114942529	12054768	0.227143838
4624	2606	0.15	0.10801	0.153256705	12050144	0.265414975
4624	2605	0.2	0.10801	0.191570881	12045520	0.303686113
4624	2603	0.25	0.10801	0.268199234	12036272	0.380228389
4625	2602	0.3	0.086408	0.30651341	12034250	0.396963735
4626	2601	0.35	0.064806	0.344827586	12032226	0.413715634
4626	2599	0.4	0.064806	0.421455939	12022974	0.490291016
4627	2598	0.45	0.043204	0.459770115	12020946	0.507076022
4628	2597	0.5	0.021602	0.498084291	12018916	0.523877581
4629	2595	0.55	0	0.574712644	12012255	0.579008215
4630	2594	0.6	-0.021602	0.61302682	12010220	0.595851157
4631	2593	0.65	-0.043204	0.651340996	12008183	0.612710653
4632	2591	0.7	-0.064806	0.727969349	12001512	0.667924052
4633	2590	0.75	-0.086408	0.766283525	11999470	0.684824931
4634	2589	0.8	-0.10801	0.804597701	11997426	0.701742363
4635	2587	0.85	-0.129612	0.881226054	11990745	0.757038529
4637	2586	0.9	-0.172816	0.91954023	11991282	0.752593979
4638	2585	0.95	-0.194418	0.957854406	11989230	0.769577624
4639	2584	1	-0.21602	0.996168582	11987176	0.786577822

Figure 5.107 Percent change in Vp, density and impedance with increasing CO_2 saturation replacing brine in a hypothetical sequestration event at core plug sample 3829.4.

Core plug 3829.4 change in impedance, density and Vp with change in CO2 saturation
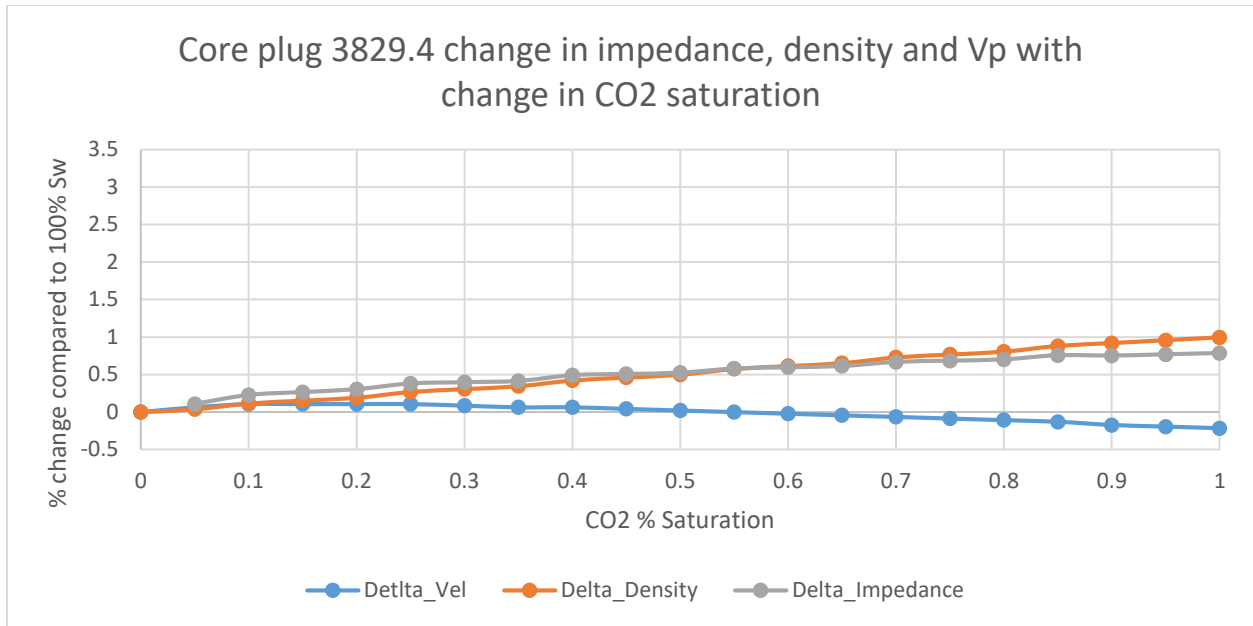
Table 5.32 Varying Vp, density and impedance with varying saturations of CO_2 replacing brine, predicting responses of hypothetical sequestration at core plug sample 3829.5.

Vp	Density	SatCO2	Detlta_Vel	Delta_Density	Impedance	Delta_Impedance
4638	2595	0	0	0	12038040	
4638	2594	0.05	0	0.038531191	12030972	0.058709892
4638	2593	0.1	0	0.077062382	12026334	0.09723776
4639	2592	0.15	-0.021559	0.115593573	12024288	0.114233883
4640	2590	0.2	-0.043118	0.192655955	12017600	0.169791102
4641	2589	0.25	-0.064677	0.231187146	12015549	0.18682876
4642	2588	0.3	-0.086237	0.269718337	12013496	0.203883032
4643	2586	0.35	-0.107796	0.346780719	12006798	0.259523321
4644	2585	0.4	-0.129355	0.38531191	12004740	0.276619128
4645	2584	0.45	-0.150914	0.423843101	12002680	0.293731549
4646	2583	0.5	-0.172473	0.462374292	12000618	0.310860584
4647	2581	0.55	-0.194032	0.539436674	11993907	0.366608865
4648	2580	0.6	-0.215592	0.577967865	11991840	0.383779435
4649	2579	0.65	-0.237151	0.616499056	11989771	0.400966619
4650	2578	0.7	-0.25871	0.655030247	11987700	0.418170417
4651	2576	0.75	-0.280269	0.732092629	11980976	0.474026688
4652	2575	0.8	-0.301828	0.77062382	11978900	0.491272021
4654	2574	0.85	-0.344947	0.809155011	11979396	0.487151748
4655	2573	0.9	-0.366506	0.847686202	11977315	0.504438616
4656	2571	0.95	-0.388065	0.924748584	11970576	0.560419493
4657	2570	1	-0.409624	0.963279775	11968490	0.577747896

Figure 5.108 Percent change in Vp, density and impedance with increasing CO_2

saturation replacing brine in a hypothetical sequestration event at core plug sample 3829.5.
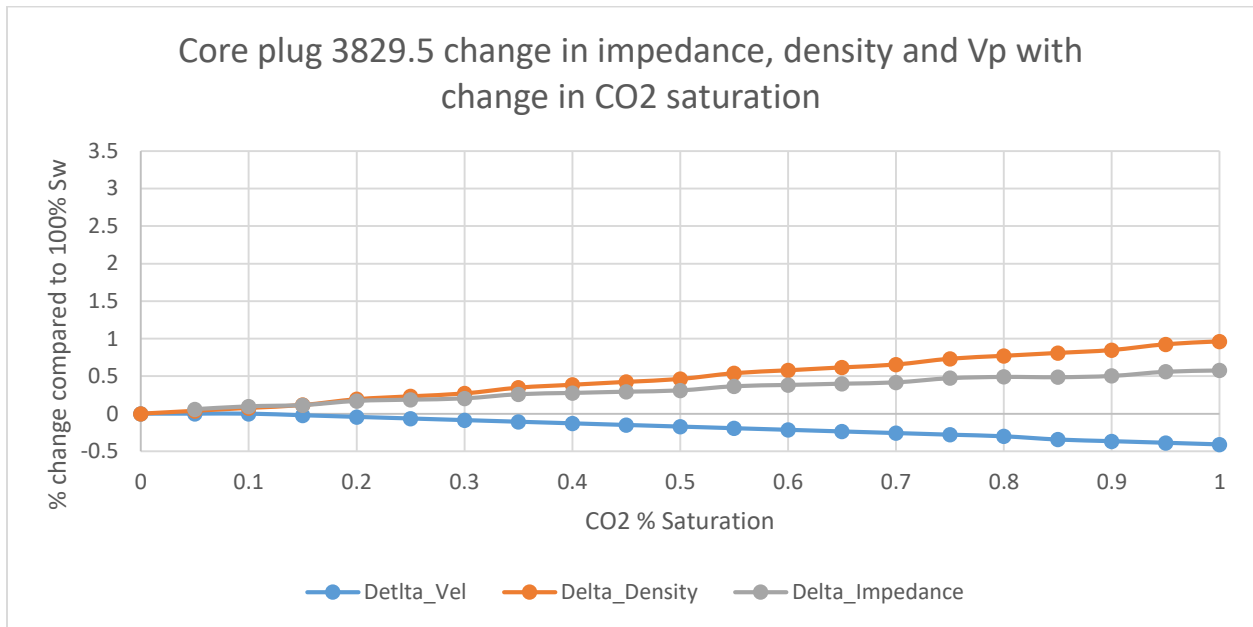
Table 5.33 Varying Vp, density and impedance with varying saturations of CO_2

replacing brine, predicting responses of hypothetical sequestration at core plug sample 4300.3.

Vp	Density	SatCO2	Detlta_Vel	Delta_Density	Impedance	Delta_Impedance
5440	2720	0	0	0	14797616	
5438	2719	0.05	0.0367627	0.036764706	14785922	0.079026243
5437	2719	0.1	0.055144	0.036764706	14783203	0.097400825
5436	2718	0.15	0.0735254	0.073529412	14775048	0.152511053
5436	2717	0.2	0.0735254	0.110294118	14769612	0.1892467
5436	2716	0.25	0.0735254	0.147058824	14764176	0.225982347
5437	2716	0.3	0.055144	0.147058824	14766892	0.20762804
5437	2715	0.35	0.055144	0.183823529	14761455	0.244370445
5437	2714	0.4	0.055144	0.220588235	14756018	0.28111285
5438	2713	0.45	0.0367627	0.257352941	14753294	0.29952122
5438	2712	0.5	0.0367627	0.294117647	14747856	0.336270383
5439	2712	0.55	0.0183813	0.294117647	14750568	0.317943107
5440	2711	0.6	0	0.330882353	14747840	0.336378509
5440	2710	0.65	0	0.367647059	14742400	0.373141187
5441	2709	0.7	-0.018381	0.404411765	14739669	0.391596863
5442	2709	0.75	-0.036763	0.404411765	14742378	0.37328986
5442	2708	0.8	-0.036763	0.441176471	14736936	0.410066054
5443	2707	0.85	-0.055144	0.477941176	14734201	0.428548761
5444	2706	0.9	-0.073525	0.514705882	14731464	0.447044983
5444	2706	0.95	-0.073525	0.514705882	14731464	0.447044983
5445	2705	1	-0.091907	0.551470588	14728725	0.465554722

Figure 5.109 Percent change in Vp, density and impedance with increasing CO_2 saturation replacing brine in a hypothetical sequestration event at core plug sample 4300.3.
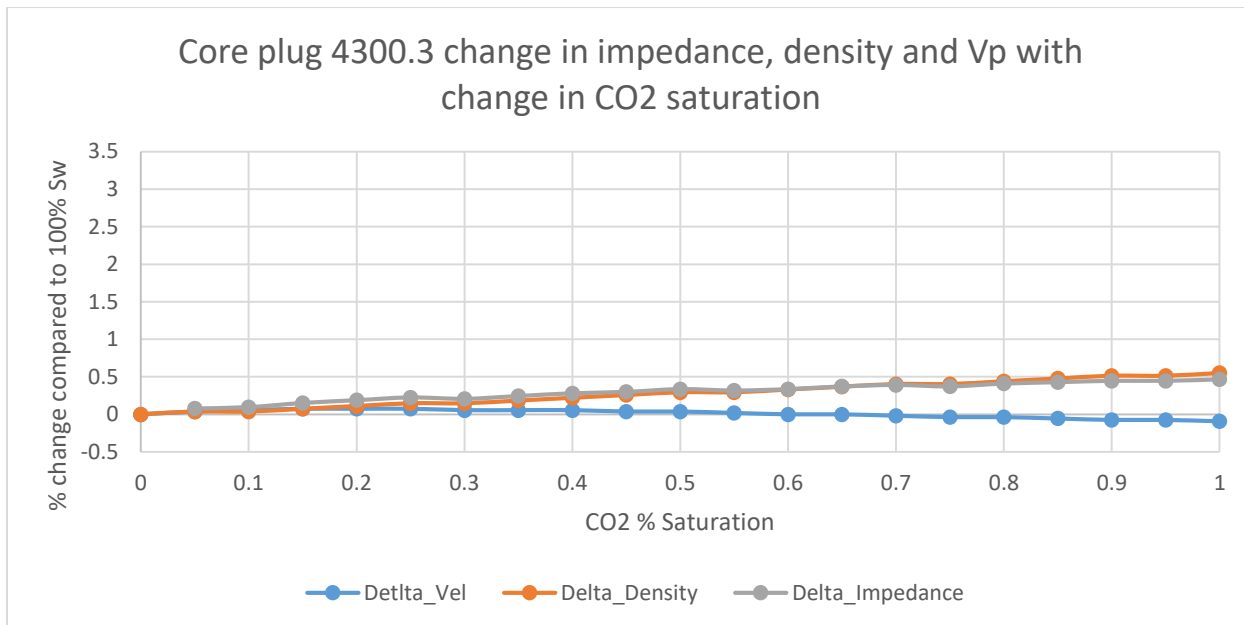
Table 5.34 Varying Vp, density and impedance with varying saturations of CO_2 replacing brine, predicting responses of hypothetical sequestration at core plug sample 4300.4.

Vp	Density	SatCO2	Detlta_Vel	Delta_Density	Impedance	Delta_Impedance
5638	2742	0	0	0	15457399	
5594	2741	0.05	0.7803771	0.036476382	15333154	0.80379271
5572	2740	0.1	1.1705656	0.072952763	15267280	1.22995754
5559	2740	0.15	1.4011315	0.072952763	15231660	1.460397337
5551	2739	0.2	1.5430183	0.109429145	15204189	1.638118047
5545	2738	0.25	1.6494333	0.145905526	15182210	1.780308847
5540	2738	0.3	1.7381126	0.145905526	15168520	1.868874845
5537	2737	0.35	1.7913201	0.182381908	15154769	1.957835475
5535	2736	0.4	1.8267918	0.218858289	15143760	2.029057029
5533	2736	0.45	1.8622634	0.218858289	15138288	2.06445755
5531	2735	0.5	1.8977351	0.255334671	15127285	2.135640287
5530	2735	0.55	1.915471	0.255334671	15124550	2.153334078
5529	2734	0.6	1.9332068	0.291811052	15116286	2.206797147
5529	2733	0.65	1.9332068	0.328287434	15110757	2.242566423
5528	2733	0.7	1.9509427	0.328287434	15108024	2.260247276
5528	2732	0.75	1.9509427	0.364763815	15102496	2.296010083
5527	2731	0.8	1.9686785	0.401240197	15094237	2.349440805
5527	2731	0.85	1.9686785	0.401240197	15094237	2.349440805
5527	2730	0.9	1.9686785	0.437716579	15088710	2.385197143
5527	2730	0.95	1.9686785	0.437716579	15088710	2.385197143
5527	2729	1	1.9686785	0.47419296	15083183	2.420953481

Figure 5.110 Percent change in Vp, density and impedance with increasing CO_2

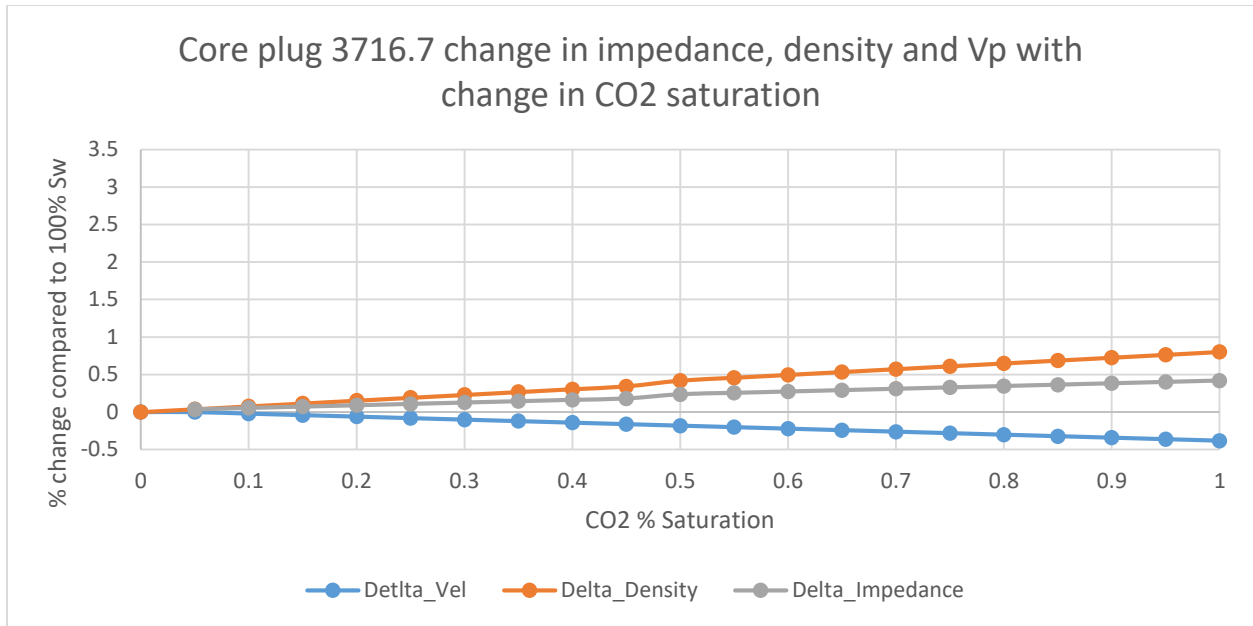saturation replacing brine in a hypothetical sequestration event at core plug sample 4300.4.

169
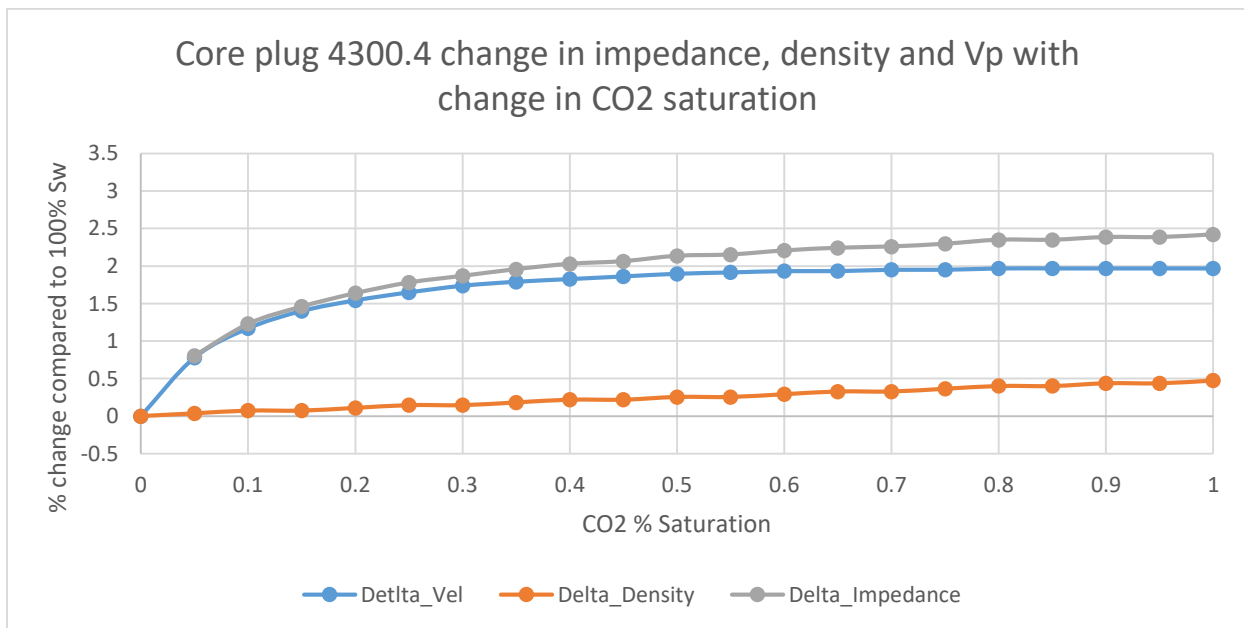
Table 5.35 Varying Vp, density and impedance with varying saturations of CO_2

replacing brine, predicting responses of hypothetical sequestration at core plug sample 4472.6.

Vp	Density	SatCO2	Detlta_Vel	Delta_Density	Impedance	Delta_Impedance
5784	2661	0	0	0	15387799.9	
5778	2660	0.05	0.103738	0.03758692	15369480	0.119054706
5774	2659	0.1	0.1728967	0.07517384	15353066	0.225723627
5772	2658	0.15	0.2074761	0.112760759	15341976	0.297793709
5770	2658	0.2	0.2420554	0.112760759	15336660	0.332340558
5769	2657	0.25	0.2593451	0.150347679	15328233	0.387104722
5769	2656	0.3	0.2593451	0.187934599	15322464	0.424595461
5769	2656	0.35	0.2593451	0.187934599	15322464	0.424595461
5768	2655	0.4	0.2766347	0.225521519	15314040	0.47934013
5768	2654	0.45	0.2766347	0.263108438	15308272	0.516824371
5769	2653	0.5	0.2593451	0.300695358	15305157	0.53706768
5769	2653	0.55	0.2593451	0.300695358	15305157	0.53706768
5769	2652	0.6	0.2593451	0.338282278	15299388	0.57455842
5769	2651	0.65	0.2593451	0.375869198	15293619	0.61204916
5770	2651	0.7	0.2420554	0.375869198	15296270	0.594821226
5770	2650	0.75	0.2420554	0.413456117	15290500	0.632318464
5771	2649	0.8	0.2247657	0.451043037	15287379	0.652600766
5771	2649	0.85	0.2247657	0.451043037	15287379	0.652600766
5772	2648	0.9	0.2074761	0.488629957	15284256	0.672896065
5772	2647	0.95	0.2074761	0.526216877	15278484	0.710406301
5773	2646	1	0.1901864	0.563803796	15275358	0.730721095

Figure 5.111 Percent change in Vp, density and impedance with increasing CO_2

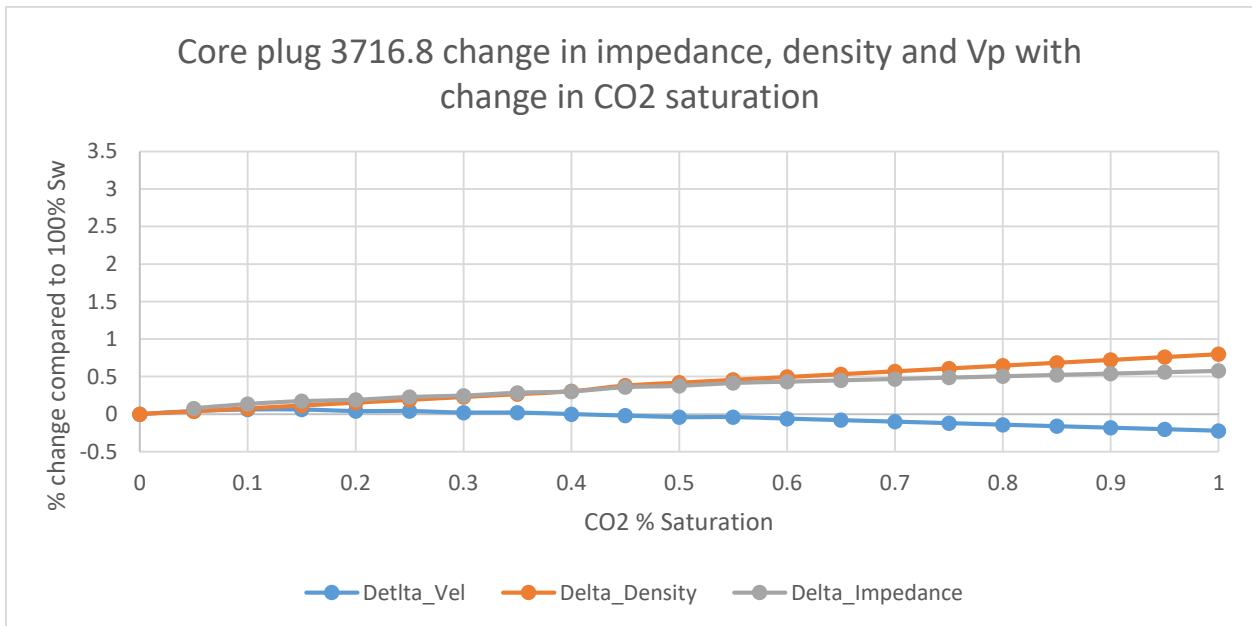saturation replacing brine in a hypothetical sequestration event at core plug sample 4472.6.
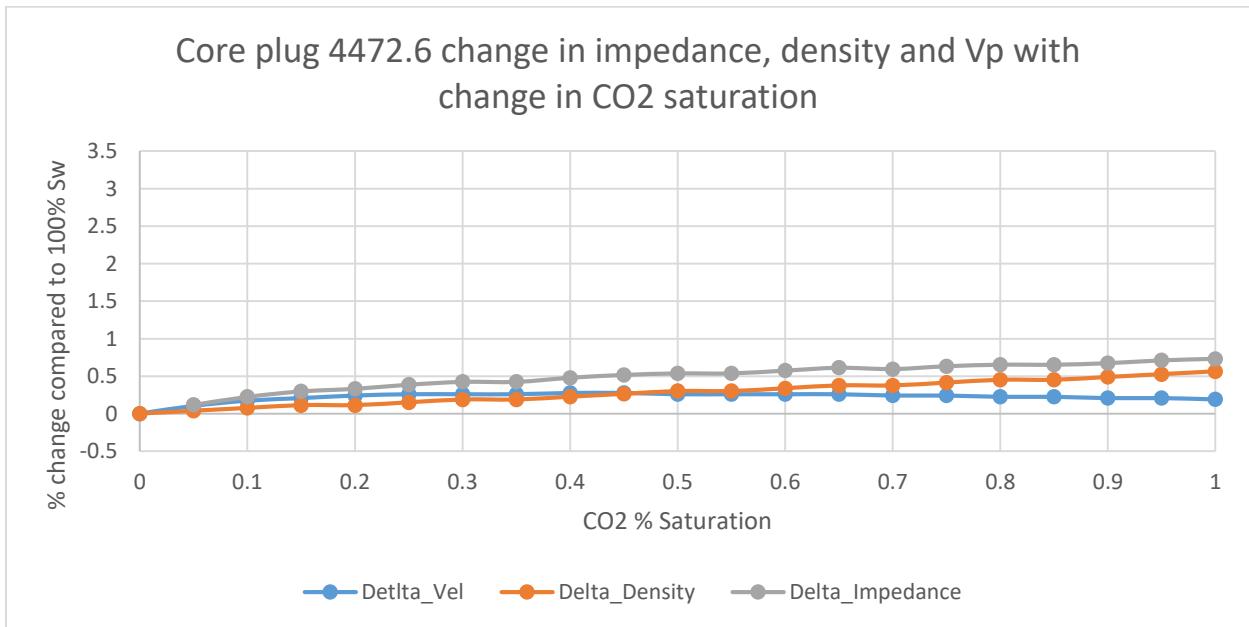
Chapter 6 - Conclusions

This study integrated lithofacies core plug samples, X-ray diffraction analysis, and well log data including sonic and dipole sonic in order to validate existing rock physics models that best represents our reservoir rock types and characteristics. Compressional and shear wave velocities at frequencies of 1.25MHz and 20MHz were estimated for Mississippian and Arbuckle core plugs by ultrasonic measurements of arrival times; these velocities were compared to sonic and dipole sonic log data from the Wellington 1-32 well. The elastic constants Young's Modulus, Bulk Modulus, Shear (Rigidity) Modulus, and Poisson's Ratio were calculated based on these velocity data at *in situ* pressures. Vp and Vs versus pressure cross plots were created and observed to ensure *in situ* pressure was reached with each core plug sample.

Saturated elastic moduli and velocities based on sonic and dipole sonic well logs, as well as dry rock moduli acquired from core plug samples allowed for the testing of various rock physics models after being compared to known values to ensure for accuracy. X-ray diffraction analysis on each core plug was conducted in order to provide inputs into various rock physics models tested; data includes diffractograms, mineral count lists, and pattern lists of analyzed samples. The Gassmann fluid replacement model was one rock physics model tested. Resulting data were compared with published literature data to determine accuracy, including data from Gardner et al. (1974), Wyllie et al. (1985), Greenberg and Castagna (1992), Rafavich et al. (1984), and Xu and Payne (2009). A comparison between this study's Gassmann model results to these datasets shows excellent fits, suggesting the Gassmann model is applicable to the subsurface rocks of interest to this study. Robustness of the model was also tested through the comparison of ultrasonic Gassmann estimated Vp, Vs, bulk modulus, shear modulus, Poisson's ratio and Young's modulus to the corresponding *in situ* KGS 1-32 well log values. These

comparisons revealed good fits between Mississippian datasets, and worse fits between Arbuckle datasets, suggesting a better applicability of the model to our core plug sample Mississippian rocks than Arbuckle rocks.

The Gregory-Pickett rock physics model was also used to compare predicted fluid-substituted Vs velocities to the Gassmann model. Our results suggest that the Gassmann model is the more accurate model. Since the Gassmann model was deemed most accurate when applied to our specific subsurface rock characteristics, it was used (through an interactive spreadsheet) to test the implications for feasibility of seismic monitoring in the associated KGS 1-32 well vicinity. Results show that of the eight core plugs, samples 3749.9 and 4300.4, display the greatest Vp and impedance contrasts between brine and CO_2 saturating fluids, suggesting exploration geophysics techniques may be able to detect physical changes in the subsurface formations of interest as a result of CO_2 sequestration and CO_2-EOR efforts at these depths. Many factors may be attributed to the fact that only two of the eight core plug samples showed favorable results in this regard, with further analysis recommended.

A transformation attempt of compressional wave sonic velocities to shear wave sonic for all wells where compressional wave sonic is available was unsuccessful due to a lack of conclusive patterns observed from a relatively limited dataset. Future studies could benefit from collecting and analyzing many more samples. Scaling up in this way is a well-known method to increase accuracy of laboratory results in studies such as this one, and could perhaps remedy many discrepancies, anomalies, and uncertainties uncovered in this study. Furthermore, the possibility exists that an alternative untested fluid replacement model may work best for our formations of interest; perhaps one which takes into consideration chemical effects of

substituting fluids, or one which takes into consideration frequency effects such as the Biot

model. Additional models may be recommended for testing in future studies.

References

Adam, L., Batzle, M., & Brevik, I. (2006). Gassmann's fluid substitution and shear modulus variability in carbonates at laboratory seismic and ultrasonic frequencies. Geophysics, 77(6), 173-183.

Adam, L. & Batzle, M. (2007). Moduli dispersion and attenuation in limestones in the laboratory. SEG Annual Meeting, San Antonio.

Adler, F.J. (1971). Future petroleum provinces of the mid-continent, region 7; in, Future Petroleum Provinces of the United States—Their Geology and Potential. American Association of Petroleum Geologists, Memoir 15, 985-1120.

Alvarado, V., & Manrique, E. (2010). Enhanced oil recovery: an updated review. Energies, 3, 1529-1575.

Assefa, S., McCann, C., & Sothcott, J. (2003). Velocities of compressional and shear waves in limestones. Geophysical Prospecting, 51, 11-13.

Atkinson, B.K., & Meredith, P.G. (1987). The theory of subcritical crack growth with applications to minerals and rocks. In: Atkinson, B.K. (Ed.), Fracture Mechanics of rock. Academic Press, London, pp. 111-166.

Averill, Bruce, and Patricia Eldredge. "General Chemistry: Principles, Patterns, and Applications, v. 1.0.1." Flat World Education, Inc, n.d. Web. 1 July 2016. <catalog.flatworldknowledge.com/bookhub/reader/26669?e=averill_1.0-ch11_s07>.

Avseth, P., Mukerji, T., & Mavko, G. (2005). Quantitative seismic interpretation: Applying rock physics tools to reduce interpretation risk. Cambridge University Press.

Avseth, P., Mukerji, T., & Mavko, G. (2006). Quantitative seismic interpretation, Cambridge University Press.

Ba J., Cao, H., Carcione, J., Tang, G., Yan, X.F., Sun, W.T., & Nie, J.X. (2013). Multiscale rock-physics templates for gas detection in carbonate reservoirs. Journal of Applied Geophysics, 93, 77-82.

Baechle, G.T., Weger, R.J., Eberli, G.P., Massaferro, J.L., & Sun, Y.-F. (2005). Changes of shear moduli in carbonate rocks: Implications for Gassmann applicability. The Leading Edge, 24, 507-510.

Barker, R. (2012). Geochemical and mineralogical characterization of the Arbuckle aquifer: Studying mineral reactions and its implications for CO_2 sequestration. Kansas State University Master's Thesis, pp. 1-117.

Baines, S.J., Worden, R.H. (2004). The long-term fate of CO_2 in the subsurface: Natural analogues for CO_2 storage. Geological Storage of Carbon Dioxide, Geological Society of London, Special Publication 233, 59-85.

Batzle, M., Hofmann, R.B., Han, D.-H., & Castagna, J. (2001). Fluid and frequency dependent seismic velocity of rocks. Leading Edge, 20, 168-171.

Batzle, M., & Wang, Z. (1992). Seismic properties of pore fluids. Geophysics, 57(11), 1396-408.

Beer, F., Johnston, R., Dewolf, J., & Mazurek, D. (2009). Mechanics of materials. New York: McGraw-Hill companies.

Benson, S.M., & Cole, D.R. (2008). Carbon dioxide sequestration: CO_2 sequestration in deep sedimentary formations. Elements, 4, 325-331.

Berryman, J. (2009). Origins of Gassmann's equations. Geophysics.

Besheli, S.A., Hendi, S.S., & Vali, J. (1998). Reservoir Characterization by Seismic Attributes With Vp & Vs Measurement of core samples (a "Rock Physics" study). Geophysics Department, RIPI---NIOC.

Bickle, M. J. (2009). Geological carbon storage. Natural Geoscience, 2, 815-818.

Blakey, R. (2010). Late Mississippian Paleogeography of North America: Colorado Plateau Geosystems, Inc., map, http://cpgeosystems.com/paleomaps.html

Blakey, Ron. "Paleogeography and Geologic Evolution of North America Images That Track the Ancient Landscapes of North America." *Middle Mississippian Paleogeography of North America*. Ron Blakey, Mar. 2011. Web. 1 July 2016. <http://www2.nau.edu/rcb7/nam.html>.

Brace, W.F. (1964). Brittle Fracture of Rocks. State of Stress in the Earth's Crust. W.R. Judd (ed), New York, Elsevier, pp. 11-114.

Brace, W.F. (1965). Some New Measurements of Linear Compressibility of Rocks. J. Geophys. Res., 70, 391-398.

Bradford, I.D.R., Fuller, J., Thompson, P.J., & Walsgrove, T.R. (1998). Benefits of assessing the solids production risk in a North Sea reservoir using elastoplastic modeling. SPE/ISRM Eurock '98, 261-269.

Bristow, J.R. (1960). Microcracks, and the static and dynamic elastic constants of annealed and heavily cold-worked metals. British Journal of Applied Physics, 11, 81-85.

Brunner, G. (2010). Applications of Supercritical Fluids. Annual Review of Chemical and Biomolecular Engineering 1, 1, 321-342.

Calvert, R. (2005). 4D technology: Where are we, and where are we going? Geophys. Prospect., 53, 161-171.

Carmichael, R.S. (1982). Handbook of physical properties of rocks, v. 2. CRC Press, Boca Raton.

Carmichael, R.S. (1989). Practical handbook of physical properties of rocks and minerals. CRC Press, Inc.

Carr, T.R., Merriam, D.F., & Bartley, J.D. (2005). Use of relational databases to evaluate regional petroleum accumulation, groundwater flow, and CO_2 sequestration in Kansas. American Association of Petroleum Geologists Bulletin, 89, 1670-1627.

Carr, J.E., McGovern, H.E., & Gogel, T. (1986). Geohydrology of and Potential for Fluid Disposal in the Arbuckle Aquifer in Kansas. US Geol. Surv. Open-file Rept. 86-491.

Castagna, J.P., Batzle, M.L., & Eastwood, R.L. (1985). Relationships between compressional-wave and shear-wave velocities in clastic silicate rocks. Geophysics, 50, 571-581.

Castagna, J.P., & Backus, M.M. (1993). Offset-dependent reflectivity—Theory and practice of AVO analysis. Soc. Expl. Geophys.

Chang, C., Zoback, M., & Khaksar, A. (2006). Empirical relations between rock strength and physical properties in sedimentary rocks. Journal of Petroleum Science and Engineering, 51, 223-237.

Cheng, C.H., & Johnston, D.H. (1981). Dynamic and static moduli. Geophys. Res. Lett. 8, 39-42.

Colback, P.S.B., & Wild, B.L. (1965). The influence of moisture content on the compressive strength of rocks. Proc. 3rd Canadian Rock Mech. Sympo. 65-83.

Cooperative Refinery Association. 1949. A geologic study of the Wellington Field with a view toward secondary recovery.

CO2CRC. (2008). Storage Capacity Estimation, Site Selection and Characterisation for CO_2 Storage Projects. Cooperative Research Centre for Greenhouse Gas Technologies, Canberra. CO2CRC Report No. RPT08-1001, pp. 52.

Clark, V.A., Tittman, B.R., & Spencer, T.W. (1980). Effects of volatiles on attenuation and velocity in sedimentary rocks. Geophysics, 85, 5190-5198.

Crain E.R. (1978). Crain's Petrophysical Handbook. Alberta, Canada.

Damen, K., Faaij, A., van Bergen, F., Gale, J., & Lysen, E. (2005). Identification of early opportunities for CO_2 sequestration—worldwide screening for CO_2-EOR and CO_2-ECBM projects. Energy, 30, 1931-1952.

Daneshfar, J., Hughes, R.G., & Civan, F. (2009). Feasibility Investigation and Modeling Analysis of CO_2 Sequestration in Arbuckle Formation Utilizing Salt Water Disposal Wells. Journal of Energy Resources Technology-Transactions of the Asme. 131, 2.

David, Arpod. "Sedimentary Rocks." *Mineralogy Petrology Prof. Árpád Dávid (2011)*. Digital Textbook Library, n.d. Web. 1 July 2016. <http://www.tankonyvtar.hu/en/tartalom/tamop425/0038_foldrajz_mineralogy_Da/ch01s12.html>.

Department of Energy (2010). Carbon Sequestration Atlas of the United States and Canada – (Atlas III) (Third Edition): 159.

Dewar J., & Pickford Sc. (2001). Rock physics for the rest of us- an informal discussion. A Core Laboratory Company.

Domenico, S.N. (1984). Rock lithology and porosity determination from shear and compressional wave velocity. Geophysics, 49, 1188-1195.

Dutta, N.C., & Ode, H. (1979). Attenuation and dispersion of compressional waves in fluid-filled porous rocks with partial gas saturation (Whiet model): Part II: Results. Geophysics, 44, 1789-1805.

Eissa, E.A., Kazi, A. (1988). Relation between static and dynamic Young's moduli of rocks. Int J Rock Mech Min Sci Geomech, 25(6), 479-82.

Emberley, S., Hutcheon, I., Shevalier, N., Durocher, K., Mayer, B., Gunter, W.D., Perkins, E.H. (2005). Monitoring of fluid-rock interaction and CO_2 storage through produced fluid sampling at the Weyburn CO_2 injection enhanced oil recovery site, Saskatchewan, Canada. Applied Geochemistry, 20, 1131-1157.

Fjaer, E. (1999). Static and dynamic moduli of weak sandstones. Rock Mechanics for Industry. Balkema, pp. 675-681.

Fjaer, E., & Holt, R.M. (1994). Rock acoustics and rock mechanics: Their link in petroleum engineering. The Leading Edge, 13, 255-258.

Fjaer, E., Holt, R.M., Horsrud, P., Raaen, A.M., & Risnes, R. (1992). Petroleum related rock mechanics. Elsevier Science Publishers B.V.

Franseen, E. K. (2006). Mississippian (Osagean) Shallow-water, mid-latitude siliceous sponge spicule and heterozoan carbonate facies: An example from Kansas with implications for regional controls and distribution of potential reservoir facies. Current Research in Earth Sciences Bulletin 252, part 1.

Franseen, E.K., Byrnes, A.P., Cansler, J.R., Steinhauff, D.M., & Carr, T.R. (2004). The geology of Kansas — Arbuckle Group. Current research in Earth sciences Bulletin, 250, pp. 13–19.

Garven, G. (1993). Genesis of stratabound ore deposits in the Midcontinent basins of North America; 1, the role of regional groundwater flow. The American Journal of Science, 293(6), 497-568.

Dolberry, Gary. "Gary Dolberry on Enhanced Oil Recovery." *HubPages*. HubPages, 27 Aug. 2008. Web. 1 July 2016. <http://hubpages.com/politics/Gary-Dolberry-on-Enhanced-Oil-Recovery#>.

Eberli, G.P., Baechle, G.T., Anselmetti, F.S., & Incze, M.L. (2003). Factors controlling elastic properties in carbonate sediments and rocks. The Leading Edge, 22, 654-660.

Gardner, G.H.F., Gardner, L.W., & Gregory, A.R. (1974). Formation velocity and density- the diagnostic basics for stratigraphic traps. Geophysics, 39, 770-780.

Gassmann, F. (1951). Elasticisy of porous media. Vierteljahrschrift der Naturforschenden. Gesellschaft 96, 1-23.

Gegenhuber, N., & Pupos, J. (2015). Rock physics template from laboratory data for carbonates. Journal of Applied Geophysics, 114, 12-18.

Gercek, H. (2007). Poisson's ratio values for rocks. International Journal of Rock Mechanics & Mining Sciences, 44, 1-13.

Greenberg, M.L., & Castagna, J.P. (1992). Shear-wave velocity estimation in porous rocks: Theoretical formulation, preliminary verification, and applications. Geophysics, 40, 195-209.

Gregory, A.R. (1977). Aspects of rock physics from laboratory and log data that are important to seismic interpretation. American Association of Petroleum Geologists. Memoir 26.

Grochau, M., & Gurevich, B. (2009). Testing Gassmann Fluid Substitution: Sonic logs Versus Ultrasonic Core Measurements. 57, 75-79.

Gunter, W. D., & Bachu, S. (1996). Technical and economic feasibility of CO_2 disposal in aquifers within the Alberta Sedimentary Basin, Canada. Energy Conversion and Management 37, 6-8: 1135-1142.

Gunter, W.D., Bachu, S., & Benson, S. (2004). The role of hydrogeological and geochemical trapping in sedimentary basins for secure geological storage of carbon dioxide. Geological Storage of Carbon Dioxide, Geological Society Special Publications, 233, 129-145.

Gunter, W.D., Wiwchar, B., & Perkins, E.H., (1997). Aquifer storage of CO_2-rich greenhouse gases: extension of the time scale of experiment for CO_2-sequestering reactions by geochemical modeling. Mineralogy and Petrology, 59, 121-140.

Gutschick, R.C., & Sandberg, C.A. (1983). Mississippian Continental Margins of the Conterminous United States: The Shelfbreak: Critical Interface on Continental Margins. SEPM Special Publication 33.

Han, D.-H. (2004). Velocity in carbonate rocks. Fluids and DHI Consortia Sponsor Meeting, Technical Report.

Herzog, H.J. (2001). What Future for Carbon Capture and Sequestration? Environmental Science and Technology, 35(7), 148-153.

Heuze, F.E. (1980). Scale Effects in the Determination of Rock Mass Strength and Deformability. Rock Mechanics, 12, 167-192.

Hill, R. (1963). Elastic properties of reinforced solids: Some theoretical principles. J. Mech. Phys. Solids, 11, 357-372.

Holtz, M.H., Nance, P.K., & Finley, R.J. (2001). Reduction of greenhouse gas emissions through CO_2 EOR in Texas. Environmental Geosciences, 8, 187-199.

Holubnyak, Y., Watney, W., Rush, J., & Fazelalavi, F. (2014). Reservoir Engineering Aspects of Pilot Scale CO_2 EOR Project in Upper Mississippian Formation at Wellington Field in Southern Kansas. Energy Procedia, 63, 7732-7739.

Horsrud, P. (2001). Estimating mechanical properties of shale from empirical correlations. SPE Drill. Complet. 16, 68-73.

Hovorka, S. (2009). Frio Brine Pilot: the first U.S. Sequestration Test. Southwest Hydrology, 8(5), 26-31.

Huff, B.L. (2014). Microbial and Geochemical Characterization of Wellington Oil Field, Southcentral Kansas, and Potential Applications to Microbial Enhanced Oil Recovery. University of Kansas Master's Thesis, pp. 1-83.

IPCC (2014). Climate Change 2014: Synthesis Report. Contribution of Working Groups I, II and III to the Fifth Assessment Report of the Intergovernmental Panel on Climate Change [Core Writing Team, R.K. Pachauri and L.A. Meyer (eds.)]. IPCC, Geneva, Switzerland, 151 pp.

Isham, R. (2012). Integration of *in situ* and laboratory velocity measurements: analysis and calibration for rock formation characterization. Kansas State University Master's Thesis, pp. 1-105.

Jaeger, J.C., & Cook, M.G.W. (1969). Fundamentals of Rock Mechanics. Methuen, London.

Jaiswal, P., Varacchi, B., Ebrahimi, P., Dvorkin, J., & Puckette, J. (2014). Can seismic velocities predict sweet spots in the Woodford Shale? A case study from McNeff 2-28 Well, Grady County, Oklahoma. Journal of Applied Geophysics, 104, 26-34.

Jizba, D. (1991). Mechanical and acoustical properties of sandstones and shales. PhD thesis, Stanford University.

Jorstad, A., Mukerji, T., & Mavko, G. (1999). Model-based shear-wave velocity estimation versus empirical regressions. Geophysical Prospecting, 47, 785-797.

Kahraman, S. (2007). The correlations between the saturated and dry P-wave velocity of rocks. Ultrasonics, 46, 341-348.

Kansas Geological Survey (KGS) website, 2015, <http://www.kgs.ku.edu> Accessed April, 2015.

Kansas Geological Survey (KGS), 2012, South-Central Kansas CO_2 Project, http://www.kgs.ku.edu/PRS/Ozark/Reports/Activities/2012_04_09.html.

Kaszuba, J.P., Janecky, D.R., & Snow, M.G. (2005). Experimental evaluation of mixed fluid reactions between supercritical carbon dioxide and NaCl brine: relevance to the integrity of a geologic carbon repository. Chemical Geology, 217, 277-293.

Kazemeini, S.H., Juhlin, C., Zinck-Jorgensen, K., & Norden, B. (2009). Application of the continuous wavelet transform on seismic data for mapping of channel deposits and gas detection at the CO_2SINK site, Ketzin, Germany. Geophysical Prospecting, 57, 111-123.

Keeling, C.D., Bacastow, R.B., Bainbridge, A.E., Ekdahl Jr, C.A., Guenther, P.R., & Waterman, L.S. (1976). Atmospheric Carbon Dioxide Variations at Mauna Loa Observatory, Hawaii. Tellus XXVIII, 6, 538-551.

King, M.S. (1983). Static and dynamic elastic properties of rocks from the Canadian shield. Int J Rock Mech Min Sci Geomech, 20(5), 237-41.

King, B. (2013). Fluid Flow, Thermal History, and Diagenesis of the Cambrian-Ordovician Arbuckle Group and Overlying Units in South-Central Kansas. University of Kansas Master's Thesis, pp. 1-255.

Kupecz, J.A., & Land, L.S. (1991). Late-stage dolomitization of the Lower Ordovician Ellenburger Group, West Texas. Journal of Sedimentary Petrology, 61(4), 551-574.

Lackner, K.S. (2003). Climate Change: A Guide to CO_2 Sequestration. Science, 300(5626), 1677-1678.

Lane, H.R. (1978). The Burlington Shelf (Mississippian, north-central United States). Geologica et Palaeontologica, 12, 165-176.

Lin, W. (1985). Ultrasonic velocities and dynamic elastic moduli of mesaverde rocks. Lawrence Livermore National Laboratory, UCID-20273-Rev.1.

Marion, D., & Jizba, D. (1997). Sonic velocity in carbonate sediments and rock. Carbonate Seismology, 75-94. Society of Exploration Geophysicists.

Mathieson, A., Wright, I., Roberts, D., & Ringrose, P. (2009). Satellite imaging to monitor CO_2 movement at Krechba, Algeria. Energy Procedia, 1, 2201-2209.

Mavko, G., Mukerji, T., & Dvorkin, J. (1998). The Rock Physics Handbook: Tools for Seismic Analysis in Porous Media (First ed.). United Kingdom: Cambridge University press.

Mavko, G., Chan, C., & Mukerji, T. (1995). Fluid substitution: Estimating changes in Vp without knowing Vs. Geophysics, 60(6), 1750-1755.

Mavko, G., Mukerji, T., & Dvorking, J. (2009). The Rock Physics Handbook: Tools for Seismic Analysis in Porous Media (Second ed.). United Kingdom: Cambridge University Press.

Mavko, G., & Jizba, D. (1991). Estimating grain-scale fluid defects on velocity dispersion in rocks. Geophysics, 56, 1940-1949. Doi:10.1088/978-1-6270-5675-5ch3.

Mayo, B. (2015). The Everyday Physics of Hearing and Vision. Morgan & Claypool Publishers, chapter 3, pp. 3-1 to 3-22.

Mazzullo, S.J., Wilhite, B.W., & Boardman, D.R. (2011). Lighostratigraphic Architecture of the Mississippian Reeds Spring Formation (Middle Osagean) in Southwest Missouri, Northwest Arkansas, and Northeast Oklahoma: Outcrop Analog of Subsurface Petroleum Reservoirs. Oklahoma City Geological Society- The Shale Shaker, 61, 16.

McBee, W. Jr. (2003). Nemaha Strike-Slip Fault Zone. AAPG Mid-Continent Section Meeting Proceedings.

Merriam, D.F. (1963). The Geologic History of Kansas. Lawrence, Kansas: University of Kansas Publications.

Merriam, D.F. (2005). Origin and development of plains-type folds in the mid-continent (United States) during the late Paleozoic. AAPG Bulletin, 89(1), 101-118.

Montgomery, S. L., Mullarkey, J.C., Longman, M.W., Colleary, W.M., & Rogers, J.P. (1998). Mississippian chat reservoirs, south Kansas-Low-resistivity pay in a complex chert reservoir. AAPG Bulletin, 82, 187-205.

Morgan, L.C. (1932). Central Kansas Uplift. American Association of Petroleum Geologists. Bull., 16, 483-484.

Muggeridge, A., Cockin, A., Webb, K., Frampton, H., Collins, I., Moulds, T., & Salino, P. (2014). Recovery rates, enhanced oil recovery and technological limits. Phil. Trans. R. Soc. A. 372, 20120320 (2013).

Ohl, D., & Raef, E.A. (2014). Rock formation characterization for carbon dioxide geosequestration: 3D seismic amplitude and coherency anomalies, and seismic petrophysical facies classification, Wellington and Anson-Bates Fields, Kansas, USA. Journal of applied geophysics, 103, 221 -231.

Oliver, J. (1986). Fluids expelled tectonically from orogenic belts: their role in hydrocarbon migration and other geologic phenomena. Geology, 14, 99-102.

Patz, J.A., Campbell-Lendrum, D., Holloway, T., & Foley, J.A. (2005). Impact of regional climate change on human health. Nature, 438, 310-317.

Pimienta, L., Fortin, J., & Gueguen, Y. (2014). Measured dispersion and attenuation effects on the bulk modulus of fully-saturated sedimentary rocks. 76th EAGE meeting, Amsterdam, The Netherlands.

Purnamasari, I.A., Khairy, H., Abdeldayem, A.L., & Ismail, W. (2014). Rock Physics Modeling and Fluid Substitution Studies in Sandstone Reservoir. Journal of Applied Sciences, 14, 1180-1185.

Raef, A.E., & Slusarczyk, R. (2001). Factor analysis of seismic multiattributes for predicting porosities using sequential nonlinear regression: the thin carbonates of the BMB Field, Poland. Petroleum Geoscience, 7, 359-369.

Raef, A.E., Miller, R.D., Franseen, E.K., Byrnes, A.P., Watney, W.L., & Harrison, W.E. (2005). 4D seismic to image a thin carbonate reservoir during a miscible CO_2 flood: Hall-Gurney Field, Kansas, USA. The Leading Edge, 24, 521-526.

Rafavich, F., Kendall, C.H.St.C., & Todd, T.P. (1984). The Relationship between Acoustic Properties and the Petrographic Character of Carbonate Rocks. Geophysics, 49, 1622-1636.

Rogen, B., Fabricius, I.L., Japsen, P., Hoier, C., Mavko, G., & Pedersen, J.M. (2005). Ultrasonic velocities of North Sea chalk samples: Influence of porosity, fluid content and texture. Geophysical Prospecting, 53, 481-496.

Romanak, K.D., Smyth, R.C., Yang, C., Hovorka, S.D., Rearick, M, & Lu, J. (2012). Sensitivity of groundwater systems to CO_2: Application of a site-specific analysis of carbonate monitoring parameters at the SACROC CO_2-enhanced oil field. Int. J. Greenhouse Gas Control, 6, 142-152.

Rudge, J.F., Kelemen, P.B., & Spiegelman, M. (2010). A simple model of reaction induced cracking applied to serpentinization and carbonation of peridotite. Earth Planet. Sci. Lett. 291, 215-227.

Rzhevsky, V., & Novick, G. (1971). The physics of rocks. MIR Publ., pp. 320

Sayers, C.M. (2008). The elastic properties of carbonates. The Leading Edge, 27(8), 1020-1024.

Sbar, M.L. (2000). Exploration risk reduction: An AVO analysis in the offshore middle Miocene, central Gulf of Mexico. The Leading Edge, 19, 21-27.

Scheffer, A. (2012). Geochemical and microbiological characterization of the Arbuckle Saline Aquifer, a Potential CO_2 Storage Reservoir; Implications for Hydraulic Separation and Caprock Integrity. University of Arkansas Master's Thesis, pp. 1-69.

Scoffin, T.P. (1986). An Introduction to Carbonate Sediments and Rocks. Blackie and Songs, pp. 124.

Siggins, A.F. (1993). Dynamic elastic tests for rock engineering. Comprehensive rock engineering, v. 3, London: Pergamon. pp. 601-18.

Simmons, G., & Brace, W.F. (1965). Comparison of Static and Dynamic Measurements of Compressibility of Rocks. J. Geophys. Res., 70, 5649-5656.

Simo, G.L., & Smith, J.A. (1997). Carbonate diagenesis and dolomitization of lower Ordovician Prairie du Chien Group. Geoscience Wisconsin, 16, 1-16.

Simm, R., & Bacon, M. (2014). Seismic Amplitude: An Interpreter's Handbook. Cambridge University Press, Cambridge.

Sirazhiev, A. (2012). Seismic Attribute Analysis of the Mississippian Chert at the Wellington Field, south-central Kansas. University of Kansas Master's Thesis, pp. 1-125.

Sloss, L.L. (1963). Sequences in the cratonic interior of North America. Geol. Soc. Am. Bull., 74, 93.

Smith, T.M., Sondergeld, C.H., & Rai, C.S. (2003). Gassmann Fluid Substitutions: A Tutorial: Geophysics, 68(2), 430-440.

Sundquist, E., Burruss, R., Faulkner, S., Gleason, R., Harden, J., Kharaka, Y., Tieszen, L., & Waldrop, M. (2008). Carbon sequestration to mitigate climate change. U.S. Geological Survey. Fact Sheet 2008-3097.

Sverjensky, D.A. (1986). Genesis of Mississippian valley-type lead-zinc deposits. Annual Review of Earth and Planetary Sciences, 14, 177-199.

Thill, R.E. (1983). Coal and Rock Properties for Pre-mine Planning and Mine Design. Mine Ground Control, pp. 15-35. U.S. Bureau of Mines, IC 8973.

Tilley, S.W. (2012). Geochemical analysis of the Mississippian limestone in the KGS 1-32 core, Sumner County Kansas: Application of elemental analysis to interpreting sequence stratigraphy. Oklahoma State University Master's Thesis, pp. 1-46.

Tucker, M.E., & Wright, V.P. (1990). Carbonate mineralogy and chemistry. Carbonate Sedimentology. Blackwell Scientific Publications, Oxford, pp. 482

Van Heerden, W.L. (1987). General relations between static and dynamic moduli of rocks. Int J Rock Mech Min Sci Geomech, 24(6), 381-5.

Vanorio, T., Nur, A., & Ebert, Y. (2011). Rock physics analysis and time-lapse rock imaging of geochemical effects due to the injection of CO_2 into reservoir rocks. Geophysics, 76, 23-33.

Vargaftik, N.B., Vinogradov, Y.K, & Yargin, V.S. (1996). Handbook of physical properties of liquids and gases: pure substances and mixtures, 3rd ed., Begell House, New York.

Walsh, J.B. (1993). The influence of microstructure on rock deformation. Comprehensive rock engineering, vol. 1. London, Pergamon, pp.243-54.

Wang, Z. (2001). Fundamentals of seismic rock physics. Geophysics, 66(2), 398-412.

Wang, Z., (2000). The Gassmann equation revisited: Comparing laboratory data with Gassmann's predictions, Recent developments. Soc. Expl. Geophys., 8-23.

Wang, Z., & Nur, A. (1992). Elastic wave velocities in porous media: a theoretical recipe. Seismic and Acoustic Velocities in Reservoir Rocks, 2, 1-32.

Wang, Z. & Nur, A. (1992). Aspects of rock physics in seismic reservoir surveillance. Reservoir Geophysics, p. 295-310, ed. Sheri, R., Soc. Explor. Geophys. Tulsa

Wang, Z., Hirsche, W.K., & Sedgwick, G. (1991). Seismic monitoring of water floods? A petrophysical study. Geophysics, 56, 1614-1623.

Wang, Z., & Nur, A. (1990). Dispersion analysis of acoustic velocities in rocks. J. Acoust. Soc. Am., 87, 2384-2395.

Wang, Z., Cates, M.E., & Langan, R.T. (1998). Seismic monitoring of a CO_2 flood in a carbonate reservoir: A rock physics study. Geophysics, 63(5), 1604-1617.

Watney, L.W., Franseen, E.K., Byrnes, A.P., & Nissen, S.E. (2007). Evaluating structural controls on the formation and properties of Carboniferous carbonate reservoirs in the northern midcontinent, U.S.A. Society for Sedimentary Geology Special Publication No. 89.

Watney, W.L., & Bhattacharya, S. (2009). Modeling CO_2 sequestration in saline aquifer and depleted oil reservoir to evaluate regional CO_2 sequestration potential of Ozark Plateau Aquifer System, South-Central Kansas. DOE Grant Proposal 076248616.

Watney, W.L., Guy, W.J., & Byrnes, A.P. (2001). Characterization of the Mississippian chat in south-central Kansas. AAPG Bulletin, 85(1), 85-113.

Watt, P. J., Davies, G.F., & O'Connell, R.J. (1976). The elastic properties of composite materials. Rev. Geophys. Space Phys., 14, 541-563.

Wilson, J.L., Fritz, R.D., & Medlock, P.L. (1991). The Arbuckle Group- Relationship of Core and Outcrop Analysis to Cyclic Stratigraphy and Correlation; in Arbuckle Core

Workshop and Field Trip, KS Johnson, ed: Oklahoma Geological Survey, Special Publication 91-3, 133-144.

Winkler, K.W. (1985). Dispersion analysis of velocity and attenuation in Berea sandstone. J. Geophys. Res., 90, 6793-6800.

Witzke, B.J. (1990). Paleoclimatic constraints for Paleozoic paleolatitudes of Laurentia and Euramerica, in McKerrow, W.S. and Scotese, C.R., eds., Paleozoic Paleogeography Biogeography. Geological Society of London, Memoir 12, 57-73.

Wojcik, K.M., McKibben, M.E., Goldstein, R.H., & Walton, A.W. (1992). Diagenesis, thermal history, and fluid migration, Middle and Upper Pennsylvanian rocks, southeastern Kansas. Oklahoma Geological Survey Circular, 93, 144-159.

Wyllie, M.R.J., Gregory, A.R., & Gardner, G.H.F. (1958). An experimental investigation of factors affecting elastic wave velocities in porous media. Geophysics, 23, 459-493.

Xu, S., & Payne, M.A. (2009). Modeling elastic properties in carbonate rocks. The Leading Edge, 28(1), 66-74.

Yam, H., Schmitt, D.R. (2011). CO_2 rock physics: A laboratory study. Canadian Well Logging Society InSite Magazine, 30(1), 13-16.

Young, E.M. (2010). Controls on reservoir character in carbonate-chert strata, Mississippian (Osagean-Meramecian), southeast Kansas. University of Kansas Master's Thesis, pp. 1-207.

Zeller, D.E. (1968). The stratigraphic succession in Kansas. Bull. Kansas Univ. Geol. Surv., 189, 1-81.

Zemke, K., Liebscher, A., Wandrey, M., & the CO2SINK Group (2010). Petrophysical analysis to investigate the effects of carbon dioxide storage in a subsurface saline aquifer at Ketzin, Germany (CO2SINK). Int. J. Greenhouse Gas Control, doi: 10.1016/j.ijggc.2010.04.008.

Zhang, J.J., & Bentley, L.R. 2005. Factors determining Poisson's ratio. CREWES Res. Rep. 17, 1-15.

Appendix A - Core Plug Pictures

Figure A.1 A longitudinal and cross section view of core plug sample DM3716.7, after flattening each end.

Figure A.2 A longitudinal and cross section view of core plug sample DM3716.8, after flattening each end.
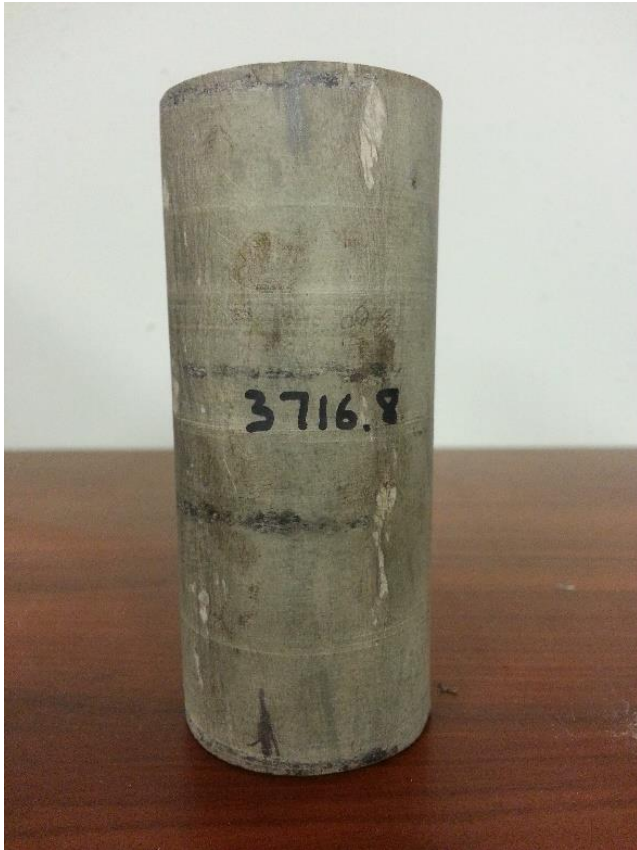
Figure A.3 A longitudinal and cross section view of core plug sample DM3749.9, after flattening each end.
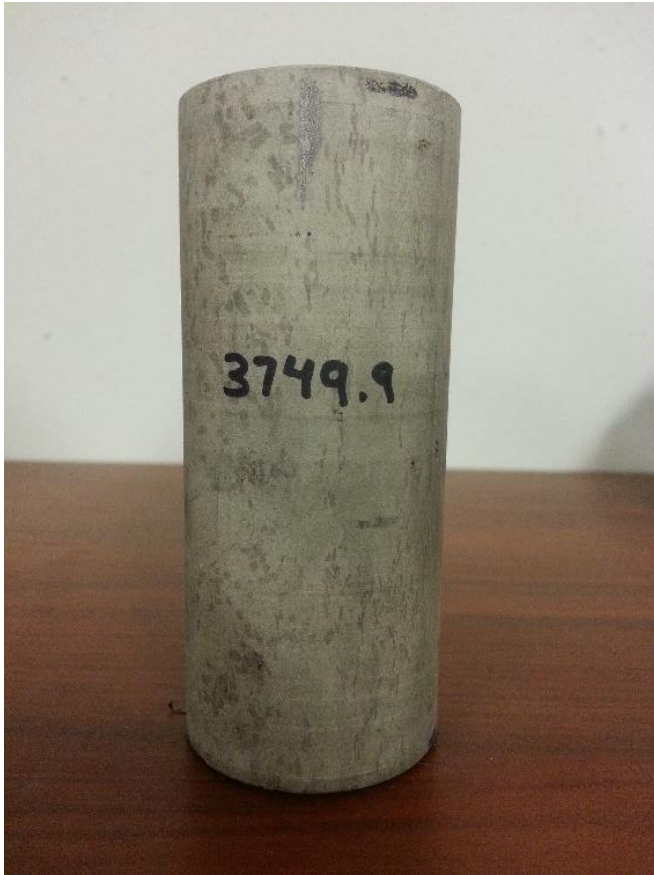
Figure A.4 A longitudinal and cross section view of core plug sample DM3829.4, after flattening each end.
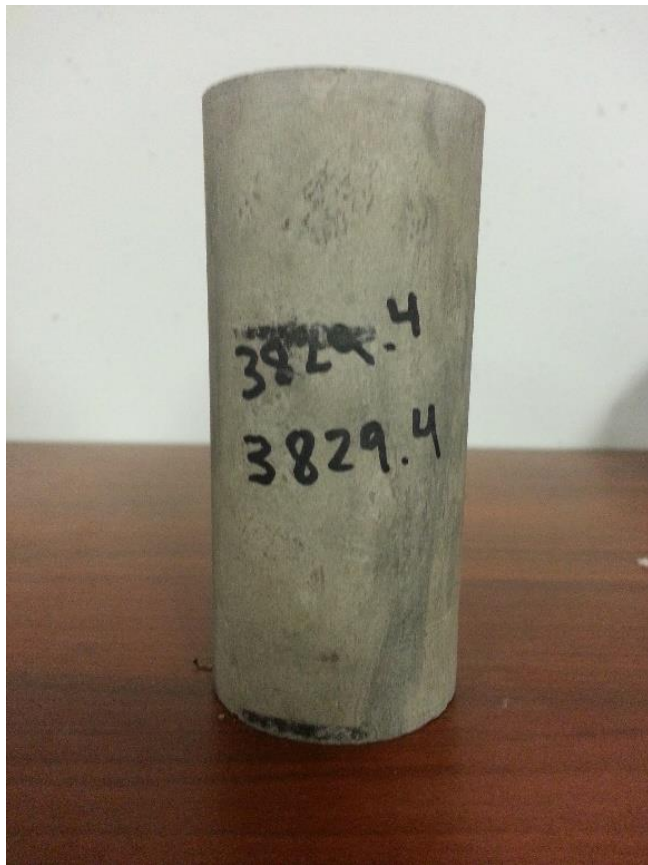
Figure A.5 A longitudinal and cross section view of core plug sample DM3829.5, after flattening each end.

Figure A.6 A longitudinal and cross section view of core plug sample DA4300.3, after flattening each end.

Figure A.7 A longitudinal and cross section view of core plug sample DA4300.4, after flattening each end.

Figure A.8 A longitudinal and cross section view of core plug sample DA4472.6, after flattening each end.

Appendix B - X-ray Diffraction Data

Figure B.1 Diffractogram for core plug sample DM3716.7.

Table B.1 Mineral count list for core plug sample DM3716.7.

Pos. [°2θ]	Height [cts]	FWHM Left [°2θ]	d-spacing [Å]	Rel. Int. [%]
20.8687	4197.24	0.0551	4.25677	11.02
22.0186	422.07	0.0827	4.03699	1.11
23.0683	559.19	0.0689	3.85562	1.47
24.0361	1223.27	0.1102	3.70252	3.21
26.6430	22569.74	0.0924	3.34310	59.26
26.7128	12106.51	0.0504	3.34281	31.79
27.8552	119.31	0.2016	3.20030	0.31
29.4211	7169.35	0.0840	3.03343	18.82
29.4962	4409.71	0.0336	3.03340	11.58
30.9020	38086.79	0.1092	2.89136	100.00
30.9937	23832.12	0.0588	2.89018	62.57
31.7030	447.62	0.0504	2.82011	1.18
33.4582	1079.64	0.0840	2.67607	2.83
35.2380	850.78	0.1008	2.54488	2.23
36.0075	675.36	0.0756	2.49224	1.77

36.5468	1575.95	0.0504	2.45669	4.14
36.6486	806.57	0.0588	2.45619	2.12
37.3474	1878.96	0.0756	2.40585	4.93
37.4412	993.51	0.0504	2.40599	2.61
39.4429	2229.04	0.0420	2.28272	5.85
39.5623	1273.98	0.0504	2.28176	3.34
40.2811	635.52	0.1008	2.23713	1.67
41.0919	4891.04	0.1008	2.19485	12.84
41.2042	2974.10	0.0672	2.19456	7.81
42.4415	935.71	0.1008	2.12812	2.46
43.1847	929.67	0.0672	2.09320	2.44
43.3133	533.64	0.0672	2.09247	1.40
43.7541	644.94	0.0588	2.06727	1.69
44.9047	2755.12	0.0924	2.01694	7.23
45.0227	1554.66	0.0672	2.01693	4.08
45.7929	608.95	0.1008	1.97986	1.60
47.1348	259.39	0.1008	1.92658	0.68
47.5387	939.41	0.0840	1.91115	2.47
48.5381	994.02	0.1008	1.87411	2.61
48.6854	578.38	0.0672	1.87343	1.52
49.2443	657.72	0.1344	1.84887	1.73
50.1267	2484.76	0.0756	1.81837	6.52
50.4661	2738.06	0.0840	1.80694	7.19
51.0060	3111.25	0.0588	1.78907	8.17
54.8616	586.80	0.1008	1.67210	1.54
55.3153	258.80	0.1344	1.65946	0.68
56.6130	150.82	0.1008	1.62446	0.40
57.4519	329.24	0.0840	1.60272	0.86
58.8645	508.36	0.1176	1.56758	1.33
59.7732	1310.17	0.1008	1.54590	3.44
59.9504	1865.05	0.0504	1.54558	4.90
60.1146	811.75	0.0840	1.53794	2.13
60.7051	197.29	0.1008	1.52438	0.52
62.0138	111.77	0.3360	1.49532	0.29
63.3717	770.41	0.1512	1.46651	2.02

Table B.2 Mineral pattern list for core plug sample DM3716.7.

Visible	Ref. Code	Score	Compound Name	Displacement [°2Th.]	Scale Factor	Chemical Formula
*	98-017-1508	66	Dolomite	-0.070	0.955	C2 Ca1 Mg1 O6
*	98-003-1228	65	Quartz low	-0.008	0.574	O2 Si1
*	98-005-2151	65	Calcite	0.039	0.196	C1 Ca1 O3

Figure B.2 Diffractogram for core plug sample DM3716.8.
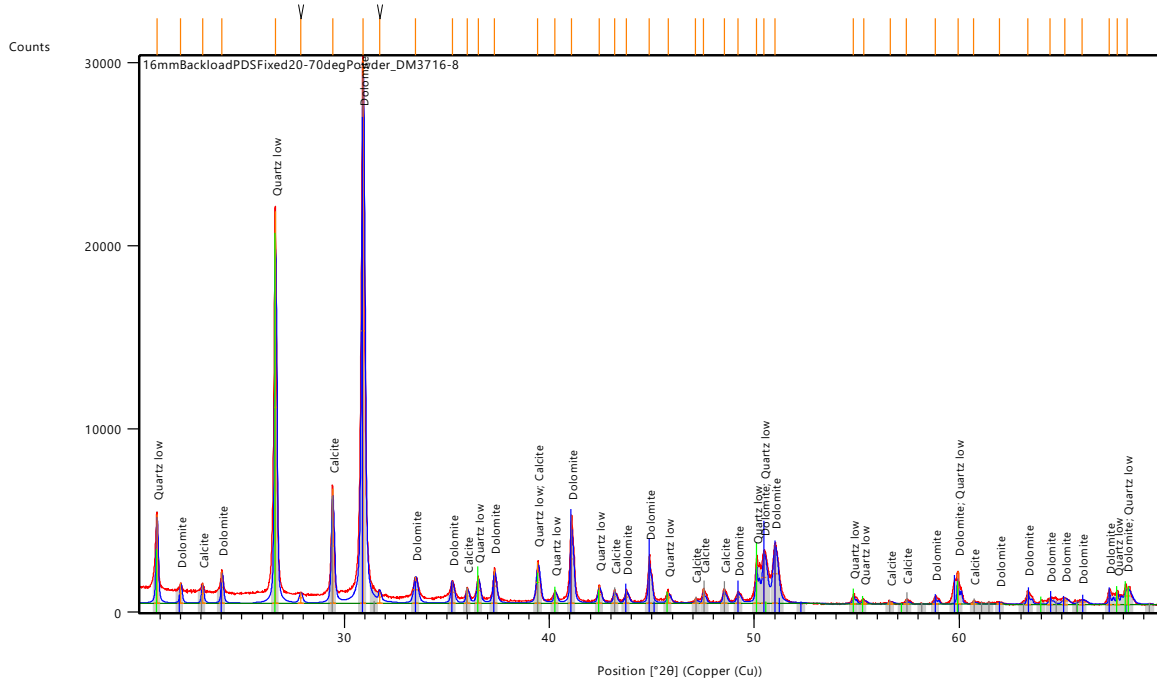
Table B.3 Mineral count list for core plug sample DM3716.8.

Pos. [°2θ]	Height [cts]	FWHM Left [°2θ]	d-spacing [Å]	Rel. Int. [%]
20.8568	4827.23	0.1102	4.25916	16.24
22.0206	1089.01	0.1102	4.03662	3.66
23.0757	1074.01	0.1102	3.85439	3.61
24.0327	1752.50	0.1102	3.70303	5.90
26.6361	21399.63	0.1102	3.34672	72.01
27.8621	582.39	0.1653	3.20218	1.96
29.4246	6261.66	0.1378	3.03559	21.07
30.9054	29717.43	0.1653	2.89344	100.00
31.7165	634.43	0.1102	2.82127	2.13
33.4688	1421.15	0.2204	2.67746	4.78
35.2629	1198.15	0.1653	2.54525	4.03
35.9944	830.74	0.1378	2.49518	2.80
36.5270	1413.76	0.1653	2.46001	4.76
37.3209	1839.13	0.1653	2.40948	6.19
39.4400	2237.30	0.1929	2.28477	7.53
40.2757	692.51	0.1378	2.23927	2.33
41.0800	4803.00	0.1378	2.19727	16.16

42.4283	960.37	0.1653	2.13052	3.23
43.1777	731.49	0.1378	2.09526	2.46
43.7560	703.26	0.1653	2.06890	2.37
44.8838	2584.81	0.1378	2.01950	8.70
45.8069	592.62	0.1653	1.98093	1.99
47.1393	244.50	0.1102	1.92800	0.82
47.5246	783.82	0.1102	1.91326	2.64
48.5275	778.75	0.1378	1.87604	2.62
49.2089	616.05	0.1653	1.85165	2.07
50.1108	2407.94	0.1102	1.82042	8.10
50.4768	2815.65	0.2204	1.80808	9.47
51.0049	3229.65	0.2480	1.79059	10.87
54.8426	514.22	0.1102	1.67402	1.73
55.3404	225.86	0.1653	1.66014	0.76
56.6487	121.17	0.2204	1.62486	0.41
57.4302	274.40	0.1102	1.60460	0.92
58.8422	451.71	0.1102	1.56942	1.52
59.9333	1792.56	0.1102	1.54343	6.03
60.7058	201.00	0.1102	1.52563	0.68
61.9571	102.93	0.2204	1.49779	0.35
63.3541	714.79	0.1378	1.46808	2.41
64.4229	361.42	0.1653	1.44629	1.22
65.1330	366.41	0.2755	1.43223	1.23
65.9886	256.78	0.3857	1.41572	0.86
67.3284	840.23	0.1102	1.39077	2.83
67.7133	743.45	0.1102	1.38380	2.50
68.1839	929.88	0.3306	1.37539	3.13

Table B.4 Mineral pattern list for core plug sample DM3716.8.

Visible	Ref. Code	Score	Compound Name	Displacement [°2Th.]	Scale Factor	Chemical Formula
*	98-018-5046	89	Dolomite	-0.093	0.872	C2 Ca1 Mg1 O6
*	98-009-0145	81	Quartz low	-0.013	0.664	O2 Si1
*	98-003-7241	79	Calcite	-0.067	0.192	C1 Ca1 O3

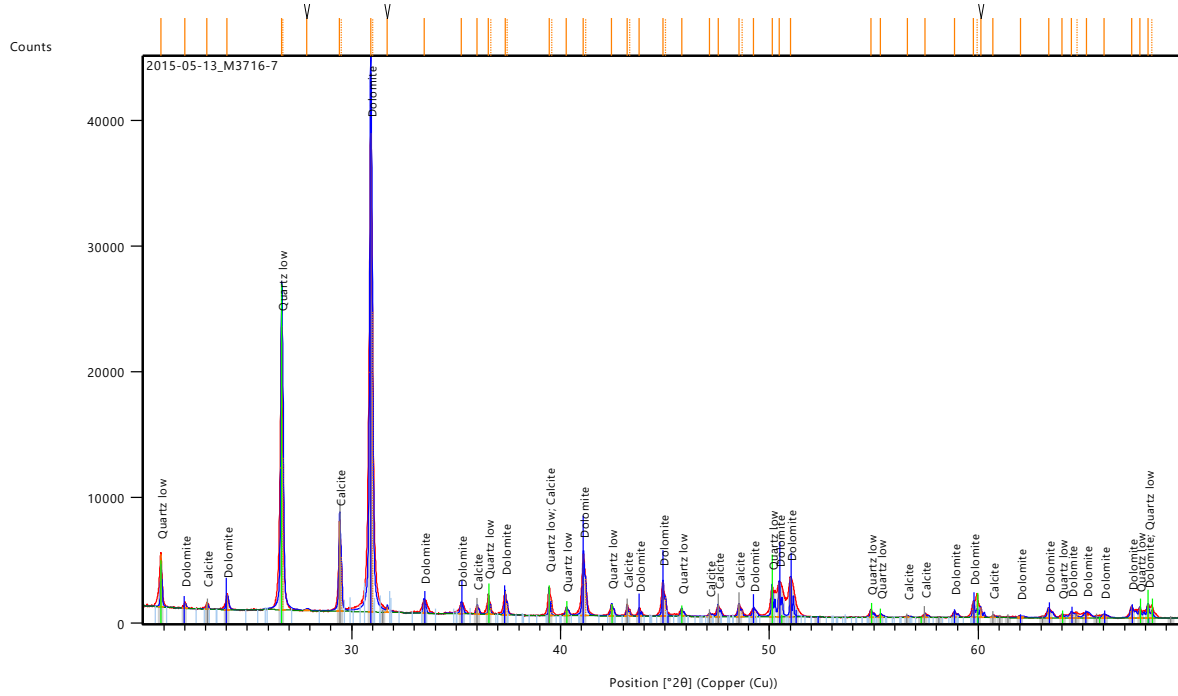**Figure B.3** Diffractogram for core plug sample DM3749.9.
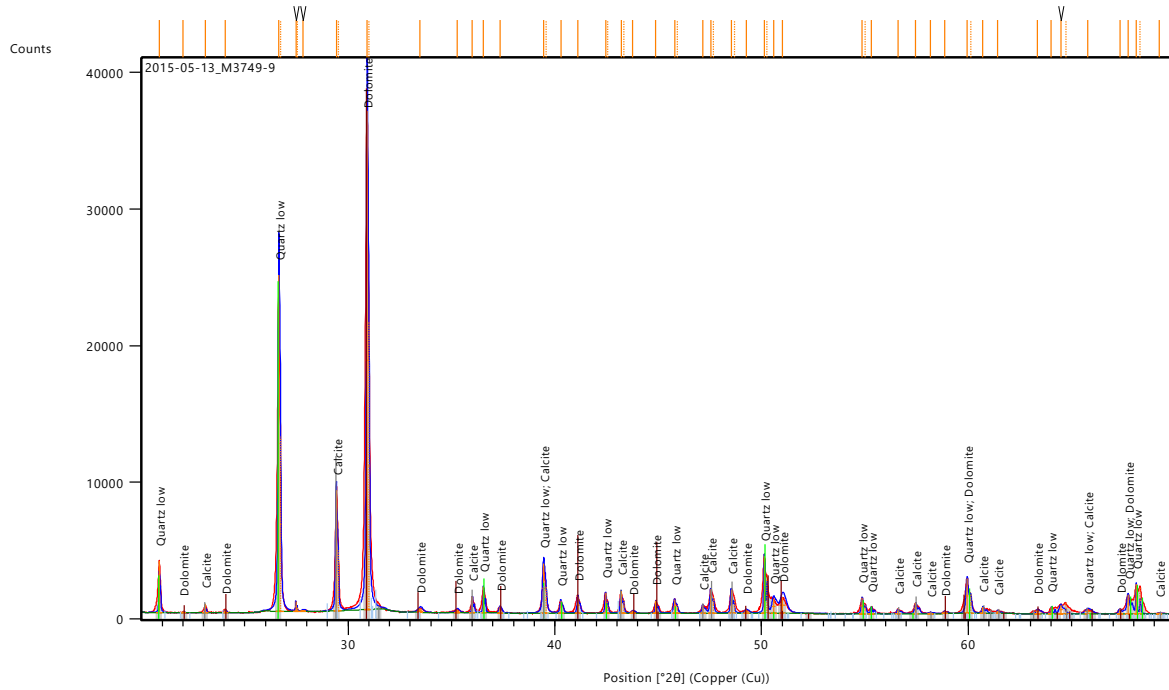
Table B.5 Mineral count list for core plug sample DM3749.9.

Pos. [°2θ]	Height [cts]	FWHM Left [°2θ]	d-spacing [Å]	Rel. Int. [%]
20.8693	3786.66	0.0551	4.25664	10.38
22.0169	79.07	0.0827	4.03729	0.22
23.0824	627.31	0.0413	3.85329	1.72
24.0465	245.76	0.0964	3.70093	0.67
26.6497	24587.01	0.0840	3.34227	67.40
26.7210	12780.62	0.0420	3.34179	35.03
27.4679	720.00	0.0336	3.24455	1.97
27.5427	356.90	0.0420	3.24394	0.98
27.8279	120.82	0.2352	3.20338	0.33
29.4258	8847.12	0.0756	3.03296	24.25
29.5290	4406.38	0.0588	3.03011	12.08
30.9163	36480.76	0.0924	2.89005	100.00
31.0031	21075.69	0.0588	2.88932	57.77
33.4668	291.50	0.2688	2.67540	0.80
35.2673	232.79	0.1680	2.54283	0.64
36.0104	1171.82	0.0588	2.49205	3.21
36.5456	1932.16	0.0588	2.45677	5.30
37.3377	462.87	0.1176	2.40645	1.27
39.4538	3616.67	0.1260	2.28212	9.91

39.5712	1944.88	0.0672	2.28127	5.33
40.2854	897.75	0.1008	2.23690	2.46
41.1130	1242.15	0.0924	2.19377	3.40
42.4541	1501.84	0.0756	2.12752	4.12
42.5598	833.05	0.0504	2.12775	2.28
43.2020	1616.09	0.0840	2.09240	4.43
43.3228	950.08	0.0504	2.09203	2.60
43.7662	181.47	0.1344	2.06673	0.50
44.8857	888.86	0.0840	2.01775	2.44
45.7915	992.25	0.1176	1.97992	2.72
45.9135	578.26	0.0504	1.97985	1.59
47.1514	587.25	0.1008	1.92594	1.61
47.5408	1771.31	0.1008	1.91107	4.86
47.6682	1264.66	0.0840	1.91099	3.47
48.5277	1743.50	0.0840	1.87448	4.78
48.6987	1078.29	0.0672	1.87294	2.96
49.2520	252.16	0.1680	1.84860	0.69
50.1363	4197.26	0.0672	1.81805	11.51
50.2702	2629.47	0.0672	1.81802	7.21
50.5747	1048.43	0.1680	1.80331	2.87
51.0043	1126.52	0.3024	1.78912	3.09
54.8692	1174.92	0.1008	1.67189	3.22
55.0093	702.68	0.0840	1.67211	1.93
55.3117	507.77	0.0840	1.65956	1.39
56.5912	308.91	0.1176	1.62503	0.85
57.4599	782.30	0.1176	1.60251	2.14
58.1636	82.43	0.2016	1.58479	0.23
58.8482	171.87	0.1008	1.56797	0.47
59.9440	2559.42	0.1344	1.54190	7.02
60.1236	1363.99	0.0840	1.54155	3.74
60.7086	462.58	0.1176	1.52430	1.27

Table B.6 Mineral pattern list for core plug sample DM3749.9.

Visible	Ref. Code	Score	Compound Name	Displacement [°2Th.]	Scale Factor	Chemical Formula
*	98-002-9210	67	Quartz low	-0.078	0.586	O2 Si1
*	98-003-7241	70	Calcite	-0.044	0.276	C1 Ca1 O3
*	98-002-7540	47	Dolomite	0.063	0.927	C2 Ca1 Mg1 O6

Figure B.4 Diffractogram for core plug sample DM3829.4.
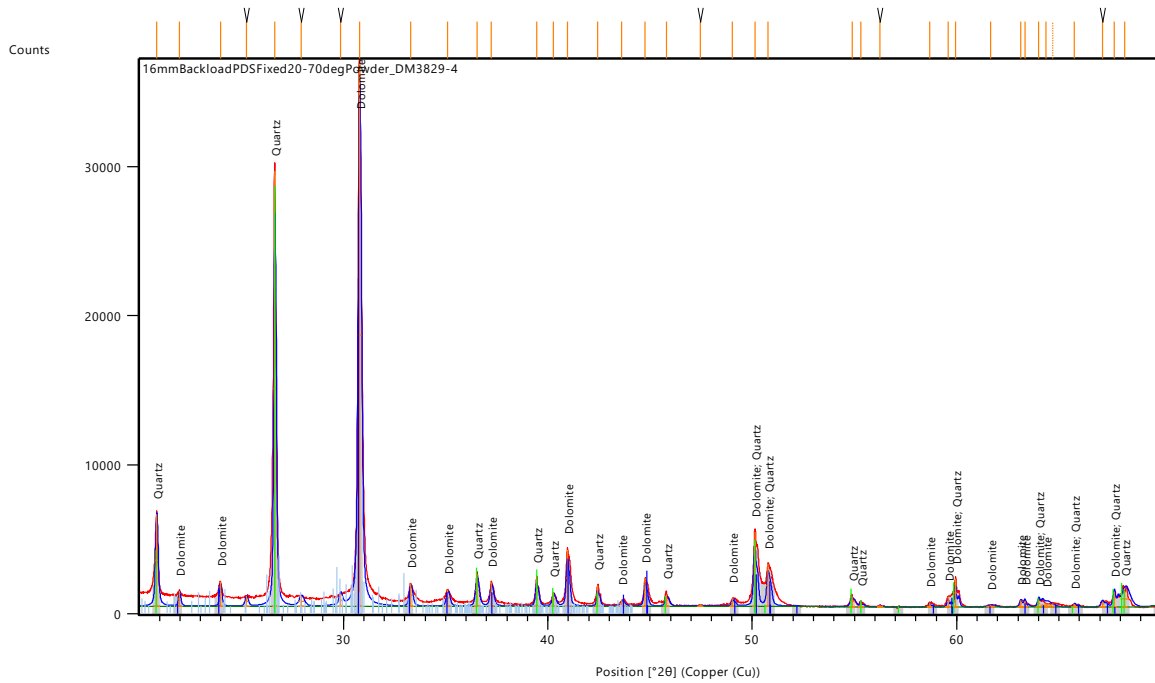
Table B.7 Mineral count list for core plug sample DM3829.4.

Pos. [°2θ]	Height [cts]	FWHM Left [°2θ]	d-spacing [Å]	Rel. Int. [%]
20.8617	6175.41	0.1378	4.25817	16.99
21.9698	1028.12	0.1102	4.04585	2.83
23.9786	1641.11	0.1102	3.71126	4.52
25.2539	673.80	0.1653	3.52667	1.85
26.6422	29168.18	0.1102	3.34596	80.26
27.9382	694.77	0.2755	3.19362	1.91
29.8493	819.02	0.1653	2.99337	2.25
30.7819	36340.73	0.1653	2.90477	100.00
33.2868	1504.17	0.1653	2.69169	4.14
35.1010	1093.19	0.1653	2.55661	3.01
36.5312	2132.98	0.1653	2.45974	5.87
37.2341	1574.75	0.1653	2.41490	4.33
39.4490	1841.99	0.1378	2.28427	5.07
40.2721	915.92	0.1653	2.23947	2.52
40.9530	3755.78	0.1378	2.20379	10.33
42.4359	1396.71	0.1102	2.13015	3.84
43.6165	373.13	0.2204	2.07519	1.03
44.7561	1858.24	0.1378	2.02497	5.11
45.8121	779.86	0.1653	1.98072	2.15

47.4530	83.91	0.1653	1.91599	0.23
49.0375	523.60	0.1378	1.85772	1.44
50.1220	4973.55	0.1378	1.82004	13.69
50.7769	2825.53	0.1653	1.79809	7.78
54.8779	692.94	0.2204	1.67303	1.91
55.3053	368.71	0.1102	1.66111	1.01
56.2301	106.46	0.1653	1.63596	0.29
58.6713	318.88	0.1102	1.57358	0.88
59.5703	699.76	0.1102	1.55197	1.93
59.9375	1907.72	0.1102	1.54333	5.25
61.6448	154.41	0.4408	1.50462	0.42
63.1348	469.25	0.1344	1.47144	1.29
63.3463	408.39	0.1102	1.46825	1.12
64.0166	530.24	0.1344	1.45328	1.46
64.3590	289.69	0.5376	1.44637	0.80
64.6917	305.77	0.2016	1.44331	0.84
65.7578	229.15	0.1344	1.41895	0.63
67.1244	409.46	0.1680	1.39334	1.13
67.7136	1061.31	0.1344	1.38265	2.92
68.2224	1073.94	0.4032	1.37357	2.96

Table B.8 Mineral pattern list for core plug sample DM3829.4.

Visible	Ref. Code	Score	Compound Name	Displacement [°2Th.]	Scale Factor	Chemical Formula
*	98-017-1520	90	Dolomite	-0.190	0.589	C2 Ca1 Mg1 O6
*	98-015-6196	87	Quartz	0.028	0.756	O2 Si1

Figure B.5 Diffractogram for core plug sample DM3829.5.
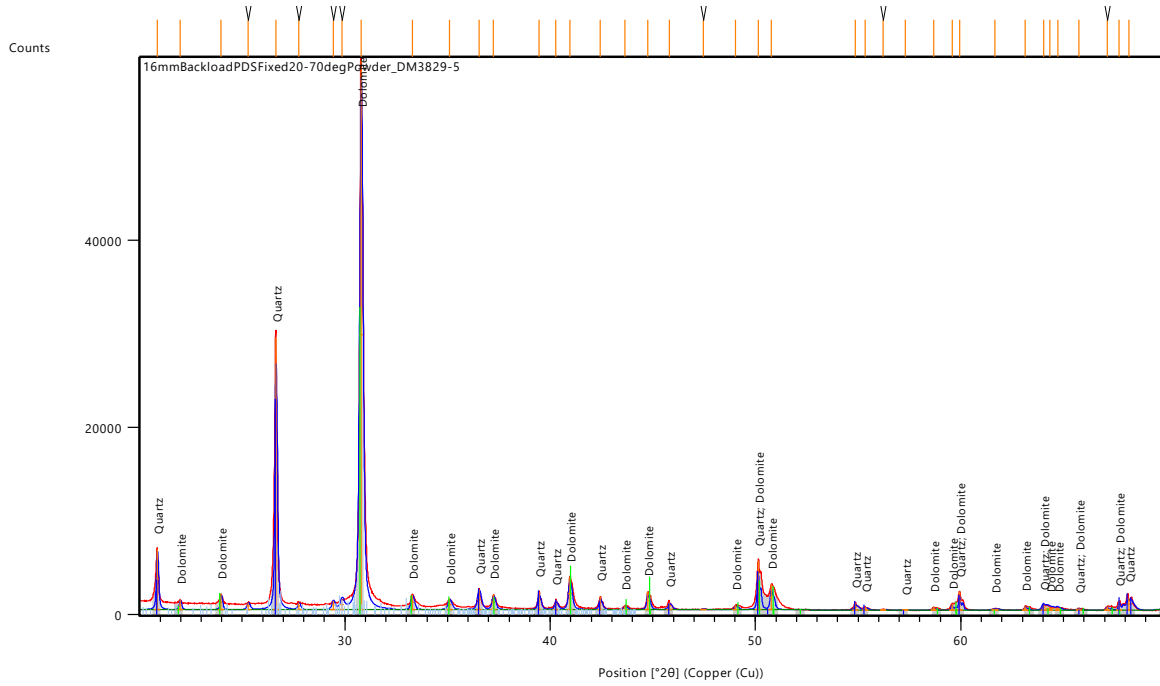
Table B.9 Mineral count list for core plug sample DM3829.5.

Pos. [°2θ]	Height [cts]	FWHM Left [°2θ]	d-spacing [Å]	Rel. Int. [%]
20.8625	6483.28	0.1102	4.25802	11.04
21.9748	1039.93	0.1102	4.04494	1.77
23.9733	1654.87	0.1102	3.71207	2.82
25.2907	756.49	0.1653	3.52162	1.29
26.6384	29112.95	0.1102	3.34643	49.59
27.7589	745.31	0.1378	3.21385	1.27
29.4287	920.57	0.1378	3.03518	1.57
29.8492	1046.82	0.1929	2.99338	1.78
30.7826	58709.48	0.1653	2.90471	100.00
33.2801	1595.20	0.1653	2.69221	2.72
35.0931	1123.79	0.1929	2.55717	1.91
36.5260	2150.47	0.1929	2.46008	3.66
37.2290	1587.30	0.1653	2.41522	2.70
39.4487	1866.59	0.1378	2.28429	3.18
40.2706	991.38	0.1378	2.23954	1.69
40.9503	3465.04	0.1653	2.20393	5.90
42.4299	1368.08	0.1378	2.13044	2.33
43.6321	436.98	0.1378	2.07449	0.74
44.7527	1901.29	0.1378	2.02511	3.24

45.8108	744.60	0.1653	1.98077	1.27
47.4574	69.63	0.2204	1.91582	0.12
49.0235	484.85	0.1378	1.85822	0.83
50.1244	5234.43	0.1102	1.81996	8.92
50.7733	2724.73	0.1378	1.79821	4.64
54.8693	696.97	0.1653	1.67327	1.19
55.3455	299.93	0.1653	1.66000	0.51
56.2017	110.12	0.2204	1.63672	0.19
57.2871	29.06	0.3306	1.60827	0.05
58.6710	323.97	0.1102	1.57359	0.55
59.5678	697.51	0.1102	1.55202	1.19
59.9339	2001.22	0.1102	1.54342	3.41
61.6556	164.82	0.3857	1.50439	0.28
63.1402	416.68	0.1378	1.47254	0.71
64.0232	584.80	0.1680	1.45314	1.00
64.3383	382.75	0.4408	1.44798	0.65
64.7169	309.48	0.2204	1.44043	0.53
65.7373	222.64	0.1378	1.42052	0.38
67.1204	434.16	0.1102	1.39457	0.74
67.7174	994.61	0.1102	1.38372	1.69
68.1817	1340.92	0.3306	1.37543	2.28

Table B.10 Mineral pattern list for core plug sample DM3829.5.

Visible	Ref. Code	Score	Compound Name	Displacement [°2Th.]	Scale Factor	Chemical Formula
*	98-016-2490	87	Quartz	-0.041	0.377	O2 Si1
*	98-017-1520	85	Dolomite	-0.191	0.542	C2 Ca1 Mg1 O6

Figure B.6 Diffractogram for core plug sample DA4300.3.

Table B.11 Mineral count list for core plug sample DA4300.3.

Pos. [°2θ]	Height [cts]	FWHM Left [°2θ]	d-spacing [Å]	Rel. Int. [%]
20.8537	1868.42	0.1102	4.25980	1.32
22.0150	1303.33	0.1102	4.03763	0.92
24.0549	2170.86	0.1102	3.69966	1.54
26.6363	5389.78	0.1102	3.34669	3.82
27.8671	704.30	0.1653	3.20161	0.50
29.4533	538.03	0.1102	3.03270	0.38
29.8973	815.42	0.1929	2.98867	0.58
30.9359	141074.00	0.1653	2.89066	100.00
33.5133	4578.42	0.1378	2.67401	3.25
35.2895	2532.02	0.1653	2.54339	1.79
36.5186	534.50	0.1653	2.46056	0.38
37.3426	3003.53	0.1378	2.40814	2.13
39.4434	348.38	0.1102	2.28459	0.25
40.2635	246.70	0.1378	2.23992	0.17
41.1068	8833.81	0.1378	2.19590	6.26
42.4154	244.32	0.1102	2.13113	0.17
43.7721	988.76	0.1102	2.06818	0.70
44.9409	3412.80	0.2204	2.01707	2.42

45.8092	151.35	0.1653	1.98083	0.11
49.2822	893.99	0.2204	1.84907	0.63
50.4920	8001.21	0.1102	1.80757	5.67
51.0751	6546.05	0.2204	1.78829	4.64
52.3426	83.50	0.2204	1.74793	0.06
54.8888	116.32	0.2204	1.67272	0.08
56.3116	32.39	0.3306	1.63379	0.02
58.8677	772.51	0.1102	1.56880	0.55
59.7909	1834.86	0.1102	1.54677	1.30
61.9718	303.61	0.1378	1.49747	0.22
63.4066	1647.64	0.1102	1.46700	1.17
64.4680	1570.13	0.1102	1.44538	1.11
65.1040	975.35	0.1102	1.43280	0.69
66.0412	552.72	0.1102	1.41472	0.39
67.3565	1323.86	0.2204	1.39026	0.94
68.1994	174.40	0.2755	1.37512	0.12

Table B.12 Mineral pattern list for core plug sample DA4300.3.

Visible	Ref. Code	Score	Compound Name	Displacement [°2Th.]	Scale Factor	Chemical Formula
*	00-036-0426	66	Calcium Magnesium Carbonate	-0.041	0.646	Ca Mg (C O3)2

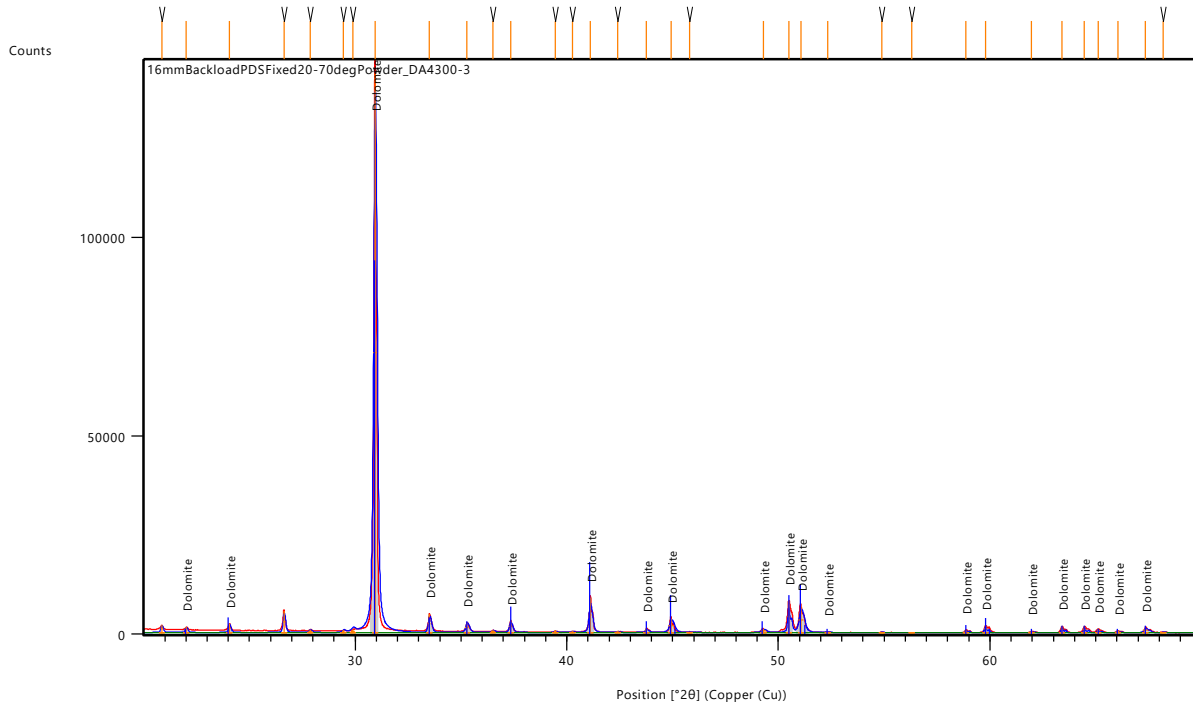**Figure B.7** Diffractogram for core plug sample DA4300.4.

Table B.13 Mineral count list for core plug sample DA4300.4.

Pos. [°2θ]	Height [cts]	FWHM Left [°2θ]	d-spacing [Å]	Rel. Int. [%]
20.8639	956.24	0.0344	4.25774	0.43
22.0403	848.36	0.0482	4.03306	0.38
24.0692	1686.41	0.0482	3.69750	0.76
25.6623	77.20	0.1653	3.47146	0.04
26.6405	4170.79	0.0588	3.34341	1.89
26.7176	2001.73	0.0336	3.34222	0.91
27.5097	153.71	0.2016	3.23971	0.07
27.9031	555.54	0.0588	3.19492	0.25
29.3989	236.31	0.0504	3.03568	0.11
29.9163	397.64	0.1344	2.98434	0.18
30.9502	220499.40	0.0756	2.88697	100.00
31.0408	106635.80	0.0504	2.88590	48.36
33.0400	220.31	0.0504	2.70898	0.10
33.5166	3670.82	0.1008	2.67154	1.66
33.6222	2093.45	0.0588	2.67001	0.95
35.2955	2590.70	0.0756	2.54086	1.17
35.4051	1374.31	0.0504	2.53955	0.62
36.5314	246.17	0.0840	2.45769	0.11
37.3585	3099.71	0.0672	2.40516	1.41
37.4686	1468.08	0.0504	2.40430	0.67
39.4562	242.56	0.0672	2.28198	0.11

40.2701	154.27	0.1008	2.23772	0.07
41.1166	8321.80	0.0840	2.19358	3.77
41.2461	4168.36	0.0672	2.19243	1.89
42.4371	157.48	0.1008	2.12833	0.07
43.7861	1184.71	0.1008	2.06584	0.54
43.9133	640.78	0.0672	2.06526	0.29
44.9377	4971.09	0.0840	2.01553	2.25
45.0572	2533.84	0.0588	2.01546	1.15
45.7887	134.17	0.1680	1.98004	0.06
47.4627	59.59	0.2688	1.91403	0.03
49.2683	1200.89	0.1008	1.84803	0.54
49.4014	699.52	0.0672	1.84794	0.32
50.1375	775.86	0.0420	1.81801	0.35
50.4816	7304.13	0.0672	1.80642	3.31
50.5139	8620.36	0.0672	1.80534	3.91
50.6530	5113.34	0.0420	1.80518	2.32
51.0465	6924.99	0.0504	1.78775	3.14
51.0845	6575.71	0.0336	1.78651	2.98
51.2090	4230.40	0.0840	1.78245	1.92
52.3281	110.29	0.1008	1.74694	0.05
54.1088	172.43	0.0504	1.69357	0.08
54.8606	124.66	0.1008	1.67213	0.06
56.2694	155.98	0.0672	1.63356	0.07
58.8905	926.14	0.0924	1.56695	0.42
59.0453	528.01	0.0672	1.56709	0.24
59.8095	1872.77	0.0924	1.54505	0.85
59.9783	1195.33	0.0504	1.54493	0.54
62.0298	282.52	0.1176	1.49497	0.13
63.4073	1429.84	0.0924	1.46577	0.65

Table B.14 Mineral pattern list for core plug sample DA4300.4.

Visible	Ref. Code	Score	Compound Name	Displacement [°2Th.]	Scale Factor	Chemical Formula
*	98-018-5049	42	Dolomite	-0.020	0.868	C2 Ca1 Mg1 O6
*	98-003-1228	53	Quartz low	-0.003	0.018	O2 Si1

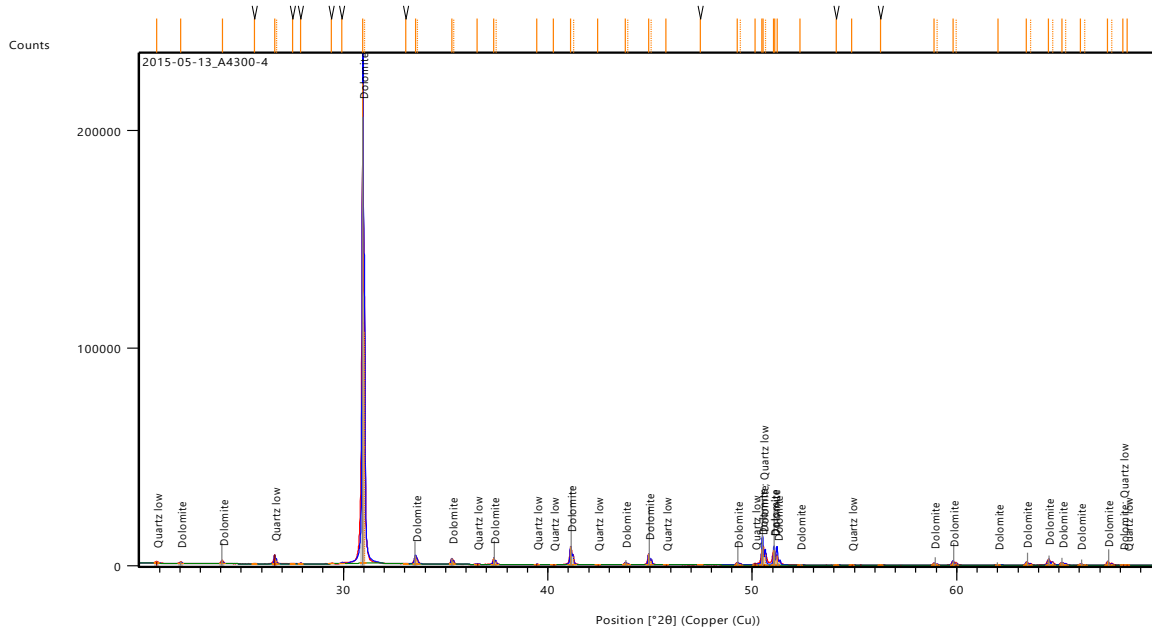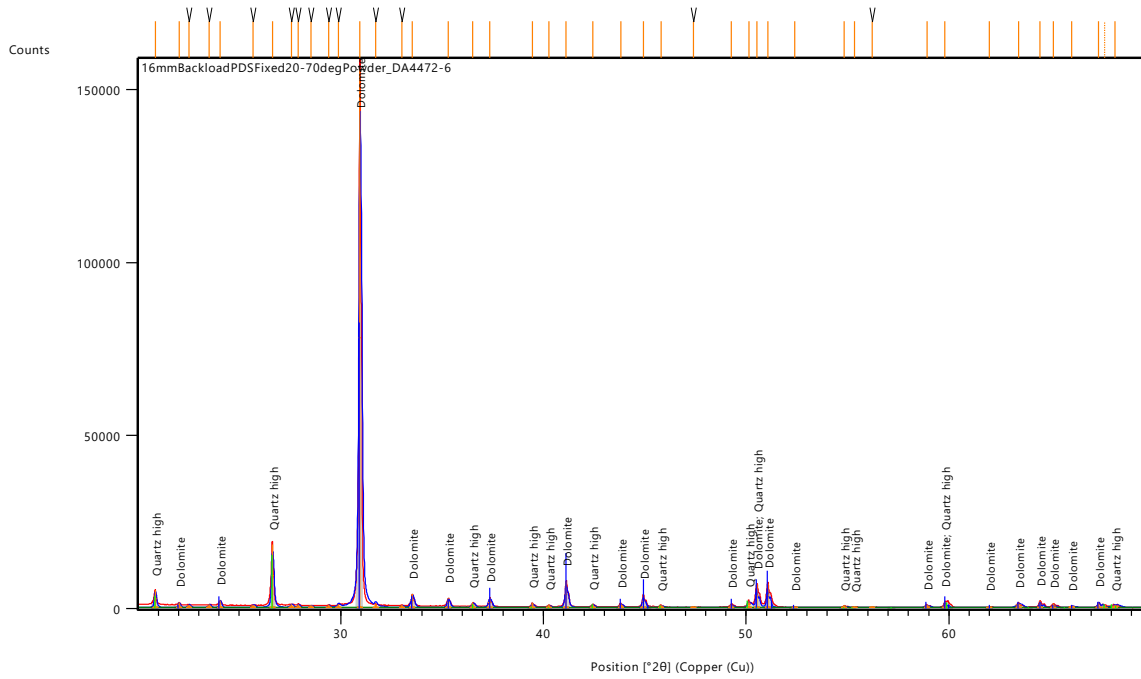**Figure B.8** Diffractogram for core plug sample DA4472.6.

Table B.15 Mineral count list for core plug sample DA4472.6.

Pos. [°2θ]	Height [cts]	FWHM Left [°2θ]	d-spacing [Å]	Rel. Int. [%]
20.8544	4940.44	0.1102	4.25965	3.17
22.0295	1394.64	0.1102	4.03501	0.90
22.5134	827.28	0.1653	3.94937	0.53
23.5123	868.23	0.1653	3.78379	0.56
24.0600	2057.75	0.1102	3.69889	1.32
25.6864	801.23	0.1653	3.46826	0.51
26.6357	18230.30	0.1102	3.34676	11.71
27.5655	960.17	0.1653	3.23596	0.62
27.9156	1000.44	0.1102	3.19616	0.64
28.5310	597.57	0.1653	3.12860	0.38
29.4084	795.45	0.1102	3.03723	0.51
29.8924	1001.16	0.1102	2.98915	0.64
30.9507	155623.40	0.1378	2.88931	100.00
31.7113	1114.11	0.1102	2.82173	0.72
33.0115	714.79	0.1102	2.71350	0.46
33.5317	3872.30	0.1653	2.67258	2.49
35.3043	2712.57	0.1378	2.54236	1.74
36.5204	1466.60	0.1653	2.46044	0.94
37.3501	2818.62	0.1653	2.40767	1.81

39.4444	1299.08	0.1102	2.28453	0.83
40.2629	762.45	0.1102	2.23995	0.49
41.1168	7431.07	0.1378	2.19539	4.78
42.4232	976.28	0.1378	2.13076	0.63
43.8229	1097.66	0.1653	2.06590	0.71
44.9182	3748.49	0.1102	2.01803	2.41
45.8047	603.41	0.1653	1.98102	0.39
47.4014	184.81	0.1653	1.91795	0.12
49.2611	1060.94	0.1102	1.84981	0.68
50.1287	1863.89	0.1653	1.81981	1.20
50.5143	6690.88	0.1102	1.80682	4.30
51.0543	6923.65	0.1102	1.78897	4.45
52.3794	175.48	0.2204	1.74679	0.11
54.8396	555.85	0.1102	1.67411	0.36
55.3386	218.35	0.1653	1.66019	0.14
56.2160	174.83	0.1102	1.63634	0.11
58.9081	733.67	0.2204	1.56782	0.47
59.8006	1689.41	0.1102	1.54654	1.09
61.9945	257.97	0.1102	1.49698	0.17
63.4234	1340.71	0.2755	1.46665	0.86
64.4945	1832.06	0.1102	1.44485	1.18
65.1374	1078.81	0.1102	1.43214	0.69
66.0580	419.05	0.2755	1.41440	0.27
67.3855	1463.38	0.1344	1.38858	0.94
67.6596	800.78	0.1344	1.38706	0.51
68.2007	608.91	0.4032	1.37395	0.39

Table B.16 Mineral pattern list for core plug sample DA4472.6.

Visible	Ref. Code	Score	Compound Name	Displacement [°2Th.]	Scale Factor	Chemical Formula
*	00-036-0426	63	Calcium Magnesium Carbonate	-0.031	0.517	Ca Mg (C O3)2
*	98-004-2498	43	Quartz high	0.013	0.095	O2 Si1